Compact and low-cost ultrashort-pulse Ti:sapphire lasers

Jamie Charles Enterkin Coyle

A thesis presented in fulfilment of the requirements for the degree of Doctorate of Engineering (EngD).

University of Strathclyde, Department of Physics

June 2021

Declaration of Authenticity and Author's Rights

This thesis is the result of the author's original research. It has been composed by the author and has not been previously submitted for examination which has led to the award of a degree.

Signed:

Date:

Contents

Abstract

The subject matter of this thesis centres around the design and development of ultrafast Ti:sapphire lasers in a compact and low-cost context. Using 450 nm laser diodes as the pump source, both semiconductor saturable absorber mirror (SESAM) mode-locking and Kerr-lens mode-locking (KLM) techniques are used. Broad wavelength tunability while maintaining femtosecond pulse operation at 100's of mW of average power and 10's of kW of peak power was demonstrated. In the SESAM mode-locked configuration, a wavelength tunability range of 37 nm (788-825 nm) was demonstrated, with average output powers up to 433 mW, and with shortest pulse duration of 62 fs at 812 nm. In the KLM regime, a wavelength tunability range of 120 nm (755-875 nm) was demonstrated, with average output powers up to 382 mW, and with shortest pulse duration of 54 fs at 810 nm.

Various cavity configurations were proposed and analysed with the intention of realising GHz pulse repetition rates in an ultrafast diode-pumped Ti:sapphire laser. Two different cavity configurations were chosen: KLM in a ring resonator configuration and SESAM mode-locking in a Z-shape standing-wave resonator configuration. Efficient continuous wave operation was achieved, however, mode-locked operation was not reached with either configuration.

Graphene saturable absorbers for femtosecond pulse generation in diode-pumped Ti:sapphire were also investigated. Monolayer graphene samples were fully characterised in a differential transmission setup. This resulted in a saturation fluence of (41± 27) μJ/cm^2, a saturable loss of (1.01 ± 0.15)% and a non-saturable loss of (0.42 ± 0.09)%, in broad agreement with values reported in the literature.

The diode-pumped Ti:sapphire laser sources developed during the course of this thesis have demonstrated important performance parameters that bring them closer to matching the performance of their conventionally pumped counterparts, namely a wide wavelength tunability while maintaining femtosecond pulse operation at 100's of mW of average power and 10's of kW of peak power, suitable for many applications.

Acknowledgements

There are a great many people I would like to thank who have been involved in my EngD journey in some manner, whether in academic/professional capacity or simply the friends I have made along the way.

At the top of the list are my supervisors Prof. Alan Kemp and Dr. Alex Lagatsky, whose guidance, support, encouragement, and patience have been invaluable to me. The knowledge and experience I have gained working with them both I am sure to take with me throughout my career.

I would next like to thank all those at Fraunhofer Centre of Applied Photonics for making the whole EngD experience so enjoyable, from the interesting, open, and collaborative work environment to the lunchtime 5-a-side games, FCAP social outings, and DnD nights!

I would also like to thank all those involved with the CDT in Applied Photonics for their support and opportunities provided – being able to present my work at a conference in Japan was a fantastic experience and a particular highlight! Also, to all the friends I made in my cohort who made my time in St. Andrews special and the annual CDT conference night out something to look forward to.

Lastly, I would like to thank my family and friends for all the support and encouragement they have given me. In particular, my Mum, Dad, brother Alex, and Gran who have always been my biggest supporters and always believed in me even when I may have doubted myself. Without their support and love this work would not have been possible.

Chapter 1: Introduction and background 2

Chapter 1: Introduction and background

1.1 Introduction

Since their initial conception and demonstration, lasers have become devices that are ubiquitous, used around the world in countless applications. A majority of the world's population carry several lasers in our pocket every day, contained within a smartphone [1]. For example, the iPhone 12 uses VCSEL-based (vertical cavity surface-emitting laser) lidar arrays for augmented-reality applications and computational photography [2]. There are many other applications that lasers are used for, too numerous to mention here.

The subject of this project and thesis is concerned with a specific category of lasers, namely ultrafast lasers, which are used in applications such as fundamental science, metrology, biomedical science, imaging, medicine, communications, industrial processing, with more applications regularly being added to the list. Although an accepted term, the name ultrafast itself is a misnomer as the laser or light generated isn't "faster". A more accurate term would be ultrashort pulse laser, as it is the pulses generated by the laser which are ultrashort. So, what is an ultrashort pulse? There is no strict definition of ultrashort pulse but is generally accepted to be a pulse with duration of a few tens of picoseconds (10^{-12} s) down to a few femtoseconds (10^{-15} s).

It is hard to grasp exactly how short a femtosecond is and understandably many analogies to understand or conceptualise the scale of a femtosecond pulse have been created. One such analogy is that more than 10 times as many femtoseconds elapse every second than hours that have passed since the big bang [3].

The applications of ultrafast lasers are numerous, with only a few mentioned here. An important application is their use in fundamental science. For example, in femtochemistry many atomic and molecular events/reactions occur on timescales of the order of femtosecond to picoseconds. Using ultrashort pulses has allowed us to witness these events, work that Zewail won the Nobel Prize in Chemistry in 1999 [4]. Hall and Hänsch won one half of the Nobel Prize in Physics in 2005 for their work on femtosecond laser based frequency combs [5], which have important applications in optical clocks and spectroscopy [6]. In 2018, Strickland and Morou won one half of the Nobel Prize in Physics for their Chirped Pulse Amplification technique [7], crucial in realising the highest intensity lasers that are vital in research areas including nuclear fusion [8] and astrophysics [9]. Another example is where an ultrafast seed laser and amplifier are used to create attosecond pulses through high-harmonic

generation [10]. These pulses are used to study research topics including electronic motion in various materials [10].

The high peak intensities of an ultrafast laser mean that nonlinear effects such as two-photon absorption effects are accessible and can be exploited in biomedical imaging modalities such as two-photon microscopy [11], and in ultrafast laser inscription [12], which along with selective chemical etching can be used to fabricate microfluidic and waveguide devices [13]. The same very high peak intensities can be used for very high precision machining through ablation effects [14] and are also used in laser eye surgery [15].

In supercontinuum generation, ultrashort pulses are launched into nonlinear fibre to generate a coherent broadband "white light source" used for frequency combs [6], which themselves have a host of applications, optical coherence tomography [16] and optical communications [17].

New applications for ultrafast lasers being demonstrated regularly, and as such they are becoming an increasingly indispensable tool in many areas. However, despite seeing a lot of progress over the last 10-15 years such as the development of turn-key designs, ultrafast lasers largely remain expensive, bulky, and complex lab-bound devices, (the reasons for this are explored in more detail in Chapter 2). Thus, there is a demand to make them less expensive, more compact, and less complex, allowing for their proliferation to many more applications or increased adoption for use in existing applications where these factors are currently holding them back.

This project and thesis aim to address some of these problems and demonstrate the improvement of ultrafast lasers in a compact and low-cost context. The rest of this chapter will include some detail on the fundamentals of ultrashort pulse generation and characterisation underpinning the work of this thesis, in addition to discussing compact and low-cost sources for ultrashort pulse generation.

1.2 Pulse propagation within a dielectric medium

In order to understand femtosecond pulse generation, it is necessary to describe the propagation and interaction of light through dielectric materials in the linear regime. This will naturally lead on to the pulse propagation in the nonlinear regime (covered in the next sub-section), where various nonlinear effects can be exploited in the generation of ultrashort pulses. We will begin with the mathematical description of an optical pulse [18]. The time dependent electric field of an optical pulse is given as:

$$E(t) = \varepsilon(t)e^{i\phi(t)}e^{-i\omega_0 t} \quad (1)$$

where $\varepsilon(t)$ is the electric field envelope varying in time, ω_0 is the optical carrier frequency, and $\phi(t)$ is the temporal phase variation across the pulse. The temporal envelope of the pulse amplitude could in general have any form, but when operating in the soliton mode-locked regime, lasers most often produce pulses described by a hyperbolic secant function, given by:

$$\varepsilon(t) = \varepsilon_0 \,\mathrm{sech}\left(\frac{1.763t}{\Delta\tau_P}\right) \quad (2)$$

where ε_0 is the real electric field amplitude and $\Delta\tau_P$ is the full width at half maximum duration of the pulse. This is commonly referred to as a sech^2 pulse due to the fact that the intensity of such a pulse is given by:

$$I(t) \approx |\varepsilon(t)|^2 = \varepsilon_0^2 \mathrm{sech}^2\left(\frac{1.763t}{\Delta\tau_P}\right) \quad (3)$$

Knowing the shape of the laser pulse is crucial in measuring the pulse duration for reasons explained later in this chapter (see section 1.5). By taking the Fourier transform of the temporal field amplitude of a pulse one can obtain its spectral field amplitude. This means that changes in the intensity or phase in the temporal domain will also translate to differences in the spectral domain of the pulse and vice-versa. This is results in the bandwidth theorem, where it can be shown that there is a minimum time-bandwidth product (TBP) given by:

$$\Delta\upsilon\Delta\tau_P \geq TBP \quad (4)$$

where $\Delta\upsilon$ is the full width at half maximum spectral bandwidth of a pulse. When the TBP is at the minimum value for a given pulse, the pulse is said to be "transform-limited", meaning that the temporal phase variation across the pulse $d\phi(t)/dt = 0$. What this value will be depends on the pulse shape, for example a sech^2 pulse profile will have a minimum TBP of 0.315, whereas for a Gaussian-shaped pulse the minimum TBP is 0.441. In the case where $\phi(t) \neq 0$, the pulse is "chirped" in frequency. Generally speaking, when a pulse with zero initial chirp or

positive chirp passes through a dielectric medium, the longer wavelength components emerge earlier than the shorter wavelength components, though for some materials and wavelength regions the opposite is true. According to the Bandwidth Theorem, as the spectral components of the pulse remain unchanged then the pulse duration will increase, also increasing the TBP. To create the shortest possible pulses, this frequency chirp must be compensated for. Details on how this chirp arises as well as methods to compensate for this chirp within a laser so that transform-limited pulses are generated are discussed in the next few sub-sections.

Understanding the interactions between dielectric media and ultrashort pulses propagating in a laser resonator is vital to the generation, control, and measurement of said pulses. Considering a dielectric medium, if an electric field is applied then an intensity-dependent polarisation response is observed:

$$P = \varepsilon_0 \chi_1 E + \varepsilon_0 \chi_2 E^2 + \varepsilon_0 \chi_3 E^3 + \cdots \quad (5)$$

where E is the applied electric field, ε_0 is the permittivity of free space, and χ_n is the nth order susceptibility of the material. The linear susceptibility term χ_1 is responsible for linear optical effects such as diffraction, refraction, and dispersion. When dealing with low-intensity electric fields only the linear susceptibility is significant. The higher order susceptibility terms give rise to various nonlinear effects. The χ_2 term is responsible for second-harmonic generation, optical parametric amplification, and sum-frequency mixing, but is zero for typical "centro-symmetric" laser gain media. The χ_3 term is responsible for third harmonic generation and the optical Kerr effect, and is non-zero in most dielectric materials. These terms, however, only become significant when dealing with extremely high electric fields, such as those generated by high peak power laser pulses.

It is important to firstly understand the effects of the low-intensity, linear term on a pulse propagating through a length L of transparent material. The frequency-dependent phase change of the pulse is given by:

$$\phi(\omega) = k(\omega)L = \frac{n_0(\omega)\omega}{c} L \quad (6)$$

where ω is the angular frequency, c is the speed of light, $k(\omega)$ is the frequency-dependent propagation constant for the material and $n_0(\omega)$ is the linear refractive index related to χ_1 by:

$$n_0(\lambda) = 1 + \frac{1}{2} Re[\chi_1(\lambda)] \tag{7}$$

In its most general form, the Sellmeier equation is given by:

$$n_0^2(\lambda) - 1 = \sum_i \frac{A_i \lambda^2}{\lambda^2 - B_i} \tag{8}$$

where each term of the sum represents an absorption resonance with strength A_i at a wavelength $\sqrt{B_i}$. Linear dispersive effects in dielectric media arise due to the dependence on frequency of the first order susceptibility. If we take a pulse of finite bandwidth, it is possible to expand $\phi(\omega)$ in a Taylor series around ω_0 the centre frequency of pulse:

$$\phi(\omega) = \phi_0 + \frac{\partial \phi}{\partial \omega}(\omega - \omega_0) + \frac{1}{2!}\frac{\partial^2 \phi}{\partial \omega^2}(\omega - \omega_0)^2 + \frac{1}{3!}\frac{\partial^3 \phi}{\partial \omega^3}(\omega - \omega_0)^3 + \cdots \tag{9}$$

where $\phi_0 = \phi(\omega_0)$,$\partial\phi/\partial\omega$ is the first order derivative of $\phi(\omega)$ with respect to ω evaluated at $\omega = \omega_0$ and so on. The terms in the expansion above determine how a pulse propagating in a dispersive dielectric medium behaves; $\partial\phi/\partial\omega$ is the group delay T_g, $\partial^2\phi/\partial\omega^2$ is the Group Delay Dispersion (GDD), and $\partial^3\phi/\partial\omega^3$ is the Third-Order Dispersion (TOD). While the first two terms in the expansion above do not affect the pulse shape, the GDD describes a linear frequency dependence of the group delay meaning that this tends to separate the frequency components of a pulse. For example, when considering positive GDD the higher frequency components are delayed compared to the components with lower frequencies, resulting in the pulse gaining a positive "chirp" (known as "up-chirp"). Higher orders of dispersion such as TOD generate more complicated distortions. The broader the spectral bandwidth of the pulse and thus the shorter the pulse duration, the more the higher order dispersion terms of the expansion become significant. The form and significance of the dispersion quantities are detailed in Table 1.

Table 1. Dispersion quantities including defining equations.

Quantity	Symbol	Defining equation	Defining equation using $n(\lambda)$
Phase velocity	v_p	$\frac{\omega}{k_n}$	$\frac{c}{n}$
Group velocity	v_g	$\frac{d\omega}{dk_n}$	$\frac{c}{n}\frac{1}{1-\frac{dn}{d\lambda}\frac{\lambda}{n}}$
Group delay	T_g	$T_g = \frac{z}{v_g} = \frac{d\phi}{d\omega}, \phi = k_n z$	$\frac{nz}{c}\left(1-\frac{dn}{d\lambda}\frac{\lambda}{n}\right)$
1st order dispersion	ϕ'	$\frac{d\phi}{d\omega}$	$\frac{nz}{c}\left(1-\frac{dn}{d\lambda}\frac{\lambda}{n}\right)$
2nd order dispersion	ϕ''	$\frac{d^2\phi}{d\omega^2}$	$\frac{\lambda^3 z}{2\pi c^2}\frac{d^2n}{d\lambda^2}$
3rd order dispersion	ϕ'''	$\frac{d^3\phi}{d\omega^3}$	$\frac{-\lambda^4 z}{4\pi^2 c^3}\left(3\frac{d^2n}{d\lambda^2}+\lambda\frac{d^3n}{d\lambda^3}\right)$

Considering an initially unchirped Gaussian pulse with FWHM pulse duration τ_0, if GDD is applied the effect will be an increase in the pulse duration according to [19]:

$$\frac{\tau_p(z)}{\tau_0} = \sqrt{1+\left(\frac{4\ln 2}{\tau_0^2}\frac{\partial^2\phi}{\partial\omega^2}\right)^2} \tag{10}$$

It is assumed that the incident pulse is transform-limited (i.e. the TBP = 0.441 for a Gaussian pulse). Only GDD and higher orders of dispersion contribute to the broadening of the pulse, with higher orders of dispersion only becoming significant at pulse durations below about 30 fs [19] and/or for large values of higher orders of dispersion associated with longer material lengths for example. The first-order dispersion ($\partial\phi/\partial\omega$) gives the group delay, which is the delay of the peak of the pulse envelope. It is obvious from the above equation that the effect of GDD becomes significant when GDD $> \tau_0^2$. In a similar vein, TOD becomes significant if TOD $> \tau_0^3$. An important point to note for dispersive pulse broadening (in the linear pulse propagation regime), is that there is no change to the pulse spectrum: the spectral content of the pulse experiences a redistribution in time. A Gaussian pulse with a linear frequency chirp is shown as:

$$\varepsilon(t) = \varepsilon_0 e^{-(1+ia)\left(\frac{t}{\tau_g}\right)^2} \tag{11}$$

where a is the chirp parameter and is negative for a positive up chirp and positive for a down chirp.

$$\frac{d\phi}{dt} = \frac{-2at}{\tau_g^2} \tag{12}$$

Shown in Figure 1 is an example of a heavily up-chirped pulse:

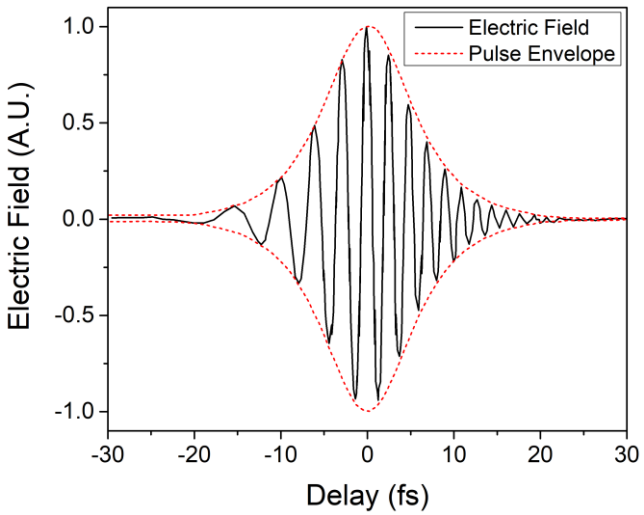

Figure 1. An example of a heavily up-chirped pulse.

The effect on pulse duration of differently chirped pulses as they propagate per unit length are listed for Ti:sapphire and a few widely used optical materials, such as fused silica or SF10 glasses. By differentiating the standard Sellmeier equation and using the expressions given in Table 1, we are able to calculate the GDD per unit length and TOD per unit length for most materials. The GDD per unit length and TOD per unit length have been calculated for a few pertinent optical materials and are shown in Table 2:

Table 2. Calculated GDD and TOD values per mm of common optical materials, calculated at 800 nm.

Material	GDD per mm (fs^2mm^{-1})	TOD per mm (fs^3mm^{-1})
Ti:sapphire	52.0	44.7
Fused silica	32.2	29.4
SF10	145.5	98.0

1.2.1 Dispersion compensation

To enable the shortest pulses to propagate within a laser cavity it is vital to compensate for the dispersive effects introduced by intracavity elements such as the gain medium or laser mirrors. This is usually achieved by introducing additional intracavity elements that provide negative dispersion such as prism pairs [20], chirped mirrors [21], Gires-Tournois interferometer (GTI) mirrors [22, 23], or diffraction grating pairs [24].

As a result of the dispersion introduced mainly by the gain medium, the net GDD for a cavity round trip is usually positive. Some other cavity components such as mirrors can also contribute to this. Whether or not dispersion compensation needs to be applied depends on how short the output pulses of the laser are. As a rough rule of thumb, dispersion effects can be ignored for pulse durations longer than 10 ps. This is due to the fact that the net cavity GDD will typically be a few thousand fs^2 at most, which is much less than the square of the pulse duration. Shorter pulse durations than 10 ps will have to take into account compensation of GDD and when the pulse duration is less than 30 fs, TOD compensation usually has to be applied and possibly even higher orders of dispersion.

For the most part the net cavity GDD is required to be negative rather than zero so that soliton formation can be exploited (see section 1.4.7). To achieve net negative GDD requires the addition of cavity elements to provide this. In the following sections the most common and important techniques are described including prism pairs, chirped mirrors, Gires-Tournois interferometer (GTI) mirrors and diffraction gratings.

1.2.2 Prism Pairs

A well-established method of intracavity dispersion compensation is through the use of pairs of Brewster-angled prisms [20]. The principle of operation of prism pairs is that of wavelength-dependent refraction. As shown in Figure 2, the different wavelength components of a pulse will travel at different angles after the first prism, resulting in them passing through a different amount of material in the second prism.

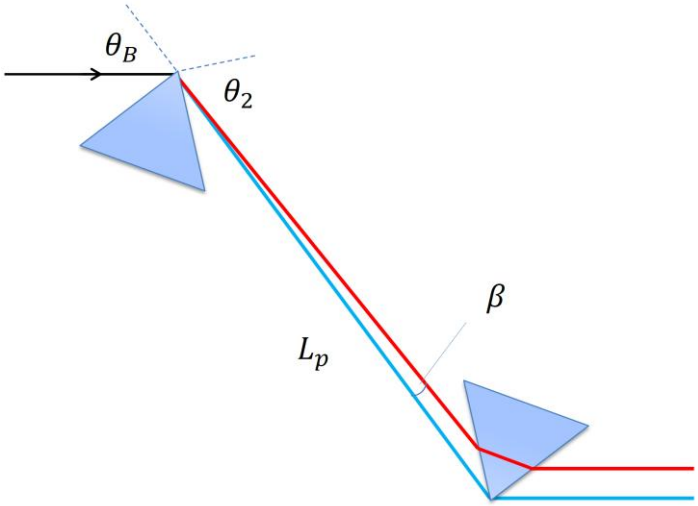

Figure 2. Light propagating through a pair of Brewster-angled prisms gives rise to geometric dispersion through wavelength-dependent refraction. θ_B is the Brewster angle at which incident light enters the prism, θ_2 is the angle at which light exits the prism (θ_2 should equal θ_B), L_p is the tip-to-tip separation of the prisms, and β is the angle of the light from the reference ray.

In a standing-wave cavity the wavelength components are simply recombined after reflection from a plane end-mirror, and for a travelling wave ring cavity a second pair of prisms can be used forming what is known as a four prism compressor. Individual temporally dispersed wavelength components of the pulse of a chirped pulse entering the prism pair will experience different optical path lengths, which can recompress the temporal envelope of the pulse thus compensating for the effect of GDD. An advantage of using a prism pair is the ability to finely tune the amount of negative GDD applied by varying the amount of prism glass the beam travels through (known as prism insertion), and thus vary the output pulse duration (albeit at the cost of affecting the TBP). Other advantages include the low insertion loss due to angle of incidence being at Brewster's angle, and the ability to tune the wavelength of the laser by placing a slit where the wavelength components of the beam are spatially separated. A disadvantage of using a prism pair is the introduction of unwanted higher-order dispersion (HOD) the control of which, as discussed, is important for pulses shorter than 30 fs. HOD is the general term that generally refers to third-order dispersion but can also include fourth-order dispersion and even higher orders [19]. Different materials introduce different amounts of HOD e.g. SF10 prisms introduce more HOD than fused silica prisms, and the amount of HOD introduced depends mostly on the prism separation with prism insertion doing little to affect HOD [19]. It can be shown that the GDD contribution of a prism pair is [20]:

$$\frac{d^2\phi_p}{d\omega^2} = \frac{\lambda_0^3}{2\pi c^2}\left(\frac{d^2P}{d\lambda^2} + L_m\frac{d^2n_p}{d\lambda^2}\right) \tag{13}$$

where L_m is the beam path length in the prisms, $d^2n_p/d\lambda^2$ is the material contribution to GDD as a result of this path length inside the prism, and $d^2P/d\lambda^2$ is the geometrical contribution to the GDD given by:

$$\frac{d^2P}{d\lambda^2} = 4\left[\frac{d^2n_p}{d\lambda^2} + \left(2n_p - \frac{1}{n_p^3}\right)\left(\frac{dn_p}{d\lambda}\right)^2\right]L_p\sin\beta - 8\left(\frac{dn_p}{d\lambda}\right)^2 L_p\cos\beta \tag{14}$$

By carefully choosing the prism separation and prism insertion, it possible to tailor the amount of negative GDD at the desired operating wavelength, as shown in Figure 3:

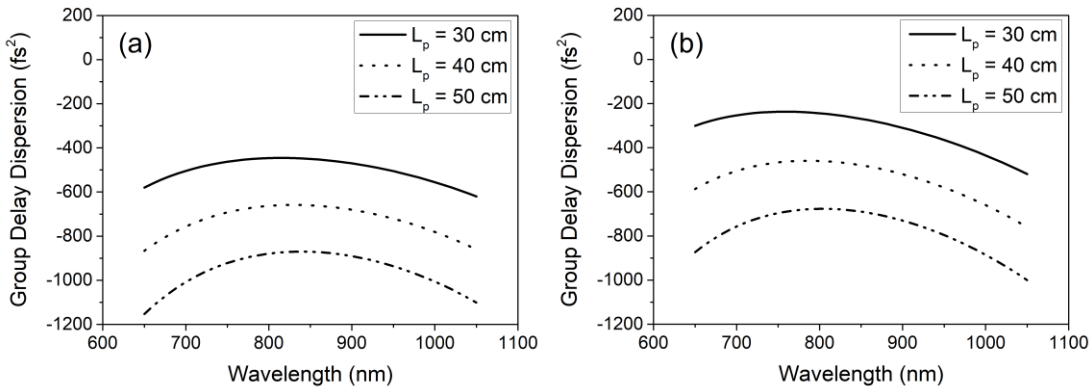

Figure 3. Shown in the figure is the effect of various amounts prism separation on the applied GDD vs. wavelength for (a) a prism insertion L_m of 2 mm, and (b) a prism insertion L_m of 4 mm.

1.2.3 Chirped mirrors

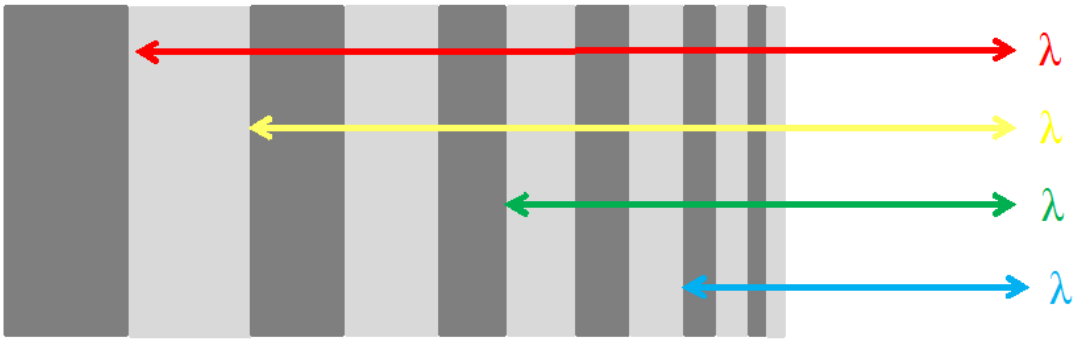

Figure 4. Chirped mirror structure showing penetration of different wavelengths to various mirror depths.

Similar to Bragg mirrors, which possess a mirror structure composed of an alternating series of quarter-wave layers of two different optical materials, chirped mirrors are a type of dispersive dielectric mirror. It is possible to obtain a well-controlled GDD over a large wavelength range using chirped mirrors. This is made possible by varying the Bragg wavelength appropriately within a Bragg mirror design, where light of longer wavelength is reflected deeper into the mirror structure (see Figure 4), gaining a larger phase change, which in turn leads to negative GDD [25].

However initial designs based on this principle using a straight-forward implementation resulted in strong oscillations of the GDD across the wavelength bandwidth, rendering the device impractical for ultrashort pulse generation [21]. This unwanted oscillatory effect could be mitigated to some extent by numerical optimisation of the layer structure. This is challenging as the parameter to be optimised is a complicated function of multiple layer thickness variables, which typically possesses numerous local maxima and minima that do not translate to satisfactory designs.

The origin of the oscillatory behaviour was later found [21] to be the result of two effects; a Fresnel reflection due to the interface between the mirror front face and the air that leads to strong additional dispersion through Gires-Tournois Interferometer effects, and also due to an impedance mismatch that is the result of the abrupt switching of the coupling of counter-propagating waves from zero in air to a finite value in the mirror structure.

These problems were eliminated by a further breakthrough in chirped mirror design, which was the concept of Double-Chirped Mirrors (DCM) [21]. Two features are added to the design; the coupling of the counter-propagating waves is turned on smoothly by varying the ratio of the optical thickness of the high and low index layers, and an additional anti-reflection structure is added on top of the double-chirped section, removing the Fresnel reflection. Even without using numerical optimisation viable designs can be created, however further numerical optimisation of, for example, the layer thickness can yield improved designs [21].

It is possible to further increase the bandwidth of the mirrors and improve the dispersion characteristics, by using pairs of specially designed double-chirped mirrors [26]. These mirrors by themselves have GDD oscillations many times larger than high quality DCMs, but when used together cancel out to form a much smoother average GDD. DCM pairs based on this concept enabled the direct generation of pulses in the 2-cycle regime from a Ti:sapphire laser [27]. Designs can also be created to compensate high order dispersion, however there are limitations to how much GDD, and particularly higher order dispersion, that can be

compensated for with double chirped mirrors. Manufacturing tolerances also limit the amount of dispersion as some layers may have to be fabricated to a precision of a few nanometres.

1.2.4 Gires-Tournois Interferometer mirrors

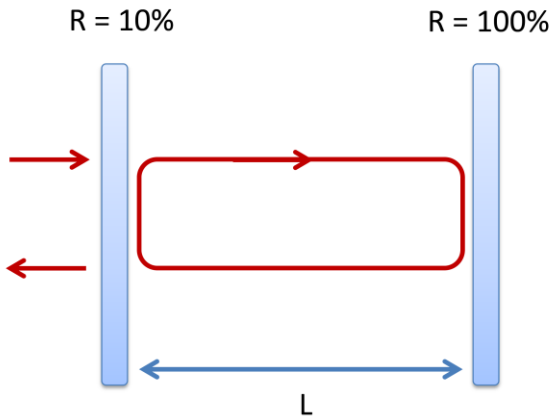

Figure 5. Basic schematic of a typical GTI mirror.

A Gires-Tournois Interferometer (GTI) is essentially an optical standing wave resonator that has broad similarities to a Fabry-Pérot interferometer but is operated in reflection rather than transmission, and is used to generate wavelength-dependent GDD [22]. A basic schematic of a GTI mirror is shown in 5. The first mirror is partially reflective while the second mirror is highly reflective.

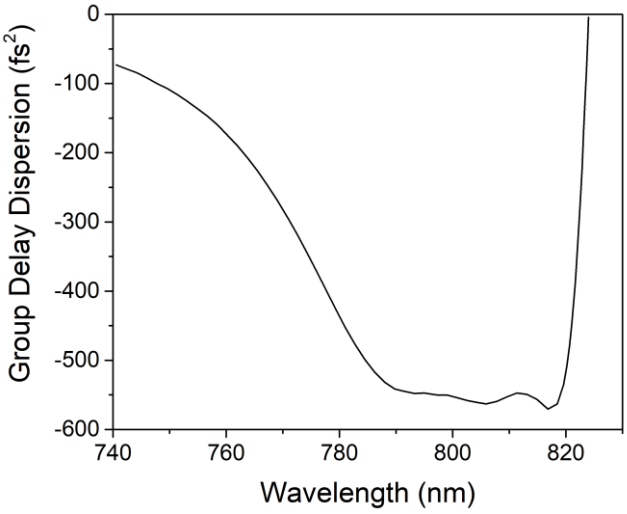

Figure 6. GDD vs wavelength of a typical GTI mirror (data from Layertec mirror [28]).

If no losses are assumed to occur in the resonator, then all of the incident optical power is reflected. However, the phase of the reflected light has a frequency dependence arising from

the resonance effect, resulting in wavelength-dependent GDD as shown in Figure 6 [28]. There is a certain periodicity to the generated wavelength dependent GDD (higher orders of dispersion too), which is dependent on the free spectral range (FSR) of the cavity (itself inversely proportional to the resonator length). In most cases it is desired to operate at a maximum or minimum of the GDD, the usable bandwidth of which is some fraction of the FSR. This bandwidth is fundamentally limited, being proportional to the square root of the magnitude of GDD [19]. The magnitude itself is proportional to the length of the GTI resonator.

It is possible to tune the GDD if a variable air gap is used between the mirrors [23]. However, in order to avoid unwanted drifts this must be carefully stabilised. By instead using thin films of dielectric media such as TiO_2 and SiO_2 between the mirrors, more stable designs can be created [23], however these have the drawback of no tunability.

1.3 Nonlinear pulse propagation

Due to the χ_2 term in Equation 5 being zero for centro-symmetric crystals, the nonlinear polarisation response is governed by the χ_3 term [18]. Nonlinear, non-resonant effects such as Raman scattering, Brillouin scattering, third harmonic generation and, importantly, the Kerr effect all arise due to this term. The strength of this term is dependent on the intensity of the incident electric field, and thus in the context of lasers usually only becomes significant with the high intensities generated by an ultrashort pulse [18].

1.3.1 The Kerr effect

In the presence of a sufficiently strong electromagnetic field $E(t)$, a transparent dielectric material will experience a change in refractive index Δn due to the χ_3 nonlinearity [18]. In this case the refractive index of this material can be separated into two terms: the linear refractive index n_0 and the nonlinear refractive index coefficient n_2.

$$n = n_0 + n_2|E(t)|^2 \tag{15}$$

where n_2 is given by:

$$n_2 = \frac{3\chi_3}{8n_0} \tag{16}$$

In order to produce a significant refractive index change the beam intensity needs to be very high, on the order of 2.5 GW/cm^2 for a typical optical glass [29]. Sufficiently high intensities of this magnitude can be produced by an intense ultra-short optical pulse and equation 15 can be rewritten in terms of intensity:

$$n = n_0 + n_2 I(t)^2 \tag{17}$$

For most materials n_2 is positive, meaning that increasing intensity also increases the refractive index of the dielectric material. This is known as the "optical Kerr effect", which is responsible for some effects important to ultrafast lasers such as self-focusing and self-phase modulation.

1.3.2 Self-focusing

Consider an optical pulse travelling through a Kerr medium. A cross section of the pulse will have a near-Gaussian spatial intensity distribution, with a higher intensity at the centre compared to the edges of the pulse. As the intensity is not uniformly distributed across the beam, it follows that there will be a non-uniform refractive index response across the beam.

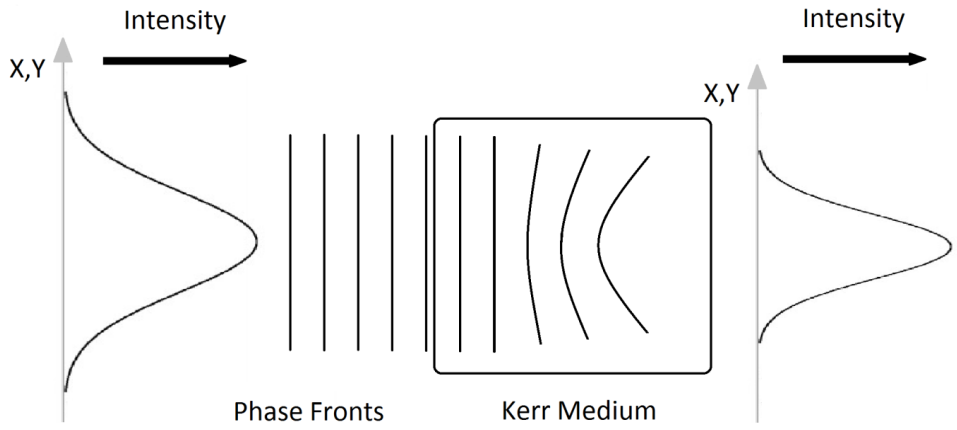

Figure 7. Self-focusing experienced by an intense beam as it passes through a Kerr medium.

In the example illustrated above in Figure 7, the phase fronts passing through a Kerr medium will experience a larger phase shift in the centre of the of beam and become retarded with respect to the edges of the beam. This means that the beam experiences a focusing effect similar to passing through a simple lens. This phenomenon is known as a Kerr-lens and can be exploited to mode-lock certain lasers.

1.3.3 Self-phase modulation

As the Kerr effect is assumed to be instantaneous [19], the change in refractive index Δn will also follow the temporal pulse profile. If the material has positive n_2 then Δn will be largest at the peak of the pulse, resulting in a phase shift $\Delta\phi(t)$ given by [18]:

$$\Delta\phi(t) = \frac{2\pi L n_2 I(t)}{\lambda} \tag{18}$$

where L is the propagation length in the material and $I(t)$ is the intensity profile of the pulse. As the pulse passes through the medium, the leading edge of the pulse (increasing in intensity) brings an increase in refractive index. The length of the medium in effect becomes longer, resulting in a delay to the arrival of the optical cycles and thus a red-shift to the frequency components at the front of the pulse. The opposite effect occurs for the trailing edge of the pulse, where a shortening of the optical path length occurs resulting in a blue-shift to the frequency components of the trailing edge of the pulse. This effect is shown in Figure 8.

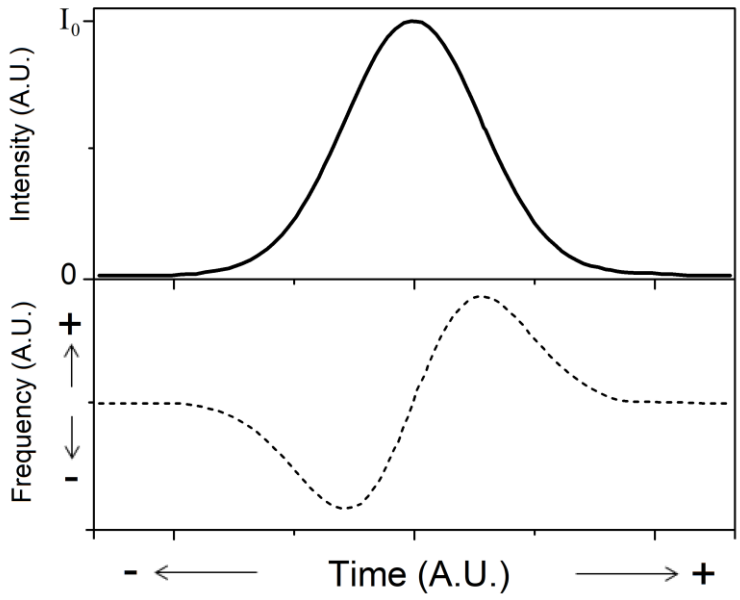

Figure 8. A pulse propagating through a Kerr medium undergoes a self-frequency shift as a result of SPM. The leading edge of the pulse is red-shifted while the back of the pulse is blue shifted.

Without taking into account the dispersion of the medium, the instantaneous frequency profile of the pulse is given by:

$$\Delta\nu = \frac{d\phi(t)}{dt} = \frac{2\pi L n_2}{\lambda}\left(\frac{dI(t)}{dt}\right) \tag{19}$$

This effect results in spectral broadening of pulse as well as a linear frequency chirp across the centre of the pulse's temporal envelope. For positive n_2 the chirp is positive, and negative for negative n_2. The effect is similar to propagation through a dispersive medium, however it is independent of the pulse duration and instead manifests in broadening of the spectral bandwidth. It can be shown that the spectrum of a pulse broadens by a factor of $\sqrt{2}$ upon propagation through a length of Kerr medium given by [18]:

$$L = \frac{\lambda}{2\pi n_2 I_0} \tag{20}$$

where I_0 is the peak intensity of the pulse. This is known as Self-Phase Modulation (SPM). If the peak intensity of the pulse in a laser system is high enough to cause significant phase shifts, then the SPM must be compensated for if the shortest pulses are desired. SPM is often approximated as a form of linear dispersion, and as such can be compensated for through the dispersion compensation techniques described in sections 1.2.1 to 1.2.4.

1.4 Ultrashort pulse generation

There are various techniques that can be applied in order to force or coax a laser into producing a periodic train of pulses, including Q-switching [29], cavity dumping [29], and gain switching [29]. In order to produce pulse in the ultrashort regime, broadly defined as pulses with less than 10 picoseconds duration, mode-locking techniques are usually required. The following sections give a brief overview of mode-locking methods, focusing on the passive mode-locking methods that were used to mode-lock the lasers discussed in later chapters.

1.4.1 Mode-locking

If we take as an example a simple two mirror laser resonator, only certain frequencies, also known as longitudinal modes, are allowed to oscillate. These modes are determined by the distance between the two mirrors, with only those that are a half-integer number of wavelengths between the two mirrors allowed to set up a standing wave and oscillate [29]. These modes are separated in frequency by:

$$\Delta\nu = \frac{c}{2nl} \tag{21}$$

where c is the speed of light, n the refractive index, and l the separation between the mirrors. The optical round-trip length of the cavity is $2nl$. The modes that actually oscillate in any laser system are then determined by a combination of the optical length of the cavity along with the gain bandwidth of the gain medium [29]. The modes oscillating will normally have random phase with respect to each other resulting in a noise-like output. However, it is possible to enforce or encourage these modes to operate with a fixed-phase relationship with respect to each other. This will result in their amplitudes being added together at one point in time due to constructive interference, producing a pulse [29]. This is what is known as mode-locking (or phase-locking) and can be achieved by introducing some sort of modulation to the cavity, either actively via an external source known as active mode-locking, or passively via passive mode-locking.

1.4.2 Active mode-locking

Active mode-locking involves the periodic modulation of either the losses of the resonator or the round-trip phase-change. This can be achieved by using an electro-optic modulator, an acousto-optic modulator, a Mach-Zehnder integrated-optic modulator, or a semiconductor electro-absorption modulator [30]. By synchronising the modulation to the resonator round-trip, ultrashort pulses can be generated [29]. Active mode-locking is associated with longer pulses compared to passive mode-locking, with the shortest pulses produced normally in picosecond regime. However, it has been shown that if used in conjunction with soliton formation, pulses as short as a few hundreds of fs can be generated [31,32]. However, if shorter pulses are desired the one must use passive mode-locking methods, which are used exclusively throughout this project.

1.4.3 Passive mode-locking

Passive mode-locking utilises a nonlinear intracavity element that possesses an intensity dependent loss, which results in modulation of the circulating optical field allowing the laser to mode-lock itself. The reason for this is that the phases of the modes in the resonator will self-organise to produce a field that experiences the least loss as it circulates in the cavity. This is known as the maximum emission principle [33], and this is what leads to a pulsed laser field building up from background amplitude noise.

Passive mode-locking techniques produce the shortest pulse durations and are most often shorter than that achieved with active mode-locking. Broadly speaking there are three main types of passive mode-locking: passive mode-locking with a slow saturable absorber and dynamic gain saturation, passive mode-locking with a slow saturable absorber without dynamic gain saturation (known as soliton mode-locking in the femtosecond regime), and passive mode-locking with a fast saturable absorber [19].

Self-amplitude modulation (SAM) is the dominant pulse-shaping process in passively mode-locked lasers in the picosecond pulse duration regime [19]; however, processes such as solitonic pulse-shaping, discussed in following sections, start to dominate for pulse durations shorter than this. In these regimes SAM can still be involved in the initiating or stabilisation of the mode-locked pulses [19].

1.4.4 Saturable absorbers

The concept of saturable absorption in the context of a laser is to add a selective loss to the cavity, suppressing low intensity CW laser operation while allowing higher intensity ML operation to saturate the absorber and thus experience less loss.

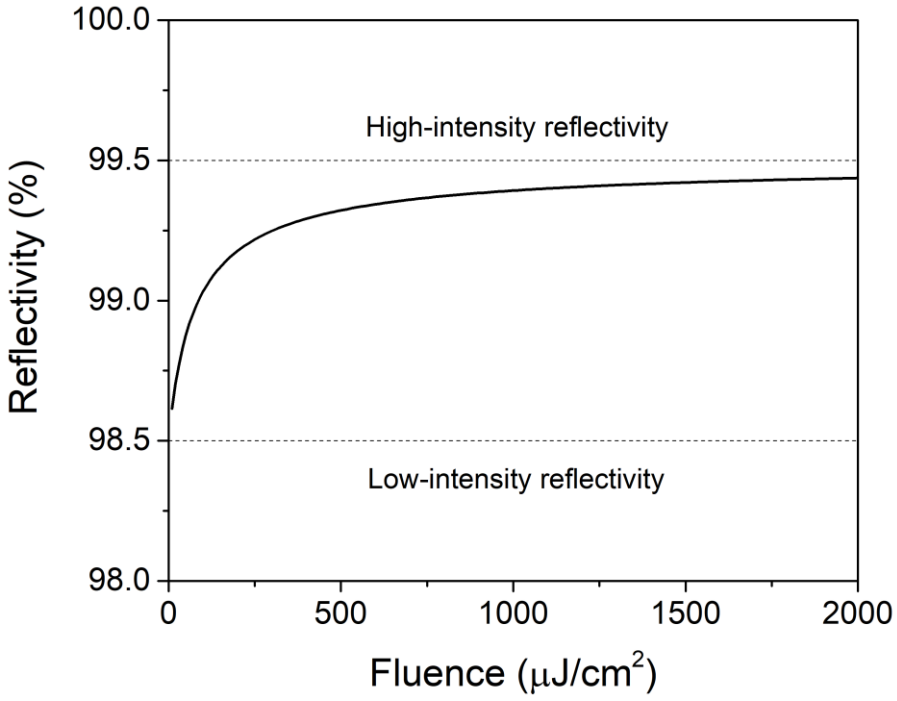

Figure 9. The reflectivity response of a typical saturable absorber mirror vs incident pulse fluence. In this case non-saturable or residual losses are 0.5%, the modulation depth is 1%, and the low-intensity reflectivity is 98.5%.

This effect is demonstrated in Figure 9; as the pulse increases in energy it experiences a higher reflectivity and thus less loss. Whether a saturable absorber is defined as slow or fast depends on the absorber recovery time with respect to the pulse duration, with slow saturable absorbers having recovery times much longer than the pulse duration whereas a fast saturable absorber will have a recovery time much shorter than the pulse duration.

1.4.5 Passive mode-locking with a slow saturable absorber and dynamic gain saturation

As mentioned previously there are two types of passive mode-locking that utilise a slow saturable absorber. The first of these is passive mode-locking with a slow saturable absorber and dynamic gain saturation. In this context dynamic gain saturation means that the gain is saturated by a short pulse, which then recovers between consecutive pulses. In passive mode-locking with a slow saturable absorber and dynamic gain saturation, a critical balance has to be struck between gain and absorber saturation, opening a net gain window small enough to support ultrashort pulses (see Figure 10). Through use of this technique, pulses below 100 fs in duration have been generated in dye lasers despite the absorber recovery time being in the nanosecond regime [34].

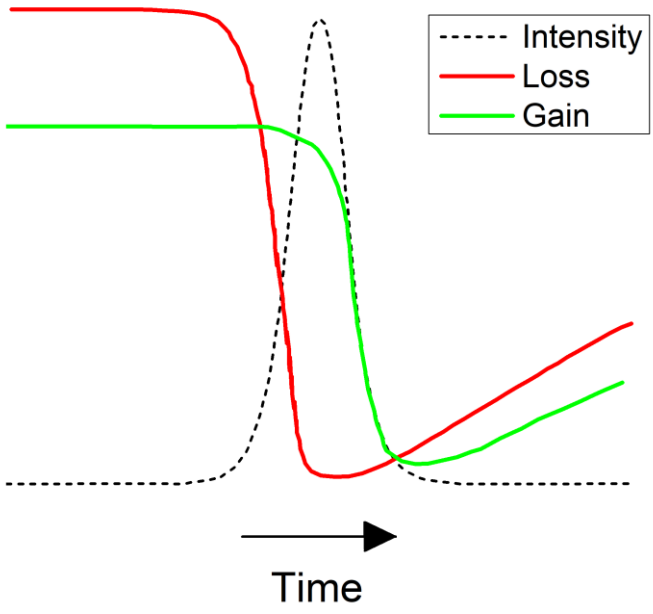

Figure 10. Model of passive mode-locking with dynamic gain saturation and a slow saturable absorber in the time domain.

This model was used to fully explain the behaviour of passively mode-locked dye lasers [35], where the pulse energy is of the order of the gain saturation energy. In solid-state lasers

however the pulse energy is orders of magnitude below the gain saturation energy. In order for dynamic gain saturation to help the following conditions must be met:

- The loss must be greater than the gain before the pulse ($q_0 > g_0$ where q_0 is unsaturated loss coefficient and g_0 is the small signal gain coefficient in the laser).
- The absorber needs to saturate faster than the gain ($E_{sat,A} < E_{sat,L}$ where $E_{sat,A}$ is the saturation energy of the absorber and $E_{sat,L}$ is the saturation energy of the gain medium).
- The absorber must recover more quickly than the gain ($\tau_A < \tau_L$ where τ_A is the absorber recovery time and τ_L is the upper state lifetime of the gain medium.

Passively mode-locked dye lasers are based on this type of mode-locking, as they are able to fulfil the above conditions. Due to the fact that solid-state gain media have a much larger saturation energy than dye-based gain media, this type of mode-locking cannot be used in solid-state lasers as no appreciable gain saturation can be achieved. As an example, we can compare well known gain media from each category; Ti:sapphire and Rhodamine 6G. The saturation energy is given by:

$$E_{sat,L} = \frac{A \times hv}{\sigma_{em} + \sigma_{abs}}$$

where σ_{em} and σ_{abs} are the stimulated emission and absorption cross sections at the emission wavelength, A is the laser mode area, and hv is the photon energy at the emission wavelength. For 4-level gain media, σ_{abs} is zero (exhibiting no reabsorption on the laser transition). In the following table we compare the saturation energy of Ti:sapphire and Rhodamine 6G:

Table 3. Comparison of saturation energies of Ti:sapphire and Rhodamine 6G.

Gain medium	λ	σ_{em}	$E_{sat,L}$
Rhodamine 6G	590 nm	1.36×10^{-16} cm^2	31.1 nJ
Ti:sapphire	800 nm	41×10^{-20} cm^2	7.6 µJ

The above assumes a circular laser mode area with a radius of 20 µm. We can see from the above that Ti:sapphire has a much larger saturation energy at around 244 times that of Rhodamine 6G. It is easy to see why it would be difficult to saturate the gain in Ti:sapphire.

1.4.6 Passive mode-locking with a fast saturable absorber

As solid-state laser gain media characteristically have smaller gain cross-sections and therefore negligible dynamic gain saturation if any at all, it was initially believed that passive mode-locking with a fast saturable was the only viable approach in solid-state lasers. In this type of mode-locking the short net gain window is formed solely by the fast-recovering saturable absorber, as shown in Figure 11.

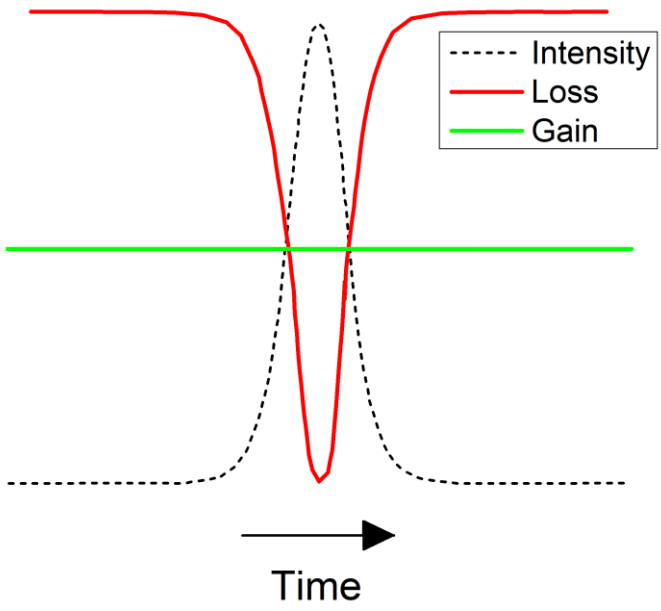

Figure 11. Model of passive mode-locking with a fast saturable absorber in the time domain.

Through the exploitation of near-instantaneous nonlinear effects that produce amplitude modulation, synthetic fast saturable absorber action can be realised and used to produce ultrashort pulses. Mode-locking through a fast saturable absorber was first realised through a technique known as additive-pulse mode-locking (APM) or coupled cavity mode-locking (CCM) [36]. In this technique the artificial fast absorber action is produce through nonlinear phase-shifts in a single mode fibre that is contained within a resonator. The fibre resonator has a round-trip time equal to the main laser resonator and is coupled to it via a semi-transparent dielectric mirror. The pulses that are returned from the fibre resonator to the main laser resonator interfere with the pulses that are circulating there. When the resonator lengths are correctly set the peak of the pulses will experience constructive interference while the wings of the pulses will not due to the different nonlinear phase shift acquired in the fibre. This results in the peak of the circulating pulse being enhanced while the wings are attenuated, thus shortening the pulse duration. However, the alignment and adjustment of the resonator length is critical, affecting the practicability of the technique.

The first passive mode-locking technique to use an intracavity fast saturable absorber was discovered during an experiment while optimising an APM Ti:sapphire laser [37]. At the time it was termed “self-mode-locking” and is better known as Kerr-lens mode-locking (KLM) today.

1.4.6.1 Kerr-lens mode-locking

Since the first demonstration in a Kerr lens mode-locked Ti:sapphire laser by Spence et al. [37], KLM has been demonstrated in many laser materials [38–41]. There are two main variants of KLM that have been identified: hard-aperture and soft-aperture.

Hard-aperture KLM involves using a physical aperture placed in the laser resonator, most often near an end mirror, where increasing laser intensity inside the gain medium with Kerr nonlinearity causes a decrease in the cavity mode size. This produces an intensity dependent loss that favours the higher intensity mode-locked mode with respect to the lower intensity CW mode. The spatiotemporal dynamics associated with this process are complex and not easily described, and as such several simplified models have been created to aid the design of hard-aperture KLM lasers, including the Magni model [42]. Brabec et al have also suggested some design guidelines for the design of hard aperture KLM resonators [43], and these were successfully deployed in chapter 3 to realise a KLM diode-pumped Ti:sapphire laser.

A variant of hard aperture KLM where a physical aperture is not required is known as virtual hard-aperture KLM [44]. This involves choosing the position of cavity stability to be slightly beyond the first stability limit in the CW regime. The result of this is that CW operation will become unstable. However, due to the Kerr lens the cavity will still be stable for mode-locked operation only, operating with a higher threshold due to increased diffraction losses. The reason that the Kerr lens keeps the cavity stable for the mode-locked mode is because it effectively shortens the separation between the folding mirrors by imaging the focus of the mode-locked mode forward. This has the effect of extending the stability limit for the mode-locked mode further than that of the CW mode. This technique was successfully demonstrated by Pe’er et al. [44].

Another variant of KLM, known as soft-aperture KLM, allows for mode-locked operation without the use of a physical intracavity aperture. Instead, the gain medium is used as a virtual aperture, with self-focusing being used to improve the extraction of gain in the gain medium. Specifically, higher intensity modes experience more self-focusing and thus a tighter, smaller waist inside the gain medium. With correct choice of pump mode waist, the smaller cavity

mode volume of the mode-locked mode will be better matched to the pump mode volume in comparison to the larger CW mode.

1.4.7 Passive mode-locking with a slow saturable absorber and soliton formation

Also known as soliton mode-locking, in this type of passive mode-locking the pulse-shaping is carried out exclusively by soliton formation through balance of intracavity negative GDD and SPM. However, in order to start the mode-locking process and stabilise the pulse, it is necessary to have an additional loss mechanism such as a saturable absorber [45] or less commonly an acousto-optic modulator [32].

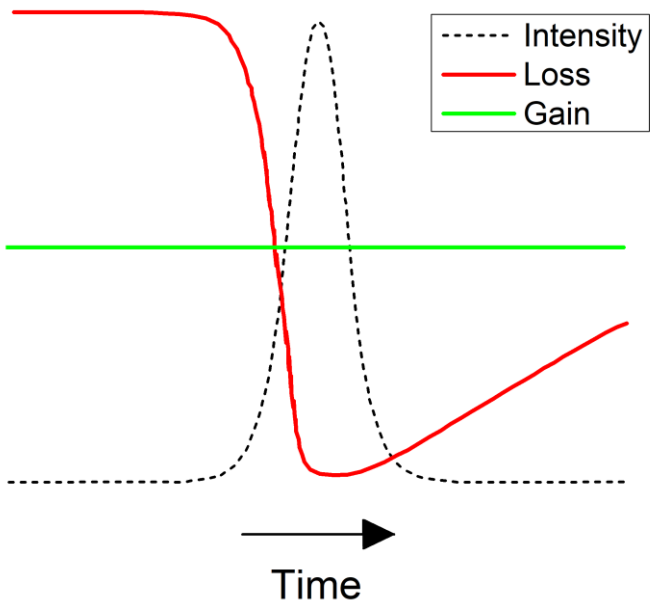

Figure 12. Model of passive mode-locking with a slow saturable absorber and soliton formation, in the time domain. This type of mode-locking is more commonly known as soliton mode-locking.

Initially it was discovered that a saturable absorber with a bitemporal recovery time of 180 fs and 15 ps was able to support pulses of around 100 fs in duration without the use of KLM [46]. It was then shown that an acousto-optically mode-locked Nd:glass laser was able to produce 310 fs pulses through soliton formation and gain filtering [31]. As shown in Figure 12, the net gain window was open for much longer than the pulse width in both these cases, which strongly contradicted mode-locking theories at the time. As a solution the soliton mode-locking model was proposed.

In the soliton mode-locking model, the saturable absorber is treated as a perturbation term, the effect of which is to initialise the formation of the soliton from noise and subsequently stabilise the soliton [45]. The explanation as to why the net gain window can remain open for

so long after the pulse is as follows; the nonlinear effects due to SPM and linear effects due to GDD are in balance. However, as the intensity of the noise or instabilities behind the pulse is too low to experience the nonlinearity, they are spread in time by dispersion. As they are spread in time, they move in regions of net loss as the saturable absorber slowly recovers. Thus, the instabilities will experience less gain per round-trip than the soliton and will decay with time.

Subsequent experimental verification was carried out by Keller et al, where pulses as short as 300 fs were generated from a Ti:sapphire laser using soliton-like pulse shaping and a slow saturable absorber with 10 ps recovery time [47]. Using ABCD-matrix calculations they were able to show that no appreciable fast saturable absorber action from KLM was present and was therefore eliminated as a contributing factor to the pulse formation, confirming that soliton mode-locking was responsible for such short pulses.

As the net-gain window in soliton mode-locking can remain for more than 10 times the length of the ultrashort pulse, the requirements on the saturable absorber are significantly relaxed. This allows for the use of passive devices with relatively long recovery times such as semiconductor saturable absorbers. Using semiconductor saturable absorbers incorporated into dielectric mirrors has resulted in devices known as semiconductor saturable absorber mirrors or SESAM. When used to mode-lock solid-state lasers, pulses as short as 10 fs have been generated through soliton mode-locking [48]. A more detailed description of these mirrors and important parameters is given in the following section.

An important difference from KLM is the fact soliton mode-locking imposes no additional requirements on the position of cavity stability. As described in section 1.3.2 the transverse component of the Kerr effect effectively forms a nonlinear lens inside the gain medium. This nonlinear lens in conjunction with a hard aperture placed strategically in the cavity creates an effective fast saturable absorber. This is because the reduction in cavity mode at the aperture introduces less loss at high intensity than at low intensity. Hence this mechanism couples the mode-locking mechanism to the cavity mode, and thus the position of cavity stability.

1.4.7.1 Semiconductor saturable absorbers

A semiconductor saturable absorber mirrors or SESAM is a device composed of a mirror structure with alternating high and low refractive index layers, and an incorporated saturable absorber that is usually a single quantum well layer (see Figure 13).

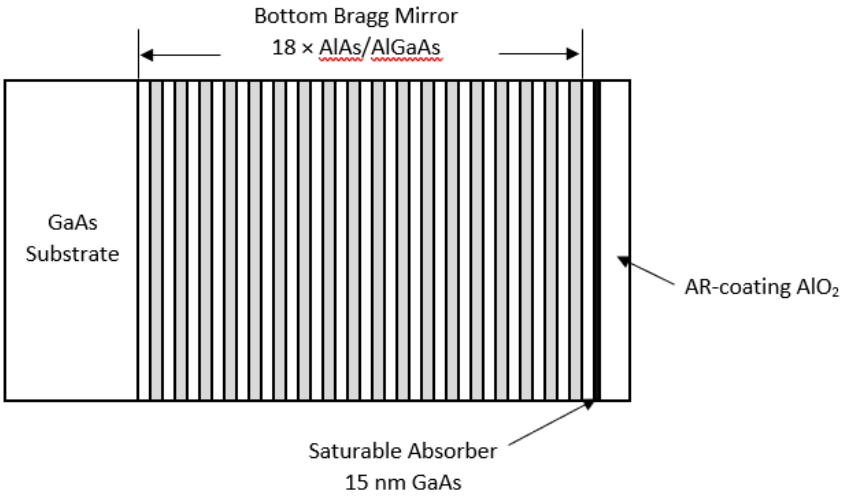

Figure 13. Schematic of an AR-coated SESAM designed for a centre wavelength of 800 nm adapted from [49]. The structure is an AlAs – AlGaAs reflector with a single GaAs quantum well saturable absorber. The additional AlO_2 AR-coating is needed to prevent Fabry-Perot effects.

The concept behind SESAMs is that they display an intensity-dependent reflectivity, where higher intensity light experiences less loss than lower intensity light. This for example favours mode-locked pulsed operation over that of CW operation. There are several different types of SESAMs which are used to achieve certain desired properties. These are discussed in the next few sub-sections.

1.4.7.2 High-finesse A-FPSA

The first intracavity SESAM device used to passively mode-lock a solid-state laser was the high-finesse anti-resonant Fabry-Perot saturable absorber (A-FPSA) [49]. The Fabry-Perot is formed by the lower semiconductor Bragg mirror and a dielectric top mirror, with a saturable absorber and, if required, transparent spacer layers sandwiched in between. To ensure the Fabry-Perot operates at anti-resonance, the total thickness of the saturable absorber and transparent spacer layer is optimised. When operated at anti-resonance, the resulting device performance will be broadband with minimal GDD. Either the free spectral range of the Fabry-Perot or the mirror bandwidth limits the bandwidth of the high-finesse A-FPSA. To optimise the saturation intensity or absorber cross section of the high-finesse A-FPSA, the top reflector reflectivity is adjusted to control the intensity reaching the saturable absorber.

1.4.7.3 AR-coated SESAM

In another design similar to the high-finesse A-FPSA , known as an AR-coated SESAM, the top reflector is replaced by an AR-coating. In this situation the incident laser mode area is

optimised to produce a pulse fluence adapted to the saturation fluence of the device. For this design, the thickness of the saturable absorber typically has to be reduced compared to other designs to keep the non-saturable loss low. AR-coated SESAM limitations include the bandwidth of the lower Bragg mirror, and the potentially higher insertion loss compared to the high-finesse A-FPSA. Compared to the low finesse A-FPSA, the additional AR-coating increases the modulation depth of this device and acts as a passivation layer for the semiconductor surface that can improve long-term reliability of this SESAM device.

1.4.7.4 Low-finesse A-FPSA

Another SESAM design variant is the low-finesse A-FPSA. This design is essentially the same as the AR-coated SESAM without the AR-coating. Instead, a top reflector is formed by the Fresnel reflection (on the order of 30%) at the semiconductor saturable absorber to air interface. A similar design known as the saturable Bragg reflector (SBR) was produced, which consists of a lower Bragg mirror plus a quarter-wave thick Fabry-Perot cavity at anti-resonance. The thickness of the spacer/absorber layer is adjusted for anti-resonance. A saturable absorber is then located inside this Fabry-Perot. The limitations of this device include the bandwidth of the lower Bragg mirror and pulses that are longer in duration due to the lower modulation depth of this device than with a similar AR-coated SESAM device.

1.4.7.5 D-SAM

The dispersive saturable absorber mirror (D-SAM) is similar to a low-finesse A-FPSA but operates close to resonance and incorporates negative dispersion as well as saturable absorption. Advantages to this approach are a reduction the number of intracavity elements, given that the DSAM provides both saturable absorption and dispersion compensation. This can eliminate the need for additional dispersion compensating elements allowing for a more compact cavity design [50]. However, the bandwidth of the device tends to be limited given that it is operated close to Fabry-Perot resonance, and it can also be restrictive working with SESAMs with fixed negative dispersion and saturable absorption combinations.

1.4.7.6 SESAM saturable absorber parameters

Since the first demonstration of an intracavity SESAM device in 1992 [51], much research and development has been undertaken and SESAMs are now routinely used for passive mode-locking, for generating pulses in both the picosecond and femtosecond regimes [49]. Through epitaxial growth techniques such as molecular beam epitaxy (MBE) and metal-organic

chemical vapour deposition (MOCVD), it is possible to precisely tailor the saturable absorption parameters. The main parameters that are used to characterise a SESAM are the recovery time τ_R, the modulation depth ΔR, the non-saturable loss ΔR_{NS}, reflectivity bandwidth $\Delta\lambda$, and saturation fluence F_{SAT}. These are discussed in more detail in the following paragraphs.

The recovery time τ_R is essentially the time it takes for the absorber to return to its initial state after a pulse with the enough intensity bleaches the absorber. When mode-locking with a fast saturable absorber, the recovery time needs to be very short and on a par with the pulse duration. However, despite semiconductor saturable absorbers generally have recovery times in the picosecond range, soliton mode-locking (as discussed in 1.4.6) can be used for femtosecond pulse generation.

The modulation depth ΔR describes the total change in reflectivity of the SESAM, from its unbleached state until its absorption is fully saturated. A large modulation depth makes self-starting more likely and allows for very short pulses. This, however, also increases the chances of unwanted Q-switching instabilities in solid-state lasers such as Q-switched mode-locking, where the mode-locked pulse train has a Q-switched envelope in μs-ms time scale [52]. This means that performance has to be traded off against sufficient suppression of Q-switching instabilities, with optimal modulation depths typically 1-2% for bulk solid state lasers.

The non-saturable loss ΔR_{NS} is the remaining absorption once the SESAM has been saturated by a sufficiently intense pulse. Contributing to this term is the scattering losses within the device, excited state absorption, and the residual absorption and transmission of the Bragg mirror stack [53]. For solid-state lasers, which have comparatively low gain compared to fibre lasers for instance, the intracavity losses need to be minimised as much as possible, meaning that the non-saturable loss should be as close to zero as possible. This is achieved through careful selection of design and growth parameters, which have a significant effect [53]

The saturation fluence F_{SAT} gives the fluence (energy per unit area) required to saturate the absorption of a SESAM. In practical systems the required fluence for is usually kept between 3-5 times the saturation fluence [54], however, it can be up to 10 times in some cases. This is an important parameter, as the SESAM can be damaged by fluences that are too high through two-photon absorption effects, and somewhat counterintuitively through fluences that are too low through Q-switching effects.

There are two main factors limiting the achievable pulse duration of SESAM mode-locked laser: the bandwidth of the gain medium and the reflectivity bandwidth of the SESAM device itself, which is determined by design of the Bragg mirror. There are other semiconductor

saturable absorber mirror designs based on quantum dots rather than a quantum well layer [55]. Other exotic designs that utilise an absorber that aren't based on semiconductors include carbon nanotubes [56] and graphene-based saturable absorbers [57]. Graphene is of particular interest to this project and is discussed more fully in Chapter 5.

1.5 Ultrashort pulse measurement and characterisation

In order to characterise the pulse train generated by an ultrashort pulse laser system there are four main features that are measured in this project: the average output power, the spectral bandwidth of the pulses, the pulse repetition rate of the laser system and the pulse duration. There are other features such as phase noise that are relevant dependent on the intended application of the laser but will not be considered here. The average output power, the spectral bandwidth, and the pulse repetition rate are fairly trivial to measure. A power meter with suitable features can be used to determine the average output power of a laser. Using a suitable spectrometer, the output pulse spectrum can be determined. A combination of a fast photodetector and an oscilloscope, providing both have high enough bandwidth, can be used to determine the pulse repetition rate. However, measuring the duration of a pulse on the ultrashort timescale is non-trivial and indirect methods must be used to estimate the pulse duration. This can be achieved through autocorrelation [58], which very simply put involves comparing pulses against themselves. Other more complex methods of pulse characterisation can be used, which are able to reveal information regarding the complex spectrum of ultrashort pulses such as spectral shape and spectral phase. The most widely used techniques in this category are frequency-resolved optical gating (FROG) [59] and spectral interferometry for direct electric field reconstruction (SPIDER) [60]. These techniques are more precise than autocorrelation when dealing with pulses that are less than 10 fs as they do not have to assume a certain pulse shape for example. However, as we are dealing with pulses greater than roughly 50 fs to around 200 fs in this project, these techniques will not be further discussed here.

1.5.1 Intensity autocorrelators

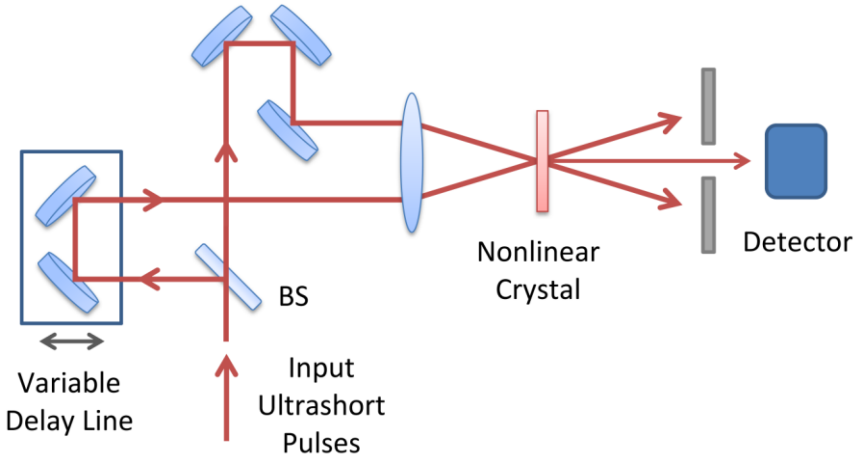

Figure 14. Basic schematic of an intensity autocorrelator.

The basic schematic of an intensity autocorrelator is shown in Figure 14. A beam splitter is first used to split an input pulse into two pulses. A delay line is then used to adjust the relative timing of one pulse with respect to the other. These pulses are then focused and directed into a crystal with χ_2 nonlinearity. The difference in arm length can be altered mechanically via the variable delay line, which translates to a change in relative timing of the pulses. By making the arm length similar and thus the difference close to zero, the pulses will meet in the nonlinear crystal, which causes sum frequency generation to occur and an additional output at a shorter wavelength/higher frequency, which is the signal that the photodetector detects. When the pulses experience the most overlap, the mixing product will be stronger. The power of this mixing product is recorded as a function of arm length difference (often carried out using computer control with a motorised translation stage to move the delay line). The dependence of the autocorrelation signal on the temporal delay τ is given by:

$$I_{AC}(\tau) = \int P(t)P(t+\tau)dt \qquad (22)$$

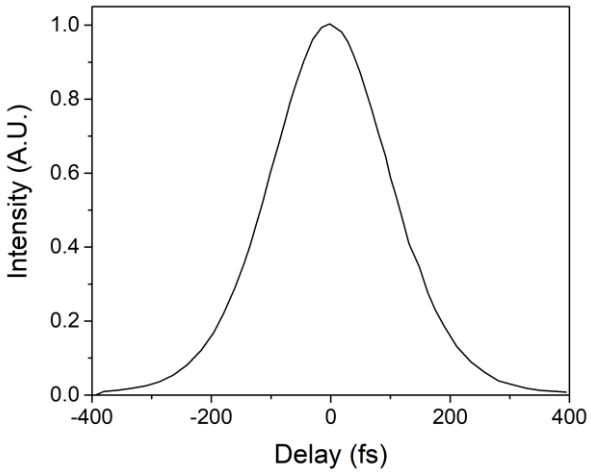

Figure 15. Typical intensity autocorrelation of an optical pulse

A typical autocorrelation signal for $sech^2$-shaped pulses is shown in Figure 15. The x-axis depicts the time delay as calculated from the arm length difference. In order to obtain the pulse duration for $sech^2$-shaped pulses, the width of the autocorrelation signal is multiplied by a conversion factor of 0.65. This value will be different depending on pulse shape. Due to the fact that the signal vanishes for large time delays, the intensity autocorrelation is often referred to as "background-free".

1.5.2 Interferometric autocorrelators

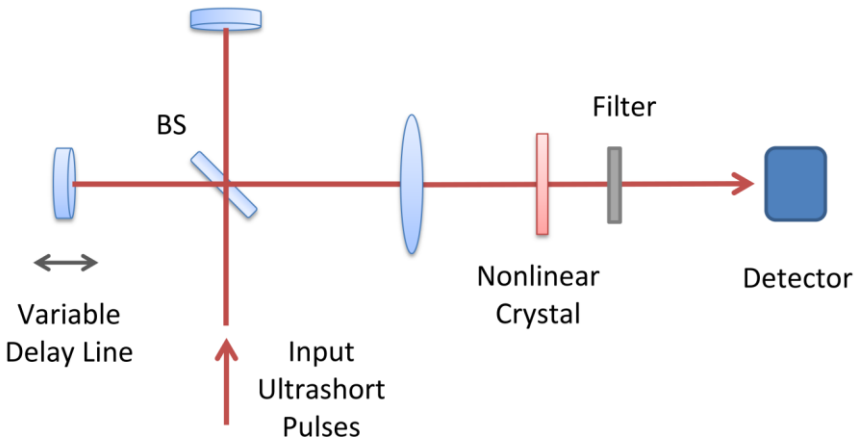

Figure 16. Basic schematic of an interferometric autocorrelator.

The basic schematic setup of an interferometric autocorrelator is shown in Figure 16. Based on a Michelson interferometer with a variable arm length difference, the incoming pulse is split into two by a beam splitter with each being reflected back to the beam splitter and superimposed. These collinearly propagating pulses have the same polarisation and are

focused into a nonlinear crystal. By recording the average power of the frequency-doubled signal, an interferometric autocorrelation can be obtained:

$$I_{AC}(\tau) = \int (E(t) + E(t+\tau))^4 dt \qquad (23)$$

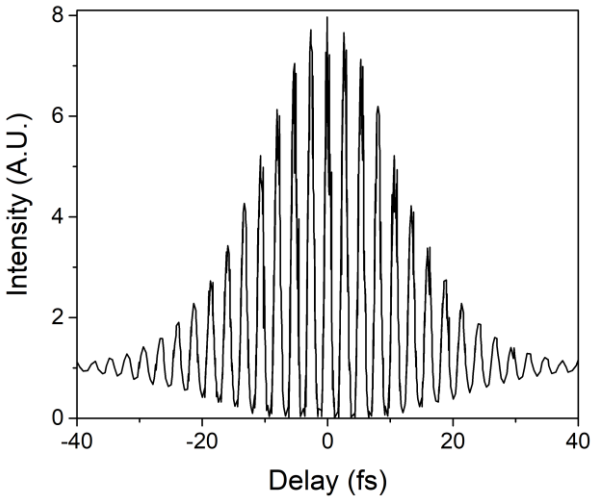

Figure 17. Typical interferometric autocorrelation of an unchirped optical pulse.

These autocorrelation traces exhibit a fast oscillation with a period equal to half the optical wavelength. When two pulses undergo perfect constructive interference, the maximum signal is obtained. This leads to a signal with twice the amplitude of a single pulse and hence 4 times the intensity. After frequency doubling the signal should be 16 times the intensity. When the arm difference is large, the pulses do not overlap in the crystal and the intensity is only twice that generated by a single pulse. This means that when the interferometer is properly aligned, an 8:1 ratio of peak signal to background should be observed as shown in Figure 17.

1.5.3 A.P.E autocorrelator

A commercial A.P.E. pulseCheck autocorrelator was used extensively throughout this project to measure pulse duration. The model used had a pulse width measurement range of <50 fs to 12 ps. By varying the beam separation, it is possible to switch between intensity (non-collinear) and interferometric (collinear) autocorrelation modes. Throughout the project intensity autocorrelation was used.

1.6 Literature review of compact and low-cost ultrafast lasers

There exist various types of ultrashort pulse laser sources based on different gain media, and these are almost always mode-locked lasers; however, ultrashort pulses have also been generated by use of gain switching [61]. Mode-locked lasers can be categorised as solid-state lasers, fibre lasers, mode-locked diode lasers and more traditionally dye lasers. Each of these will be briefly discussed below with the main focus being on solid-state lasers, as this was the type used exclusively throughout this project.

1.6.1 Solid-state lasers

Solid-state lasers (SSLs) are based on solid-state gain media such as glasses [62], crystals [29], or, increasingly, ceramics [63], doped with lasing ions. These lasers can be sub-divided into two categories dependent on the dopant: transition-metal ions or rare-earth ions.

1.6.1.1 Transition metal ion doped SSLs

Transition metal ion dopants include Ti^{3+}, Cr^{2+}, Cr^{3+}, Cr^{4+}, Ni^{2+} and Co^{2+}. A key advantage that transition metal ion-based gain media possesses over their rare-earth counterparts is the much broader gain bandwidth. This intrinsically leads to the possibility of much shorter pulses, down to a few femtoseconds in duration [19]. The characteristically broad gain bandwidth is a result of the vibronic interaction between the electronics states and lattice vibrations: as the laser transition is due to 3d electrons and as they are not well -shielded from the field of the crystal host, the vibronic interaction leads to strong homogeneous broadening resulting in a large gain bandwidth [19]. The main disadvantage of this type of gain medium is the generally lower emission cross sections compared to rare-earth-doped lasers.

1.6.1.2 Ti:sapphire lasers

Ti:sapphire is one of the most widely used laser sources today for a wide range of applications in areas such as industrial, to applied and fundamental research [11,14,64]. The unique properties of Ti:sapphire include an unrivalled gain bandwidth [65], which allows for ultra-broad wavelength tunability and femtosecond pulse generation at pulse energies and average powers suitable for a wide range of applications. However, conventional Ti:sapphire systems tend to be expensive and possess a large footprint, mainly due to the pump source, which is usually a frequency-doubled diode-pumped solid state laser. An important breakthrough in reducing the size, cost, and complexity of Ti:sapphire was made by Roth et al. in 2009 with the

first demonstration of a directly diode-pumped Ti:sapphire laser operating in the CW regime [66]. Soon after, operation in the mode-locked femtosecond regime was demonstrated in diode-pumped Ti:sapphire, with a SESAM device [67] and with KLM methods [68]. This was made possible by advancements in GaN laser diode technology with around 1 W in output power possible in the blue spectral region at the time [66]. Further development of GaN laser diode technology in the years since [69] has resulted in corresponding improvements to diode-pumped Ti:sapphire laser technology (see Chapters 2 and 3), thus representing an attractive direction in the pursuit of compact and low-cost ultrafast laser sources.

1.6.1.3 Rare-earth ion doped SSLs

The rare-earth dopants used for lasing action include Nd^{3+}, Tm^{3+}, Ho^{3+}, Er^{3+}, Pr^{3+} and Yb^{3+} [29]. The main advantages of lasers based on rare-earth doped gain media are the high cross sections and long upper state lifetimes, resulting in low thresholds and high slope efficiencies [19,29]; however, their narrower gain bandwidth compared to their transition-metal ion-based counterparts makes them less suitable for femtosecond pulse operation. These lasing ions are in most cases trivalent (i.e. possess a positive charge of three), although some divalent ions have been used for some exotic laser devices in cryogenic operation [29]. When doping a host crystal with the desired laser ion, it replaces an ion of similar size and charge e.g. a Nd^{3+} ion replaces a Y^{3+} ion in Nd:YAG. The electronic/laser transitions usually occur in the 4f electron shell, and as such are shielded from the crystal host outer electronic shells that are optically passive [29]. The result of this is that the crystal host's influence over the lasing properties such as wavelength, bandwidths and cross sections of the optical transitions is diminished [19]. A consequence of this is that the minimum pulse duration tends to be limited to 100's of femtoseconds, due to this reduction in influence on the gain bandwidth (related to pulse duration as discussed in Chapter 1.2). However, if a glass is used as the host, strong inhomogeneous broadening is experienced and thus it is possible to generate shorter pulses [70]. This has to be traded off against lower power operation as the poorer thermal conductivity of glasses limits the achievable output power [29].

1.6.2 Fibre lasers

Although fibre lasers are technically still solid-state lasers, they are mostly considered a separate category. Lasers in this category use an optical fibre as the gain medium, typically doped with rare-earth ions [71]. They are mostly diode-pumped, using fibre-coupled diode laser sources. As a gain medium they share a lot of similarities with their solid-state bulk laser

counterparts; however, their different physical properties mean that the waveguiding effect and small effective mode area present lead to different laser properties, such as much higher gain and ability to operate with higher resonator losses as a result [71]. Despite the comparatively low thermal conductivity of the glass host, the large surface-to-volume ratio of a fibre means that heat can be dissipated easily. This is an important aspect for generating high CW output powers, with kW range CW output powers now commercially available with single mode fibre [72] and 100's of kW with multi-mode fibre [73].

As they are based on rare-earth ions, they normally possess a fairly broad gain bandwidth making ultrashort pulse generation down to the femtosecond regime possible. The shortest pulses generated directly from a fibre oscillator were 28.3 fs in duration with an average output power of 56 mW [74]. Pulses as short as 8 fs have been generated with a passively mode-locked fibre laser system [75]; however, despite being quite compact the system had a lot of complexity, consisting of fibre oscillator, amplifier, and various pulse compression/stretching stages. Compared to ultrafast bulk solid-state lasers, ultrafast fibre lasers exhibit much stronger dispersive and nonlinear effects, which limit the achievable pulse energy, peak power, and pulse quality.

The strong dispersive effects arise from the inherent long path lengths involved. This can generally be compensated by using dispersion compensation in the form of fibres with different signs of dispersion [76]. However, it can be difficult to compensate for both GDD and higher orders of dispersion, which is required for very short pulses (see section 1.2.1).

The strong nonlinear effects arise from the high optical intensities associated with the small fibre mode areas, in particular single mode fibres. This is a problem especially for soliton mode-locked fibre lasers, where the pulses can become unstable when the nonlinear effects per resonator round-trip become too strong. This means pulse durations are limited to several hundred fs, pulse energies are limited to the pJ region and average output powers to a few mW. Other more complicated techniques can produce shorter pulses and higher pulse energies from fibre lasers at the expense of a lot more complexity, such as stretched pulse fibre lasers [77] or using a master oscillator fibre amplifier (MOFA) arrangement [78]. These are beyond the scope of this thesis and as such will not be discussed further.

1.6.3 Diode lasers

Diode lasers have been used to produce ultrashort pulses, either using various mode-locking techniques [79,80] or by gain switching [81]. Pulse durations between 0.5 to 5 picoseconds

are typically generated, with repetition rates from 1 GHz to hundreds of GHz, and even as high as 1 THz [82]. These high repetition rates are particularly useful for fast data transmitters in optical fibre communications systems.

Both active and passive mode-locking methods are used to generate ultrashort pulses. Active mode-locking can be realised using an optical modulator within the resonator. The optical modulator either comes in the form of an electro-absorption modulator, which changes the absorption of an unpumped region through an applied voltage, or through drive current modulation in an amplifying section [79]. Passive mode-locking in diode lasers rely on the use of a saturable absorber within the resonator and can be as simple as an unpumped region of the device with an electrical bias applied to adjust the absorption properties.

In some cases, a combination of the active and passive mode-locking is used, known as hybrid mode-locking [83]. This gives the ability to control the pulse timing similar to actively mode-locked diode lasers while also achieving shorter pulse durations associated with passively mode-locked diode lasers. This is achieved by creating a multisegmented semiconductor structure containing a gain section, an absorber or modulator section and possibly a section for control of the repetition rate.

Given the very short resonator lengths, monolithic mode-locked diode lasers have very high repetition rates on the order of 10 GHz. If repetition rates lower than this are desired an external cavity setup is required, where one end of the laser diode chip is AR-coated and the resonator completed by an external mirror. This is known as an external cavity diode laser (ECDL).

The limitations of mode-locked diode lasers are that the pulse energy is often limited to far below 1 pJ, with average output powers similarly limited to below 1 mW [84]. Low repetition rate designs below 1 GHz are generally unsuitable due to the short upper state lifetime of the semiconductor gain material [84]. Although in principle pulse durations as short of a few tens of femtoseconds are possible due to the gain bandwidth, in reality durations generated are much longer, from a minimum of a few hundred femtoseconds and more often a few picoseconds. This is mainly due to the complex pulse formation dynamics [84]. Pulse quality is also another issue, being poorer than in both mode-locked fibre and bulk solid-state lasers [84].

1.6.4 Vertical External-Cavity Surface Emitting Lasers (VECSELs)

VECSELs or semiconductor disk lasers (SDLs) are a type of semiconductor laser that comprise a surface-emitting semiconductor gain chip and a laser resonator completed with one or more external optical elements. VECSELs can often generate high powers with high beam quality. They can be pumped either electrically or optically, however, as electrically pumped devices appear to be limited to output powers of around 1 W [85] in the CW regime, they tend to be pumped optically with tens of Watts of output power achievable in the CW regime [86]. They can be quite versatile in terms of emission wavelength depending on the semiconductor material used, with VECSELs demonstrated emitting around 610 nm, 650 nm, 850 nm, 960 nm, 1030 nm, 1500 nm, and 2 µm.

Extraction of heat can be an issue due to the thermal impedance of the semiconductor structure. However, this can be circumvented by the use cooling techniques such as attaching a transparent heat spreader, such as diamond, to the emitting surface [87]. Another approach is to mount a very thin (5 to 10 µm thick) specially-processed semiconductor structure to an efficient heat sink [88]. Both techniques enable power scaling, such that twice the output power can be achieved by applying twice the pump power to twice the active area. Doubling the active area also doubles the cooling capability, meaning that the increase in active area does not significantly increase the temperature. However, the higher powers can lead to thermally-induced stress effects, which can affect beam quality and make power scaling more complicated.

In terms of ultrashort pulse generation, VECSELs passively mode-locked using a SESAM have been demonstrated producing average output powers well in excess of 1 W [89], pulse durations are typically in the picosecond range but can be as low as 60 fs [90], and pulse repetition rates are typically in the GHz range.

1.6.5 Dye lasers

Dye lasers utilise a dye based on organic molecules as its gain medium, normally in the form of a liquid solution [71]; however, solid dyes and vapour dyes used for lasers do exist [91,92]. Covering a wide wavelength range from the ultraviolet to the near-infrared region [71], typical characteristics associated with laser dye-based gain media are broad gain bandwidth (allowing for ultrashort pulse generation and broad wavelength tunability), short upper state lifetime typically around a few nanoseconds, high gain per unit length (around 10^3 cm^{-1}), and efficiency on the order of 10 to 30% for laser pumping [71,93].

While these lasers were widespread in the 1970s, they have nearly been completed replaced by solid state lasers, which typically provide more power, better wall-plug efficiency and do not suffer from the same degradation issues. In addition, many of the laser dyes and the solvents used for them are difficult to handle, poisonous and even carcinogenic, requiring extra care and precautions to be taken. That being said, there are still a few specific spectral regions where dye lasers find use [93].

1.6.6 Summary

In order to compare the various options for ultrashort pulse generation, Table 4 has been compiled:

Table 4. Comparison of various ultrafast laser oscillators. Green-coloured cells represent state-of the art performance, orange-coloured cells represent mid-range performance, and red-coloured cells represent lower-end performance.

Ultrafast Laser Type	Transition-Metal Ion Lasers	Rare-Earth Ion Lasers	Fibre Lasers	Diode Lasers	VECSELs
Output Power	>1 W	>10's W	~100 mW	<1 mW	>1W
Minimum Pulse Duration	<10 fs	10's of fs	100's of fs	>500 fs	100's of fs
Tunability	Very Large	Medium	Small	Small	Small
Size	Large	Small	Small	Small	Small
Maximum Repetition Rate	10 GHz	10 GHz	100's MHz	50-100 GHz	50-100 GHz

To evaluate the various ultrafast laser options described above, it is useful to compare and contrast against the requirements for a typical application of ultrafast lasers. In this case multiphoton microscopy is used, an important application for ultrafast lasers operating in the femtosecond regime. The ultrafast laser parameters focused on in this analysis are average output power, pulse duration, wavelength tunability, size and maximum repetition rate.

The average power required for two-photon microscopy is only a few 10's of mW at the sample, however, attenuation due to microscope optics usually means that the laser source must have an average output power equal to a few hundred mW. This is a requirement easily satisfied by transition metal ion, rare earth ion based lasers, and VECSELs, but is much more challenging for fibre lasers and especially diode lasers.

Pulse duration is another vital parameter as the efficiency of the two-photon mechanism increases with the inverse of pulse duration, assuming that the average power and pulse repetition rate are held constant [94]. However, pulses much shorter than 100 fs are severely distorted by the material dispersion due to the microscope optics. Therefore, pulses of 100-

200 fs are optimal, which can be routinely achieved by transition metal ion lasers such as Ti:sapphire [29] and, with more difficulty, rare-earth ion lasers such as Yb:KGW [95].

An important aspect in multiphoton microscopy is wavelength tunability, as different multiphoton microscopy markers have different excitation wavelengths distributed over a broad spectral range [96]. Therefore, if one wishes to be able to access various multiphoton microscopy markers without the need for multiple laser sources, then a laser source with wavelength tunability is required. In this aspect Ti:sapphire lasers are unrivalled with the ability to tune over 100's of nm while maintaining fs pulse operation [97]. Lasers based on rare-earth gain media such as Yb:CYA have been demonstrated to produce fs pulses over 10's of nm [98]. Ultrafast fibre lasers have also been shown to produce femtosecond pulses over a range of 10's of nm [99], albeit with pulse durations >500 fs.

To summarise, transition-metal ion lasers, in particular Ti:sapphire, have an ideal combination of high average output powers >1 W, short pulse durations <100 fs and wide wavelength tunability over 100's of nm. However, Ti:sapphire lasers are bulky, expensive, and complex, due mainly to the frequency-doubled diode-pumped solid state laser pump source. An attractive option to reduce the size, cost, and complexity of Ti:sapphire lasers that this thesis sets out to explore, is to replace the frequency-doubled DPSSL pump source with a laser diode pump source. This was first demonstrated in 2009 [66], but with GaN laser diode performance levels having improved significantly since then, diode-pumping is an even more attractive possibility than ever. This approach comes with its own challenges which are discussed in more detail in Chapter 2.

One performance aspect of ultrafast Ti:sapphire lasers that this thesis sets out to address is wavelength tunability during femtosecond pulse operation of diode-pumped Ti:sapphire lasers. This is explored in more detail in Chapter 3.

Another area where diode-pumped Ti:sapphire lasers could be developed is in realising a diode-pumped Ti:sapphire laser with ≥1 GHz pulse repetition rate, which is important for some frequency comb applications [100,101]. This is covered in more detail in Chapter 4.

Finally, novel saturable absorbers will be investigated in chapter 5 focusing on the use of monolayer graphene as a mode-locking element in ultrafast lasers. Graphene has been shown as an attractive element for mode-locking various types of lasers including solid-state and fibre lasers [102–104].

1.7 Conclusion

Presented in this chapter is an overview of the applications of ultrafast lasers and their properties, as well as basic details concerning ultrashort pulse generation and characterisation. This included the propagation of ultrashort pulses through dispersive materials and the host of effects this gives rise to. Of particular importance are the Kerr-lens and SESAM mode-locking techniques, which were used extensively throughout this project. A review of the various ultrafast laser sources available is also given, including justification of why diode-pumped Ti:sapphire lasers are an attractive option to consider in the pursuit of lower-cost and compact ultrafast laser sources, and identification of areas/parameters in which they could be improved.

1.8 References

1. "Number of smartphone users worldwide from 2016 to 2026," https://www.statista.com/statistics/330695/number-of-smartphone-users-worldwide/.
2. S. Rangwala, "The iPhone 12 - LiDAR At Your Fingertips," https://www.forbes.com/sites/sabbirrangwala/2020/11/12/the-iphone-12lidar-at-your-fingertips/?sh=23bd23f93e28.
3. J.-M. Hopkins and W. Sibbett, "Ultrashort-Pulse Lasers: Big Payoffs in a Flash," Sci. Am. **283**(3), 72–79 (2000).
4. A. Zewail, "The Nobel Prize in Chemistry 1999," https://www.nobelprize.org/prizes/chemistry/1999/summary/.
5. T. W. Hänsch and J. L. Hall, "The Nobel Prize in Physics 2005," https://www.nobelprize.org/prizes/physics/2005/summary/.
6. T. Udem, R. Holzwarth, and T. W. Hänsch, "Optical frequency metrology," Nature **416**(6877), 233–237 (2002).
7. G. Morou and D. Strickland, "The Nobel Prize in Physics 2018," https://www.nobelprize.org/prizes/physics/2018/summary/.
8. "Vulcan laser facility," https://www.clf.stfc.ac.uk/Pages/Vulcan.aspx.
9. J. Meinecke, H. W. Doyle, F. Miniati, A. R. Bell, R. Bingham, R. Crowston, R. P. Drake, M. Fatenejad, M. Koenig, Y. Kuramitsu, C. C. Kuranz, D. Q. Lamb, D. Lee, M. J. MacDonald, C. D. Murphy, H.-S. Park, A. Pelka, A. Ravasio, Y. Sakawa, A. A. Schekochihin, A. Scopatz, P. Tzeferacos, W. C. Wan, N. C. Woolsey, R. Yurchak, B. Reville, and G. Gregori, "Turbulent amplification of magnetic fields in laboratory laser-produced shock waves," Nat. Phys. **10**(7), 520–524 (2014).
10. M. Drescher, "X-ray Pulses Approaching the Attosecond Frontier," Science (80-.). **291**(5510), 1923–1927 (2001).
11. F. Helmchen and W. Denk, "Deep tissue two-photon microscopy," Nat. Methods **2**(12), 932–940 (2005).
12. K. Itoh, W. Watanabe, S. Nolte, and C. B. Schaffer, "Ultrafast processes for bulk modification of transparent materials," MRS Bull. **31**(8), 620–625 (2006).
13. F. Chen and J. R. V. de Aldana, "Optical waveguides in crystalline dielectric materials produced by femtosecond-laser micromachining," Laser Photonics Rev. **8**(2), 251–275 (2014).
14. N. Bärsch, K. Körber, A. Ostendorf, and K. H. Tönshoff, "Ablation and cutting of planar silicon devices using femtosecond laser pulses," Appl. Phys. A Mater. Sci. Process. **77**(2), 237–242 (2003).
15. R. Paschotta, "Medical Lasers," https://www.rp-photonics.com/medical_lasers.html.
16. W. Drexler, U. Morgner, R. K. Ghanta, F. X. Kärtner, J. S. Schuman, and J. G. Fujimoto, "Ultrahigh-resolution ophthalmic optical coherence tomography," Nat. Med. **7**(4), 502–506 (2001).

17. V. Torres-Company, J. Schroder, A. Fulop, M. Mazur, L. Lundberg, O. B. Helgason, M. Karlsson, and P. A. Andrekson, "Laser frequency combs for coherent optical communications," J. Light. Technol. **37**(7), 1663–1670 (2019).
18. A. E. Siegman, "Lasers," (1986).
19. U. Keller, *Ultrafast Solid State Lasers* (2007).
20. R. L. Fork, O. E. Martinez, and J. P. Gordon, "Negative dispersion using pairs of prisms," Opt. Lett. **9**(5), 150 (1984).
21. F. X. Kärtner, N. Matuschek, T. R. Schibli, U. Keller, H. A. Haus, C. Heine, R. Morf, V. Scheuer, M. Tilsch, and T. Tschudi, "Design and fabrication of double-chirped mirrors," Opt. Lett. **22**(11), 831 (1997).
22. B. Golubovic, R. R. Austin, M. K. Steiner-Shepard, M. K. Reed, S. A. Diddams, D. J. Jones, and A. G. Van Engen, "Double Gires–Tournois interferometer negative-dispersion mirrors for use in tunable mode-locked lasers," Opt. Lett. **25**(4), 275 (2000).
23. R. Paschotta, "Gires-Tournois interferometers," https://www.rp-photonics.com/gires_tournois_interferometers.html.
24. E. Treacy, "Optical pulse compression with diffraction gratings," IEEE J. Quantum Electron. **5**(9), 454–458 (1969).
25. R. Szipöcs, C. Spielmann, F. Krausz, and K. Ferencz, "Chirped multilayer coatings for broadband dispersion control in femtosecond lasers," Opt. Lett. **19**(3), 201 (1994).
26. F. X. Kärtner, U. Morgner, R. Ell, T. Schibli, J. G. Fujimoto, E. P. Ippen, V. Scheuer, G. Angelow, and T. Tschudi, "Ultrabroadband double-chirped mirror pairs for generation of octave spectra," J. Opt. Soc. Am. B **18**(6), 882 (2001).
27. R. Ell, U. Morgner, F. X. Kärtner, J. G. Fujimoto, E. P. Ippen, V. Scheuer, G. Angelow, T. Tschudi, M. J. Lederer, A. Boiko, and B. Luther-Davies, "Generation of 5-fs pulses and octave-spanning spectra directly from a Ti:sapphire laser," Opt. Lett. **26**(6), 373 (2001).
28. "Layertec website," https://www.layertec.de/en/.
29. W. Koechner, *Solid-State Laser Engineering - 6th Edition* (2014).
30. R. Paschotta, "Mode locking," https://www.rp-photonics.com/mode_locking.html.
31. D. Kopf, F. X. Kärtner, K. J. Weingarten, and U. Keller, "Pulse shortening in a Nd:glass laser by gain reshaping and soliton formation," Opt. Lett. **19**(24), 2146 (1994).
32. F. X. Kärtner, D. Kopf, and U. Keller, "Solitary-pulse stabilization and shortening in actively mode-locked lasers," J. Opt. Soc. Am. B **12**(3), 486 (1995).
33. C. L. Tang and H. Statz, "Maximum-emission principle and phase locking in multimode lasers," J. Appl. Phys. **38**(7), 2963–2968 (1967).
34. J. A. VALDMANIS, R. L. FORK, and J. P. GORDON, "Generation of femtosecond optical pulses directly from lasers balancing self-phase modulation, group velocity dispersion, saturable absorption, and saturable gain," in *Conference on Lasers and Electro-Optics* (OSA, 1985), **10**(3), p. WE2.
35. G. H. C. New, "Mode-locking of quasi-continuous lasers," Opt. Commun. **6**(2), 188–192 (1972).
36. H. A. Haus, U. Keller, and W. H. Knox, "Theory of coupled-cavity mode locking with a resonant nonlinearity," J. Opt. Soc. Am. B **8**(6), 1252 (1991).
37. D. E. Spence, P. N. Kean, and W. Sibbett, "60-fsec pulse generation from a self-mode-locked Ti:sapphire laser," Opt. Lett. **16**(1), 42 (1991).
38. S. Uemura and K. Torizuka, "Generation of 12-fs pulses from a diode-pumped Kerr-lens mode-locked Cr : LiSAF laser," **24**(11), 780–782 (1999).
39. E. Sorokin, N. Tolstik, and I. T. Sorokina, "Kerr-Lens Mode-locked Cr:ZnS Laser," in *Lasers, Sources, and Related Photonic Devices* (OSA, 2012), **38**(3), p. AW5A.5.
40. G. Machinet, P. Sevillano, F. Guichard, R. Dubrasquet, P. Camy, J. Doualan, and R. Moncorgé, "Kerr-lens mode-locked Yb : CaF 2 oscillator," Opt. Lett. **38**(20), 4008–4010 (2013).
41. H. Zhao and A. Major, "Powerful 67 fs Kerr-lens mode-locked prismless Yb:KGW oscillator," Opt. Express **21**(26), 31846 (2013).
42. V. Magni, G. Cerullo, S. De Silvestri, and A. Monguzzi, "Astigmatism in Gaussian-beam self-focusing and in resonators for Kerr-lens mode locking," J. Opt. Soc. Am. B **12**(3), 476 (1995).
43. T. Brabec, P. F. Curley, C. Spielmann, E. Wintner, and A. J. Schmidt, "Hard-aperture Kerr-lens mode locking," **10**(6), 1029–1034 (1993).
44. S. Yefet and A. Pe'er, "Mode locking with enhanced nonlinearity - a detailed study," Opt. Express **21**(16), 19040 (2013).

45. F. X. Kärtner and U. Keller, "Stabilization of solitonlike pulses with a slow saturable absorber," Opt. Lett. **20**(1), 16 (1995).

46. D. Kopf, K. J. Weingarten, F. X. Kärtner, and U. Keller, "Diode-pumped mode-locked Nd:glass lasers with an antiresonant Fabry–Perot saturable absorber," Opt. Lett. **20**(10), 1169 (1995).

47. I. D. Jung, F. X. Kärtner, L. R. Brovelli, M. Kamp, and U. Keller, "Experimental verification of soliton mode locking using only a slow saturable absorber," Opt. Lett. **20**(18), 1892 (1995).

48. I. D. Jung, R. Fluck, G. Zhang, F. X. Kartner, and U. Keller, "Broadband saturable absorber for 10-fs pulse generation," Conf. Proc. - Lasers Electro-Optics Soc. Annu. Meet. **21**(10), 26–27 (1996).

49. U. Keller, K. J. Weingarten, F. X. Kärtner, D. Kopf, B. Braun, I. D. Jung, R. Fluck, C. Hönninger, N. Matuschek, and J. Aus Der Au, "Semiconductor saturable absorber mirrors (SESAM's) for femtosecond to nanosecond pulse generation in solid-state lasers," IEEE J. Sel. Top. Quantum Electron. **2**(3), 435–451 (1996).

50. D. Kopf, G. Zhang, R. Fluck, M. Moser, and U. Keller, "All-in-one dispersion-compensating saturable absorber mirror for compact femtosecond laser sources," Opt. Lett. **21**(7), 486 (1996).

51. U. Keller, D. A. B. Miller, G. D. Boyd, T. H. Chiu, J. F. Ferguson, and M. T. Asom, "Solid-state low-loss intracavity saturable absorber for Nd:YLF lasers: an antiresonant semiconductor Fabry–Perot saturable absorber," Opt. Lett. **17**(7), 505 (1992).

52. C. Hönninger, R. Paschotta, F. Morier-Genoud, M. Moser, and U. Keller, "Q-switching stability limits of continuous-wave passive mode locking," J. Opt. Soc. Am. B **16**(1), 46 (1999).

53. L. R. Brovelli, U. Keller, and T. H. Chiu, "Design and operation of antiresonant Fabry–Perot saturable semiconductor absorbers for mode-locked solid-state lasers," J. Opt. Soc. Am. B **12**(2), 311 (1995).

54. C. J. Saraceno, C. Schriber, M. Mangold, M. Hoffmann, O. H. Heckl, C. R. E. Baer, M. Golling, T. Südmeyer, and U. Keller, "SESAMs for High-Power Oscillators: Design Guidelines and Damage Thresholds," IEEE J. Sel. Top. Quantum Electron. **18**(1), 29–41 (2012).

55. P. T. Guerreiro, S. Ten, N. F. Borrelli, J. Butty, G. E. Jabbour, and N. Peyghambarian, "PbS quantum-dot doped glasses as saturable absorbers for mode locking of a Cr:forsterite laser," Appl. Phys. Lett. **71**(12), 1595–1597 (1997).

56. S. Y. Set, H. Yaguchi, Y. Tanaka, and M. Jablonski, "Laser Mode Locking Using a Saturable Absorber Incorporating Carbon Nanotubes," J. Light. Technol. **22**(1), 51–56 (2004).

57. Z. Sun, T. Hasan, F. Torrisi, D. Popa, G. Privitera, F. Wang, F. Bonaccorso, D. M. Basko, and A. C. Ferrari, "Graphene Mode-Locked Ultrafast Laser," ACS Nano **4**(2), 803–810 (2010).

58. K. Sala, G. Kenney-Wallace, and G. Hall, "CW autocorrelation measurements of picosecond laser pulses," IEEE J. Quantum Electron. **16**(9), 990–996 (1980).

59. D. J. Kane and R. Trebino, "Characterization of arbitrary femtosecond pulses using frequency-resolved optical gating," IEEE J. Quantum Electron. **29**(2), 571–579 (1993).

60. C. Iaconis and I. A. Walmsley, "Spectral phase interferometry for direct electric-field reconstruction of ultrashort optical pulses," Opt. Lett. **23**(10), 792 (1998).

61. T. Sogawa, Y. Arakawa, M. Tanaka, and H. Sakaki, "Observation of a short optical pulse (<1.3 ps) from a gain-switched quantum well laser," Appl. Phys. Lett. **53**(17), 1580–1582 (1988).

62. W. J. Kozlovsky, T. Y. Fan, and R. L. Byer, "Diode-pumped continuous-wave Nd:glass laser," Opt. Lett. **11**(12), 788 (1986).

63. A. Ikesue and Y. L. Aung, "Ceramic laser materials," Nat. Photonics **2**(12), 721–727 (2008).

64. P. M. Paul, E. S. Toma, P. Breger, G. Mullot, F. Augé, P. Balcou, H. G. Muller, and P. Agostini, "Observation of a train of attosecond pulses from high harmonic generation," Science (80-.). **292**(5522), 1689–1692 (2001).

65. P. F. Moulton, "Spectroscopic and laser characteristics of Ti:Al2O3," J. Opt. Soc. Am. B **3**(1), 125 (1986).

66. P. W. Roth, A. J. Maclean, D. Burns, and A. J. Kemp, "Directly diode-laser-pumped Ti:sapphire laser.," Opt. Lett. **34**(21), 3334–3336 (2009).

67. P. W. Roth, A. J. Maclean, D. Burns, and A. J. Kemp, "Direct diode-laser pumping of a mode-locked Ti : sapphire laser," Opt. Lett. **36**(2), 304–306 (2011).

68. C. G. Durfee, T. Storz, J. Garlick, S. Hill, J. A. Squier, M. Kirchner, G. Taft, K. Shea, H. Kapteyn, M. Murnane, and S. Backus, "Direct diode-pumped Kerr-lens mode-locked Ti : sapphire laser," Opt. Express **20**(13), 1223–1227 (2012).

69. Nichia, "Nichia Laser Diode Product Range," https://www.nichia.co.jp/en/product/laser.html.

70. S. Han, W. Lu, B. Y. Sheh, L. Yan, M. Wraback, H. Shen, J. Pamulapati, and P. G. Newman, "Generation of sub-40 fs pulses from a mode-locked dual-gain-media Nd:glass laser," Appl. Phys. B Lasers Opt. **74**(SUPPL.), 177–179 (2002).

71. O. Svelto, *Principles of Lasers* (n.d.).

72. IPG Photonics, "High Power CW Fiber Lasers," https://www.ipgphotonics.com/en/products/lasers/high-power-cw-fiber-lasers.

73. J. Hecht, "High-Power Fiber Lasers," Opt. Photonics News (October), 30–37 (2018).

74. X. Zhou, D. Yoshitomi, Y. Kobayashi, and K. Torizuka, "Generation of 28-fs pulses from a mode-locked ytterbium fiber oscillator," Opt. Express **16**(10), 7055 (2008).

75. A. Sell, G. Krauss, R. Scheu, R. Huber, and A. Leitenstorfer, "8-fs pulses from a compact Er:fiber system: quantitative modeling and experimental implementation," Opt. Express **17**(2), 1070 (2009).

76. R. Paschotta, "Mode-locked Fiber Lasers," https://www.rp-photonics.com/mode_locked_fiber_lasers.html.

77. M. Guina, N. Xiang, and O. G. Okhotnikov, "Stretched-pulse fiber lasers based on semiconductor saturable absorbers," Appl. Phys. B Lasers Opt. **74**(SUPPL.), 193–200 (2002).

78. R. Paschotta, "Master Oscillator Fiber Amplifier," https://www.rp-photonics.com/master_oscillator_fiber_amplifier.html.

79. J. E. Bowers, P. A. Morton, A. Mar, and S. W. Corzine, "Actively mode-locked semiconductor lasers," IEEE J. Quantum Electron. **25**(6), 1426–1439 (1989).

80. Young-Kai Chen and M. C. Wu, "Monolithic colliding-pulse mode-locked quantum-well lasers," IEEE J. Quantum Electron. **28**(10), 2176–2185 (1992).

81. T. Sogawa, Y. Arakawa, M. Tanaka, and H. Sakaki, "Observation of a short optical pulse (<1.3 ps) from a gain-switched quantum well laser," Appl. Phys. Lett. **53**(17), 1580–1582 (1988).

82. S. Arahira, Y. Matsui, and Y. Ogawa, "Mode-locking at very high repetition rates more than terahertz in passively mode-locked distributed-Bragg-reflector laser diodes," IEEE J. Quantum Electron. **32**(7), 1211–1224 (1996).

83. I. Ogura, H. Kurita, T. Sasaki, and H. Yokoyama, "Precise operation-frequency control of monolithic mode-locked laser diodes for high-speed optical communication and all-optical signal processing," Opt. Quantum Electron. **33**(7–10), 709–725 (2001).

84. R. Paschotta, "Mode-locked Diode Lasers," https://www.rp-photonics.com/mode_locked_diode_lasers.html.

85. J. G. McInerney, A. Mooradian, A. Lewis, A. V. Shchegrov, E. M. Strzelecka, D. Lee, J. P. Watson, M. K. Liebman, G. P. Carey, A. Umbrasas, C. A. Amsden, B. D. Cantos, W. R. Hitchens, D. L. Heald, and V. Doan, "Novel 980-nm and 490-nm light sources using vertical-cavity lasers with extended coupled cavities," in *Vertical-Cavity Surface-Emitting Lasers VII*, C. Lei and S. P. Kilcoyne, eds. (2003), p. 21.

86. J. L. A. Chilla, S. D. Butterworth, A. Zeitschel, J. P. Charles, A. L. Caprara, M. K. Reed, and L. Spinelli, "High-power optically pumped semiconductor lasers," in *Solid State Lasers XIII: Technology and Devices*, R. Scheps and H. J. Hoffman, eds. (2004), p. 143.

87. A. Chernikov, J. Herrmann, M. Koch, B. Kunert, W. Stolz, S. Chatterjee, S. W. Koch, T. L. Wang, Y. Kaneda, J. M. Yarborough, J. Hader, and J. V Moloney, "Heat Management in High-Power Vertical-External-Cavity Surface-Emitting Lasers," IEEE J. Sel. Top. Quantum Electron. **17**(6), 1772–1778 (2011).

88. M. Kuznetsov, F. Hakimi, R. Sprague, and A. Mooradian, "Design and characteristics of high-power (>0.5-W CW) diode-pumped vertical-external-cavity surface-emitting semiconductor lasers with circular TEM00 beams," IEEE J. Sel. Top. Quantum Electron. **5**(3), 561–573 (1999).

89. R. Haring, M. Paschotta, A. Aschwanden, E. Gini, F. Morier-Genoud, and U. Keller, "High-power passively mode-locked semiconductor lasers," IEEE J. Quantum Electron. **38**(9), 1268–1275 (2002).

90. A. H. Quarterman, K. G. Wilcox, V. Apostolopoulos, Z. Mihoubi, S. P. Elsmere, I. Farrer, D. A. Ritchie, and A. Tropper, "A passively mode-locked external-cavity semiconductor laser emitting 60-fs pulses," Nat. Photonics **3**(12), 729–731 (2009).

91. R. Bornemann, U. Lemmer, and E. Thiel, "Continuous-wave solid-state dye laser," Opt. Lett. **31**(11), 1669 (2006).

92. P. W. Smith, "Dye Vapour Lasers," Opt. Acta Int. J. Opt. **23**(11), 901–909 (1976).

93. R. Paschotta, "Dye Lasers," https://www.rp-photonics.com/dye_lasers.html.

94. S. Tang, T. B. Krasieva, Z. Chen, G. Tempea, and B. J. Tromberg, "Effect of pulse duration on two-photon excited fluorescence and second harmonic generation in nonlinear optical microscopy," J. Biomed. Opt. **11**(2), 020501 (2006).

95. F. Brunner, G. J. Spühler, J. Aus der Au, L. Krainer, F. Morier-Genoud, R. Paschotta, N. Lichtenstein, S. Weiss, C. Harder, A. A. Lagatsky, A. Abdolvand, N. V. Kuleshov, and U. Keller, "Diode-pumped femtosecond Yb:KGd(WO_4)_2 laser with 1.1-W average power," Opt. Lett. **25**(15), 1119 (2000).

96. K. Koenig, "Multiphoton microscopy in life sciences," J. Microsc. **200**(2), 83–104 (2000).

97. Coherent Inc, "Chameleon Ultra Family," https://www.coherent.com/lasers/oscillators/chameleon-ultra.

98. F. Pirzio, S. D. D. D. Cafiso, M. Kemnitzer, A. Guandalini, F. Kienle, S. Veronesi, M. Tonelli, J. Aus der Au, and A. Agnesi, "Sub-50-fs widely tunable Yb:CaYAlO_4 laser pumped by 400-mW single-mode fiber-coupled laser diode," Opt. Express **23**(8), 9790 (2015).

99. B. Nyushkov, S. Kobtsev, A. Antropov, D. Kolker, and V. Pivtsov, "Femtosecond 78-nm Tunable Er:Fibre Laser Based on Drop-Shaped Resonator Topology," J. Light. Technol. **37**(4), 1359–1363 (2019).

100. R. A. McCracken, É. Depagne, R. B. Kuhn, N. Erasmus, L. A. Crause, and D. T. Reid, "Wavelength calibration of a high resolution spectrograph with a partially stabilized 15-GHz astrocomb from 550 to 890 nm," Opt. Express **25**(6), 6450 (2017).

101. D. C. Heinecke, A. Bartels, T. M. Fortier, D. A. Braje, L. Hollberg, and S. A. Diddams, "Optical frequency stabilization of a 10 GHz Ti:sapphire frequency comb by saturated absorption spectroscopy in r 87 ubidium," Phys. Rev. A - At. Mol. Opt. Phys. **80**(5), 1–7 (2009).

102. I. H. Baek, H. W. Lee, S. Bae, B. H. Hong, Y. H. Ahn, D.-I. Yeom, and F. Rotermund, "Efficient Mode-Locking of Sub-70-fs Ti:Sapphire Laser by Graphene Saturable Absorber," Appl. Phys. Express **5**(3), 032701 (2012).

103. E. Ugolotti, A. Schmidt, V. Petrov, J. Wan Kim, D.-I. Yeom, F. Rotermund, S. Bae, B. Hee Hong, A. Agnesi, C. Fiebig, G. Erbert, X. Mateos, M. Aguiló, F. Diaz, and U. Griebner, "Graphene mode-locked femtosecond Yb:KLuW laser," Appl. Phys. Lett. **101**(16), 161112 (2012).

104. H. Zhang, D. Y. Tang, L. M. Zhao, Q. L. Bao, and K. P. Loh, "Large energy mode locking of an erbium-doped fiber laser with atomic layer graphene," Opt. Express **17**(20), 17630 (2009).

Chapter 2: CW diode-pumped Ti:sapphire lasers

2.1 Background Ti:sapphire theory

Titanium-doped sapphire (Ti^{3+}:Al_2O_3 or Ti:sapphire) is one of the most widely used and useful laser gain medium today [1,2]. The main reason for this is the ultrabroad gain bandwidth extending from 650 nm to 1100 nm, allowing for broad laser tunability, femtosecond pulse generation, and excellent thermo-mechanical properties which can support high power and high pulse energy operation [3]. The application of Ti:sapphire lasers are numerous, including imaging [4,5], spectroscopy [6], materials processing [7], and fundamental science [8]. The importance of these lasers as tools for scientific research is underlined by their instrumental use in the Nobel prize winning work in both femtochemistry [9] and frequency comb precision spectroscopy [10].

Despite their success, Ti:sapphire lasers remain expensive, bulky, and complex. This all but rules them out for many applications where they would otherwise prove very useful and inhibits the proliferation of applications where a Ti:sapphire laser is required, such as two-photon microscopy. The reasons for this are explained in more detail in the following sections of this chapter.

2.1.1 Ti:sapphire material properties

Table 5. A summary of selected important material and optical properties of Ti:sapphire.

Ti:sapphire material and optical properties	
Laser type	4-level vibronic
Fluorescent linewidth (FWHM)	230 nm
Peak emission wavelength	795 nm
Stimulated emission cross-section - π-polarisation - σ-polarisation	 4.1 x 10^{-19} cm^2 2.0 x 10^{-19} cm^2
Peak absorption wavelength	490 nm
Upper state lifetime	3.2 µs
Refractive index - At 800 nm - At 532 nm	 1.76 1.77
Thermal conductivity	33 W m^{-1} K^{-1}

Ti:sapphire consists of a sapphire host (Al_2O_3) where trivalent Titanium ions (Ti^{3+}) replace some of the Al^{3+} ions in the crystal lattice. This is achieved by adding Ti_2O_3 to the crystal melt, the amount of which determines the doping level. Typical doping values are between 0.02 to 0.5 wt. %. Different growth methods are used with the Czochralski method [11] and Heat Exchange Method (HEM) [12] being two of the most developed, providing excellent optical quality crystals. A summary of the most important material and optical properties is listed in Table 5.

The large fluorescent bandwidth of Ti:sapphire, as shown in Figure 18, is a result of the strong interaction between the Ti^{3+} lasing ions and the sapphire host, and the large difference in electron distribution between the two energy levels of the lasing transition. Uniquely among transition metal laser ions, the lack of d-state energy levels above the upper laser level in Ti^{3+} means that Ti:sapphire does not normally (see section 2.3.2) experience excited state absorption (ESA), an effect that would restrict the tuning range. As a result, Ti:sapphire lasers can potentially be tuned over 400 nm and can support femtosecond pulse generation.

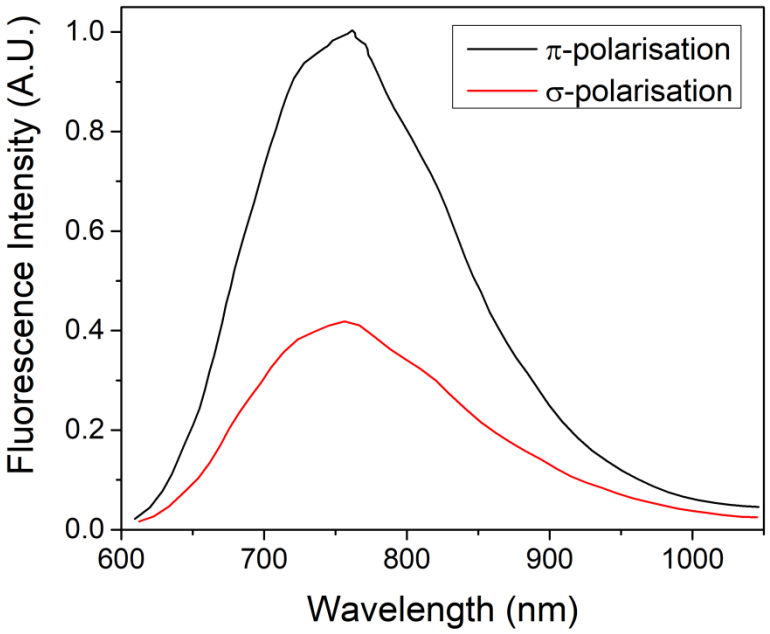

Figure 18. Fluorescence linewidth versus wavelength for Ti:sapphire in the π and σ polarisations [1].

Other favourable properties include the excellent thermal conductivity, which alleviates detrimental thermal effects such as thermal lensing, a large stimulated emission cross section, reducing the likelihood of Q-Switching instabilities, as well as good mechanical properties and chemical inertness.

One downside is that the upper state lifetime is very short at 3.2 μs. As the lasing threshold is inversely proportional to the product of the upper state lifetime and stimulated emission cross-section, a very short upper state lifetime means that the threshold will be high. As a comparison, a table of the stimulated emission cross section and upper state lifetime of different laser materials at room temperature is shown in Table 6.

Table 6. Stimulated emission cross section (σ), upper state lifetime (τ), and normalised σ – τ product of different laser materials at room temperature.

Gain medium	**τ** (μs)	**σ** (cm^2)	**Normalised σ – τ product**
Ti:sapphire	3.2	4.1 x 10^{-19} (at 795 nm)	1
Nd:YAG	230	2.8 ×10^{-19} (at 1064 nm)	49
Alexandrite	262	0.7×10^{-19} (at 750 nm)	14

It is apparent from Table 6 that despite having a larger stimulated emission cross section, Ti:sapphire has a σ – τ product 49 times smaller than Nd:YAG and that this is due to the very short upper state lifetime. Thus, a high pump flux is required to reach the lasing threshold for Ti:sapphire. This is further complicated by the fact that Ti:sapphire possesses a relatively low pump absorption coefficient. The small signal pump absorption A_p is simply calculated from:

$$A_p = 1 - \exp\left(-N_{dop}\sigma_{abs}L\right) \tag{24}$$

where N_{dop} is the doping concentration, σ_{abs} pump absorption cross section and L is the length of material. The pump absorption cross section of Ti:sapphire versus wavelength is shown in Figure 19.

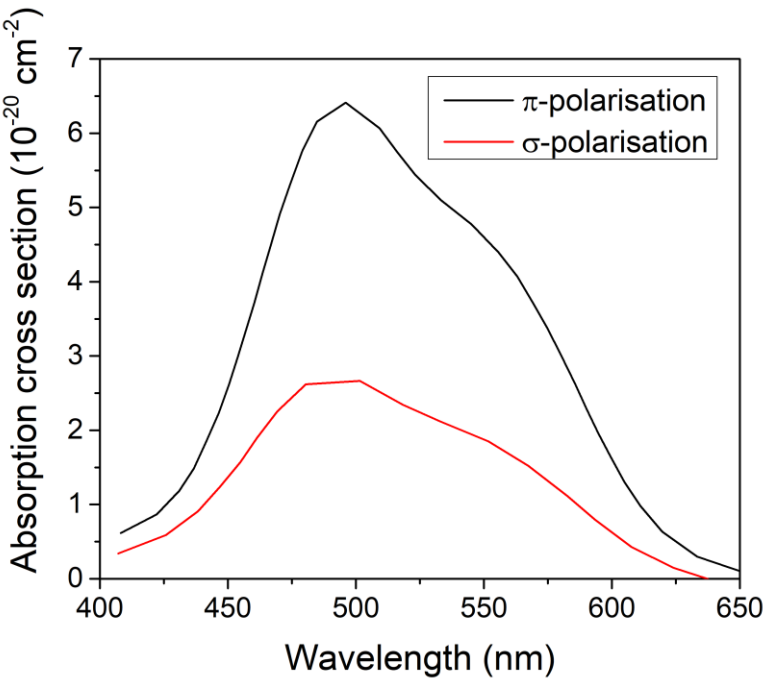

Figure 19. Absorption cross section versus wavelength for Ti:sapphire in the π and σ polarisations [1].

As can be seen from Figure 19, the peak of the Ti:sapphire absorption spectrum is around 490 nm. The absorption remains fairly high in the green region of the spectrum between 500-550 nm and drops off quite sharply below 490 nm. Historically, the blue-green region of the spectrum has not been a laser-rich region and as such the choice of candidate pump lasers has been limited. More detail on lasers used to pump Ti:sapphire lasers is discussed in section 2.2.

Ti:sapphire also exhibits a weak absorption band extending into the infrared region, overlapping with its fluorescence bandwidth. This is due to both the presence of Ti^{3+} - Ti^{4+} pairs in the crystal, and a second effect related to Ti^{3+} concentration in the crystal but not yet fully understood. This absorption results in parasitic losses at the laser wavelength. Improved crystal growth processes including post-growth annealing have reduced but not completely eliminated these losses [13].

A useful metric used to quantify the amount of parasitic absorption in Ti:sapphire is what is referred to as the Figure of Merit (FOM). This gives a ratio between the pump absorption coefficient (often given at 514 nm or 532 nm for Ti:sapphire) and the laser wavelength absorption coefficient (often given at 800 nm for Ti:sapphire).

$$FOM = \frac{\alpha_{514\,nm}}{\alpha_{800\,nm}} \tag{25}$$

As shown in Figure 20 this ratio is dependent on the doping concentration, with higher doping resulting in a lower FOM and lower doping resulting in a higher FOM generally speaking. In most cases, commercially available crystals will have a FOM between 100 and 500.

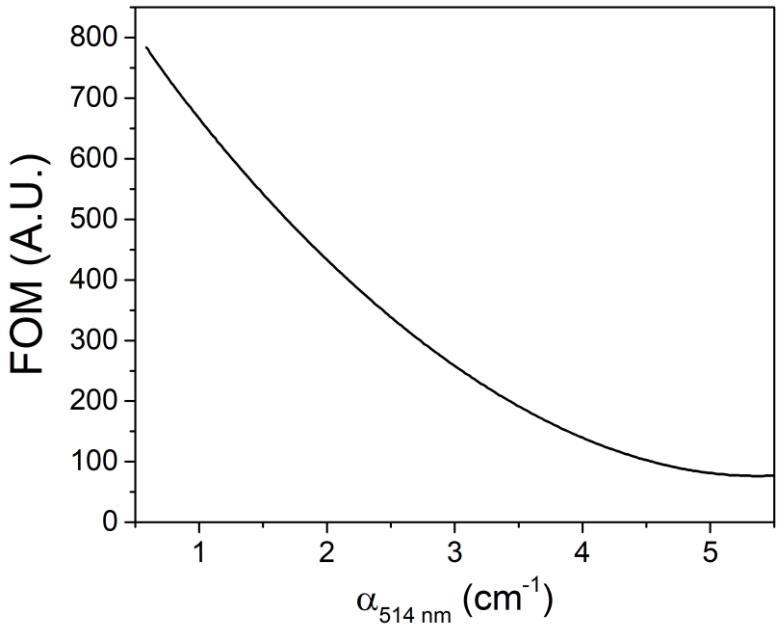

Figure 20. Figure of Merit (FOM) vs. pump absorption of Ti:sapphire, adapted from [14].

As the pump absorption cross section of Ti:sapphire is small and FOM decreases with increased doping, long crystal lengths of several millimetres with low pump absorption and high FOM tend to be used to ensure that a reasonable fraction of the incident pump power is absorbed. As a high pump flux needs to be maintained over this length, this places constraints upon the beam quality of the pump, as a higher quality beam will be able to maintain a tight beam waist over a longer distance when focused than a lower quality beam.

To summarise, a high-intrinsic threshold due to the small σ-τ-product, the tendency to use lower doping and thus lower pump absorption in combination with a long crystal length to avoid high parasitic losses, means that a high power and high brightness pump source is usually required. This is covered in more detail in 2.2.

2.1.2 Conventional Ti:sapphire systems

As concluded from the previous section, it becomes clear that Ti:sapphire lasers tend to need a pump source with high power and high brightness in order to maintain the required pump

intensity over a long length of crystal. In the next section several conventional pump options are discussed.

2.2 Conventional pump options

Historically, pumping of Ti:sapphire was done with an argon-ion or copper-vapour laser [3,15]. In the last two decades or so, the advances seen in frequency-doubled solid-state lasers and frequency-doubled optically pumped semiconductor lasers, mean that they have almost completely replaced argon-ion lasers for most applications, including pumping of Ti:sapphire [16]. This is due to the much better efficiency and lifetimes offered by these systems. This will be discussed in more detail in the following sections.

2.2.1 Argon-ion lasers

Argon-ion lasers consist of an argon gas-filled tube constructed from a ceramic such as beryllium oxide, and inside which there are two hollow electrodes (see Figure 21). An intense electrical discharge between these two electrodes creates a plasma containing a high density of argon ions. Some systems include a solenoid around the discharge tube, used to generate a magnetic field in order to better confine the plasma, thus allowing for higher output power.

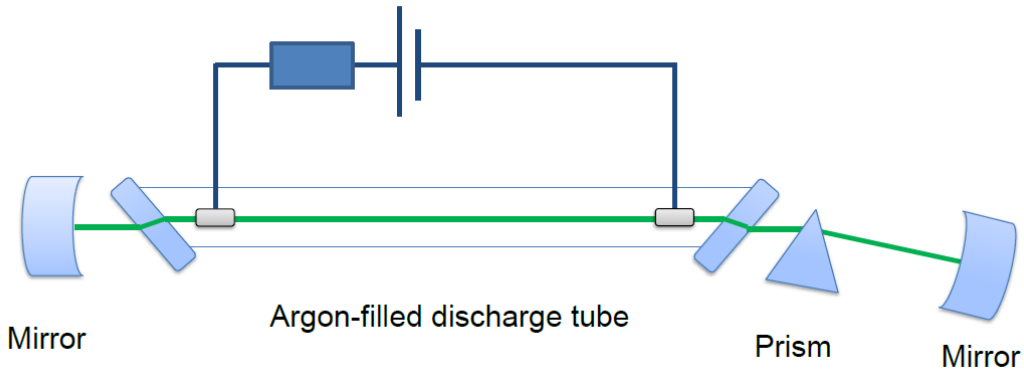

Figure 21. Schematic of a typical argon-ion laser.

This discharge tube is placed within an optical resonator. These discharge tubes often utilise Brewster-angled windows, shown here on either end of the tube, in order to reduce intracavity losses. An intracavity prism is also often included as this allows for emission wavelength selection of different argon-ion lines such as 457.9 nm, 488 nm, 351 nm or the main line 514.5 nm. In addition, it also acts to prevent multi-line operation, where several wavelengths are emitted at the same time.

On the main 514.5 nm line, up to 20 W is achievable with near diffraction-limited beam quality, making argon-ion lasers well-suited to pumping Ti:sapphire lasers. However, typical devices have a large footprint, with the discharge tube alone possessing a length of around 1 m. They also require large high voltage power supplies and chillers to remove the dissipated heat from the discharge tube, further adding to the lab space requirements.

In addition to this large footprint they are also inefficient, often requiring tens of kilowatts of electrical power to produce up to 20 W. Factor in the power required for the chillers and the total wall-plug efficiency is only around 0.1%. There are also safety issues that arise as a result of the required high voltage power supplies.

Argon-ion lasers have thus been almost completely replaced by frequency-doubled solid-state lasers and frequency-doubled optically pumped semiconductor lasers, due to the much better efficiency and lifetimes offered by these systems. These will be discussed in the following sections.

2.2.2 Diode-pumped solid-state lasers

Diode-pumped solid state lasers (DPSSLs) used to pump Ti:sapphire are based on Nd-doped gain media, such as Nd:YAG, Nd:YVO_4, and Nd:YLF. Emission is typically strongest around the 1 µm region, so a nonlinear crystal, such as $LiNbO_3$, LBO, or KTP, is used to produce light in the 523 - 532 nm region through second harmonic generation.

The cavity is often based on a ring design, with unidirectional operation enforced through use of a unidirectional device consisting of a Faraday rotator and half-wave plate as shown in Figure 22. The nonlinear doubling crystal is placed inside the cavity for intracavity frequency doubling. In order to achieve non-critical phase-matching, the crystal is often placed inside a crystal oven to raise and then maintain a stable temperature, such that the phase velocities of the interacting beams are equal and the phase mismatch is minimised. An etalon is placed in the cavity to enforce single longitudinal mode operation to eliminate the so-called “green problem” that results in large output intensity fluctuations [17].

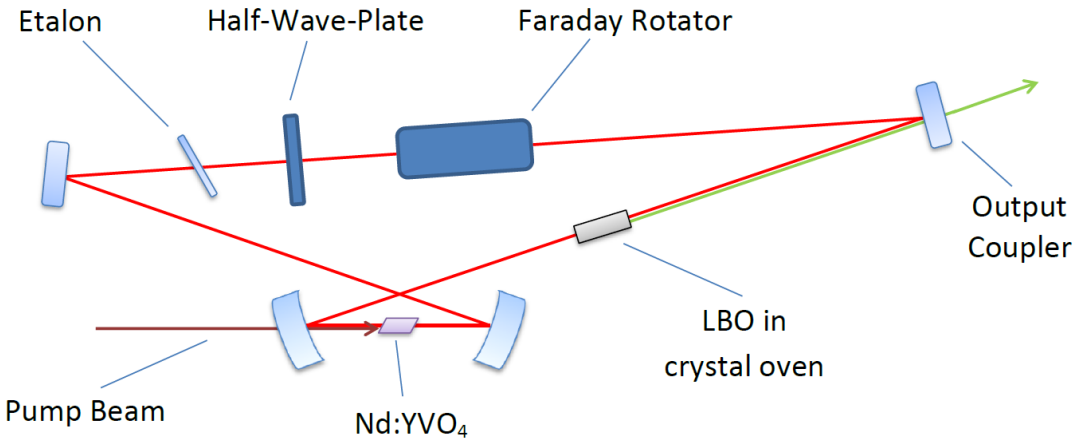

Figure 22. Schematic of the cavity from a Coherent Verdi laser, adapted from [18].

With a setup such as this it is possible to achieve tens of watts of output power with diffraction limited beam quality in the green region of the spectrum, making these lasers ideal for pumping of Ti:sapphire. The longer operational lifetimes and much higher efficiencies (1-10%), due to diode pumping at around 800 nm, means that they have largely taken over from argon-ion lasers for most applications, despite being more expensive in terms of initial capital cost.

2.2.3 Vertical external-cavity surface-emitting lasers (VECSELs)

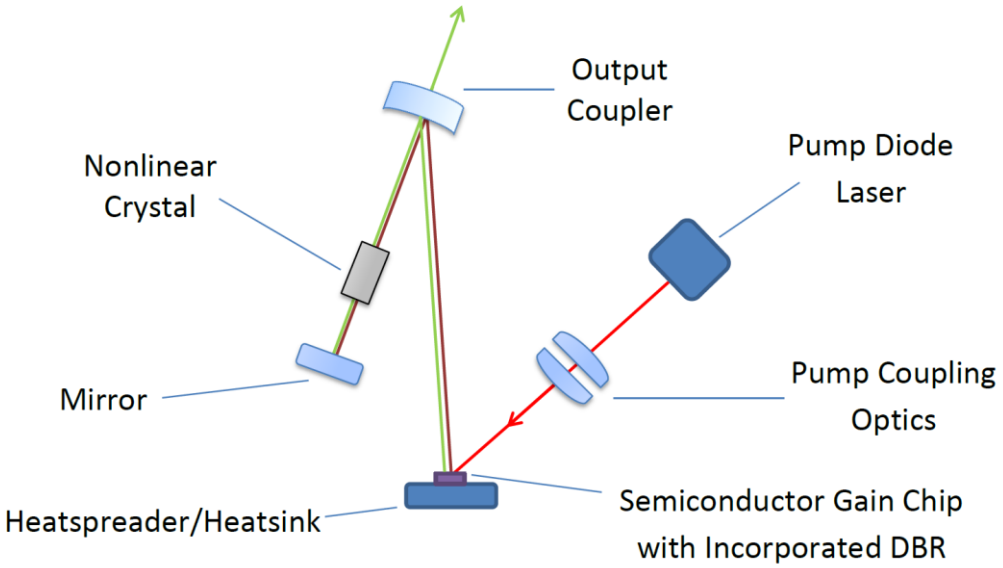

Figure 23. Schematic of a VECSEL with intracavity frequency doubling.

Vertical external-cavity surface-emitting lasers (VECSELs), also known as optically-pumped semiconductor lasers (OPSLs), are a relatively recent development that rival diode-pumped solid-state lasers in terms of performance. A schematic of a typical VECSEL is shown in Figure

23. The gain medium consists of layers of InGaAs quantum wells with GaAs or AlGaAs barriers. By varying the indium content of the quantum wells, the bandgap energy can be varied and thus the emission wavelength around the 1 µm region. The gain chip also incorporates a distributed Bragg reflector (DBR) that consists of quarter-wavelength pairs of GaAs/AlAs (or GaAs/AlGaAs), which functions as an end mirror forming the resonator. The entire gain chip with incorporated Bragg reflector is then usually mounted on a heatsink, often with a heat-spreader to improve the transfer of heat to the heatsink.

The primary advantage of VECSELs in comparison to solid-state lasers is the elimination of the so-called "green noise" problem. Arising as a result of the nonlinear dynamics of the resonator modes, this can cause strong intensity noise on the output of frequency-doubled DPSSLs [17]. This can usually only be eliminated through the use of a very long resonator (and thus increasing the number of oscillating longitudinal modes) or by enforcing single mode operation through the addition of intracavity elements. The VECSEL bypasses this problem completely as the very short upper state lifetime of the gain chip does not store gain and therefore does not experience the mode interference problem that leads to the "green noise" problem.

Similarly to DPSSLs, output powers of tens of watts are achievable with diffraction limited beam quality in the green region of the spectrum makes these lasers well suited to pumping of Ti:sapphire. They also offer similar wall-plug efficiencies (1-10%) and operational lifetimes.

2.2.4 Unconventional pump lasers for Ti:sapphire

Other less widely used pumping schemes that have demonstrated for Ti:sapphire lasers include the use of frequency-doubled DBR-tapered diode lasers and frequency-doubled Yb:fibre lasers. A brief description of each is given in the next sub-sections.

2.2.4.1 Frequency-doubled DBR-tapered diode lasers

A tapered diode is a variant of a broad stripe laser diode, which instead of having constant height and width along the whole active region, has a section where the active region width is increased along the direction of propagation (see Figure 24). The ridge waveguide section defines the high beam quality, while the tapered amplifier section provides the high output power while maintaining the beam quality of the ridge waveguide. This allows tapered diodes to produce higher beam quality and brightness than more conventional broad area laser diodes.

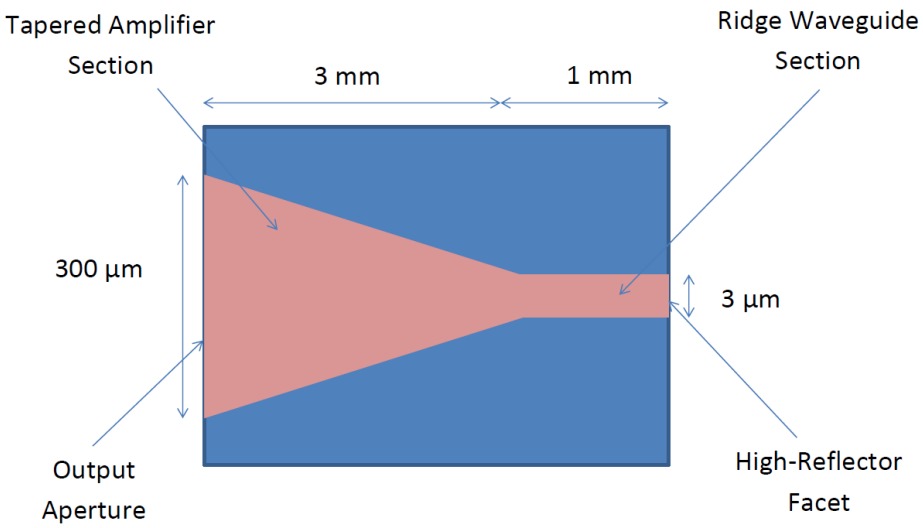

Figure 24. Schematic of a typical tapered diode laser [19].

As laser diodes emitting in the green region of the spectrum were limited to 10's of mW until recently, Müller et al. approached the problem by frequency-doubling a 1060 nm tapered diode laser (see Figure 25) [20]. The system included an optical isolator to avoid harmful feedback into the laser diode. A focusing lens is then used to focus the 1060 nm light into a plain-cut periodically poled, MgO-doped lithium niobate PPMgLN bulk crystal, where both facets are AR-coated at 531 nm and 1060 nm. The generated divergent green light is then subsequently collimated by a lens.

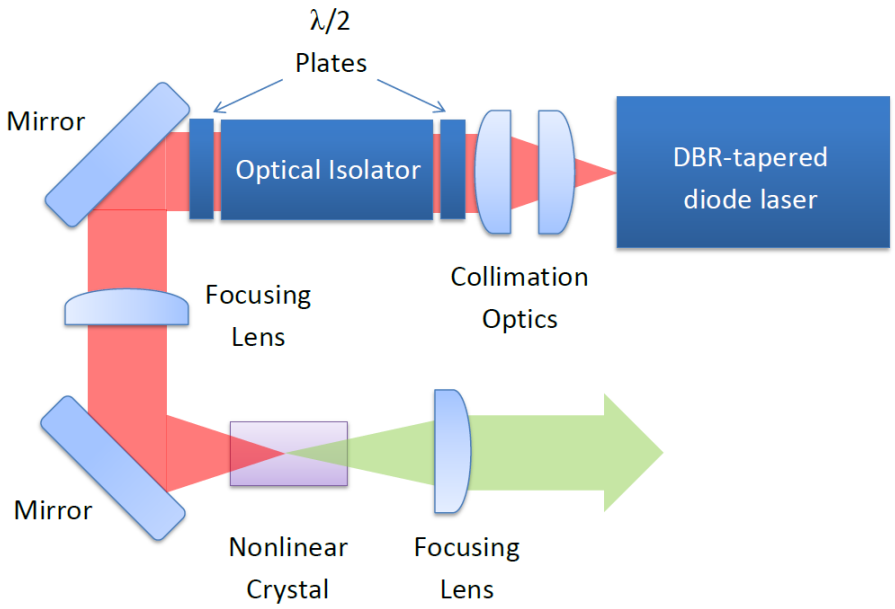

Figure 25. Schematic of frequency-doubled tapered diode setup as described in [20].

The maximum available power from the tapered diode laser was 8.8 W in the 1060 nm region. This was used to generate a maximum of 1.28 W of near diffraction-limited light around the 531 nm region. The total electro-optical efficiency of this setup was around 4%. The system was then used to pump a Ti:sapphire laser, producing pulses as short as 20 fs in duration with powers as high as 82 mW.

Further developments of the pump system involved spectrally combining two tapered laser diodes followed by sum frequency generation (SFG) to produce up to 3.9 W of diffraction-limited green light [21]. In another slightly different scheme, where cascading of nonlinear crystals was used, up to 5.5 W of diffraction limited green light has been demonstrated [22].

2.2.4.2 Frequency-doubled Yb-fibre laser

Other less commonly-used pump sources include frequency doubled Yb-fibre lasers. Fibre lasers in general are more robust and cheaper than bulk solid-state lasers. Generating very high average powers with high beam quality is routinely achievable, generally needed for Ti:sapphire lasers. However, in order to produce light in the required wavelength region for absorption in Ti:sapphire, these sources must be frequency-doubled.

Samanta et al. demonstrated a 30 W Yb-fibre with an emission wavelength of 1064 nm, which was frequency-doubled using a MgO-doped stoichiometric periodically-poled lithium tantalite (MgO:sPPLT) crystal to produce 9.6 W at 532 nm [23]. This was subsequently used to pump a Ti:sapphire laser, producing up to 2.7 W in the CW regime [24].

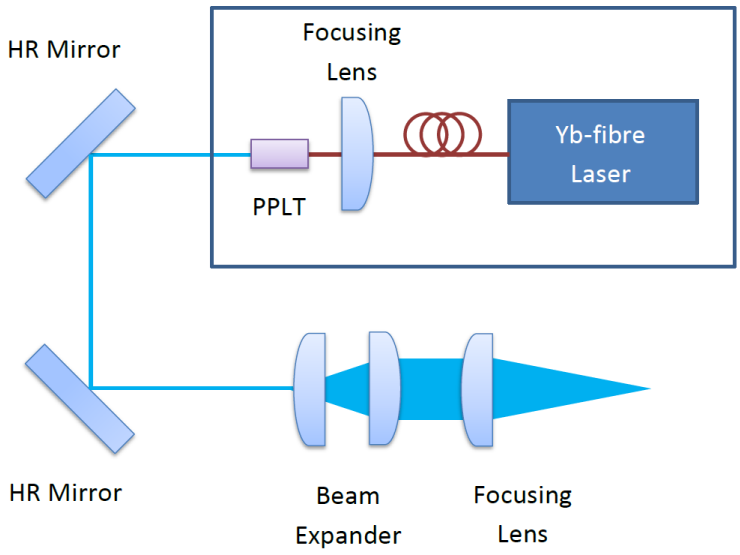

Figure 26. Frequency-doubled 488 nm Yb-fibre laser as described in [25].

In a slightly different scheme, as shown in Figure 26, an Yb-fibre laser emitting at 976 nm was frequency doubled to 488 nm using a periodically-poled lithium tantalite (PPLT) crystal and was capable of producing 2 W of 488 nm light. This was then used to pump a KLM Ti:sapphire laser, producing pulses as short as 8.2 fs and powers as high as 175 mW [25].

2.3 Diode-pumping

In this section an overview of direct diode-pumping of Ti:sapphire lasers will be given, with the aim of conveying the attractiveness of this method of pumping when in pursuit of lower-cost, lower complexity, and more compact ultrafast lasers. It should be noted however that the lower cost and complexity comes at the expense of some reduction in performance, given that current state-of-the-art laser diodes do not yet meet the performance levels of conventional frequency-doubled DPSSLs where the beam quality is superior and maximum output power is higher.

Included is some general background information regarding GaN laser diode technology, available sources at target wavelengths for Ti:sapphire pumping, a comparison of laser diode pump sources with the conventional as well as more unconventional methods of Ti:sapphire pumping described earlier, a description of the pump-induced loss associated with blue pump wavelengths, finishing with a review of existing diode-pumped Ti:sapphire lasers.

2.3.1 GaN laser diodes

GaN laser diode technology has seen rapid progress over the past 10 years or so, with commercially available high-power laser diodes emitting up to 5 W in the blue region of the spectrum now available, though it should be noted these only became available towards the end of the project [26], and up to 1.5 W in the green region of the spectrum [27]. These devices are mass-produced for markets such as the laser projector industry and the optical data storage industry (Blu-ray). Table 7 provides a summary of commercially available laser diodes emitting in the blue to green region of the spectrum. Figure 27 shows the wavelengths various diode lasers and conventional pump lasers compared to absorption spectrum of Ti:sapphire. It can be seen that the absorption is the lowest in the blue region of the spectrum. This also happens to be where the highest output power laser diodes are available as shown in Table 7.

Table 7. Commercially available GaN laser diodes with >1 W output power in the blue-green region of the spectrum.

Wavelength (nm)	Output Power (W)	Manufacturer	Model
400-405	1.2	Nichia	NDV7375
445	6	Lasertack	LDM-445-6000
448	3.5	Lasertack	LDM-448-3500
448-462	5	Nichia	NDB7Y75
440-455	3.5	Nichia	NDB7K75
465	3.5	Lasertack	LDM-465-3500
520	1	Lasertack	LDM-520-1000-A
525	1	Nichia	NDG7D75

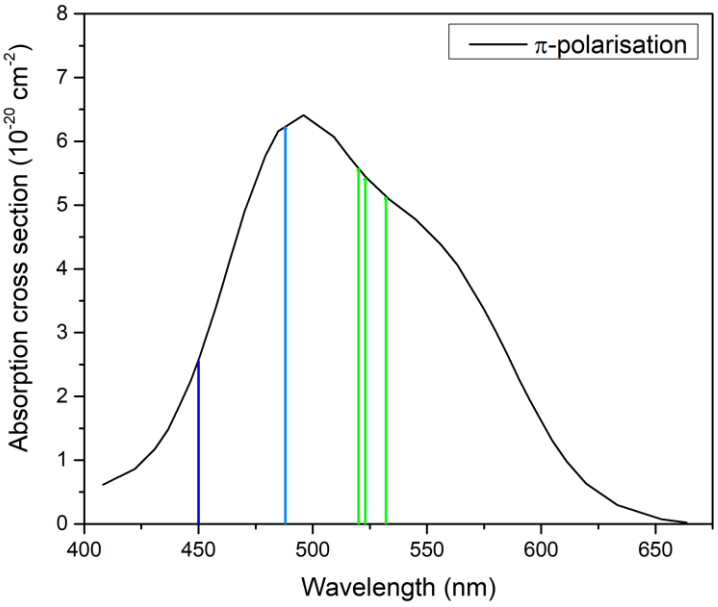

Figure 27. Absorption spectrum of Ti:sapphire (p-polarisation) compared to emission wavelengths of conventional pump sources and GaN laser diodes.

For the bulk of the project only units up to 3.5 W output power were available in the 450 nm region. However, towards the end of the project, new 5 W units became available and were used in the high repetition rate Ti:sapphire laser experiments described later in this thesis (see Chapter 4). An analysis of various pump options including conventional, unconventional, and diode laser pumps is given in Table 8.

Table 8. Traffic light table displaying various properties of possible Ti:sapphire pump lasers. Green-coloured cells represent state-of the art performance, orange-coloured cells represent mid-range performance, and red-coloured cells represent lower-end performance.

Source	M^2	Output Power	Footprint	Complexity	Efficiency	Cost
Frequency-doubled DPSSL	1	10's W	Large	High	1-5%	$10k's
Frequency-doubled OPSL	1	10's W	Large	High	1-5%	$10k's
Frequency-doubled Yb-fibre laser	1-1.5	~10 W	Medium/ Small	High/ Medium	5%	$1-10k's
Frequency-doubled tapered diode laser	1-1.5	~5W	Medium/ Small	High/ Medium	~10%	$1-10k's
Diode (450 nm)	x ~ 9 y ~ 1.6	3.5 W	Small	Low	35%	$100's
Diode (520 nm)	x ~ 6 y ~ 3	1 W	Small	Low	35%	$100's

It becomes clear from the above table why diode-pumping is an attractive option for pumping Ti:sapphire lasers. The cost is drastically less than the conventional pump options with laser diodes now costing $100's rather than $10k's. The inherent complexity is also lot lower, as the required light is generated directly. Note that all other options involve an extra stage of frequency-doubling or sum-frequency generation in order to produce the required light in the blue-green region of the spectrum. The overall efficiency is also higher, with all of the other options (excluding the frequency-doubled tapered diode laser) requiring at least an initial diode-pump stage.

While the beam quality in the x-axis is not as good as that of the conventional pump options, it can be managed by using additional pump beam re-shaping optics. The output power levels do not at this point rival that of conventional pump sources, however, significant improvements have been made in this area over the past decade especially regarding laser diodes emitting in the blue region of the spectrum. For example, the first demonstration of diode-pumped Ti:sapphire used 1 W laser diodes emitting at 452 nm or 454 nm. At the beginning of this project 3.5 W laser diodes emitting at 450 nm were available. Towards the end of the project, new laser diodes with output powers up to 5 W at 450 nm were available. It is possible in the future that diode laser technology may close the gap with conventional pump sources and provide similar output powers. Indeed a 450 nm fibre-coupled laser source based on many individual diode emitters in a bar configuration has been demonstrated with output power in excess of 1000 W [28].

Despite the disadvantages, this provides an opportunity to replace the costly, bulky, and complex conventional pump lasers with GaN diode lasers, bringing with it a simultaneous reduction in size, cost, and complexity of the Ti:sapphire laser system as a whole. This makes it an option well worth pursuing towards the goal of creating low-cost and compact ultrafast laser sources. This has already been demonstrated to be viable option and has become a hot research topic, with a number of groups around the world researching the topic [29–32].

2.3.2 Blue pump-induced loss

In addition to the lower pump absorption in the blue region of the spectrum, an additional loss mechanism at the lasing wavelength associated with pumping in the blue region of the spectrum. This was first identified by Roth et al. in the context of diode-pumped Ti:sapphire, where an additional "photo-darkening" loss is observed around the 800 nm region, associated with pumping at wavelengths below 478 nm [29,33].

A similar phenomenon was witnessed by Hoffstadt et al. in flash lamp-pumped Ti:sapphire laser experiments, where the effect was suggested to be related to charge transfer between Ti^{3+} and Ti^{4+} ions in the Ti:sapphire crystal [34]. In a separate work, Wong et al. calculated the threshold energy for this charge transfer from the ground state of Ti^{3+} to Ti^{4+} in agreement with the analysis of Hoffstadt et al. [35].

Sawada et al. later expanded upon this mechanism to explain their observed effect on laser output power when pumping under dual wavelength conditions [36]. Assuming that the charge transfer would also occur when pumped with 451 nm (2.75 eV) laser diode light, they proposed the following energy diagram (see Figure 28) to explain their results.

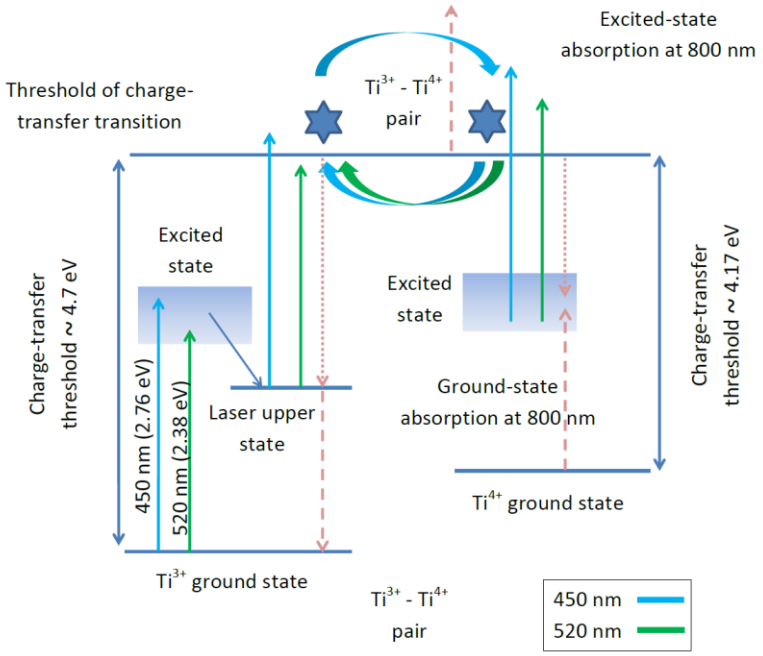

Figure 28. Schematic of energy diagram and pump-induced, charge-transfer transition model as described, figure adapted from [36].

The model proposes that 451 nm radiation is able to induce a charge transfer from the excited state of Ti^{3+} to Ti^{4+} and also able to induce a reverse charge transfer from the excited state of Ti^{4+} to Ti^{3+}. These processes will reach a steady-state balance quite quickly meaning that it is difficult to witness the effect on laser output power when pumping with 451 nm radiation alone, which may explain why some research groups did not witness this effect [37].

Conversely, it has been observed that by pumping in the green region of the spectrum it is possible to reverse this effect [29,36]. Using their model, Sawada et al. explained this by concluding that the 520 nm pump radiation used in their experiments must be able to induce a reverse charge transfer from the excited state of Ti^{4+} to Ti^{3+} but, crucially, not a charge transfer from Ti^{3+} to Ti^{4+}. This is due to the smaller photon energy compared to radiation in the blue region of the spectrum. Therefore, it is postulated that a slow reverse charge transfer rate of Ti^{4+} to Ti^{3+} induced by green radiation reduces the laser output power degradation when under dual wavelength pumping conditions (both green and blue wavelengths simultaneously).

Sawada et al. then replaced the 520 nm laser diode with a 478 nm laser diode in the dual wavelength pumping scheme, believing the 478 nm photon energy to be close to threshold but still enough to induce charge transfer from Ti^{3+} to Ti^{4+}. After terminating the 451 nm laser diode power, they witnessed a similar slow output power increase in this scheme as when

terminating the 451 nm laser diode power in the 451 nm and 520 nm laser diode scheme, confirming that the 520 nm and 478 nm radiation play a similar role in the reverse charge transfer process.

However, when pumping with a combination of 520 nm and 478 nm diodes, no slow power decrease was observed. They explain this by postulating that both the forward and reverse charge transfer reactions with 478 nm radiation occur at a similar slow rate to that of the reverse charge transfer with 520 nm radiation, therefore a steady-state balance is quickly reached between the forward and reverse charge transfer rates.

They concluded that even if a Ti:sapphire crystal demonstrates excellent lasing performance and a high figure of merit for pump wavelengths in the green region of the spectrum, the loss induced by pumping with wavelengths less than 478 nm is significant and as such must be considered when designing a Ti:sapphire laser pumped in this region. The next section will review the performance of diode-pumped Ti:sapphire lasers demonstrated by various research groups, in order to compare and contrast the effect of different design choices such as blue diode pumping or green diode pumping.

2.3.3 Review of diode-pumped Ti:sapphire lasers operating in the CW regime

Diode-pumping of Ti:sapphire lasers has seen significant progress since the first demonstration by Roth et al in 2009 [29,36]. Presented in this section is a review of diode-pumped Ti:sapphire lasers operating in the CW regime. Table 9 details the performance of diode-pumped Ti:sapphire lasers, organised in chronological order.

Table 9. Performance of various CW diode-pumped Ti:sapphire lasers.

Year	Pump Power (W)	Pump Wavelength (nm)	Average Output Power (mW)	Tuning Range (nm)	Optical Efficiency (%)	Reference
2012	2 × 1	452/454	160	700 - 875 (175)	8.0	[38]
2015	2 × 1	518/520	92	-	4.6	[39]
2015	2 × 1.5	520	650	-	21.7	[30]
2017	2 × 1 2 × 1	478 520	593	-	14.8	[36]
2017	2 × 2.9	450	470	-	8.1	[40]
2018	1 × 4.4	461	310	710 - 945 (235)	7.0	[41]
2018	1 × 0.88	520	90	-	10.2	[42]

Reviewing literature regarding the CW performance of diode-pumped Ti:sapphire lasers reveals that the highest power achieved was by Gurel et al., where 650 mW of output power was achieved for 2 × 1.5 W of pump light at 520 nm. However, the pump diodes in this configuration were driven above the recommended power levels of 1 W most likely with detrimental effects on their operational lifetime.

The second highest power achieved was by Sawada et al., where the pump arrangement consisted of a pair of 520 nm laser diodes (1 W each) and a pair of 478 nm laser diodes (1 W each). The scheme used a wavelength-multiplexed, double-end pumped configuration, where a 520 nm diode and a 478 nm diode were used at each end. In this configuration they were able to achieve an output power of 593 mW.

The highest output power in terms of pumping solely with laser diodes in the blue region of the spectrum was achieved by Rohrbacher et al., where they used 2 × 2.9 W laser diodes emitting at 450 nm to achieve an Ti:sapphire laser output of 470 mW.

2.3.4 Conclusions

It is worth noting that some of these results were published after the start of this research project (summer of 2015). At the beginning of the project, we had access to both 3.5 W blue laser diodes emitting at 450 nm, and also to 1 W green laser diodes emitting around 520-525 nm. Despite the lower absorption in the blue region of the spectrum and the additional pump-induced loss, the 450 nm laser diodes were considered to be the better option due to the higher output power offered at recommended drive current levels. Running within specified drive current limits prolongs the laser diodes operational lifetime, which would be an important aspect in an industrial setting. For these reasons, the blue laser diodes were chosen for our laser experiments.

2.4 CW Diode-pumped Ti:sapphire laser

This section describes the design, construction and experimental results obtained from our CW diode-pumped Ti:sapphire laser. It begins with characterisation of the laser diode pumps, then details the pump focusing system chosen, the Ti:sapphire laser resonator design, results from the various crystals used, and finishes with the final crystal choice and discussion of results.

2.4.1 Alfrey model

A useful tool in designing end-pumped solid-state lasers is the theoretical model developed by Alfrey [43], which allows one to calculate the expected output power, pump threshold and slope efficiency for a given gain medium, laser cavity design and pump parameters. Due to the fact that the GaN laser diodes used in this project have a far lower brightness (in the slow-axis/x-axis at least) than the diffraction-limited conventional pump sources, it is important to take this into account in the modelling.

Although other models are available [44,45], the Alfrey model incorporates diffraction of the pump and resonator modes inside the laser gain medium, which is important as these modes must be tightly-focused and well overlapped in order to achieve a low-threshold and efficiently operating laser. It is worth noting that the Alfrey model can account for differing pump beam properties in the fast and slow axes. The following equations allow us to calculate the pump power required to obtain a specified laser output power for specified laser/pump parameters.

$$P_p = \frac{(T + 2\alpha_r L + \eta) hc\pi^2}{8\sigma\tau\lambda_p \alpha_p \int_0^L \frac{exp\,[-\alpha_p z]}{\omega_{rx}\omega_{ry}\omega_{px}\omega_{py}} Q'(z) dz} \tag{26}$$

$$Q'(z) = \int_{-\infty}^{\infty}\int_{-\infty}^{\infty} \frac{exp\,[-A_x x^2 - A_y y^2]}{1 + Bexp[-D_x x^2 - D_y y^2]} dx\, dy \tag{27}$$

$$A_{x/y} = 2\frac{\omega_{rx/y}^2 + \omega_{px/y}^2}{\omega_{rx/y}^2 \omega_{px/y}^2} \tag{28}$$

$$D_{x/y} = \frac{2}{\omega_{rx/y}^2} \tag{29}$$

$$B = \frac{4sP_r}{\pi\omega_{rx}\omega_{ry}} \tag{30}$$

$$s = \frac{\sigma\tau\lambda_r}{hc} \tag{31}$$

$$\omega_{px/y}(z) = \omega_{p0x/y}\sqrt{1 + \left(\frac{M^2{}_{px/y}\lambda_p}{\pi\omega_{p0x/y}^2 n_p}\right)^2 \left(z - z_{p0x/y}\right)^2} \tag{32}$$

$$\omega_{rx/y}(z) = \omega_{r0x/y}\sqrt{1 + \left(\frac{M^2{}_{rx/y}\lambda_r}{\pi\omega_{r0x/y}^2 n_r}\right)^2 \left(z - z_{r0x/y}\right)^2} \tag{33}$$

x Index to denote horizontal plane

y Index to denote vertical plane

p Index to denote pump mode

r Index to denote resonator mode

P_p Pump power incident upon the crystal (W)

P_{th} Threshold pump power (W)

P_r Intracavity power (W)

s Saturation parameter ($m^2\ W^{-1}$)

T Transmission of output coupler

L Length of crystal (m)

η Resonator roundtrip loss excluding crystal and output coupler losses

α_p Pump absorption coefficient (m^{-1})

α_r Parasitic crystal loss coefficient (m^{-1})

σ Stimulated emission cross section (m^2)

τ Fluorescence lifetime (s)

h Planck constant (J s)

c Speed of light in vacuum ($m\ s^{-1}$)

λ Wavelength in vacuum (m)

n Index of refraction

M^2 Beam propagation factor

ω Mode radius (m)

ω_0 Mode waist radius (m)

z Position along the optical axis (m)

z_0 Mode waist location (m)

At laser threshold $P_r = 0$ and it is possible to reduce the above equations to obtain an expression for the threshold pump power:

$$P_{th} = \frac{(T + 2\alpha_r L + \eta)hc\pi}{4\sigma\tau\lambda_p\alpha_p \int_0^L \frac{\exp[-\alpha_p z]}{(\omega_{rx}{}^2 + \omega_{px}{}^2)(\omega_{ry}{}^2 + \omega_{py}{}^2)} dz} \tag{34}$$

It should be noted that the model only takes into account end-pumping with a single pump laser. As the intention was always to use a double-end pumped scheme for pumping, the model will have limited use when the second pump diode is brought into play. However, it can still be used to model initial experiments using only one laser diode and for identifying general trends, for example the effect of the M^2 value of the pump with respect to the threshold of a given laser design. We implemented this model in Mathcad, beginning with a non-astigmatic Mathcad model created by another researcher [33] and extending the model to the astigmatic case.

For this project, the typical M^2 value of the 450 nm laser diode pump (experimentally measured later in this chapter) was around 1.5 in the fast axis and 9 in the slow axis. Comparing this to a diffraction-limited pump source such as frequency-doubled DPSSL the effects on the Ti:sapphire laser threshold are modelled for the parameters set out in Table 10 and Table 11. For a more direct comparison we keep the wavelength the same in both cases (even though a diffraction-limited laser source at 450 nm with multiple-Watts of output power does not exist at the time of writing) and add an extra 1% loss to approximate the pump-induced loss (η_p) associated with pumping at 450 nm (Roth estimated this pump-induced loss to be around 1-2% in their case [33]).

Table 10. Pump parameters used in Mathcad model.

Pump Parameters		
Parameter	Diode Pump	Diffraction-Limited Pump
$M^2{}_x$	9	1
$M^2{}_y$	1.5	1
ω_{px}	50 µm	
ω_{py}	50 µm	
λ_p	450 nm	

Table 11. Laser parameters used in Mathcad model

Laser Parameters	
σ	4.1 x 10^{-19} cm^2
τ	3.2 µs
α_p	2 cm^{-1}
α_r	0.01 cm^{-1}
T	2%
η_p	1%
η_o	0.1%
η_T	$\eta_p + \eta_o$= 1.1%
L	5 mm
$M^2{}_x$	1
$M^2{}_y$	1
ω_{rx}	50 µm
ω_{ry}	50 µm

When using a diffraction-limited pump source with an M^2 of close to 1 in both axes and the other pump and laser parameters described in Table 10 and Table 11, the threshold was calculated to be 0.86 W. Using the same pump and laser parameters but this time with a pump laser source with an M^2 of 9 in the x-axis and 1.5 in the y-axis (thus approximating pump diode laser beam quality), the threshold would be 0.90 W. This represents a 4% increase in threshold. However, as stated in section 2.1.1 generally long crystal lengths are used in combination with low doping to keep parasitic losses low. Therefore, if the same calculations are repeated with a 15 mm-long crystal, a threshold of 0.89 W is obtained for the diffraction-limited pump source, while a threshold of 1.14 W is obtained for the diode pump source, representing a 28% increase in threshold moving to diode pumping.

Thus, it holds that an increase in pump source M^2, and therefore decrease in beam quality, results in an increase in laser threshold. A more general trend of the effect of decreasing pump source beam quality is shown in Figure 29, where the M^2 value of the pump beam is the same in both axes.

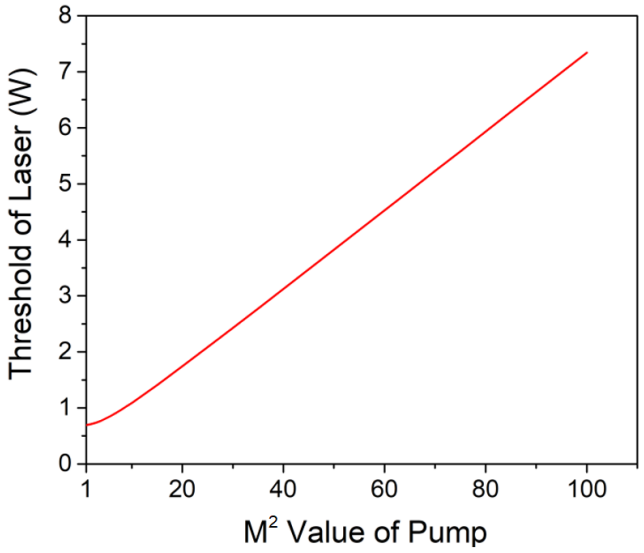

Figure 29. The effect of decreasing pump beam quality on the laser threshold calculated using the Alfrey model via Mathcad. The M^2 value is kept equal in both axes for simplicity.

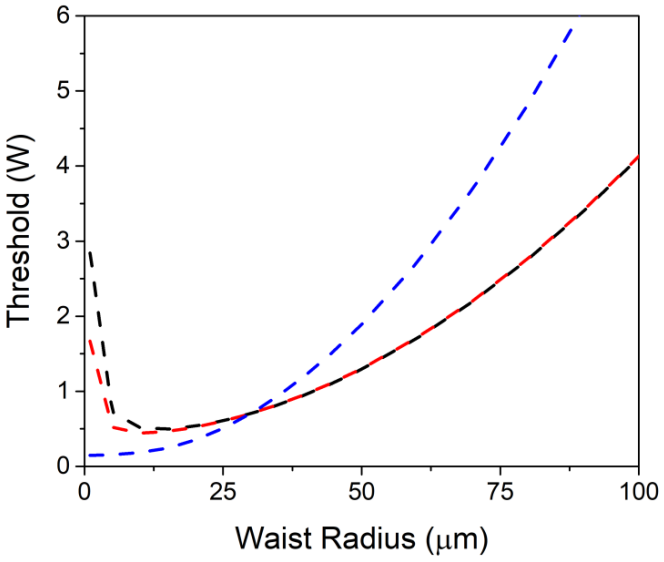

Figure 30. The effect on threshold with variation of equal sized pump and cavity modes (blue dashed line), with variation of cavity mode while pump mode fixed at 30 μm (dashed black line), and with variation of pump mode while cavity mode fixed at 30 μm (dashed red line).

The effect of both the pump mode waist size and cavity mode waist size on the threshold of a laser is shown in Figure 30. It can be seen that the laser threshold drastically increases as the spot sizes increase, and when the cavity waist and the pump waist are significantly different from each other. This means that in order to obtain a low-threshold, the pump and cavity modes must be tightly focused and similar in size to achieve a good pump mode - cavity mode overlap.

As shown in Figure 31 the Alfrey model is used to predict the required incident pump power to achieve 100 mW Ti:sapphire laser output for a variety of mode sizes. For simplicity, the cavity and pump modes are assumed equal to each other and equal in both axes.

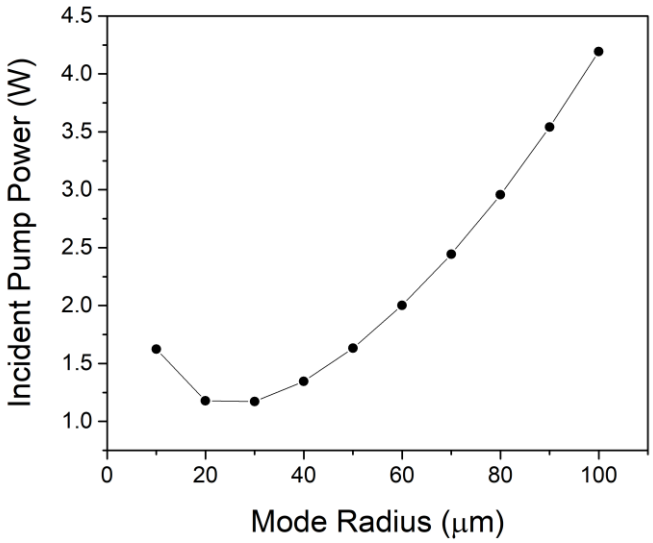

Figure 31. Incident pump power required to produce 100 mW Ti:sapphire output power at a given cavity and pump mode size. Cavity and pump mode radii are assumed to be equal for simplicities sake.

Given that up to 3.5 W output power is available from the 450 nm laser diodes, in order to achieve around 100 mW output power, a pump mode and cavity mode radius less than 90 μm would be required and ideally between 20 μm to 50 μm for maximum efficiency.

2.4.2 Laser diode pump system

In the next section we describe our laser diode pump system, from design through to characterisation. This includes characterising the drive current vs. optical output power, the spectral output, and the design of the pump beam focusing system.

We used Nichia (model NDB7K75) diode lasers which have a specified typical optical output power of 3.2 W and wavelength around 450 nm when driven at 2.3 A. The diode lasers were mounted within a Thorlabs TO can mount (TCLDM9). We used a Thorlabs ITC4020 combined power supply and thermo-electric cooler for the laser diodes. This provides both the power for our laser diodes and temperature-control capabilities.

2.4.2.1 Drive current vs. diode laser optical power

During some initial testing at a drive current of 2.3 A, it was observed that the laser diode cooling system was unable to maintain the set temperature of 22°C. After a few minutes of

operation, the temperature would gradually increase, with the heatsink attached to the laser diode mount feeling hot to the touch. It was then decided to add a small fan to aid the circulation of air around the heatsink fins. This improved the performance of the cooling system and allowed the laser diode to be operated sustainably at drive currents up to 2.5 A. Initial characterisation of the pump diode lasers was carried out in terms of power vs current shown in Figure 32.

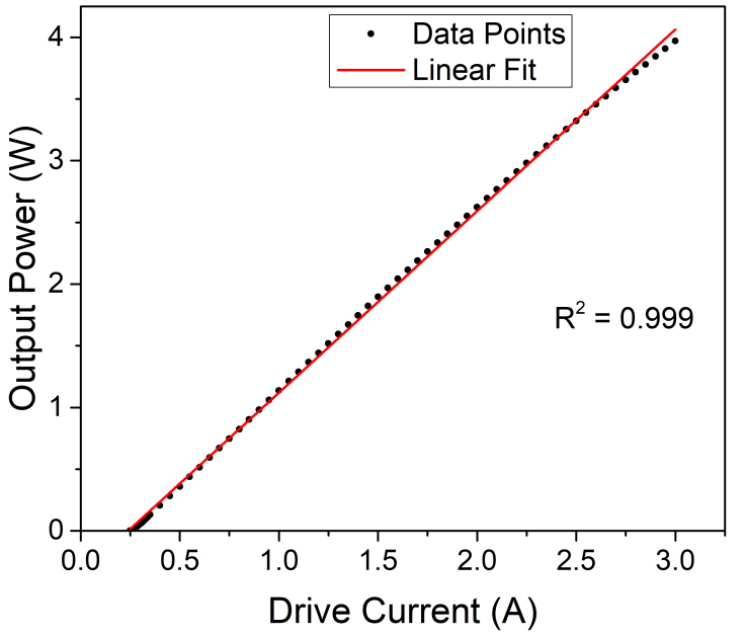

Figure 32. Measured optical output power versus drive current of Nichia NDB7K75 laser diode with AR-coated aspheric lens (f = 4.51 mm) in beam path used for collimation.

As shown in Figure 32, the 450 nm laser diode can provide an optical power output of up to 4 W when driven at the absolute maximum current of 3.0 A. However, operation at this level was unsustainable with given the mounting arrangements and cooling system, with the cooling system unable to maintain the laser diode at the set temperature. Given that these high current levels would most likely also significantly shorten the operational lifetime of the laser diode, it was decided to operate the laser diode within the recommended drive current maximum of 2.3 A for the most part, and only up to 2.5 A for short periods of time.

2.4.2.2 Spectral characterisation of laser diodes

The spectral output of the laser diode (shown in Figure 33) was measured with a Thorlabs spectrometer (model CCS200) with a spectral accuracy of < 2 nm at 633 nm. The laser diode was driven at 2.3 A , while the TEC was set to maintain the temperature at 22°C.

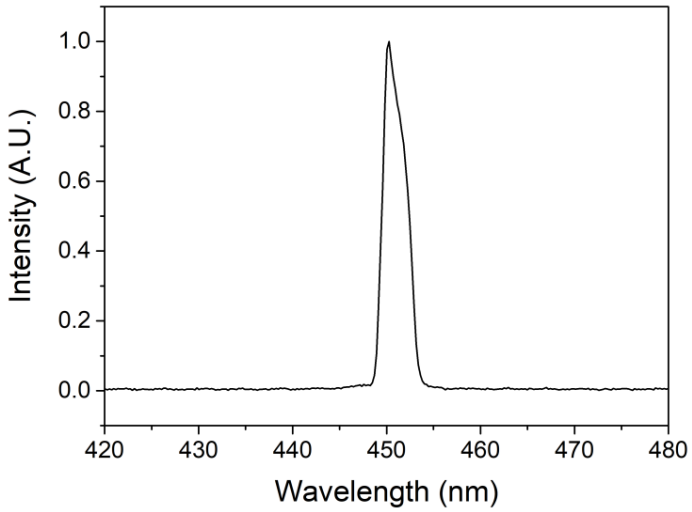

Figure 33. Spectral content of Nichia NDB7K75 laser diode when driven at 2.3 A, with the temperature set to 22°C.

2.4.2.3 Pump beam focusing system

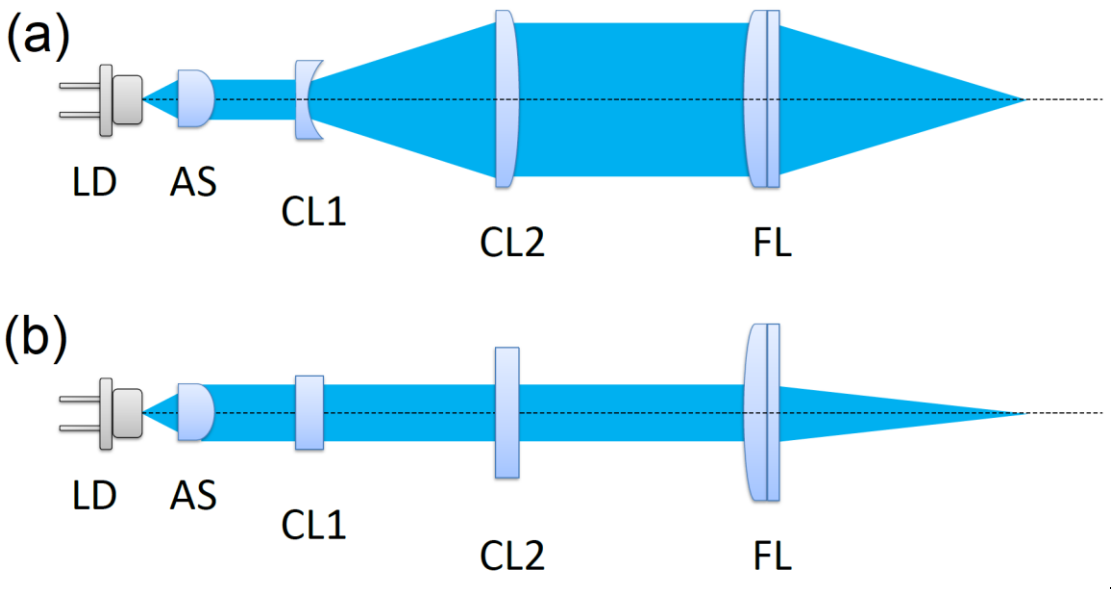

Figure 34. Pump focusing system in (a) top down view (slow axis) and (b) side on view (fast axis). LD - laser diode, AS - aspheric lens, CL1 - concave cylindrical lens, CL2 - convex cylindrical lens, FL - focusing lens.

Our pump focusing system is shown in Figure 34. The entire pump system consists of four lenses: an aspheric lens, a concave cylindrical lens, a convex cylindrical lens, and an achromatic doublet focusing lens.

In addition to the focusing lens used to focus the pump beam to a tight waist in the gain medium, it is necessary to use additional beam reshaping optics when dealing with laser diode

beams for end-pumping solid-state lasers. The first additional lens is a short focal length aspheric lens, which is used to collimate the highly divergent light exiting the laser diode. In order to circumvent the lower brightness of the laser diode in the X-axis, two cylindrical lenses are used to expand then collimate the beam in the X-direction only. This allows for a smaller minimum spot size when focused with a focusing lens than would be possible for an input beam with a smaller radius. If an initially collimated laser beam with a beam diameter of D and wavelength λ is focused by a lens with focal length f, from Gaussian beam optics it is possible to calculate that the minimum spot size ω_0 that the beam can be focused to [46]:

$$\omega_0 = \frac{4M^2\lambda f}{\pi D} \tag{35}$$

From the above equation it is apparent that the larger the input beam is, the smaller the minimum spot size can be. Therefore, when dealing with a beam of λ = 450 nm and an M^2 = 9, in order to produce a beam waist radius of around 50 µm when focused with a 100 mm focal length lens, the beam diameter D must be expanded to around 10 mm.

To aid the design of the pump focusing system and lens choice, ABCD matrix Gaussian beam propagation software LASCAD was used to model the pump beam propagation for various combinations of standard lenses available from Thorlabs. All lens used were sourced from Thorlabs and had a broadband anti-reflection coating (see Figure 35).

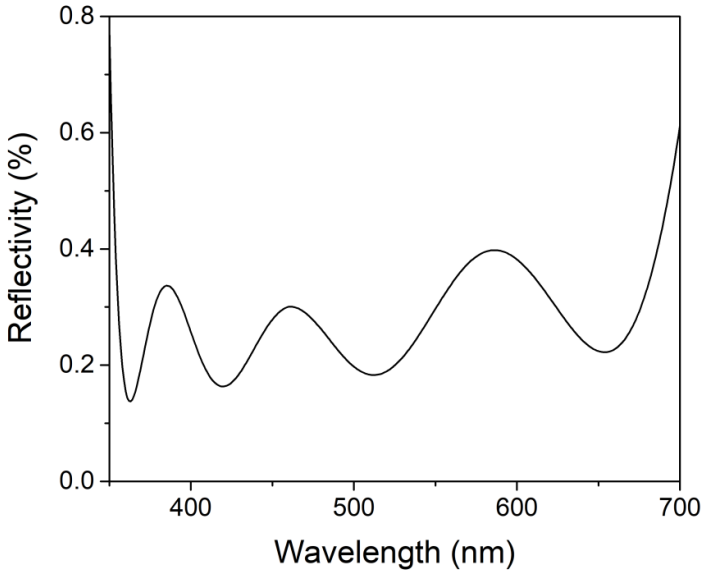

Figure 35. Reflectance versus wavelength of Thorlabs' broadband anti-reflection "A" coating, available for various substrates [47]. All pump optics used possessed this coating.

As the emitter of the diode has a size of 28 µm in the x-axis by 1 µm in the y-axis, this defines the initial dimensions of the beam. Assuming a wavelength of 451 nm and M^2 values of 9 in the x-axis and 1.5 in the y-axis, this defines our initial conditions for the diode beam. As previous calculations in section 2.4.1 have shown, a resonator and pump mode radius of around 50 µm is required to achieve efficient operation. A LASCAD model was created using only an aspheric lens with f = 4.51 mm to collimate the highly divergent beam emerging from the diode, and a subsequent focusing lens with f = 100 mm. This would result in a beam waist radius of 106 µm in the x-axis by 20 µm in the y axis according to the LASCAD model. In order to optimise the beam waist radius in the x-axis, additional reshaping optics are required to first expand and subsequently collimate the beam in the x-axis as the larger input beam size will be able to be focused to a smaller beam waist using the focusing lens. When the LASCAD model described above is updated with the additional reshaping optics, the resultant beam waist is 57 µm in the x-axis by 19 µm in the y axis. This is modelled for the different focal length lenses available with the results shown in Table 12. Critical distances are the distance between the laser diode and aspheric lens, and between CL1 and CL2.

After calculating the expected beam waist for various pump focusing systems using lenses with differing focal length values, in Table 12 are the final lens values used for all experiments. For these calculations, the wavelength was assumed to be 450 nm, the initial far-field beam divergence to be 46° in the fast axis and 14° in the slow axis, and the fast and slow axes to have an M^2 of 1.5 and 9 respectively.

Table 12. Calculated beam waists obtained for different focusing lenses from LASCAD model of pump focusing system.

Focusing Lens Focal Length	AS (mm)	CL1 (mm)	CL2 (mm)	FL (mm)	ω_{0x} (µm)	ω_{0y} (µm)
60 mm	4.51	-9.7	80	60	20	11
75 mm	4.51	-9.7	80	75	47	16
100 mm	4.51	-9.7	80	100	57	19

2.4.3 Beam waist and M^2 Measurement

In order to confirm the LASCAD-calculated values for the beam waist, direct measurements of the beam were taken using a CCD camera (Thorlabs BC106N-VIS/M). M^2 measurements were also taken to ascertain the laser diode beam quality. The M^2 measurements were carried out in accordance with ISO 11146 - 1. This involves experimentally obtaining the beam diameter at certain positions around the focus and applying hyperbolic fitting function to the measured

data. Parameters such as the M^2 value, beam divergence Θ and Rayleigh range z_R can then be extracted from the fitting function. The hyperbolic fit is given by [48]:

$$d(z) = \sqrt{a + bz + cz^2} \tag{36}$$

where $d(z)$ is the beam width (or diameter), and z is the position along the propagation direction. The coefficients a, b, and c are used to calculate various beam parameters.

$$z_0 = -\frac{b}{2c} \qquad z_R = \frac{1}{2c}\sqrt{4ac - b^2} \qquad d_0 = \frac{1}{2\sqrt{c}}\sqrt{4ac - b^2}$$
$$\Theta = \sqrt{c} \qquad M^2 = \frac{\pi}{8\lambda}\sqrt{4ac - b^2} \tag{37}$$

where z_0 is the location of the beam waist along the propagation axis, z_R is the Rayleigh range, d_0 is the beam waist diameter, Θ is the beam divergence angle, and M^2 is the beam quality factor. For astigmatic beam, as in our case, the measurements, curve fitting and subsequent parameter extraction are carried out for both axes.

Using the beam profiler and monitoring the beam waist values in each axis, the focal points in each axis can be made to coincide by varying the z-position of CL2 to find the correct distance between CL1 and CL2. After this was achieved, the measurements detailed by ISO 11146 - 1 were carried out for each blue laser diode. The results are shown in Figure 36 and Figure 37.

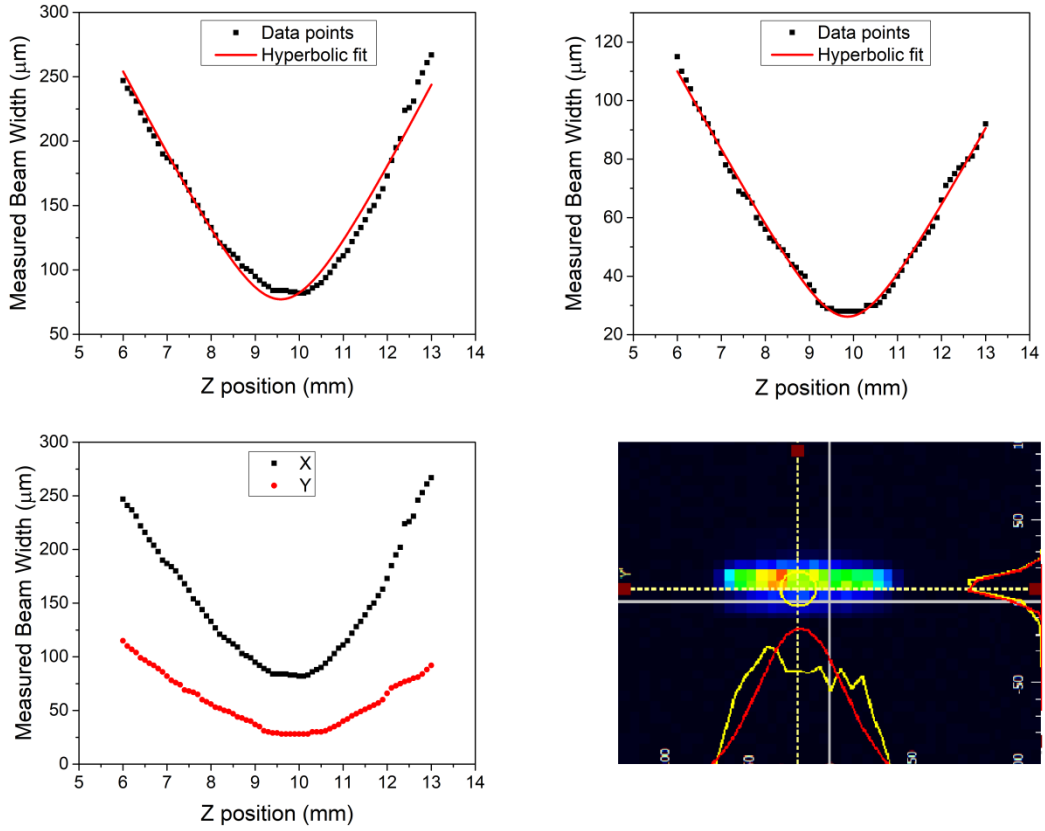

Figure 36. Blue diode 1 with f = 100 mm focusing lens, M2 measurement with hyperbolic fit according to by ISO 11146 - 1 for (a) X-axis of blue diode and (b) Y-axis of blue diode. (c) Beam waists in X and Y axes coincide. (d) beam profile image of beam waist taken with CCD camera. The "widths" in (a), (b) and (c) refer to beam diameter.

The extracted parameters for the laser diode with 100 mm focusing lens are given in Table 13. As we use two laser diodes for double-end pumping later in this chapter, this particular laser diode is named Blue Diode 1 in order to distinguish them from each other.

The extracted parameters for the laser diode with 100 mm focusing lens are given in Table 13. As we use two laser diodes for double-end pumping later in this chapter, this particular laser diode is named Blue Diode 1 in order to distinguish them from each other.

Table 13. Extracted parameters for Blue Diode 1 with 100 mm focusing lens.

Axis	$z_R\ (mm)$	$\omega_0(\mu m)$	$\Theta(°)$	M^2
X	1.15 ± 0.10	39 ± 7	3.9 ± 0.1	9.2 ± 0.8
Y	0.91 ± 0.20	13 ± 1	1.6 ± 0.1	1.2 ± 0.1

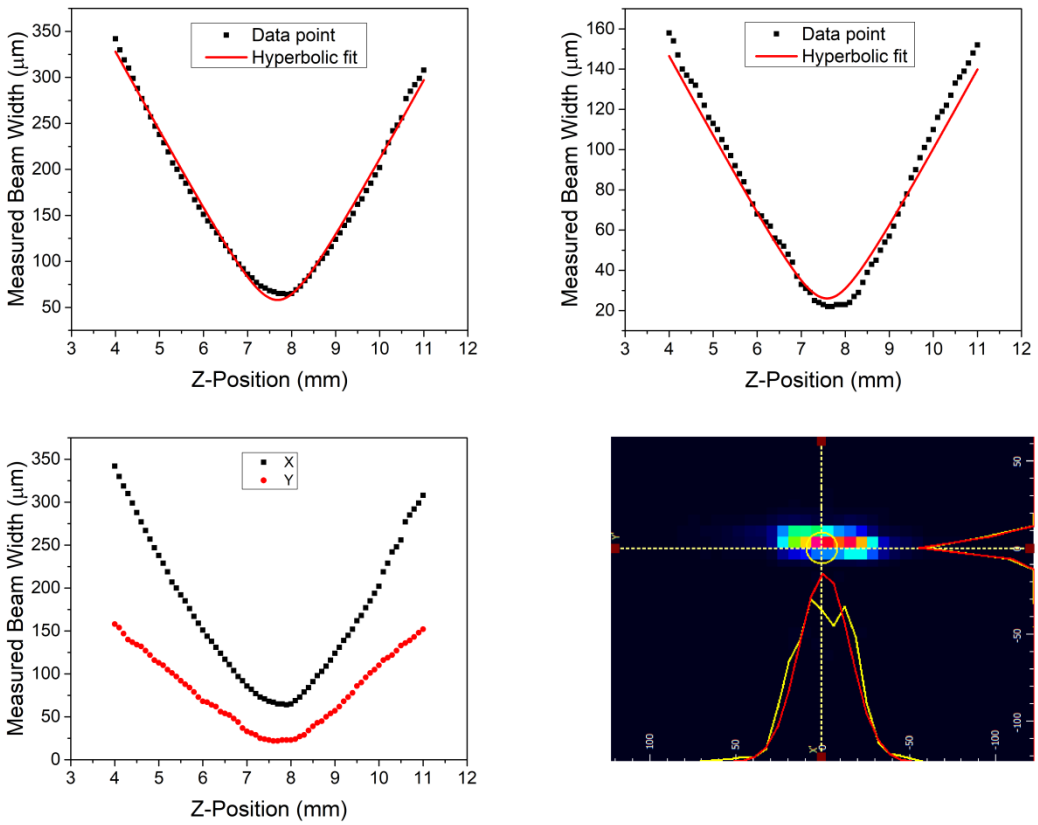

Figure 37. Blue diode 2 with f = 75 mm focusing lens, M2 measurement with hyperbolic fit according to by ISO 11146 - 1 for (a) X-axis of blue diode and (b) Y-axis of blue diode. (c) Beam waists in X and Y axes coincide. (d) beam profile image of beam waist taken with CCD camera.

The extracted parameters for Blue Diode 2 with 75 mm focusing lens are given in Table 14. A different focal length focusing lens is used for each of the laser diode pump configurations so that tight focusing of any residual pump light not absorbed by the crystal onto the other laser diode facet is avoided, as this can cause damage to the laser diode.

Table 14. Extracted parameters for Blue Diode 2 with 75 mm focusing lens.

Axis	$z_R\ (mm)$	$\omega_0(\mu m)$	Θ(°)	M^2
X	0.67 ± 0.02	30 ± 2	5.0 ± 0.1	9.0 ± 0.3
Y	0.49 ± 0.01	11 ± 1	2.5 ± 0.1	1.6 ± 0.1

In both cases the measured beam waist is smaller than the beam waist predicted by the LASCAD model. This is likely due to the imperfect nature of the Gaussian fit in the beam profiler software underestimating the beam size, as can be seen in Figure 36 and Figure 37. It should also be noted that due to an oversight at the time, the ISO 11146 requirement of >20 pixels across the beam width was not taken into account. Therefore, the error values, taken

directly from the curve-fitting software, are likely over-optimistic, especially so for the beam waist.

From the values presented in Table 13 and Table 14 it is apparent that the beam quality in the x-axis is not as good as a typical conventional pump source with a near diffraction-limited beam quality of $M^2 \approx 1$ in both axes. As calculated in section 2.4.1 this means that in moving to diode pumping we can expect an increase in threshold and drop in optical to optical efficiency compared to a hypothetical pump source with the same parameters but diffraction limited beam quality.

2.4.4 Ti:sapphire laser resonator design

In the following section the design of CW regime diode-pumped Ti:sapphire laser resonator is described. To aid in this goal the software package LASCAD (Laser Cavity Analysis and Design) was used extensively, mainly for its ABCD beam propagation analysis tools.

As the ultimate goal is to build an ultrafast diode-pumped Ti:sapphire laser, a X-fold resonator arrangement, commonly used for bulk solid-state ultrafast oscillators [49], was used. This allows for the addition of prisms and additional chirped mirrors at a later stage while also incorporating folding angles to compensate for the astigmatism introduced by the Brewster-angled crystal. A Brewster-angled crystal was chosen as p-polarised light incident upon the crystal experiences almost no reflection loss, thus keeping cavity losses low. A disadvantage is that astigmatism is introduced, and as such the folding mirrors must be set at a certain angle to compensate for this.

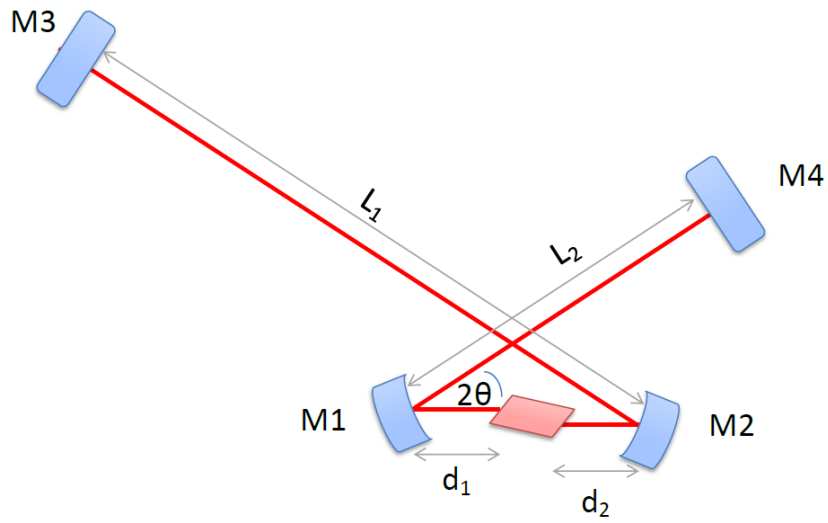

Figure 38. CW cavity designed in LASCAD.

Using LASCAD the design shown in Figure 38 was created. The design goals of this resonator were to create a resonator mode waist closely matched in size to the pump beam waists, set folding angles such that the astigmatism introduced by the Brewster crystal is well compensated for, and to operate roughly in the middle of stability region I in order that the cavity wasn't too sensitive to small misalignments and that the cavity mode was collimated in each arm.

This results in a resonator beam waist of ω_{c0} = 29 µm × 16 µm inside the Ti:sapphire crystal. The pump beam waist inside the Brewster crystal will be larger by a factor of $n_{sapphire}$ = 1.76 in the x-axis than that measured in 2.4.3, therefore the pump beam waist inside the crystal will be ω_{p0} = 69 µm × 13 µm for BD1 and ω_{p0} = 53 µm × 11 µm for BD2. Thus, the pump and resonator modes are well matched in the y-axis and slightly less well matched in the x-axis.

Folding ½-angles of 8° were introduced for compensation of the astigmatism of the Brewster-cut crystal, making sure the position of cavity stability is not significantly different in the X and Y axes. The folding mirror separation was adjusted such that the cavity would operate near the centre of the first stability zone.

Mirrors M1, M2 and M4 all possessed a highly-reflective coating (99.95%) over a wavelength range of 700-900 nm. In addition, mirrors M1 and M2 were highly transmissive (>95%) over the wavelength range 450-532 nm. Mirrors M1 and M2 also had a -75 mm ROC and were based on a zero-lens design helping to ameliorate the pump beam waist expanding effect experienced when the pump beam is transmitted through normal substrate mirrors. θ = 9°, L_1 = 655 mm, L_2 = 270 mm, d_1 = 36.5 mm and d_1 = 37.7 mm. M3 is the output coupler. A number of output couplers with various percentage transmittance were available; 1%, 2%, 3% and 5%.

2.4.5 Crystal absorption measurements

For our laser experiments we had four Ti:sapphire crystals available from different suppliers to characterise, all Brewster-cut with lengths ranging from 3.5 to 5.2 mm. Manufacturer-supplied FOM ranged from 120 to 400, comparing absorption at 514 nm to 800 nm. All crystals were grown by Czochralski method except crystal A, which was grown by the Heat Exchange Method (HEM).

In order to fully characterise the various crystals available, crystal absorption measurements at 450 nm were carried out. Both the percentage absorption at 450 nm and the $\alpha_{450\ nm}$ absorption coefficient at 450 nm were calculated. These parameters are used later for calculating the slope efficiency of the diode-pumped Ti:sapphire laser. The pump power

transmitted through all pump optics and one folding mirror was measured, giving the power incident upon the crystal. The crystal was then placed in the pump beam path and aligned at Brewster's angle. The power transmitted through the crystal was then measured. In order to calculate the absorption coefficient at 450 nm, Beer's Law was used:

$$P(z) = P_0 \, exp(-\alpha z) \tag{38}$$

where z is the length of optical material, $P(z)$ is the transmitted power, P_0 is the incident power, and α is absorption coefficient. Rearranging allows us to calculate the absorption coefficient at 450 nm ($\alpha_{450\ nm}$) for each crystal, the results of which are shown in Table 15.

Table 15. Absorption measurements and absorption coefficient calculations of available crystals.

Crystal	Supplier	Growth Method	z (mm)	Supplier FOM	% abs at 450 nm	$\alpha_{450\ nm}$ (cm^{-1})
A	Crystal Systems	HEM	4.8	>200	64%	2.13
B	Saint Gobain	Czochralski	3.5	-	42%	1.56
C	Saint Gobain	Czochralski	5.2	>400	80%	3.10
D	Altechna	Czochralski	5	>120	46%	1.23

2.4.6 CW regime characterisation of single end pump configuration

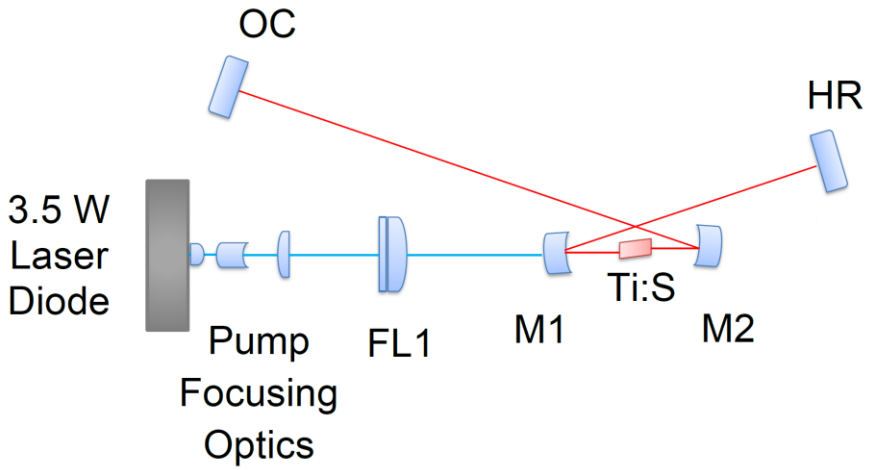

Figure 39. Single end-pumped CW Ti:sapphire laser configuration. OC – output coupler, HR – high reflecting mirror, FL1 – focusing lens, M1 and M2 – curved mirror 1 and 2, Ti:S – Ti:sapphire crystal.

Initial experiments were carried out with one 450 nm laser diode pump in a single end-pumped configuration. Specifically, this was the laser diode referred to as Blue Diode 1. After

focusing with a 100 mm focal length lens through mirror M2 the beam waist was measured to be 39 µm × 13 µm with the focus intended to be located around 1 mm from the front crystal facet. These parameters, including calculated absorption values at 450 nm etc., were then entered into the Alfrey model described in section 2.4.1

With the cavity set up and aligned as described in section 2.4.4 lasing was achieved using a photodiode to maximise the fluorescence signal. The output power as a function of incident pump power upon the crystal (Crystal A) is shown in Figure 40:

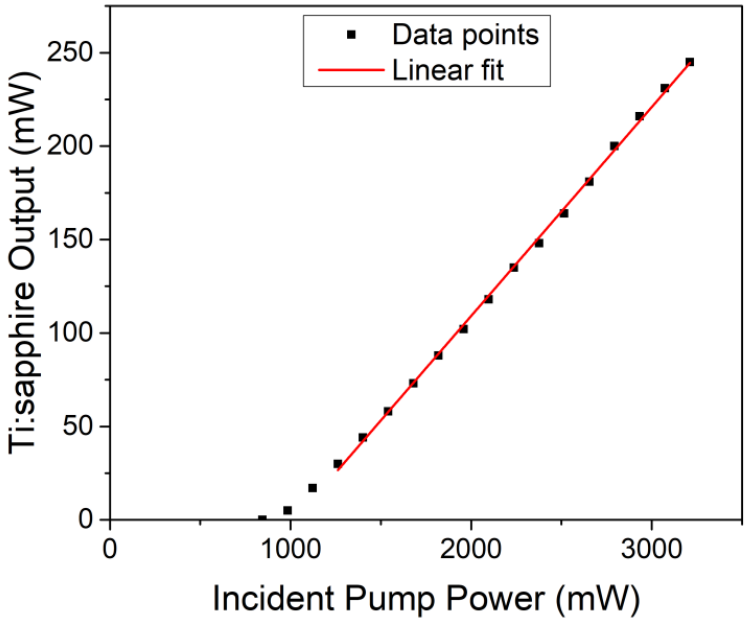

Figure 40. Single laser diode-pumped Ti:sapphire laser power output with 2% output coupler.

We achieved up to 245 mW output power with a single pump laser diode, the slope efficiency was 11.1 %, and the laser reached threshold for around 1 W of incident pump power. These results agreed well with the threshold of 0.9 W and slope efficiency of 10% predicted by our Alfrey model, and as such provided a good basis for further experiments using double-end pumping.

2.4.7 CW regime characterisation of double end-pumped configuration

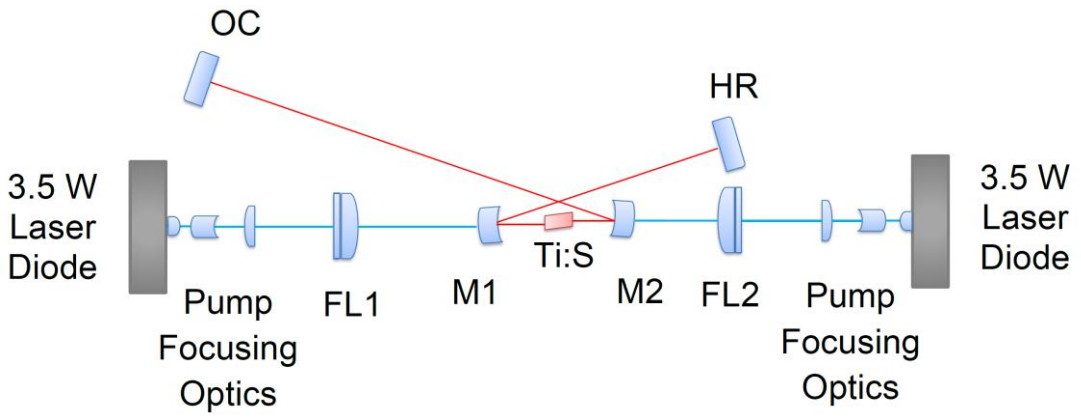

Figure 41. Double end-pumped CW Ti:sapphire laser configuration. OC – output coupler, HR – high reflecting mirror, FL1 and FL2 – focusing lens 1 and 2, M1 and M2 – curved mirror 1 and 2, Ti:S – Ti:sapphire crystal.

The cavity was set up and aligned as per the LASCAD model. Lasing was realised with the use of only one pump diode initially. The second pump diode and its associated pump optics were mounted on a mini-removeable breadboard. This was then dropped into the setup and aligned for pumping the crystal via the other direction as shown in Figure 41. The pump beam waist is focused to around 1 mm from the surface of the crystal facet closest to the second pump diode in order to create a more uniform pump distribution. Once this had been optimised for maximum output power, the performance was recorded. The pump power was varied by changing the drive current in 100 mA increments, which was done simultaneously for each diode. The remaining output couplers were then each in turn installed, aligned and then the performance optimised and recorded for each. The results for each crystal are shown in Figure 42.

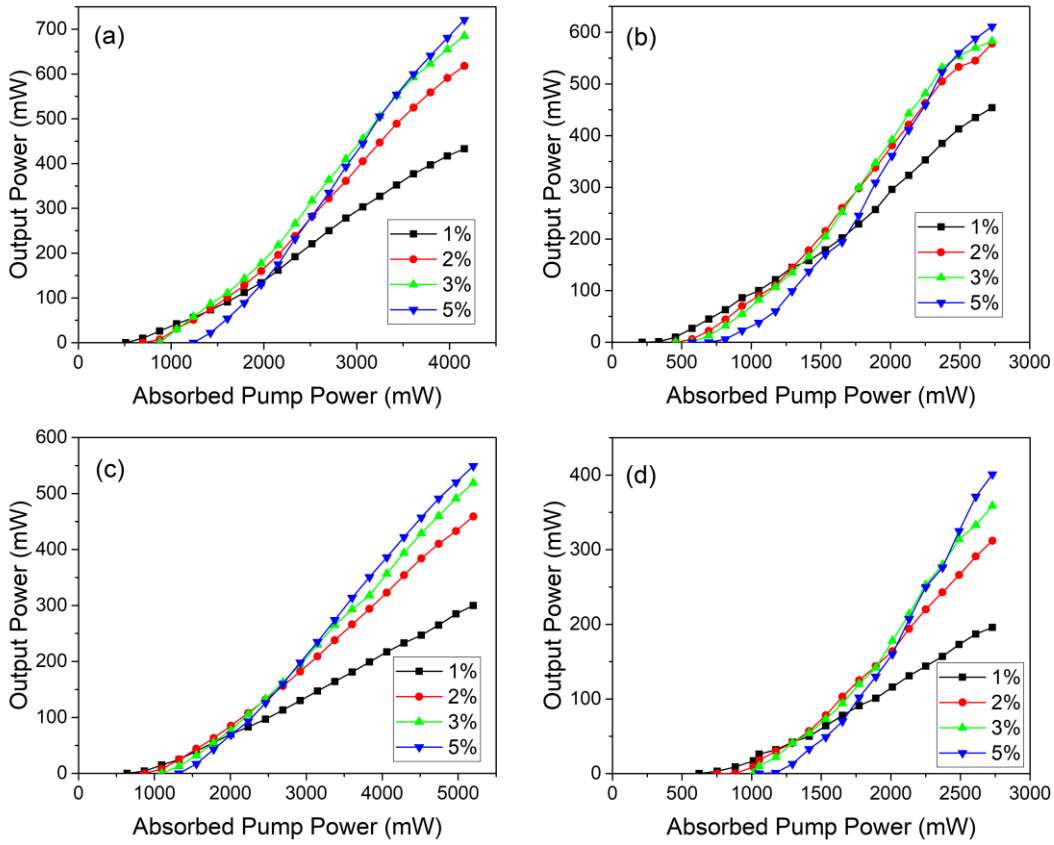

Figure 42. Ti:sapphire output power vs pump power with different OCs, recorded for each of the available crystals. (a) Crystal A, (b) Crystal B, (c) Crystal C, and (d) Crystal D.

In terms of output power, we can see that setup with Crystal A has the highest output power with >700 mW when using a 5% output coupler. The poorest performing crystal in terms of output power was crystal D, which given its relatively low absorption at 450 nm compared to the other crystals is to be expected. Crystal C has the highest absorption at 450 nm by some way but only produces the 3rd highest output power compared to the other crystals. Although FOM > 400 is claimed by the supplier for this crystal, this is measured for a pump wavelength of 514 nm. The high absorption combined with the relatively low output power would indicate that the FOM at 450 nm is lower. This is most likely due to this crystal being particularly affected by the pump-induced loss associated with pumping in the blue region, resulting in a higher residual absorption around 800 nm and thus a larger parasitic loss. The setup with Crystal B (with the lowest % absorption at 450 nm) has the second highest output power. Therefore, this crystal seems to have low residual 800 nm absorption and thus is not as badly affected by the blue pump-induced loss.

A Caird analysis [50] was then performed to obtain the total cavity losses minus output coupling. This is carried out by plotting the inverse of the output coupling (T^{-1}) against the

inverse of the slope efficiency (η_S) and applying a linear fit to the data points. The inverse slope efficiency is related to the inverse output coupling via the following relation:

$$\eta_S{}^{-1} = \frac{LT^{-1}}{\eta_0} + \frac{1}{\eta_0} \tag{39}$$

where

$$\eta_0 = \eta_{pe} \cdot \frac{\lambda_p}{\lambda_0} \cdot \frac{\sigma_E - \sigma_{EA}}{\sigma_E} \tag{40}$$

where L is the total cavity loss minus the output coupling, η_{pe} is a factor associated with non-unity pumping efficiency, λ_p is the pump wavelength, λ_0 is the laser wavelength, σ_E is the stimulated emission cross section and σ_{EA} is the excited state absorption cross section. By extracting gradient and intercept values from the straight line fit it is possible to determine L. This process was in turn repeated for the several crystals available (see Figure 43).

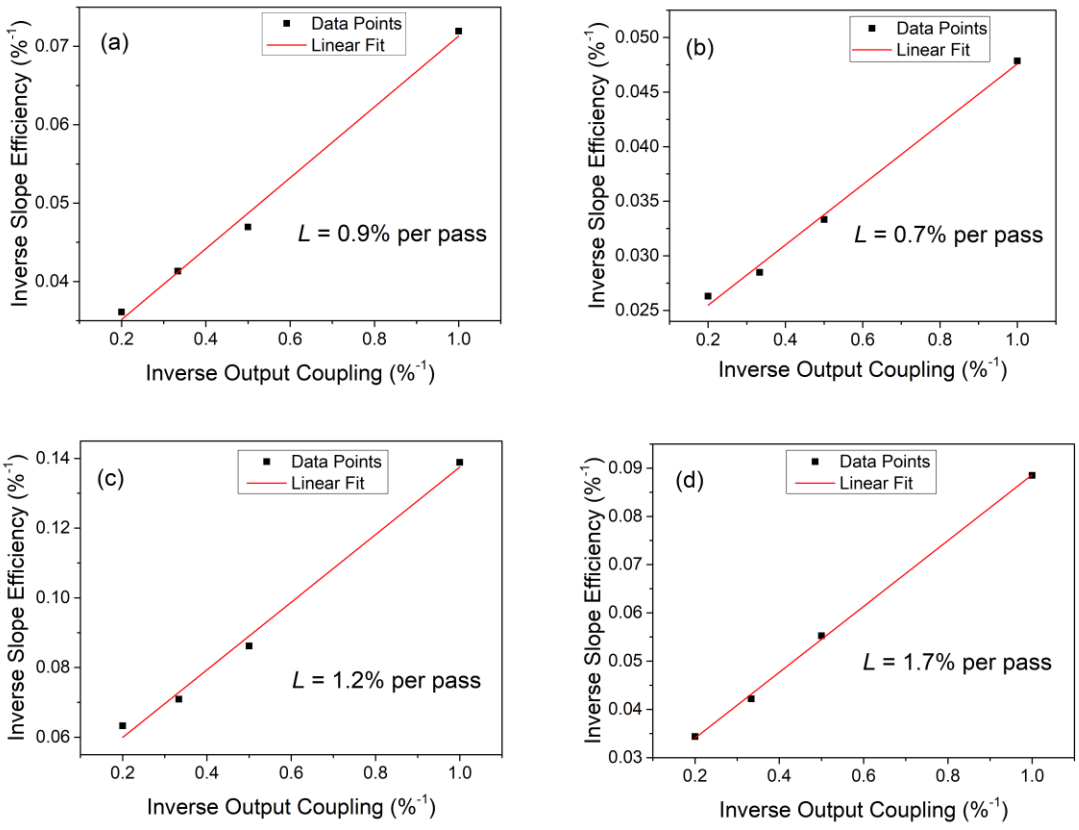

Figure 43. Caird analysis for each of the available crystals. (a) Crystal System 4.8 mm long crystal, (b) Saint Gobain 3.5 mm long crystal, (c) Saint Gobain 5.2 mm long crystal, and (d) Altechna 5 mm long crystal .

From the Caird analysis, we can expand Table 15 and create a table that contains a comprehensive set of results for each of the crystals, shown in Table 16. The slope efficiency

η_s is defined as the absorbed pump power to output power, and the optical-to-optical efficiency η_{opt} is defined as the incident pump power to output power.

Table 16. Data obtained from Ti:sapphire crystals.

Crystal	Company	Z (mm)	FOM	% abs at 450 nm	$\alpha_{450\ nm}$ (cm^{-1})	Single pass loss (%)	η_s at 5% OC (%)	η_{opt} at 5% OC (%)	Max power out at 5% OC (mW)
A	Crystal Systems	4.8	>200	64	2.13	0.9	27.7	11.1	721
B	Saint Gobain	3.5	-	42	1.56	0.7	20.0	9.4	611
C	Saint Gobain	5.2	>400	80	3.10	1.2	15.8	8.4	549
D	Altechna	5	>120	46	1.23	1.7	29.1	6.2	402

Analysing the data presented in Figure 43 and Table 16, we see that the best performing crystal (Crystal A) has the second lowest single-pass loss. The worst performing crystal has the highest single-pass loss of 1.7%, which combined with its relatively low absorption at 450 nm ties in with the low output power. Crystal C, ranked 3rd in terms of output power, also has a comparatively high single-pass loss of 1.2%, which explains the lower output power despite having the highest absorption.

2.4.8 Crystal choice and discussion of results

In Table 16 the maximum output power was measured with a 5% output coupler and under a combined incident pump power of 6.5 W. This combined pump power is the power measured incident upon the crystal at 2.5 A drive current for each diode. If the diodes were driven harder than this, thus producing a higher incident pump power, the crystal TEC was unable to maintain a crystal temperature of 25°C and the crystal would gradually heat up.

In terms of output power Crystal A is the clear winner, with an output power of 721 mW this is 110 mW greater than the crystal with the second highest output power under the described conditions above. For this reason, it was decided to proceed with this crystal for mode-locking experiments.

This output power was higher than that generated from any other CW diode-pumped Ti:sapphire at the time and to the best of our knowledge, with the closest being that achieved with Gurel et al with 650 mW [30]. We believe the reason for this is mainly due to the higher available pump power when using blue diodes compared to green diodes, despite the lower

overall efficiency. It is worth pointing out that Gurel et al. generated this higher power by driving their green diodes at higher than recommended current levels (2.5 A versus an absolute maximum of 2.0 A most likely having detrimental effects to their operational lifetime. Our diodes were also driven at slightly higher than recommended levels (at 2.5 A versus a recommended current of 2.3 A), though still short of the absolute maximum of 3.0 A. Therefore, as well as producing a higher output power our laser most likely offers a more reliable architecture and longer operational lifetime. It should be noted that higher powers have now been achieved with CW diode-pumped Ti:sapphire lasers by Miao et al., with 1.36 W output power achieved using a fibre-coupled green diode module containing forty 1 W emitters [51].

We can see that despite absorbing the largest percentage of the 450 nm pump light at 80%, the crystal C only outputs up to 549 mW. The fact that the FOM is greater than 400 when considering the absorption at 532 nm to absorption at the laser wavelength suggests that this crystal may suffer more from the blue pump-induced loss than crystals A or B. This would then seem to suggest that the rule of thumb that higher FOM equals lower parasitic loss at the lasing wavelength cannot be relied upon when pumping at blue wavelengths, even if it still applies when pumping with green wavelengths.

2.5 Summary and Conclusions

To summarise this chapter, we have discussed the background theory on Ti:sapphire properties, the advantages and disadvantages of diode-pumping Ti:sapphire compared to conventional Ti:sapphire pumping, and the design and experimental results of our own CW diode-pumped Ti:sapphire laser.

Various available Ti:sapphire crystals were characterised in our experimental setup and the performance recorded for each. These experiments revealed that Crystal A, a 4.8 mm long Brewster-cut crystal with $\alpha_{450\,nm}$ = 2.13 cm^{-1} and FOM > 200 procured from GT Crystal Systems, to be the best performing crystal in terms of maximum output power, therefore this crystal was chosen for the mode-locking experiments described in Chapter 3.

We can also see that when pumping at 450 nm, the supplier stated FOM cannot be relied upon as the pump-induced loss associated with pumping Ti:sapphire in the blue region of the spectrum can result in significant parasitic losses at the laser wavelength.

2.6 References

1. P. F. Moulton, "Spectroscopic and laser characteristics of Ti:Al2O3," J. Opt. Soc. Am. B **3**(1), 125 (1986).
2. P. Albers, E. Stark, and G. Huber, "Continuous-wave laser operation and quantum efficiency of titanium-doped sapphire," J. Opt. Soc. Am. B **3**(1), 134 (1986).
3. W. Koechner, *Solid-State Laser Engineering - 6th Edition* (2014).
4. C. Xu, W. Zipfel, J. B. Shear, R. M. Williams, and W. W. Webb, "Multiphoton fluorescence excitation: New spectral windows for biological nonlinear microscopy," Proc. Natl. Acad. Sci. U. S. A. **93**(20), 10763–10768 (1996).
5. W. Drexler, U. Morgner, R. K. Ghanta, F. X. Kärtner, J. S. Schuman, and J. G. Fujimoto, "Ultrahigh-resolution ophthalmic optical coherence tomography," Nat. Med. **7**(4), 502–506 (2001).
6. V. M. Baev, T. Latz, and P. E. Toschek, "Laser intracavity absorption spectroscopy," Appl. Phys. B Lasers Opt. **69**(3), 171–202 (1999).
7. A. Zoubir, L. Shah, K. Richardson, and M. Richardson, "Practical uses of femtosecond laser micro-materials processing," Appl. Phys. A Mater. Sci. Process. **77**(2), 311–315 (2003).
8. M. Drescher, M. Hentschel, R. Kienberger, G. Tempea, C. Spielmann, G. A. Reider, P. B. Corkum, and F. Krausz, "X-ray pulses approaching the attosecond frontier," Science (80-.). **291**(5510), 1923–1927 (2001).
9. A. Zewail, "The Nobel Prize in Chemistry 1999," https://www.nobelprize.org/prizes/chemistry/1999/summary/.
10. T. W. Hänsch and J. L. Hall, "The Nobel Prize in Physics 2005," https://www.nobelprize.org/prizes/physics/2005/summary/.
11. R. Uecker, D. Klimm, S. Ganschow, P. Reiche, R. Bertram, M. Roßberg, and R. Fornari, "Czochralski growth of Ti:sapphire laser crystals," in *SPIE 5990, Optically Based Materials and Optically Based Biological and Chemical Sensing for Defence II*, J. C. Carrano, A. Zukauskas, A. W. Vere, J. G. Grote, and F. Kajzar, eds. (2005), p. 599006.
12. D. Viechnicki and F. Schmid, "Crystal growth using the heat exchanger method (HEM)," J. Cryst. Growth **26**(1), 162–164 (1974).
13. R. L. Aggarwal, A. Sanchez, M. M. Stuppi, R. E. Fahey, A. J. Strauss, W. R. Rapoport, and C. P. Khattak, "Residual Infrared Absorption in As-Grown and Annealed Crystals of Ti: Al," IEEE J. Quantum Electron. **24**(6), 1003–1008 (1988).
14. GT Crystal Systems, "HEM Ti:sapphire Crystals for Ultrafast Lasers," https://gtat.com/products/ti-sapphire/.
15. M. R. H. Knowles and C. E. Webb, "Cavity configurations for copper vapour laser pumped titanium sapphire lasers," Opt. Commun. **89**(5–6), 493–506 (1992).
16. R. Paschotta, "Argon Ion Lasers," https://www.rp-photonics.com/argon_ion_lasers.html.
17. T. Baer, "Large-amplitude fluctuations due to longitudinal mode coupling in diode-pumped intracavity-doubled Nd:YAG lasers," J. Opt. Soc. Am. B **3**(9), 1175 (1986).
18. R. Paschotta, "Green Lasers," https://www.rp-photonics.com/green_lasers.html.
19. J. N. Walpole, "Semiconductor amplifiers and lasers with tapered gain regions," Opt. Quantum Electron. **28**(6), 623–645 (1996).
20. A. Müller, O. B. Jensen, A. Unterhuber, T. Le, A. Stingl, K.-H. Hasler, B. Sumpf, G. Erbert, P. E. Andersen, and P. M. Petersen, "Frequency-doubled DBR-tapered diode laser for direct pumping of Ti:sapphire lasers generating sub-20 fs pulses," Opt. Express **19**(13), 12156 (2011).
21. A. Müller, O. B. Jensen, K.-H. Hasler, B. Sumpf, G. Erbert, P. E. Andersen, and P. M. Petersen, "Efficient concept for generation of diffraction-limited green light by sum-frequency generation of spectrally combined tapered diode lasers," Opt. Lett. **37**(18), 3753 (2012).
22. A. K. Hansen, P. E. Andersen, O. B. Jensen, B. Sumpf, G. Erbert, and P. M. Petersen, "Highly efficient single-pass sum frequency generation by cascaded nonlinear crystals," Opt. Lett. **40**(23), 5526 (2015).
23. G. K. Samanta, S. C. Kumar, and M. Ebrahim-Zadeh, "Stable, 9.6 W, continuous-wave, single-frequency, fiber-based green source at 532 nm," Opt. Lett. **34**(10), 1561 (2009).
24. G. K. Samanta, S. Chaitanya Kumar, K. Devi, and M. Ebrahim-Zadeh, "High-power, continuous-wave Ti:sapphire laser pumped by fiber-laser green source at 532 nm," Opt. Lasers Eng. **50**(2), 215–219 (2012).
25. Z. Yu, H. Han, L. Zhang, H. Teng, Z. Wang, and Z. Wei, "Low-threshold sub-10 fs mode-locked Ti:sapphire laser pumped by 488 nm fiber laser," Appl. Phys. Express **7**(10), 102702 (2014).

26. Nichia, "Nichia NDB7Y75 Datasheet," https://www.nichia.co.jp/specification/products/ld/NDB7Y75.pdf.
27. Nichia, "Nichia NDG7D75 Datasheet," https://www.nichia.co.jp/specification/products/ld/NDG7D75.pdf.
28. M. Baumann, A. Balck, J. Malchus, R. V. Chacko, S. Marfels, U. Witte, D. Dinakaran, S. Ocylok, M. Weinbach, C. Bachert, A. Kösters, V. Krause, H. König, A. Lell, B. Stojetz, M. Ali, and U. Strauss, "1000 W blue fiber-coupled diode-laser emitting at 450 nm," in *High-Power Diode Laser Technology XVII*, M. S. Zediker, ed. (SPIE, 2019), p. 3.
29. P. W. Roth, A. J. Maclean, D. Burns, and A. J. Kemp, "Directly diode-laser-pumped Ti:sapphire laser.," Opt. Lett. **34**(21), 3334–3336 (2009).
30. K. Gürel, V. J. Wittwer, M. Hoffmann, C. J. Saraceno, S. Hakobyan, B. Resan, A. Rohrbacher, K. Weingarten, S. Schilt, and T. Südmeyer, "Green-diode-pumped femtosecond Ti:Sapphire laser with up to 450 mW average power," Opt. Express **23**(23), 30043 (2015).
31. S. Backus, M. Kirchner, C. Durfee, M. Murnane, and H. Kapteyn, "Direct diode-pumped Kerr Lens 13 fs Ti:sapphire ultrafast oscillator using a single blue laser diode," Opt. Express **25**(11), 12469 (2017).
32. S. Sawai, A. Hosaka, K. Hirosawa, and F. Kannari, "A Mode-Locked Ti:sapphire Laser Pumped Directly with a Green Diode Laser," in *CLEO: 2014* (OSA, 2014), p. SM4F.2.
33. P. W. Roth, "Directly diode-laser-pumped Titanium-doped Sapphire Lasers," University of Strathclyde (2012).
34. A. Hoffstädt, "Design and performance of a high-average-power flashlamp-pumped Ti:sapphire laser and amplifier," IEEE J. Quantum Electron. **33**(10), 1850–1863 (1997).
35. W. C. Wong, D. S. McClure, S. A. Basun, and M. R. Kokta, "Charge-exchange processes in titanium-doped sapphire crystals. I. Charge-exchange energies and titanium-bound excitons," Phys. Rev. B **51**(9), 5682–5692 (1995).
36. R. Sawada, H. Tanaka, N. Sugiyama, and F. Kannari, "Wavelength-multiplexed pumping with 478- and 520-nm indium gallium nitride laser diodes for Ti:sapphire laser," Appl. Opt. **56**(6), 1654 (2017).
37. C. G. Durfee, T. Storz, J. Garlick, S. Hill, J. a. Squier, M. Kirchner, G. Taft, K. Shea, H. Kapteyn, M. Murnane, and S. Backus, "Direct diode-pumped Kerr-lens mode-locked Ti:sapphire laser," Opt. Express **20**(13), 13677 (2012).
38. P. W. Roth, D. Burns, and A. J. Kemp, "Power scaling of a directly diode-laser-pumped Ti:sapphire laser," Opt. Express **20**(18), 20629 (2012).
39. H. Tanaka, R. Sawada, R. Kariyama, A. Hosaka, K. Hirosawa, and F. Kannari, "Power scaling of modelocked Ti: Sapphire laser pumped by high power ingan green Laser Diode," Proc. 2015 Eur. Conf. Lasers Electro-Optics - Eur. Quantum Electron. Conf. CLEO/Europe-EQEC 2015 **249**(2), 22702 (2015).
40. A. Rohrbacher, O. E. Olarte, V. Villamaina, P. Loza-Alvarez, and B. Resan, "Multiphoton imaging with blue-diode-pumped SESAM-modelocked Ti:sapphire oscillator generating 5 nJ 82 fs pulses," Opt. Express **25**(9), 10677 (2017).
41. D. A. Kopylov, M. N. Esaulkov, I. I. Kuritsyn, A. O. Mavritskiy, B. E. Perminov, A. V. Konyashchenko, T. V. Murzina, and A. I. Maydykovskiy, "Kerr-lens mode-locked Ti:Sapphire laser pumped by a single laser diode," Laser Phys. Lett. **15**(4), 0–5 (2018).
42. A. Muti, A. Kocabas, and A. Sennaroglu, "5-nJ Femtosecond Ti3+:sapphire laser pumped with a single 1 W green diode," Laser Phys. Lett. **15**(5), 1–6 (2018).
43. A. J. Alfrey, "Modeling of Longitudinally Pumped CW Ti: Sapphire Laser Oscillators," IEEE J. Quantum Electron. **25**(4), 760–766 (1989).
44. W. P. Risk, "Modeling of longitudinally pumped solid-state lasers exhibiting reabsorption losses," J. Opt. Soc. Am. B **5**(7), 1412 (1988).
45. E. P. Maldonado and N. D. Vieira, "Optimization of the active medium length in longitudinally pumped continuous-wave lasers," J. Opt. Soc. Am. B **12**(12), 2482 (1995).
46. A. E. Siegman, *Lasers* (1986).
47. "Thorlabs," https://www.thorlabs.com/.
48. International Organization for Standardization, "ISO 11146-1," **1**(15), 16 (2005).
49. U. Keller, *Ultrafast Solid State Lasers* (2007).
50. J. A. Caird, S. A. Payne, P. R. Staber, A. J. Ramponi, L. L. Chase, and W. F. Krupke, "Quantum electronic properties of the Na3Ga2Li3F12:Cr3+ laser," IEEE J. Quantum Electron. **24**(6), 1077–1099 (1988).
51. Z. W. Miao, H. J. Yu, J. Y. Zhang, S. Z. Zou, P. F. Zhao, B. J. Lou, and X. C. Lin, "Watt-Level CW Ti: Sapphire Oscillator Directly Pumped with Green Laser Diodes Module," IEEE Photonics Technol. Lett. **32**(5), 247–250 (2020).

Chapter 3: Broadly-tunable ultrafast diode-pumped Ti:sapphire lasers 89

Chapter 3: Broadly-tunable ultrafast diode-pumped Ti:sapphire lasers

3.1 Introduction

As presented in chapter 1, ultrafast diode-pumped Ti:sapphire laser technology provides a promising platform in the pursuit of more compact and lower-cost ultrafast laser sources. In chapter 2 work carried out on diode-pumped Ti:sapphire lasers operating in the continuous wave (CW) regime was presented. A CW output power of up to 721 mW was obtained in a double-end pumped scheme using two 3.5 W 450 nm laser diodes (see Chapter 2), providing a good foundation going forward with experiments in the ultrafast regime. In this chapter ultrafast diode-pumped Ti:sapphire lasers are investigated, using SESAM mode-locking methods and also using KLM methods. In the next section a literature review of ultrafast diode-pumped Ti:sapphire technology is given, providing context regarding the state of the art and where this work lies.

3.2 Review of ultrafast diode-pumped Ti:sapphire lasers

A comparison of the performance of various ultrafast diode-pumped Ti:sapphire lasers is given in Table 17.

Table 17. Reported performance of various ultrafast diode-pumped Ti:sapphire lasers.

Year	Pump Power (W)	Pump Wavelength (nm)	Mode-locking Mechanism	Self-Starting	Average Output Power (mW)	Pulse Duration (fs)	Tuning Range (nm)	Optical Efficiency (%)	Reference
2011	2 × 1	452/454	SESAM	Yes	101	111	-	5.1	[1]
2012	2 × 1	445	KLM	No	34	15	-	1.7	[2]
2013	2 × 2	445	KLM		105 70	50 15	-	2.6 1.8	[3]
2014	1 × 1	518	SESAM	Yes	23.5	62	-	2.4	[4]
2015	2 × 1	518/520	SESAM	Yes	44.8	74	-	2.2	[5]
2015	2 × 1 2 × 1.5	520	SESAM KLM KLM	Yes No No	200 350 450	68 39 58	-	10.0 11.7 15.0	[6]
2017	2 × 2.9	450	SESAM SESAM	Yes	350 460	65 82	-	6.0 7.9	[7]
2017	1 × 4	465	KLM	No	173 145	15 13	-	4.3 3.6	[8]
2018	1 × 4.4	461	KLM	No	217 170	24 15	-	4.9 3.9	[9]
2018	1 × 0.88	520	KLM	No	30	95	-	3.4	[10]
2019	1 × 3.5	450	KLM	No	22	8.6	-	0.6	[11]

One noticeable aspect of diode-pumped Ti:sapphire lasers summarised in this table is their lack of tunability in the ultrafast mode-locked regime. While tunability has been demonstrated in the CW regime by several groups, only fixed wavelength operation has been demonstrated in ultrafast mode-locked regime. This is one performance aspect of diode-pumped Ti:sapphire this thesis sets out to address in order to bring diode-pumped Ti:sapphire lasers a step closer to matching the performance of their conventionally-pumped counterparts.

The highest average output power achieved using KLM was that by Gurel et al., with an output power of 450 mW using two 1.5 W 520 nm diodes. The highest average output power achieved using SESAM mode-locking was slightly higher at 460 mW, using two 2.9 W 450 nm diodes. The shortest pulses achieved were by Liu et al., with 8.6 fs pulses generated through KLM and extracavity pulse compression. Pumped using a single 3.5 W 450 nm diode, the average output power was 22 mW in this case.

As can be seen from Table 17 either SESAM mode-locking or KLM methods for passive mode-locking are used. Each possess various advantages and disadvantages compared to each other, and both methods were investigated in the course of this work. As SESAM mode-locking is arguably easier to realise from a purely experimental point of view, it was with this method that it was decided to begin mode-locking experiments.

3.3 SESAM mode-locking

As discussed in Chapter 1, SESAM devices are a well-established method used to mode-lock solid-state lasers producing pulses from 10's of picoseconds down to less than 10 fs [12,13]. Initially it was believed that pure CW mode-locking could not be achieved using saturable absorbers and solid-state lasers with long upper state lifetimes without Q-switching or Q-switched mode-locking behaviour occurring. The main reason for this was due to the parameters of the saturable absorbers available at the time [14]. However, progress in bandgap engineering and modern semiconductor growth technology has allowed for the ability to accurately control and tailor saturable absorber device parameters such as recovery time, absorption wavelength, and saturation energy. This in turn has enabled devices for Q-switching, Q-switched mode-locking, and pure CW mode-locking [15].

3.3.1 Soliton mode-locking

In soliton mode-locking regime the pulse-shaping process is governed solely by soliton formation through the balance of self-phase modulation (SPM) and group delay dispersion

(GDD). In this regime an additional loss mechanism, provided by a SESAM [16] or in some cases by an acousto-optic modulator [17], is only required to start the mode-locking process and stabilise the soliton. Through soliton mode-locking it is possible to reach pulse durations in the femtosecond regime that would otherwise be impossible using only the slow saturable absorber for pulse-shaping (see section 1.4.7 of Chapter 1).

3.3.2 SESAM parameters

When selecting a SESAM for mode-locking a laser, there are a few absorber parameters that are important to consider, and these parameters will vary depending on the type of laser one wishes to mode-lock. For example, bulk solid-state lasers have very different requirements compared to fibre lasers and it is important to select the correct parameters to ensure CW mode-locking and to avoid Q-Switching instabilities. Q-switching instabilities can occur in a laser passively mode-locked with a saturable absorber, such that the intracavity pulse energy undergoes large oscillations related to undamped relaxation oscillations [18]. This means that the instead of obtaining a steady train of pulses with constant pulse energy, the pulse energy undergoes large fluctuations from pulse to pulse as shown in Figure 44.

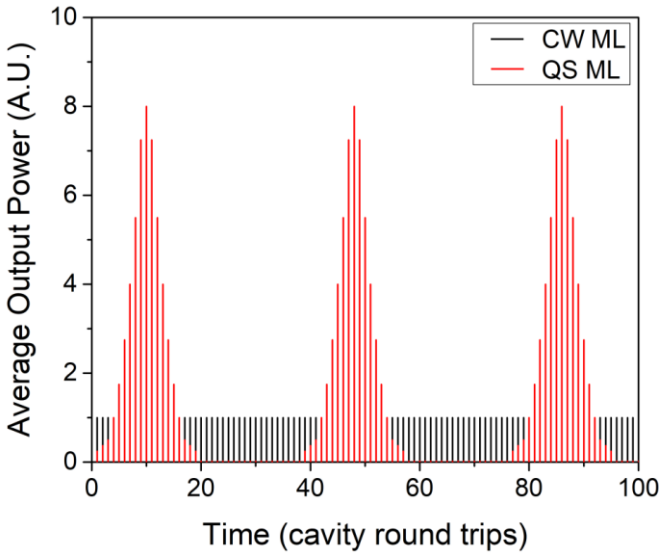

Figure 44. The evolution of optical output power in a Q-switched mode-locked laser (in red) where ultrashort pulses are generated in bunches, and in a CW mode-locked laser with constant pulse energy (in black).

In some cases, these Q-switched instabilities can display fairly stable parameters within this type of behaviour, termed Q-switched mode-locking. Despite this, Q-switched mode-locking is largely undesirable, as it often leads to damage of the SESAM due to the periodic high pulse energies, and as such steps must be taken to suppress these instabilities. Depending on

whether the laser is operating in the soliton or non-soliton regime, the suppression condition is different.

3.3.2.1 Q-switching instabilities – non-soliton regime

The following equation gives the threshold above which Q-switched mode-locking is suppressed for the non-soliton regime:

$$E_p{}^2 > E_{sat,L}E_{sat,A}\Delta R \tag{41}$$

where E_p is the intracavity pulse energy, $E_{sat,L}$ is the saturation energy of the gain medium, $E_{sat,A}$ is the saturation energy of the saturable absorber, and ΔR is the modulation depth of the absorber.

As shown in Equation 1 above the threshold is dependent on the saturation energy of the absorber, the saturation energy of the gain medium, and the modulation depth. Therefore, in order to reduce the threshold pulse for CW mode-locking, a small modulation depth and a small absorber saturation energy are desirable. For solid-state lasers generally a modulation depth of 1-2% is used [18,19]. A low saturation fluence (related to the saturation energy through $E_{sat,A} = F_{sat,A} \times A_{mode}$) in the region of 1-100 μJ/cm^2 is also typical [18,19].

3.3.2.2 Q-switching instabilities – soliton regime

When considering lasers operating in the soliton regime, it has been demonstrated that Equation 1 overestimates the critical pulse energy by up to a factor of 4 [18]. The following equation was derived by Hönninger et al. giving the intracavity pulse energy threshold above which Q-switched mode-locking is suppressed for the soliton regime:

$$E_{sat,L}gK^2E_p{}^2 + E_p{}^2 > E_{sat,L}E_{sat,A}\Delta R \tag{42}$$

$$where\ K = \frac{4\pi n_2 L_K}{D_2 A_{eff,L}\lambda_0 \Delta v_g}\frac{0.315}{1.76} \tag{43}$$

where g is the round-trip gain, n_2 is the nonlinear refractive index of the Kerr medium, L_K is the propagation length in the Kerr medium per round trip (the gain medium itself usually acts as the Kerr medium), D_2 is the amount of negative intracavity GDD per round trip, $A_{eff,L}$ is

the laser mode area inside the gain medium, Δv_g is the FWHM of the gain spectrum, λ_0 is the centre wavelength of the mode-locked pulse.

The difference between the intracavity pulse energy Q-switched mode-locking suppression threshold for the soliton and non-soliton regimes has been explained by Hönninger et al. as being attributable to the interplay of soliton effects and gain filtering. The basic idea is that if relaxation oscillations cause the energy of an ultrashort pulse to slightly increase, then self-phase modulation and/or self-amplitude modulation will broaden the spectrum of the pulse. This results in a reduction in the effective gain due to the finite gain bandwidth, which decreases the threshold pulse energy for stable mode-locking.

3.3.2.3 SESAM recovery time

As stated in section 1.4.6 of Chapter 1, as a rule of thumb the recovery time of the absorber can be roughly 10 times the desired pulse duration in soliton mode-locking [20]. Thus, if a pulse duration of around 100 fs is desired, then an absorber with a recovery time of around 1 ps should be used.

3.3.2.4 SESAM non-saturable loss

Another important parameter is the non-saturable loss, which represents the amount of loss the absorber introduces when fully saturated. It is important that the non-saturable loss is kept to a minimum in solid-state lasers, as the gain is typically low and as such significant amounts of loss result in inefficient operation and a high lasing threshold. Usually, some non-saturable loss is unavoidable, due to defects, residual transmission and scattering losses, with typical saturable absorbers for solid state lasers displaying <1% [20].

3.3.2.5 SESAM used in laser experiments

For SESAM mode-locking experiments a GaAs quantum well-based SESAM sourced from Reflekron Limited was used. The low-signal reflectivity R_{LS} (when the SESAM is unsaturated) is 97.5% over the range of 775 nm to 840 nm as shown in Figure 45. The saturable loss or modulation depth is represented by q_S and is estimated to be 1.5 to 2% over the SESAM operating range. The non-saturable loss q_{NS} is estimated to be less than 1%. The saturation fluence (F_{SAT}) is estimated to be in the region of 50 μJ/cm^2 based on another researcher's experience with this particular SESAM [21]. The key parameters for the SESAM used in the laser experiments are summarised in Table 18:

Table 18. Key parameters of SESAM used for passive mode-locking of diode-pumped Ti:sapphire laser.

R_{LS}	q_S	q_{NS}	λ_{SESAM}	F_{SAT}
97.5%	1.5 - 2%	<1%	775 - 840 nm	50 μJ/cm^2

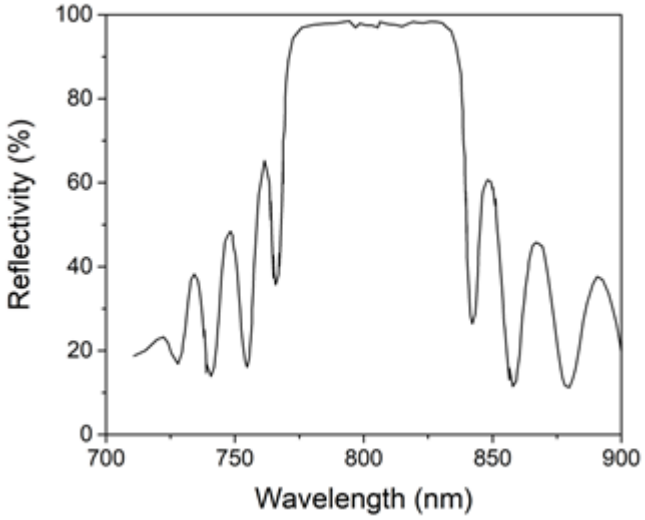

Figure 45. Low-signal reflectivity of the SESAM vs wavelength.

As discussed in section 1.4.7.6 of Chapter 1 the optimal intracavity fluence upon the SESAM F_{SESAM} should be between 3 and 5 times that of its saturation fluence. This meant that it was desired to keep F_{SESAM} between 150 and 250 μJ/cm^2. The intracavity fluence upon the SESAM is given by the following equation:

$$F_{SESAM} = \frac{E_P}{\pi {\omega_0}^2} \tag{44}$$

where E_P is the intracavity pulse energy and ω_0 is the beam waist radius on the SESAM. The intracavity pulse energy is given by:

$$E_P = \frac{P_{IC}}{f_{rep}} \tag{45}$$

$$P_{IC} = \frac{P_{av}}{T} \tag{46}$$

$$f_{rep} = \frac{\mathrm{c}}{2L} \tag{47}$$

where P_{IC} is the average power circulating inside the resonator, P_{av} is the average power output from the laser, T is the fractional output coupling, and f_{rep} is the repetition rate, which is dictated by the resonator length L. Using these equations and assuming a certain average output power, it is possible to optimise the resonator design and estimate the required beam waist radius on the SESAM such that the intracavity fluence is 3-5 times F_{SAT}.

Fluence calculations were then carried out, assuming an average output power for the SESAM mode-locked regime will be 300 mW (roughly half that of the CW regime), an output coupling of 5%, and a repetition rate of 130 MHz (based on the cavity length).

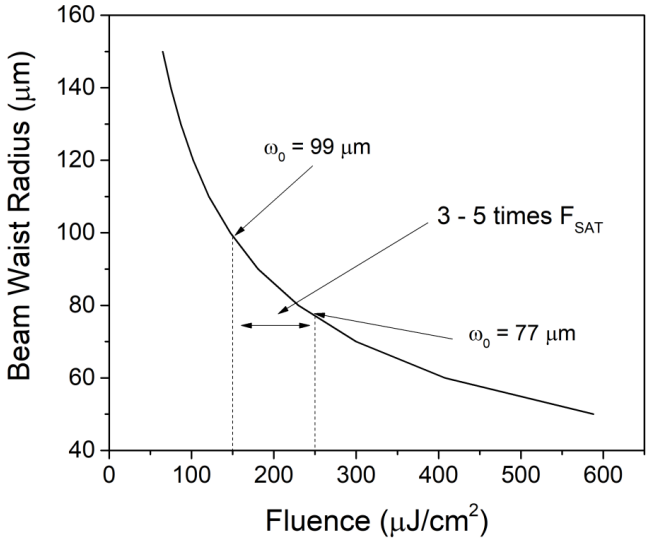

Figure 46. Calculated intracavity fluence incident upon the SESAM (F_{SESAM}) vs the beam waist radius for P_{av}= 300 mW, T = 5%, and f_{rep} = 130 MHz.

Based on the above assumptions, in order to obtain F_{SESAM} between 150 and 250 μJ/cm^2 a beam waist radius of between 99 and 77 μm on the SESAM is required, as can be seen from Figure 46. This was considered when designing the resonator.

3.3.3 Resonator design

Using the CW resonator as a starting point, the cavity design was modified using ABCD matrix software (LASCAD) to produce a resonator design for SESAM mode-locking. The goal was to, ideally, keep the cavity beam waist inside the crystal as close as possible to that in the CW resonator ensuring a consistent pump-cavity mode overlap, while creating a second beam waist upon the end mirror in the short arm where the SESAM would be placed. This is often achieved by adding an additional curved mirror to the cavity or by adjusting the folding mirror separation such that the cavity operates in stability region II as shown in Figure 47. The latter option was chosen as it is simpler, potentially more compact, and introduces less residual loss

to the cavity by using fewer optics. To this end, the folding mirror separation was increased to 86.8 mm from 79.0 mm in the CW resonator. The short arm of the resonator was also reduced to 220 mm (from 270 mm in the CW resonator) in order to produce a tighter beam waist upon the SESAM. Additionally, the long arm had to be extended from 655 mm to 768 mm in order to comfortably insert the fused silica prism pair (with 50 cm tip-to-tip separation required to produce the correct amount of negative GDD) and double chirped mirror (DCM) pair.

Using LASCAD it is possible to calculate the mode size at any point in the cavity, allowing the beam waist inside the crystal and the beam waist incident upon the SESAM to be calculated. The beam waist inside the crystal is calculated to be 29 × 16 µm in the setup shown in Figure 48, which is similar in size to the beam waist of 26 × 16 µm inside the crystal for the CW resonator. A beam waist of around 85 µm on the SESAM was calculated, in the correct range to provide a fluence of around 3-5 times F_{SAT} (see Figure 47).

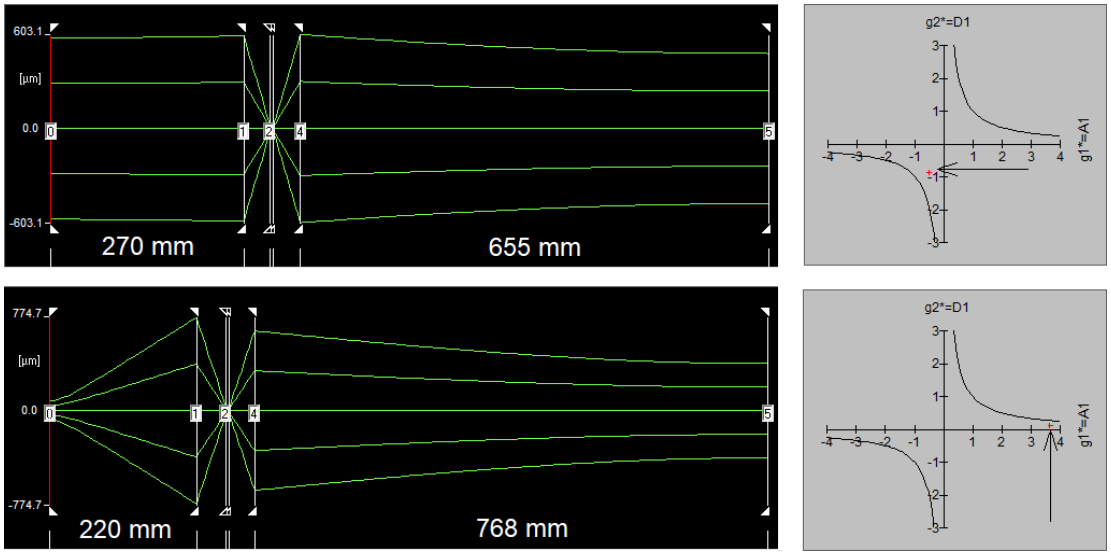

Figure 47. Cavity mode plot and corresponding cavity stability diagram for CW resonator (top row) and resonator for SESAM mode-locking (bottom row). The arrows on the stability diagram point to the cavity stability position.

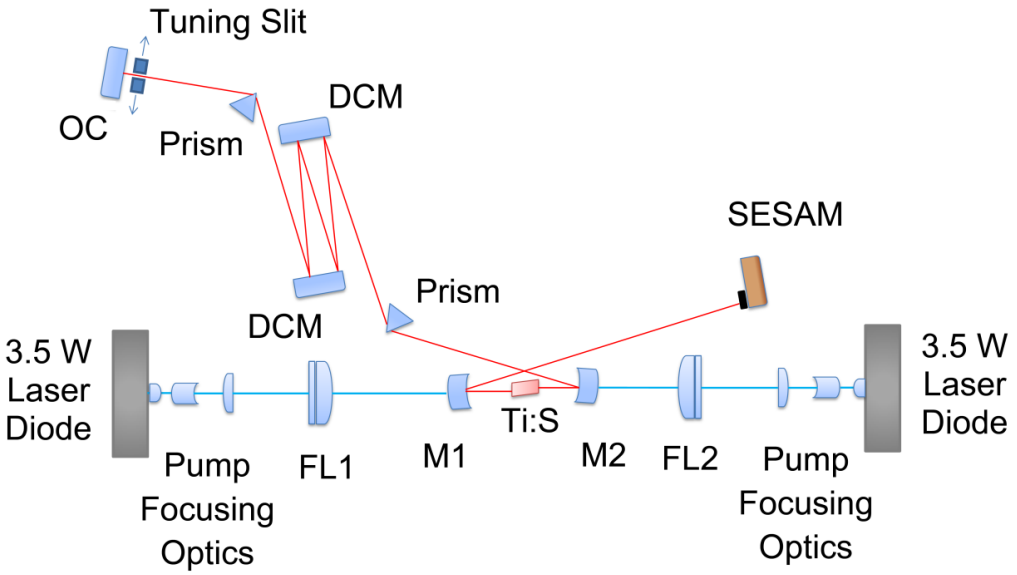

Figure 48. Experimental setup of SESAM mode-locked diode-pumped Ti:sapphire laser.

The final cavity design is shown in Figure 48. In addition to the described cavity alterations, a tuning slit for output wavelength selection is added to cavity, as well as dispersion compensating optics, which are further described in the next section.

3.3.4 Dispersion compensation

As stated in section 1.4.7 of Chapter 1, in soliton mode-locking it is assumed that the pulse-shaping process is entirely achieved through soliton effects. In this case, the expected FWHM pulse-duration is given by [22]:

$$\tau_{FWHM} = 1.76 \cdot \frac{4|D|}{\delta E_p} \tag{48}$$

where E_p is the intracavity pulse energy, D is the net negative cavity GDD and δ is the SPM coefficient given by:

$$\delta = \frac{2\pi n_2}{\lambda_0 A_{eff}} \cdot l \tag{49}$$

where n_2 is the nonlinear refractive index, λ_0 is the wavelength, A_{eff} is the effective mode area inside the crystal, and l is the crystal length. As can be seen from Figure 49 as the intracavity pulse energy increases, the pulse duration decreases.

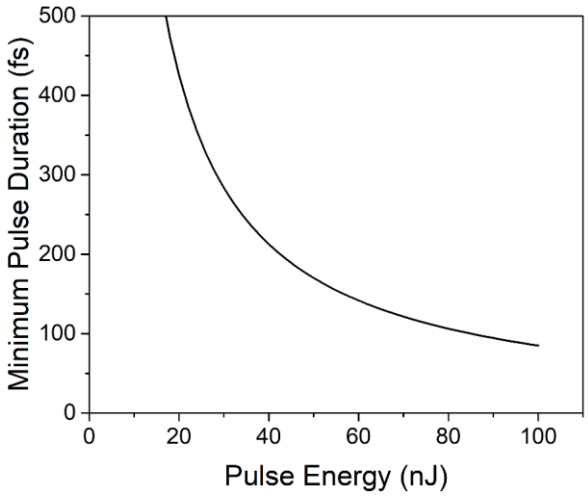

Figure 49. Minimum pulse duration vs. intracavity pulse energy in a soliton mode-locked laser according to Equation 8. D = -1000 fs^2, n_2 = 3.2 × 10^{-20} m^2/W, λ_0 = 800 nm, ω_0 = 29 × 16 µm, and l = 4.8 mm.

This effect is the result of the increasing saturation of the absorber, leading to broader gain and thus shorter pulses [22]. As the pulse energy is increased, it will eventually reach a point where the absorber will become completely saturated and will not be able to contribute to any further stabilisation of the pulse. No such saturation occurs with the Kerr nonlinearity; therefore, the soliton formula dictates that the pulse width will continue to decrease indefinitely with increasing pulse energy. However, this is only the case until either the soliton loss becomes larger than the continuum loss and the continuum breaks through, or the pulse breaks up into two pulses known as the double pulse regime [19,22,23].

It is apparent from Equation 8 that the amount of negative dispersion applied to the cavity is critical in the generation of ultrashort pulses. Not only does it balance against the amount of SPM to enable soliton mode-locking and discriminate against undesirable background continuum (see section 1.4.7 of Chapter 1), it is also important in determining the final pulse duration. It would seem from Equation 8 that in order to produce the shortest pulse duration, then D should be kept as small as possible. However, if it is too small the continuum will break through. Thus, there is an optimum value of negative intracavity GDD for which transform-limited pulses will be produced for a given set of laser parameters. This can be estimated using Equation 8 . The required intracavity negative GDD is estimated for the laser parameters given in Table 19:

Table 19. Laser parameters used to estimate required negative intracavity GDD for a pulse duration of 100 fs.

T_{OC}	P_{av}	f_{rep}	n_2	l_c	λ_0	ω_0	τ_D	D
2%	300 mW	100 MHz	3 × 10^{-20} m^2/W	4.8 mm	800 nm	30 µm	100 fs	852 fs^2

After a review of published results on ultrafast diode-pumped Ti:sapphire (see section 3.2), the intracavity GDD estimate of around 850 fs^2 is in broad agreement with typical values described in the literature. It was decided that the net intracavity GDD would be set close to this initially and then optimised through empirical means. This process was carried out in an iterative manner in order to arrive at the configuration as described in the following paragraphs. For dispersion compensation a combination of a DCM pair and a fused silica prism pair was used, each with its associated advantages and disadvantages.

The advantage of a prism pair is that the applied GDD can be fine-tuned through variation of the prism insertion, and it is also possible to tune the output wavelength of the laser by placing a knife edge slit in the section of the beam where the wavelength components are spatially dispersed. Disadvantages of prism pair are that the amount of negative GDD that can be applied is dependent on the tip-to-tip separation, thus it is conceivable that the required negative GDD would dictate a prism separation longer than is possible within one of the cavity arms.

The fused silica prism pair used was set up for a tip-to-tip separation L_p = 50 cm and an insertion L_m = 4 mm, which provided a total of -677 fs^2 per round trip at 800 nm. The insertion was varied by around +/- 2 mm when fine-tuning the optimal amount of GDD for certain configurations, corresponding to roughly +/- 200 fs^2 in applied negative GDD at 800 nm. The applied GDD as a function of wavelength is shown in Figure 50.

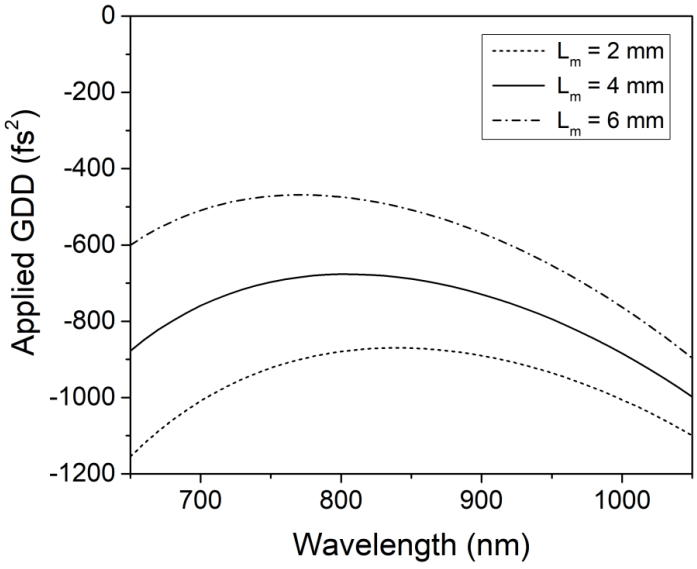

Figure 50. Applied GDD vs wavelength of the prism pair for various values of prism insertion L_m. Calculated in Mathcad using equations defined in section 1.2.2 of Chapter 1.

In addition to the prism pair a DCM pair was also used. By using DCMs, discrete amounts of negative GDD can be added by simply adding more mirror bounces, while also allowing for a more compact geometry through folding of the beam path as shown in Figure 48. However, it is important that there is an equal number of bounces on each mirror in order to avoid unwanted oscillations in intracavity GDD with respect to wavelength. A disadvantage is the introduction of loss through imperfect mirror coatings (however, this is usually only a fraction of a %) and contamination of mirrors with e.g. dust particulate.

The DCM pair provided -120 fs^2 GDD per mirror per bounce over a wavelength range of 700 nm to 900 nm. This value is only valid when the DCMs are used as a pair as the individual mirrors have oscillations in GDD vs wavelength (see Figure 51), which cancel to form a flat average GDD over the specified wavelength range. The cavity was set up for a total of 8 mirror bounces per round trip to contribute a total GDD of -960 fs^2 per round trip.

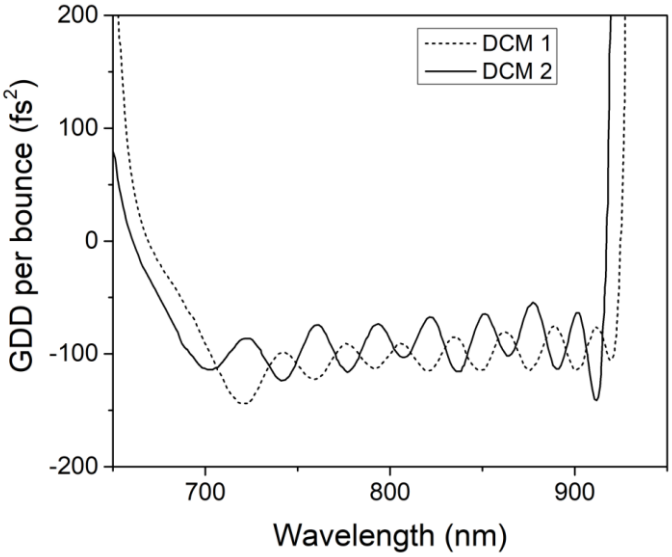

Figure 51. The individual oscillations in GDD vs wavelength for each mirror in the DCM pair are shown above. However, when used as a pair the oscillations mostly balance, the resulting average GDD is a fairly flat -120 fs^2 per mirror bounce over the 700-900 nm range.

Considering all sources of GDD within the cavity (neglecting air), Figure 52 shows the net cavity GDD. For a prism separation of 50 cm, a prism insertion of 4 mm, and a total of 8 DCM bounces (per round trip), this equates to a GDD of -1080 fs^2 per round trip at 800 nm.

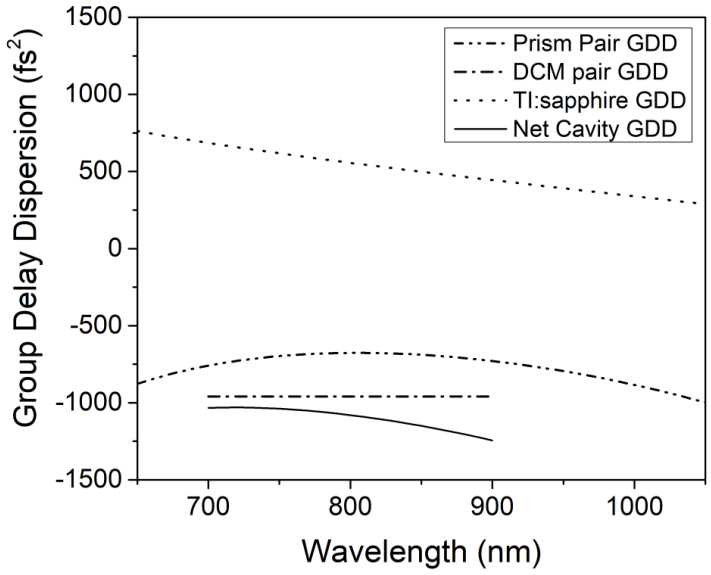

Figure 52. Net intracavity GDD vs. wavelength, considering the negative GDD contributions from the prism pair and the DCM pair as well as the positive GDD arising from the material dispersion of Ti:sapphire.

3.3.5 SESAM mode-locked results

The input-output characteristics of the SESAM mode-locked diode-pumped Ti:sapphire laser are shown in Figure 53. Mode-locking was self-starting and was initiated at around 5.4 W incident pump power. No Q-switching instabilities or multiple pulsing was observed. The maximum average output power achieved during stable mode-locked operation with the SESAM was 433 mW (from 6.5 W of incident pump power), resulting in an optical-optical efficiency of 6.6%. To estimate the expected output power drop moving from the CW regime to the SESAM mode-locked regime, the HR end mirror in the CW resonator was replaced with the SESAM and the output power was monitored. Using this method an output power drop of around 50% was observed compared to the CW regime with the HR mirror. In the mode-locked regime the actual performance was slightly better than the 50% drop anticipated, given that 433 mW was achieved in SESAM mode-locked operation where the output power in the CW configuration was 721 mW for the same pump power. As can be seen from Figure 53, the mode-locking threshold was achieved at around 5.4 W of the incident pump power when an average output power of 264 mW was generated, resulting in 172 μJ/cm^2 fluence on the SESAM. At the maximum average output power of 433 mW, the fluence on the SESAM was 283 μJ/cm^2.

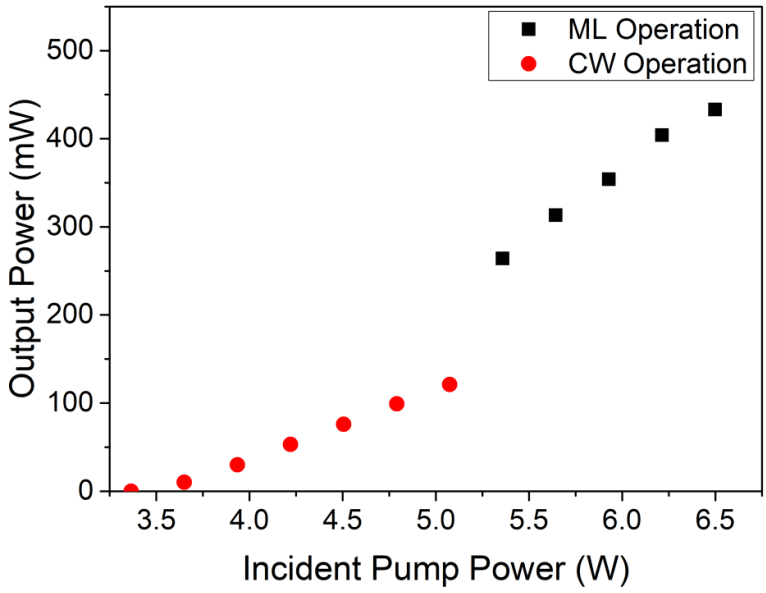

Figure 53. The input-output characteristic of the SESAM mode-locked diode-pumped Ti:sapphire laser, showing average output power vs pump power incident upon the crystal.

At the maximum output power, the pulse duration was deduced to be 85 fs based on the intensity autocorrelation measurements and assuming a sech^2 pulse shape (see Figure 54). The full width at half maximum (FWHM) of the optical spectrum centred at 810 nm is 8.5 nm (see Figure 55). This equates to a time-bandwidth product (TBP) of 0.33.

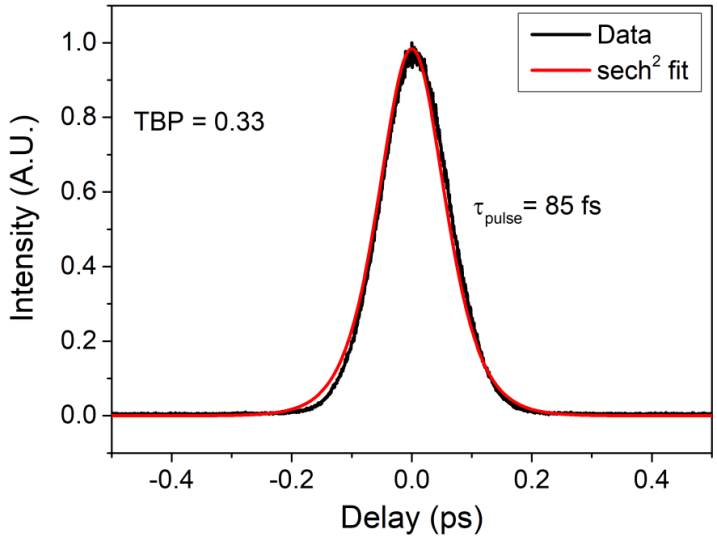

Figure 54. Intensity autocorrelation of the SESAM mode-locked Ti:sapphire laser producing a maximum average output power of 433 mW. TBP (time-bandwidth product) is 0.33.

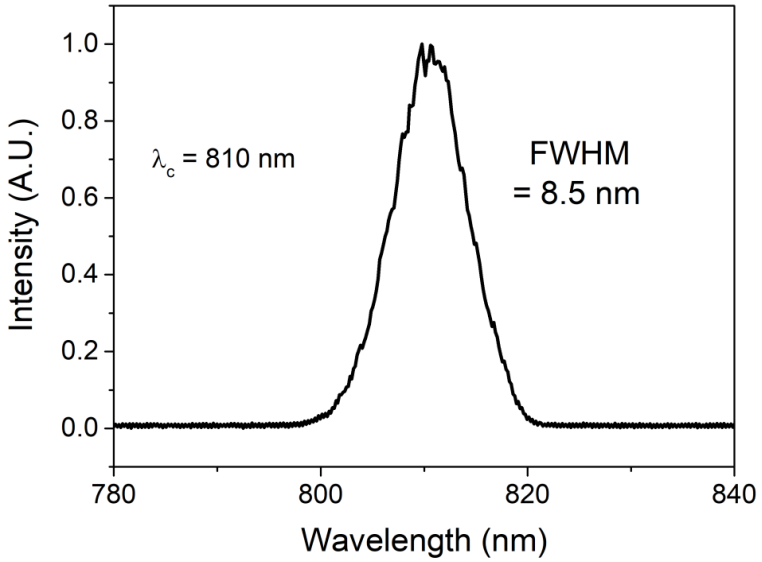

Figure 55. Optical spectrum of the SESAM mode-locked Ti:sapphire laser producing a maximum average output power of 433 mW.

The radio frequency (RF) spectrum taken with a fast silicon photodetector with 2 GHz bandwidth shows stable pulsed operation with the pulse repetition frequency of around 135 MHz, as shown in Figure 56.

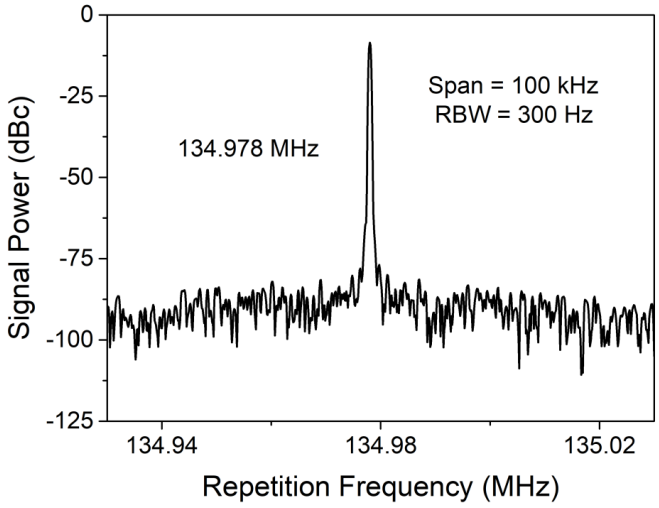

Figure 56. Radio frequency spectrum of the SESAM mode-locked Ti:sapphire laser recorded with 100 kHz frequency span and 300 Hz resolution bandwidth.

By further dispersion optimization (increasing the insertion of the second prism by 1-2 mm into the intracavity beam) shorter pulses were generated. Namely, pulses of 62 fs in duration were achieved with 12.1 nm FWHM spectral bandwidth resulting in a TBP of 0.34. In this configuration the average output power was slightly reduced to 331 mW.

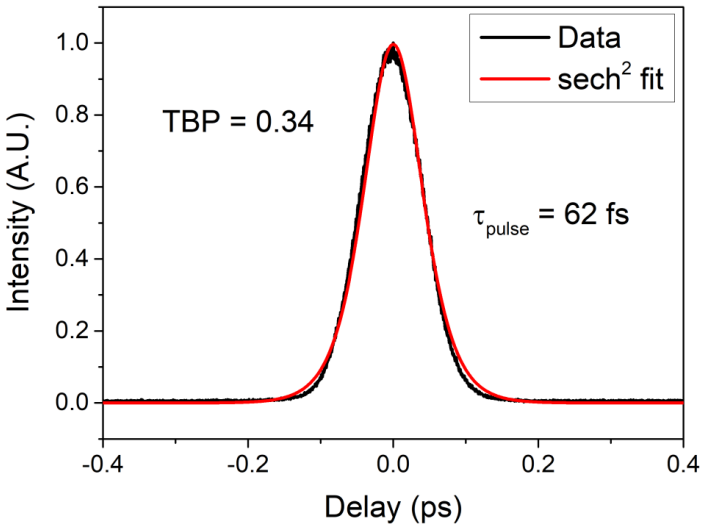

Figure 57. Intensity autocorrelation of the SESAM mode-locked Ti:sapphire laser producing 62 fs pulses with an average output power of 331 mW.

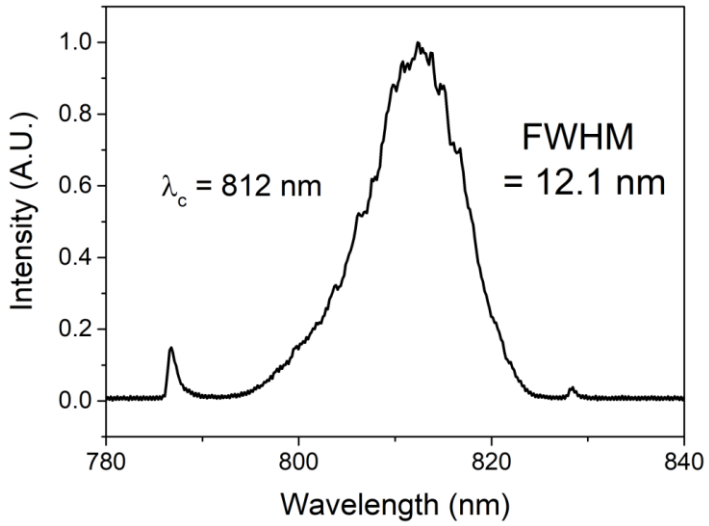

Figure 58. Optical spectrum of the SESAM mode-locked Ti:sapphire laser producing 62 fs pulses with an average output power of 331 mW.

Comparing the spectra shown in Figure 58 to that in Figure 55, there is additional spectral structure in the form of "spikes" either side of the main pulse spectrum. These are assumed to be the phenomenon known as Kelly Sidebands. The explanation for this effect is as follows: in soliton mode-locked lasers, the soliton pulse circulating in the resonator generally experiences the average values of the chromatic dispersion and nonlinearity. However, it also experiences a weak periodic disturbance given the discrete nature of the dispersion and nonlinearity in the resonator. These periodic disturbances couple the soliton to the co-propagating dispersive wave, also known as background continuum (see section 1.4.7 of Chapter 1). This does not usually have a strong effect as the relative phase of the soliton and dispersive wave is continually changing given that only the soliton experiences the

nonlinearity. However, when the relative phase of the soliton and dispersive wave changes by an integer multiple of 2π per resonator round trip, it can result in a kind of resonant coupling. This results in the formation of narrow peaks on the pulse spectrum known as Kelly Sidebands [24,25].

For the laser tunability, a knife edge slit mounted on a translation stage was placed between the OC and the second fused silica prism where the wavelength components of the beam are spatially dispersed.

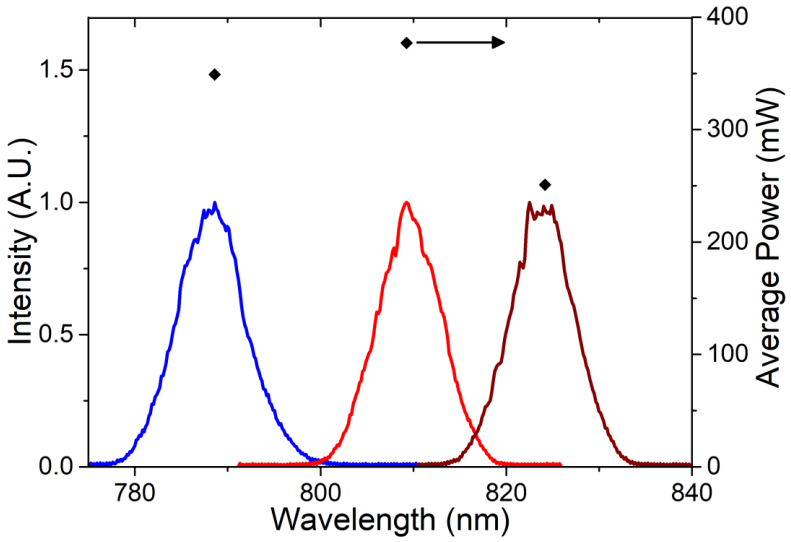

Figure 59. Tuning range of the SESAM mode-locked Ti:sapphire laser from 788 nm to 825 nm, with corresponding average output powers.

A maximum tuning range of 788-825 nm was achieved (see Figure 59). Tuning to 788 nm and fine-tuning the intracavity dispersion appropriately via prism insertion, 84 fs pulses were obtained with an 8.1 nm FWHM spectral bandwidth (TBP of 0.33) and an average output power 349 mW. 91 fs pulses were generated with the corresponding spectral bandwidth of 7.9 nm (TBP of 0.33) at 825 nm, at an average output power of 251 mW. This represents a 37 nm tuning range with average output powers in excess of 250 mW and sub-100 fs pulse durations. The main factor limiting tunability here is the reflectivity bandwidth of the SESAM, which has high reflectivity over the range of 780-830 nm (see Figure 45). Given the limited reflectivity bandwidth of the SESAM, it was decided to switch to the KLM regime, with the goal of further extending the wavelength tuning range.

3.4 Kerr-lens mode-locking

As was discussed in section 1.3.1 of Chapter 1 the Kerr-lens mode-locking mechanism is made possible through the Kerr effect, which produces an intensity-dependent refractive index

change. The magnitude of n_2 in sapphire is fairly constant over the gain bandwidth range of Ti:sapphire. This means that at sufficient optical intensities, the nonlinear refractive index variation responsible for the nonlinear effects of Kerr-lensing and self-phase modulation is present over the entire gain bandwidth of Ti:sapphire, and that in theory KLM is therefore possible over the entire gain bandwidth of Ti:sapphire [26]. Therefore, a larger tuning range should be achievable in the ultrafast diode-pumped Ti:sapphire laser by using KLM methods rather than with the SESAM and its limited bandwidth.

3.4.1 Initial KLM results from SESAM-optimised cavity

Initial KLM experiments were carried out with only minor modifications to the SESAM-optimised cavity as shown in Figure 60. The purpose of these experiments was to assess whether KLM could be realised with the laser in its current configuration with only minor adjustments. This involved replacing the SESAM with a HR mirror, and also placing an additional slit in the cavity for better discrimination between the high intensity and low-intensity modes. The results described in this section are for this non-optimised setup. Further improvements were subsequently made, which are described in more detail in the sections following this one.

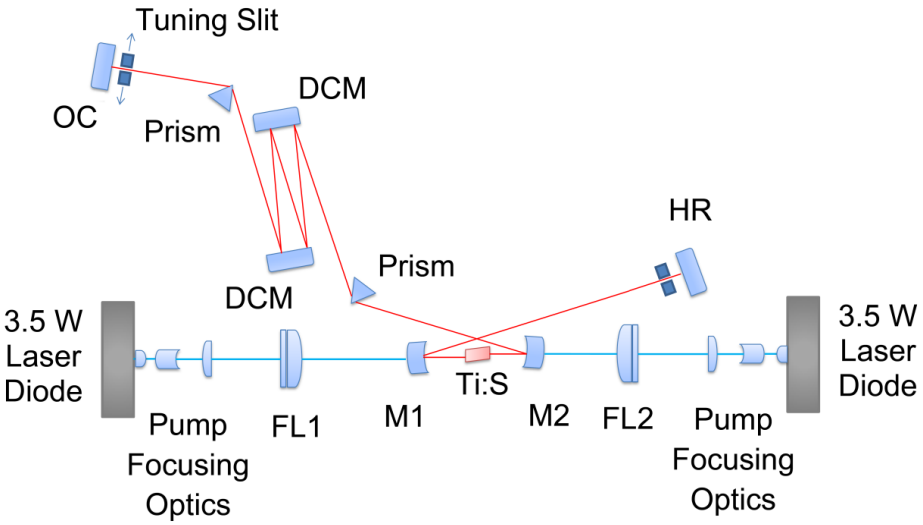

Figure 60. Experimental setup of KLM diode-pumped Ti:sapphire laser with SESAM mode-locking optimised cavity.

In addition to this, the folding mirror separation is decreased until the cavity is close to the inner edge of stability region II, where KLM is most likely to occur. KLM can then be initiated by translating one of the folding mirrors back and forth rapidly.

The highest average output power achieved with this configuration during KLM operation was 158 mW at a central wavelength of 822 nm (see Figure 61). The generated pulses were measured to be 61 fs in duration (see Figure 62) with the corresponding spectral bandwidth of 12.6 nm (see Figure 63), resulting in a TBP of 0.34. The RF spectrum shows a pulse repetition frequency of 134.7 MHz (see Figure 64), similar to the SESAM mode-locked setup as expected.

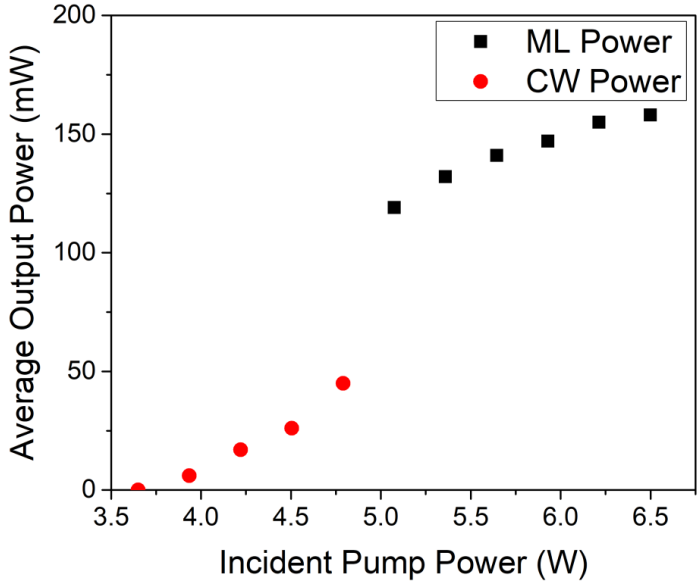

Figure 61. The input-output characteristic of the SESAM mode-locked diode-pumped Ti:sapphire laser operating at 822 nm, showing average output power vs pump power incident upon the crystal.

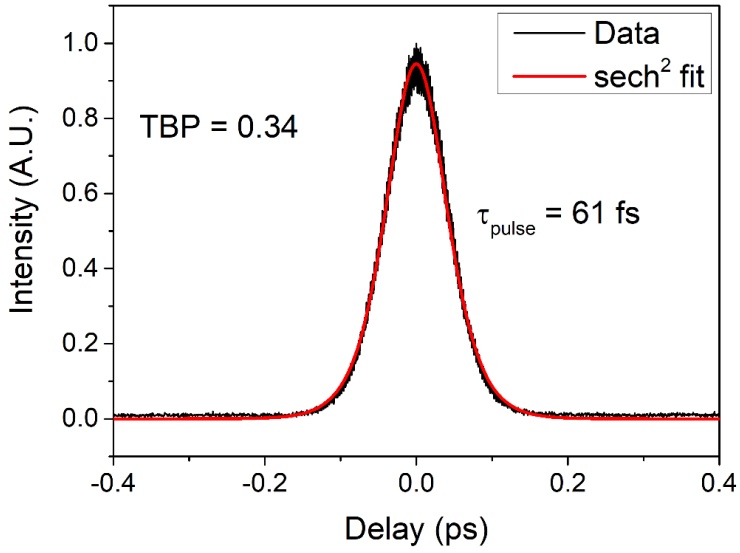

Figure 62. Intensity autocorrelation of the KLM Ti:sapphire laser producing 61 fs pulses with an average output power of 158 mW.

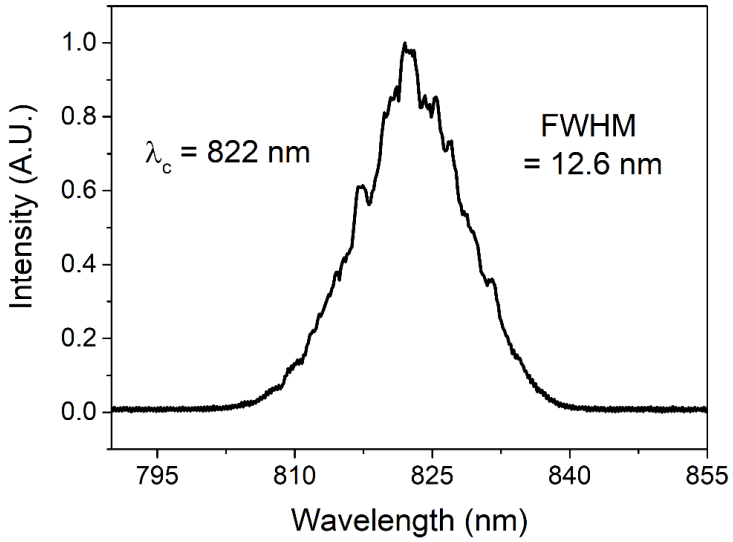

Figure 63. Optical spectrum of the KLM Ti:sapphire laser producing 61 fs pulses with an average output power of 158 mW.

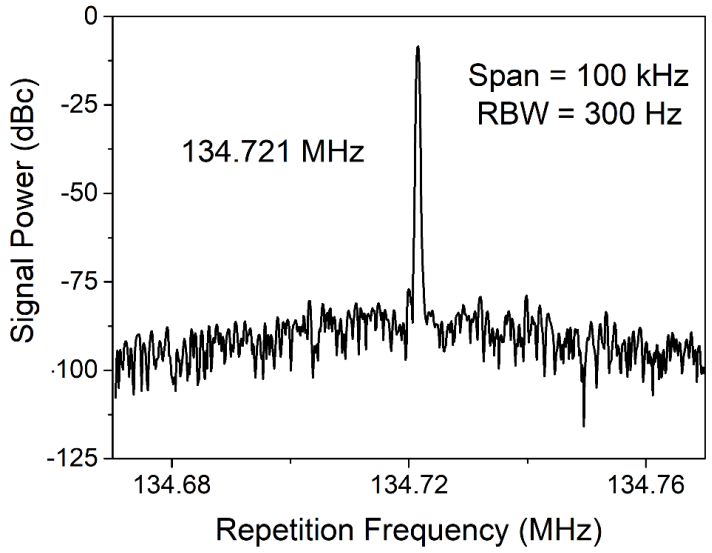

Figure 64. Radio frequency spectrum of the KLM Ti:sapphire laser producing 61 fs pulses with an average output power of 158 mW, recorded with 100 kHz frequency span and 300 Hz resolution bandwidth.

A shorter pulse duration of 40 fs was obtained (see Figure 65) by increasing the second prism insertion by around 1-2 mm. A 31 nm FWHM spectral bandwidth (see Figure 66) was recorded resulting in a TBP of 0.56. In this configuration the average output power was slightly reduced to 94 mW during stable mode-locked operation.

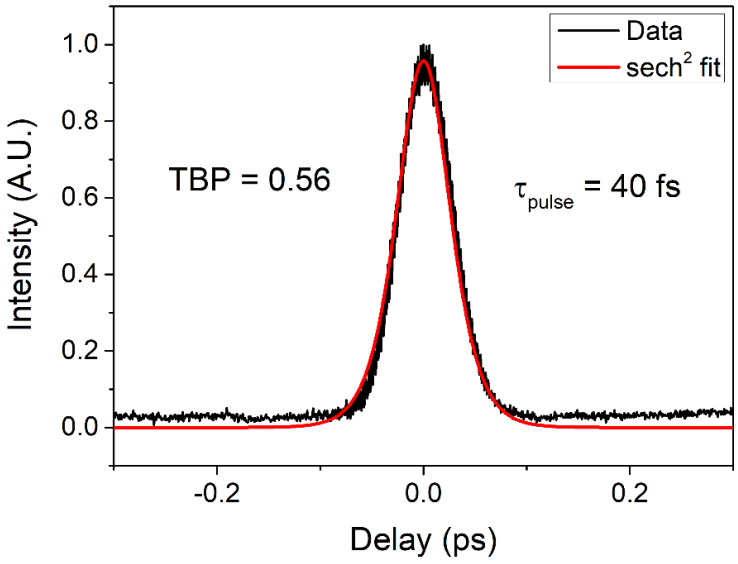

Figure 65. Intensity autocorrelation of the KLM Ti:sapphire laser producing 40 fs pulses with an average output power of 94 mW.

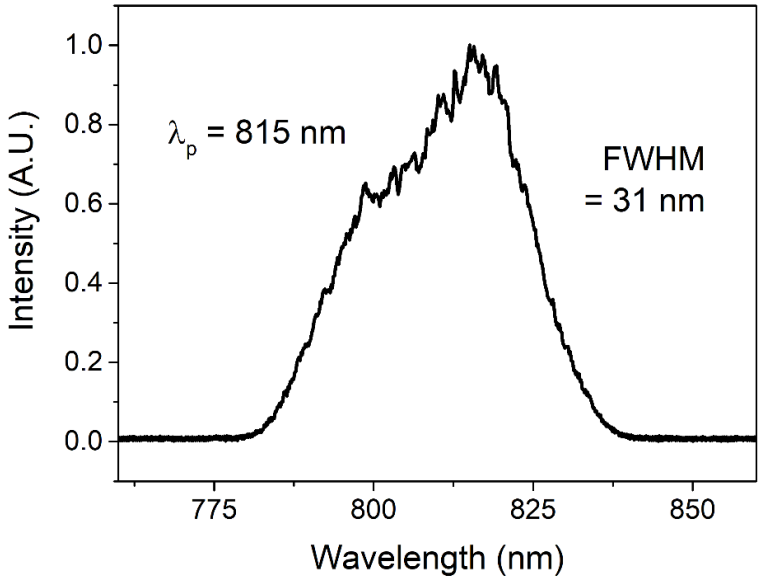

Figure 66. Optical spectrum of the KLM Ti:sapphire laser producing 40 fs pulses with an average output power of 94 mW.

The laser was wavelength tuned in the same manner as the SESAM mode-locked one. In the KLM configuration the maximum tuning range of 120 nm was achieved (755-875 nm) (see Figure 67). Average output power was between 40-140 mW over this range, while the pulse durations ranged from 58 to 174 fs.

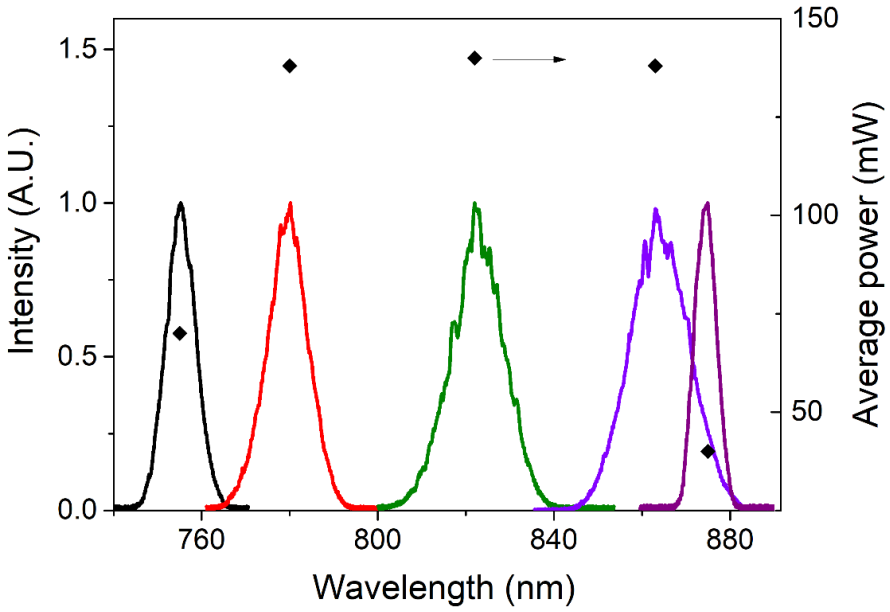

Figure 67. Tuning range and corresponding average output power of KLM Ti:sapphire laser.

Table 20. Comparison of selected results from SESAM ML setup and non-optimised KLM setup.

Setup	SESAM ML	Non-Optimised KLM
Shortest Pulse Duration	62 fs	40 fs
Highest Average Power	433 mW	158 mW
Tuning Range	788 -825 nm (37 nm)	755 -875 nm (120 nm)

A comparison between selected results from the SESAM ML setup and the non-optimised KLM setup is shown in Table 20. By switching from SESAM mode-locked to KLM operation the tuning range was successfully expanded from 37 nm to 120 nm, while maintaining short pulse durations. Even shorter pulses were generated with KLM at 40 fs pulse duration compared to 62 fs duration achieved in the SESAM mode-locked setup. However, the pulses were chirped in this configuration with a TBP of 0.56. The average output power at 158 mW is also substantially less than in the SESAM mode-locked setup with a highest average power of 433 mW. The main reasons for this are that the current KLM setup uses a cavity that is optimised for SESAM mode-locking rather than KLM, and also because a 1% output coupler is used compared to the 5% output coupler in the SESAM mode-locked setup. Various output couplers with transmissions ranging from 1-5% were used in KLM attempts, however only KLM was only possible with the 1% output coupler. This is likely due to the lower intracavity intensity associated with higher transmission output couplers does not provide a strong enough Kerr lens to initiate KLM. It is also possible that the pump mode-cavity mode overlap is poorer at the edge of stability where the KLM laser operates, resulting in lower efficiency and thus output power.

The tightly focused mode waist upon the HR end mirror in the second arm is also a problem, as it makes it difficult to achieve a good discrimination in mode size between the CW mode and mode-locked mode when using a hard aperture. This is what provides the artificial fast saturable absorber mechanism, so it is an important aspect. In order to improve the performance of the KLM diode-pumped Ti:sapphire laser it was decided to optimise the cavity for hard-aperture KLM operation.

3.4.2 Hard-aperture KLM

In order to optimise the diode-pumped Ti:sapphire laser for hard-aperture KLM design guidelines established by Brabec et al. were followed [27]. Based on an analytical treatment and backed up by numerical investigations to check the reliability of the analytical expressions, their analysis was based on the following assumptions:

- Two curved mirrors (or lenses) and two flat end mirrors comprise the resonator, with a Kerr medium placed in the section of the resonator where the cavity mode is tightly focused.
- The only mode oscillating in the resonator is the fundamental Gaussian mode.
- The hard aperture placed at the output coupler only creates small perturbations to the mode profile allowing for a Gaussian-mode analysis. This condition holds as long as the aperture only perturbs the wings of the spatial mode distribution.

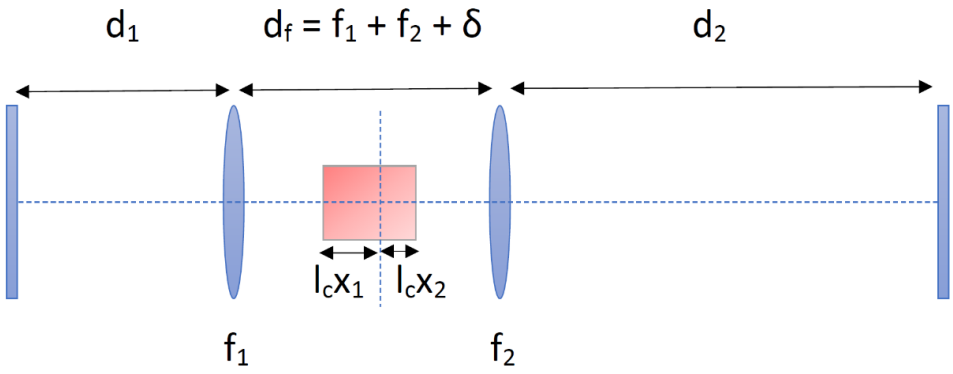

Figure 68. Linear schematic of the cavity used in the following explanation of hard-aperture KLM. The lengths of the short and long arms of the resonator are given by d_1 and d_2 respectively. The parameters f_1 and f_2 represent the focal lengths of the lens equivalent of the curved mirrors. The Kerr medium length is given by l_c. The distances between the focal point and each surface of the Kerr medium are given by $l_c x_1$ and $l_c x_2$ ($x_1 + x_2 = 1$).

The diagram in Figure 68 shows a typical resonator used for KLM laid out in a linear fashion, where the lenses are representative of the curved mirrors normally used in this type of resonator. The lenses have focal lengths of f_1 and f_2, and d_1 and d_2 represent the distances

between the lenses and end mirrors (one high reflector and one partially transmissive output coupler). The distance d_f represents the distance between the two lenses and is given by f_1 + f_2 + δ, where δ is known as the stability parameter and defines the range of stable operation.

Kogelnik et al. showed that resonators containing lenses or similar optical structures (such as curved mirrors) are equivalent to an empty resonator, which consists only of two curved mirrors with radius of curvature $R1$ and $R2$, and separated by a distance t. This is known as an "equivalent resonator", and this possesses the same diffraction losses and mode patterns (except for a scaling factor) as the resonator with internal optical elements [28].

By determining the fundamental eigenmode solution of the equivalent two-mirror resonator (for which standard solutions exist), it is possible to calculate the position of the beam waist in the linear resonator. The radii of curvature of the mirrors of this equivalent two-mirror resonator are given by:

$$R_1 = -\frac{{f_1}^2}{(d_1 - f_1)} \qquad R_2 = -\frac{{f_2}^2}{(d_2 - f_2)} \tag{50}$$

while the length of the equivalent resonator is given by:

$$t = R_1 + R_2 + \delta \tag{51}$$

Where δ is the stability parameter. Providing that $|R_1| < |R_2|$, $d_1 > f_1$ and $d_2 > f_2$, stable operation is possible for two distinct ranges, known as stability zones I and II. The range of operation for stability zone I is given for values of δ where $0 < \delta < -R_2$ and in stability zone II for $-R_1 < \delta < -(R_1 + R_2)$. The resonator mode at the end mirrors by tracing the central beam waist to the end mirrors using ABCD law. In the below figure the beam radii at each end mirror is plotted as a function of δ/δ_{max}, the normalised stability parameter.

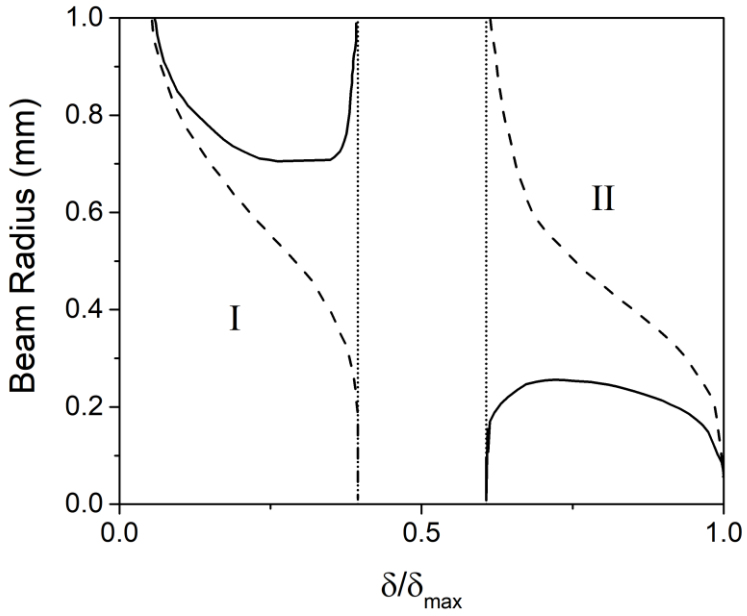

Figure 69. Beam waist radius variation at the end mirror in the short arm (solid line) and at the end mirror in the long arm (dashed line) as a function of the normalised stability parameter δ/δ_{max}. The dotted line on the left denotes the end of stability zone I and the dotted line on the right the beginning of stability zone II. Cavity parameters are $f_1 = f_2 = 60$ mm, $d_1 = 80$ cm and $d_2 = 120$ cm.

In Figure 69 it can be seen that the beam radius at the end mirror in the short arm (solid lines) has a strong dependence on the position in either of the two stability zones. Conversely, the beam radius at the end mirror in the long arm (dashed lines) behaves in a similar way for both stability zones.

However, when a nonlinear Kerr medium is present in the cavity, the parameters of the linear resonator are modified in a way that is dependent on the intracavity intensity. In order to obtain the greatest nonlinear effect, the Kerr medium is placed near the focal plane of the resonator. As a result of the self-similar solution of the propagation equation, the nonlinearity of the Kerr medium changes the confocal parameter of the linear resonator mode by a factor of $1/(1 - P/P_{cr})^{1/2}$, where P/P_{cr} is the ratio of circulating pulse peak power to the critical power for self-focusing [29]. The critical power $P_{cr} = \alpha\lambda^2/8\pi n n_2$ where α is a correction factor, n_2 is the nonlinear refractive index, and n is the refractive index of the medium.

Brabec et al. showed that the parameters of this new nonlinear resonator can be calculated, and that from this the change in the beam radius at the end mirrors can be calculated from the following equation:

$$\Delta\omega_{ci}{}^2 = A\left(1+(-1)^i\left\{\frac{{R_1}^2-{R_2}^2}{(R_1+R_2+2\delta)^2}-\frac{8l\varepsilon}{n\left[1+\left(\frac{l}{2z_{r0}}\right)^2\right]}\frac{1}{R_1+R_2+2\delta}\right\}\right) \quad (52)$$

$$where\ \ A=\frac{P}{P_{cr}}\frac{nR_i}{l\left[1+\left(\frac{2z_{r0}}{l}\right)^2\right]} \quad (53)$$

where ε is the shift of the centre of the nonlinear medium with respect to the position of the beam waist for P = 0 (positive ε denotes a shift of the nonlinear medium towards the short resonator arm). Brabec et al. further showed that a power-dependent change in position and radius of the beam waist in the short resonator arm can be converted into a power-dependent round-trip gain providing a hard aperture is inserted into the resonator short arm. Providing the linear loss L introduced by a hard aperture placed at the end mirror is $L \leq 0.1$, then the absolute change in gain Δg_i is given by [27]:

$$\Delta g_i = L\Delta\omega_{ci}{}^2 \quad (54)$$

where i = 1 denotes the short arm, i = 2 denotes the long arm, and $\Delta\omega_{ci}$ denotes the change in the beam radius at the end mirror of the short or long arm. To better illustrate the effect this has on KLM, the parameter Δg_i is plotted as a function of the normalised stability parameter in Figure 70 using Equations 12 and 14 (data taken from [27]).

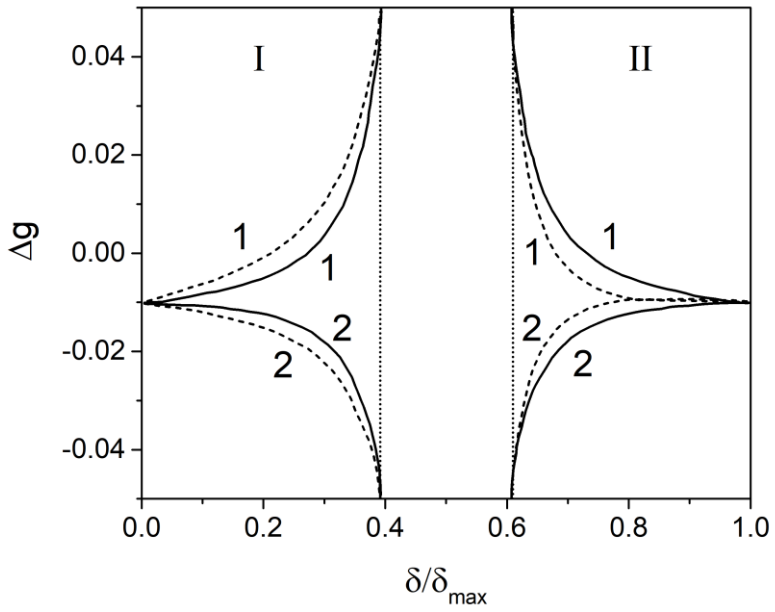

Figure 70. Absolute change in gain Δg vs. the normalised stability parameter δ/δ_{max} (where $\delta_{max} = -(R_1 + R_2)$). Mode-locked operation is possible where Δg > 0. The parameters used to create Fig _ are L = 0.1, $P/P_{cr} = 0.25$, $d_1 = 80$ cm, $d_2 = 120$ cm. The limits of the stability range are denoted by the vertical dotted lines. Curves denoted with 1 represent the results when the aperture is inserted at the end mirror of the short arm. Curves denoted with 2 represent the results when the aperture is inserted at the end mirror of the long arm. The solid curves represent the results obtained when ε = 0. The dashed curves represent the results obtained when ε = 0.25.

As shown in Figure 70, the maximum amplitude modulation is realised at the limits of the stability ranges where $\delta = -R_2$ or $-R_1$. This means that the most efficient operation is realised near the limits of the stability ranges for hard-aperture KLM lasers. Therefore, in order to reach a compromise between stable operation and modulation efficiency, they must be traded off against each other.

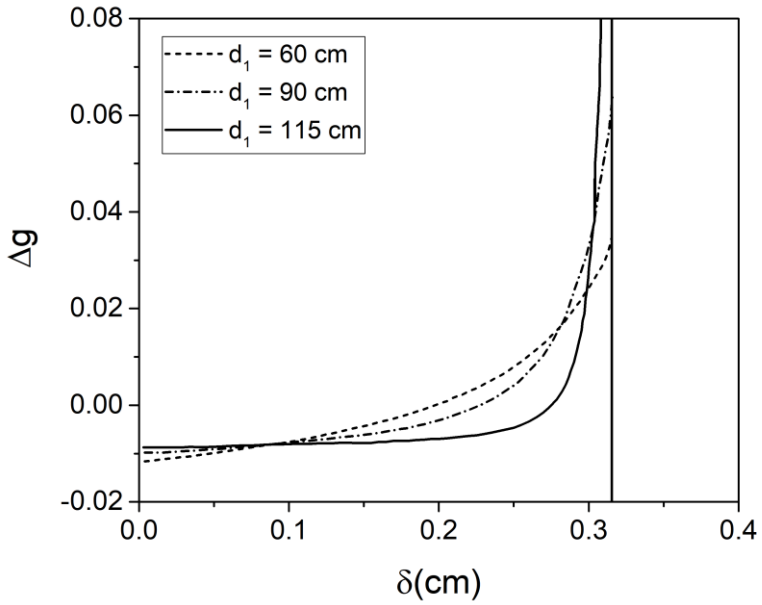

Figure 71. The absolute change in gain Δg vs. stability parameter δ is shown. The parameters used are L = 0.1, P = 0.25, d_2 = 120 cm and d_1 = 60 cm, 90 cm and 115 cm (respectively the dash, dot-dash, and solid line curves). The vertical line represents the edge of stability. Figure adapted from [27].

Also explored is the effect of different ratios of R_1 and R_2 on the mode-locking performance. This is shown in Figure 71. When R_1 and R_2 are set nearly equal, it can be seen that the range for which mode-locked operation can be realised is small and can only be realised close to the stability edge. A high modulation can theoretically be obtained but this is difficult to achieve experimentally. This is due to the strong dependence of the amplitude modulation on δ close to the stability boundary, therefore mode-locked operation is sensitive to small fluctuations in cavity length, which can lead to unstable operation. This means that the ratio of R_1 to R_2 is also a compromise between high modulation efficiency and stable operation. In practical terms a good compromise can be reached if one chooses $2/3 \leq R_1/R_2 \leq 3/4$ [27].

3.4.3 Resonator design and optimisation for Hard Aperture KLM

From the analysis presented by Brabec et al. in [27], the following design and optimisation guidelines are given for the optimisation of hard-aperture KLM systems:

- The folding angles for compensation of astigmatism are given such that $\theta_1 \approx< \theta_2$ where θ_1 is the folding half-angle for the short resonator arm. However, it should also be noted that large disparity between θ_1 and θ_2 leads to an undesirable degradation in the pump mode – cavity mode overlap.

- For $f_1 = f_2$ the ratio of the cavity arms d_1/d_2 should be kept between 2/3 and 3/4 in order that a good compromise between high modulation efficiency and stable mode-locked operation is reached.
- Using the relation z_{r0} (δ = -R_2/2) ≈ l_c/n_2, determine f_1, f_2, d_1, and d_2.
- Place a physical aperture into the Brewster plane close to the end mirror in the short cavity arm.
- Align the cavity such that operates in stability region I.
- Increase the focusing mirror separation until the resonator is close to edge of stability, which can be confirmed by a deformation of the cavity mode. A compromise must be made between high-modulation efficiency and laser stability.
- Translate the Kerr medium towards the shorter arm until a decrease in gain is witnessed.

The resonator design described section 3.4.1 is used as the basis for the optimised hard aperture KLM design. The folding angles are already set equal to each other. The curved mirrors are also already integrated into the system, and as such f_1 and f_2 are already set.

The length of the long arm of the resonator (d_2.) does not have much room to change given that in order to apply enough negative GDD, the prism separation dictates a certain length. The additional DCMs and tuning slit also make the practicality of alterations more complicated. In order to fulfil the second condition where 2/3 < d_1/d_2 < 3/4 then the best course of action is to alter the length of the short resonator arm d_1.

To this end the range of acceptable values for d_1 was calculated if a ratio of between 2/3 and 3/4 is required for d_1/d_2. If the current long arm length d_2 is 768 mm then the short arm length d_1 should be in the range of 512 mm to 576 mm for optimal hard-aperture KLM.

Using LASCAD the resonator design shown in Figure 72 was created. It was decided to keep the short arm as long as possible (thus d_1 = 576 mm) in order to have more flexibility and space for adding additional components, such as the additional hard aperture. Another benefit is that the closer in size the arms are, the larger the range of stability is.

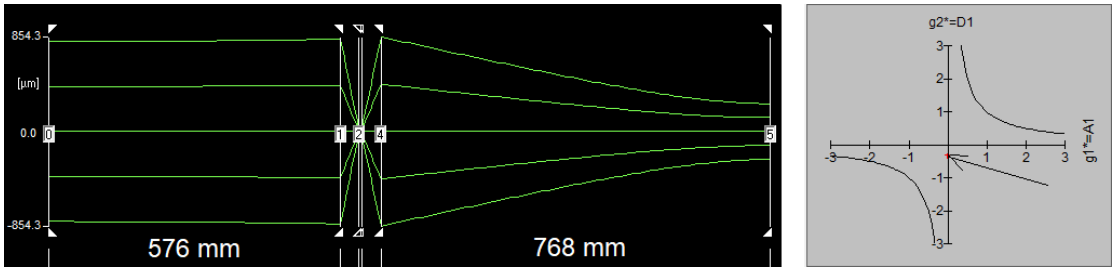

Figure 72. Cavity mode plot and corresponding cavity stability diagram for optimised hard-aperture KLM resonator. The arrows on the stability diagram point to the cavity stability position.

The existing KLM system was then augmented according to the new LASCAD model to create the experimental setup shown in Figure 73.

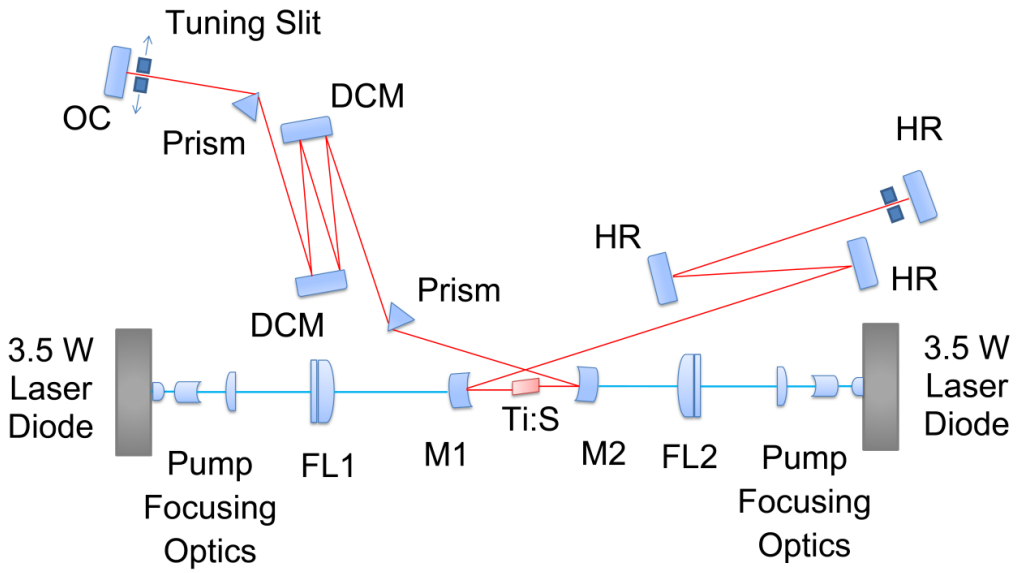

Figure 73. Experimental setup of KLM diode-pumped Ti:sapphire laser after optimisation for hard-aperture KLM.

3.4.4 Hard-aperture KLM results

As shown in Figure 74, the mode-locking threshold was achieved at around 3.4 W of absorbed pump power when the average output power was around 308 mW. Stable mode-locked operation was observed from around 5.4 W to 6.5 W of incident pump power.

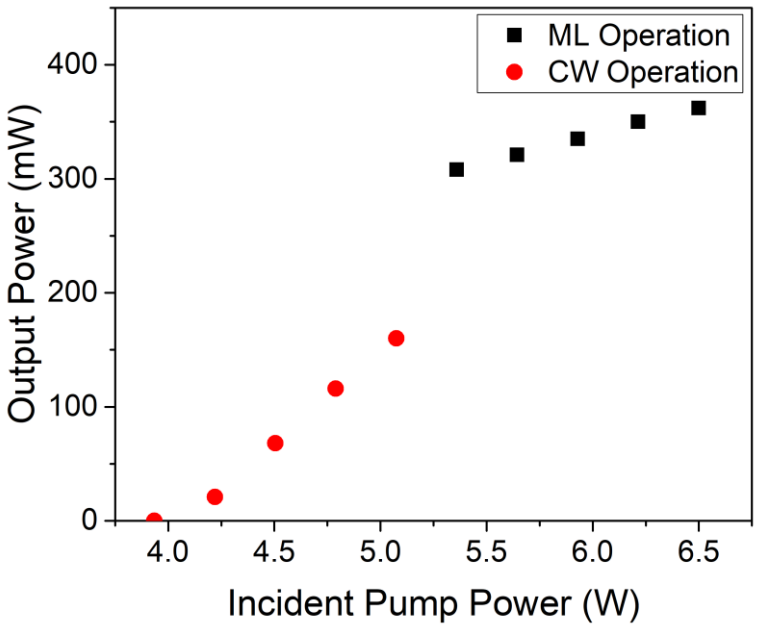

Figure 74. The input-output characteristic of the KLM diode-pumped Ti:sapphire laser operating at 790 nm, showing average output power vs pump power incident upon the crystal.

The highest average output power achieved during KLM operation was 382 mW (from 6.5 W incident pump power) (see Figure 74) resulting in an optical-to-optical efficiency of 5.9%. The generated pulses were measured to be 66 fs in duration (see Figure 75) with the corresponding spectral bandwidth of 10.4 nm at a central wavelength of 790 nm see (Figure 76), resulting in a TBP of 0.33. The RF spectrum shows a pulse repetition frequency of 102.6 MHz (see Figure 77).

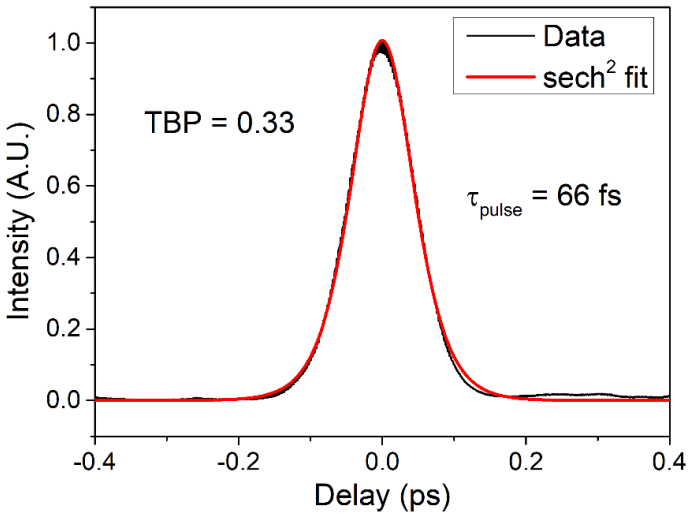

Figure 75. Intensity autocorrelation of the KLM diode-pumped Ti:sapphire laser producing 66 fs pulses with an average output power of 382 mW.

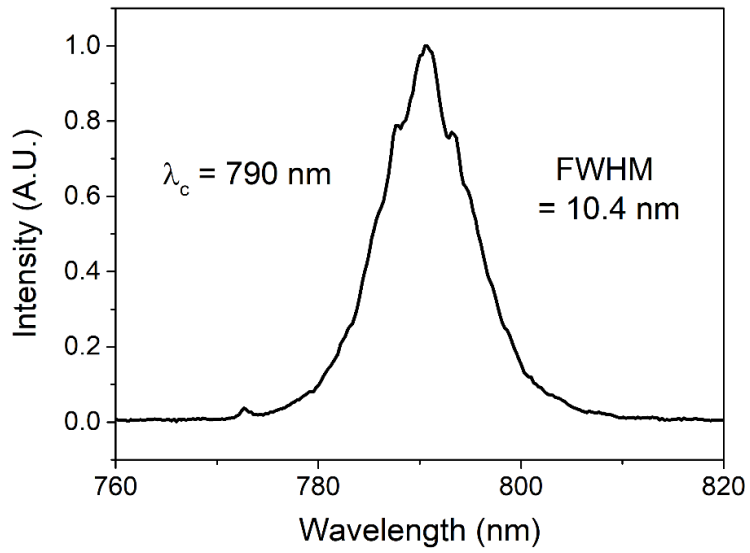

Figure 76. Optical spectrum of the KLM diode-pumped Ti:sapphire laser producing 66 fs pulses with an average output power of 382 mW.

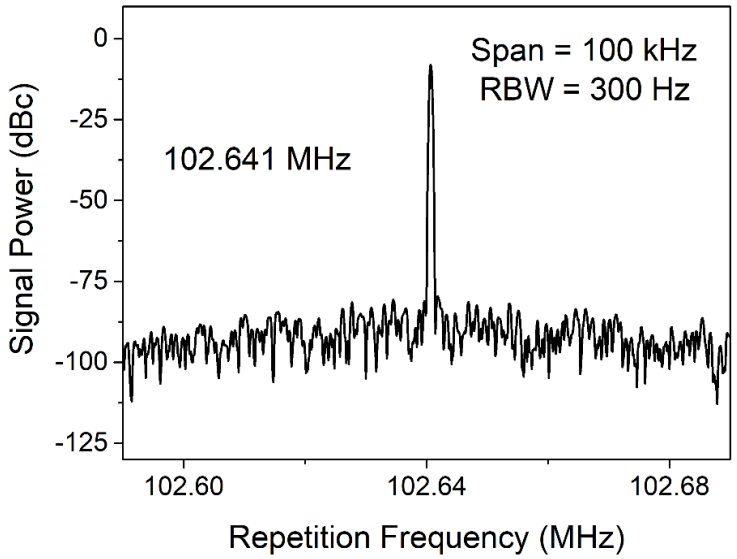

Figure 77. Optical spectrum of the KLM diode-pumped Ti:sapphire laser producing 66 fs pulses with an average output power of 382 mW, recorded with 100 kHz frequency span and 300 Hz resolution bandwidth.

A shorter pulse duration of 54 fs was obtained (see Figure 78) when the laser was tuned to a central wavelength of 810 nm. A 15.7 nm FWHM spectral bandwidth (see Figure 79) was recorded resulting in a TBP of 0.39. Shorter pulses at 40 fs were generated with the unoptimised configuration, however, these were more heavily chirped with a TBP of 0.56. In this configuration the average output power was much improved with 327 mW generated during stable mode-locked operation, compared to 94 mW generated with the shortest pulses

in the unoptimised configuration. This represents an almost 3.5 times increase in average output power.

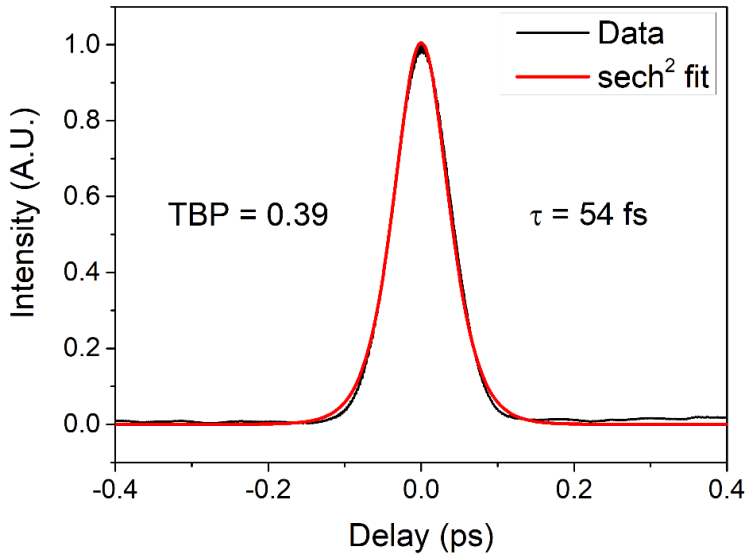

Figure 78. Intensity autocorrelation of the KLM diode-pumped Ti:sapphire laser producing 54 fs pulses with an average output power of 327 mW.

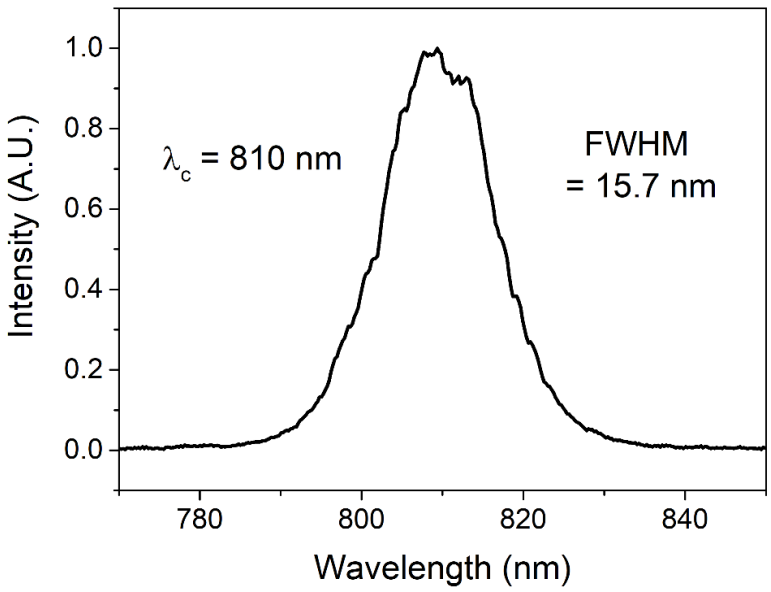

Figure 79. Optical spectrum of the KLM diode-pumped Ti:sapphire laser producing 54 fs pulses with an average output power of 327 mW.

The laser was wavelength tuned in the same manner as the SESAM mode-locked one. In the KLM configuration the maximum tuning range of 120 nm was achieved (755-875 nm) (see Figure 80). Average output power was between 164 and 382 mW over this range with the corresponding pulse durations ranged from 54 to 219 fs.

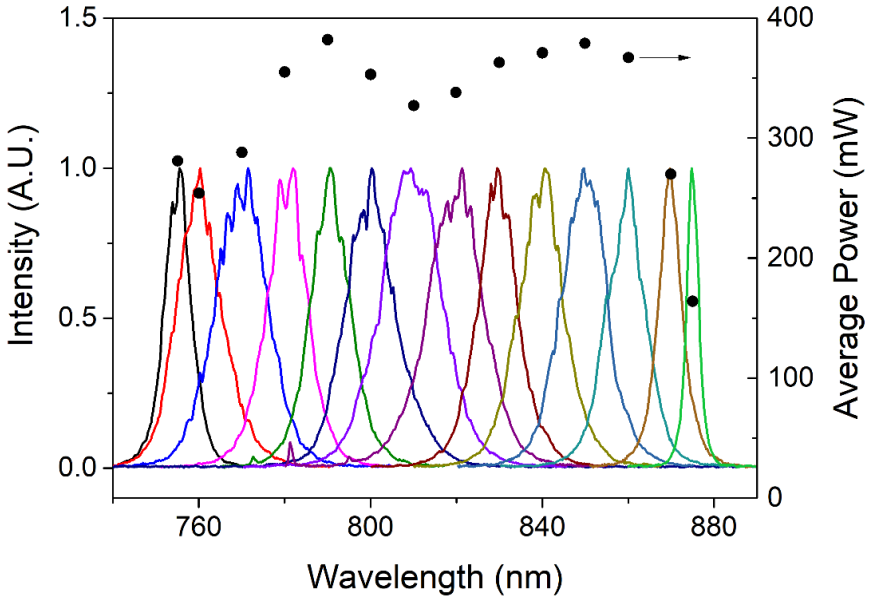

Figure 80. Tuning range and corresponding average output power of KLM diode-pumped Ti:sapphire laser.

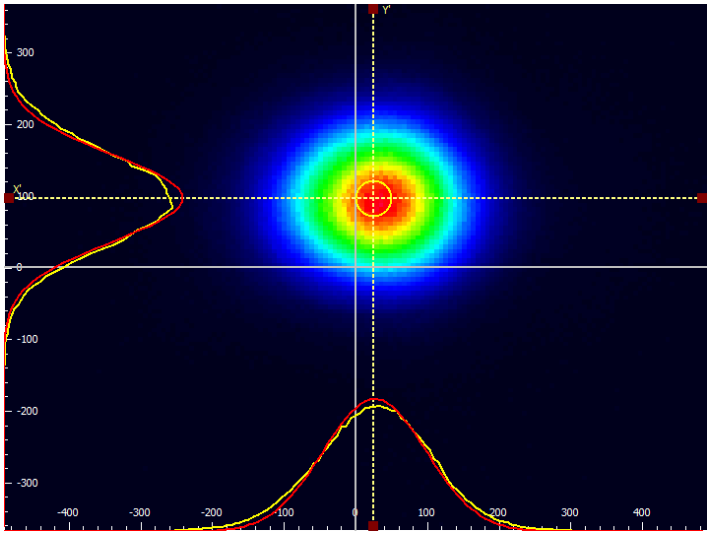

Figure 81. Image of beam waist of KLM diode-pumped Ti:sapphire laser with 382 mW average output power, focused with an f = 100 mm lens.

Beam quality measurements of the KLM diode-pumped Ti:sapphire laser were taken according to ISO 11146-1 guidelines [30], in a similar manner to the pump beam measurements described in section 2.4.3 of Chapter 2. A Thorlabs B-coated achromatic lens with f = 100 mm and designed for use over the 650 to 1050 nm range was used to focus the output beam. As can be seen from Figure 81 the beam profile is circular for the KLM diode-pumped Ti:sapphire laser whilst operating at highest output power, indicating good beam quality. Further analysis and measurement of beam widths and extraction of parameters using

a hyperbolic fit method yielded an M^2 of 1.9 in the x-axis and 1.2 in the y-axis, confirming good beam quality.

3.5 Conclusion

3.5.1 Summary of results

Returning to the table presented at the start of this chapter, the table can now be updated with the ultrafast diode-pumped Ti:sapphire laser results presented in this paper in order to compare and contrast.

Table 21. Reported performance of various ultrafast diode-pumped Ti:sapphire lasers, including results from this work.

Year	Pump power (W)	Pump wavelength (nm)	Mode-locking mechanism	Self-starting	Average output power (mW)	Pulse duration (fs)	Tuning range (nm)	Optical efficiency (%)	Reference
2011	2 × 1	452/454	SESAM	Yes	101	111	-	5.1	[1]
2012	2 × 1	445	KLM	No	34	15	-	1.7	[2]
2013	2 × 2	445	KLM	-	105 70	50 15	-	2.6 1.8	[3]
2014	1 × 1	518	SESAM	Yes	23.5	62	-	2.4	[4]
2015	2 × 1	518/520	SESAM	Yes	44.8	74	-	2.2	[5]
2015	2 × 1 2 × 1.5	520	SESAM KLM KLM	Yes No No	200 350 450	68 39 58	-	10.0 11.7 15.0	[6]
2017	2 × 2.9	450	SESAM SESAM	Yes	350 460	65 82	-	6.0 7.9	[7]
2017	1 × 4	465	KLM	No	173 145	15 13	-	4.3 3.6	[8]
2018	1 × 4.4	461	KLM	No	217 170	24 15	-	4.9 3.9	[9]
2018	1 × 0.88	520	KLM	No	30	95	-	3.4	[10]
2017 - 2018	**2 × 3.5**	**450**	**SESAM KLM KLM**	**Yes No No**	**433 158 382**	**62 40 54**	**37 120 120**	**6.7 2.4 5.9**	[31,32]

As shown in Table 21, a high degree of tunability was successfully demonstrated with the lasers described in this work, the first time this has been demonstrated in an ultrafast diode-pumped Ti:sapphire laser to the best of the author's knowledge. This was achieved while producing pulse durations as short as 40 fs and average powers as high as 433 mW comparable to the current state-of-the-art in ultrafast diode-pumped Ti:sapphire laser technology.

3.5.2 Discussion

In conclusion, this work represents the first time broad wavelength tunability has been demonstrated in an ultrafast diode-pumped Ti:sapphire laser to the best of the author's knowledge. Towards this goal both KLM and SESAM passive mode-locking techniques were investigated.

In the SESAM mode-locked configuration, average output powers as high as 433 mW were produced, along with pulses as short as 62 fs in duration, and a wavelength tunability of 37 nm (788-825 nm). The tunability in this configuration was ultimately limited by the reflectivity bandwidth of the SESAM device itself, which had a reflectivity of 775-840 nm.

In an attempt to further increase the wavelength tunability of the diode-pumped Ti:sapphire laser, the passive mode-locking mechanism used was changed from SESAM mode-locking to KLM. This was because KLM is not limited in bandwidth the same way the SESAM is.

In the first KLM diode-pumped Ti:sapphire laser iteration, a resonator design optimised for SESAM mode-locking was used. This was successful in extending the tuning range to 120 nm (755-875 nm). Using this configuration, the shortest pulses achieved during this project were produced, which were 40 fs in duration. However, the average output power was low with this configuration, with the highest average output power produced being 158 mW.

In order to improve the performance from the KLM diode-pumped Ti:sapphire laser, it was decided to further optimise the resonator design for hard-aperture KLM. After carrying out the necessary resonator modifications, significantly higher average output powers were produced, up to 382 mW. This was thought to be due to the better pump-cavity mode overlap at the edge of cavity stability in the optimised resonator in comparison to the unoptimised resonator. The collimated section in the optimised resonator had a larger cavity mode allowing for more precise use of the hard aperture compared to the focused mode in the unoptimised resonator. Therefore, a better discrimination between the KLM and CW cavity modes was achieved. Mode-locking was also achieved with a higher transmission output coupler in this configuration, most likely due to a stronger Kerr effect, which allowed for a higher average output power. In this configuration a large tuning range of 120 nm (755-875 nm) was maintained. The shortest pulses produced were 54 fs in duration for this configuration.

The degree of tunability demonstrated by the ultrafast diode-pumped Ti:sapphire lasers described in this thesis moves ultrafast diode-pumped Ti:sapphire laser technology an

important step closer to the performance of conventional DPSSL-pumped Ti:sapphire technology and thus a step closer to making more compact, less costly, and less complex ultrafast lasers. Wide wavelength tunability benefits a number of applications, including two-photon microscopy where the wide tunability of conventional Ti:sapphire systems enables the excitation of virtually any marker [33], from short wavelength dyes (Indo) to fluorescent probes (eGFP). Another example of the benefits of wide wavelength tunability are for applications in supercontinuum generation, where the output of a femtosecond laser is spectrally broadened using a highly nonlinear fibre; in order to optimise the parameters of the generated supercontinuum, it is useful to fine tune the central wavelength of the femtosecond laser around the zero-dispersion wavelength of the fibre [34].

3.6 References

1. P. W. Roth, A. J. Maclean, D. Burns, and A. J. Kemp, "Direct diode-laser pumping of a mode-locked Ti : sapphire laser," Opt. Lett. **36**(2), 304–306 (2011).
2. C. G. Durfee, T. Storz, J. Garlick, S. Hill, J. A. Squier, M. Kirchner, G. Taft, K. Shea, H. Kapteyn, M. Murnane, and S. Backus, "Direct diode-pumped Kerr-lens mode-locked Ti : sapphire laser," Opt. Express **20**(13), 1223–1227 (2012).
3. M. D. Young, S. Backus, C. Durfee, and J. Squier, "Multiphoton imaging with a direct-diode pumped femtosecond Ti: Sapphire laser," J. Microsc. **249**(2), 83–86 (2013).
4. S. Sawai, A. Hosaka, K. Hirosawa, and F. Kannari, "A Mode-Locked Ti:sapphire Laser Pumped Directly with a Green Diode Laser," in *CLEO: 2014* (OSA, 2014), p. SM4F.2.
5. H. Tanaka, R. Sawada, R. Kariyama, A. Hosaka, K. Hirosawa, and F. Kannari, "Power scaling of modelocked Ti: Sapphire laser pumped by high power ingan green Laser Diode," Proc. 2015 Eur. Conf. Lasers Electro-Optics - Eur. Quantum Electron. Conf. CLEO/Europe-EQEC 2015 **249**(2), 22702 (2015).
6. K. Gürel, V. J. Wittwer, M. Hoffmann, C. J. Saraceno, S. Hakobyan, B. Resan, A. Rohrbacher, K. Weingarten, S. Schilt, and T. Südmeyer, "Green-diode-pumped femtosecond Ti:Sapphire laser with up to 450 mW average power," Opt. Express **23**(23), 30043 (2015).
7. A. Rohrbacher, O. E. Olarte, V. Villamaina, P. Loza-Alvarez, and B. Resan, "Multiphoton imaging with blue-diode-pumped SESAM-modelocked Ti:sapphire oscillator generating 5 nJ 82 fs pulses," Opt. Express **25**(9), 10677 (2017).
8. S. Backus, M. Kirchner, C. Durfee, M. Murnane, and H. Kapteyn, "Direct diode-pumped Kerr Lens 13 fs Ti:sapphire ultrafast oscillator using a single blue laser diode," Opt. Express **25**(11), 12469 (2017).
9. D. A. Kopylov, M. N. Esaulkov, I. I. Kuritsyn, A. O. Mavritskiy, B. E. Perminov, A. V. Konyashchenko, T. V. Murzina, and A. I. Maydykovskiy, "Kerr-lens mode-locked Ti:Sapphire laser pumped by a single laser diode," Laser Phys. Lett. **15**(4), (2018).
10. A. Muti, A. Kocabas, and A. Sennaroglu, "5-nJ Femtosecond Ti3+:sapphire laser pumped with a single 1 W green diode," Laser Phys. Lett. **15**(5), 1–6 (2018).
11. H. Liu, G. Wang, K. Yang, R. Kang, W. Tian, D. Zhang, L. Guo, J. Zhu, and Z. Wei, "Sub-10 fs Pulse Generation from a Blue-Diode-Pumped Kerr-Lens Mode-Locked Ti:Sapphire Laser," 2019 Conf. Lasers Electro-Optics, CLEO 2019 - Proc. 41–42 (2019).
12. U. Keller, K. J. Weingarten, F. X. Kärtner, D. Kopf, B. Braun, I. D. Jung, R. Fluck, C. Hönninger, N. Matuschek, and J. Aus Der Au, "Semiconductor saturable absorber mirrors (SESAM's) for femtosecond to nanosecond pulse generation in solid-state lasers," IEEE J. Sel. Top. Quantum Electron. **2**(3), 435–451 (1996).
13. I. D. Jung, R. Fluck, G. Zhang, F. X. Kartner, and U. Keller, "Broadband saturable absorber for 10-fs pulse generation," Conf. Proc. - Lasers Electro-Optics Soc. Annu. Meet. **21**(10), 26–27 (1996).
14. H. A. Haus, "Parameter Ranges for CW Passive Mode Locking," IEEE J. Quantum Electron. **12**(3), 169–176 (1976).

15. F. X. Kärtner, L. R. Brovelli, D. Kopf, M. Kamp, I. G. Calasso, and U. Keller, "Control of solid state laser dynamics by semiconductor devices," Opt. Eng. **34**(7), 2024–2036 (1995).
16. F. X. Kärtner, I. D. Jung, and U. Keller, "Soliton mode-locking with saturable absorbers," IEEE J. Sel. Top. Quantum Electron. **2**(3), 540–556 (1996).
17. D. Kopf, F. X. Kärtner, K. J. Weingarten, and U. Keller, "Pulse shortening in a Nd:glass laser by gain reshaping and soliton formation," Opt. Lett. **19**(24), 2146 (1994).
18. C. Hönninger, R. Paschotta, F. Morier-Genoud, M. Moser, and U. Keller, "Q-switching stability limits of continuous-wave passive mode locking," J. Opt. Soc. Am. B **16**(1), 46 (1999).
19. U. Keller, "Ultrafast Solid State Lasers," Book (2007).
20. I. D. Jung, F. X. Kärtner, L. R. Brovelli, M. Kamp, and U. Keller, "Experimental verification of soliton mode locking using only a slow saturable absorber," Opt. Lett. **20**(18), 1892 (1995).
21. A. A. Lagatsky, *Private Communication* (2016).
22. F. X. Kärtner, J. Aus Der Au, and U. Keller, "Mode-locking with slow and fast saturable absorbers - What's the difference?," IEEE J. Sel. Top. Quantum Electron. **4**(2), 159–168 (1998).
23. R. Paschotta and U. Keller, "Passive mode locking with slow saturable absorbers," Appl. Phys. B Lasers Opt. **73**(7), 653–662 (2001).
24. S. M. J. Kelly, "Characteristic sideband instability of periodically amplified average soliton," Electron. Lett. **28**(8), 806–807 (1992).
25. R. Paschotta, "Kelly sidebands," https://www.rp-photonics.com/kelly_sidebands.html.
26. U. Morgner, F. X. Kartner, S. H. Cho, E. Chen, H. A. Haus, J. G. Fujimoto, E. P. Ippen, V. Scheuer, G. Angelow, and T. Tschudi, "Sub-two-cycle pulses from a Kerr-lens mode-locked Ti : sapphire laser (vol 24, pg 411, 1999)," Opt. Lett. **24**(13), 920 (1999).
27. T. Brabec, P. F. Curley, C. Spielmann, E. Wintner, and A. J. Schmidt, "Hard-aperture Kerr-lens mode locking," **10**(6), 1029–1034 (1993).
28. H. Kogelnik, "Imaging of Optical Modes — Resonators with Internal Lenses," Bell Syst. Tech. J. **44**(3), 455–494 (1965).
29. W. Koechner, *Solid-State Laser Engineering - 6th Edition* (2014).
30. International Organization for Standardization, "ISO 11146-1," **1**(15), 16 (2005).
31. J. C. E. Coyle, A. J. Kemp, J.-M. Hopkins, and A. A. Lagatsky, "A Broadly Tunable Ultrafast Diode-Pumped Ti:sapphire Laser," in *Laser Congress 2017 (ASSL, LAC)* (OSA, 2017), **Part F75-A**, p. JTh2A.21.
32. J. C. E. Coyle, A. J. Kemp, J.-M. Hopkins, and A. A. Lagatsky, "Ultrafast diode-pumped Ti:sapphire laser with broad tunability," Opt. Express **26**(6), 6826 (2018).
33. K. Koenig, "Multiphoton microscopy in life sciences," J. Microsc. **200**(2), 83–104 (2000).
34. K. P. Hansen, J. R. Jensen, D. Birkedal, J. M. Hvam, and A. Bjarklev, "Pumping wavelength dependence of super continuum generation in photonic crystal fibers," in *Optical Fiber Communication Conference and Exhibit* (Opt Soc. America, 2002), (3), pp. 622–624.

Chapter 4: Towards ultrafast diode-pumped Ti:sapphire lasers at GHz repetition rates 128

Chapter 4: Towards ultrafast diode-pumped Ti:sapphire lasers at GHz repetition rates

4.1 Background

Before looking into the details of ultrafast lasers with GHz repetition rate, it is beneficial to understand the motivations as to why it would be desirable to construct a GHz repetition laser instead of a conventional ultrafast laser in the 100 MHz range. To do this it is necessary to look at the potential applications to understand why a GHz repetition rate is preferable to repetition rate in the MHz range. Over the next sub-sections, a few selected applications will be explored for which GHz repetition rate ultrafast lasers have been shown to be promising or offer certain advantages over their counterparts in the 100 MHz repetition rate range.

4.1.1 Femtosecond laser-based optical frequency combs

One of the most attractive applications for ultrafast lasers is the role they can play in generating femtosecond-laser based optical frequency combs. Ultrafast lasers with GHz repetition rate are particularly attractive for frequency comb generation, as they enable a comb with better resolution and higher power per mode (further discussed later in this section). Frequency combs have been a hot topic in research since half of the Nobel Prize in Physics was awarded to John L. Hall and Theodor W. Hänsch in 2005 for their pioneering contributions to the development of the optical frequency comb technique [1].

The first efforts towards realising broadband frequency combs were based on the use of a strongly-driven electro-optic modulator and single-frequency lasers [2–4], where the modulator would create dozens of sidebands. This was further developed when it was discovered that placing the modulator within a resonant cavity and minimising intracavity dispersion improved the efficiency, thus creating more sidebands [5].

It was soon realised that these devices were becoming increasingly similar to ultrafast mode-locked lasers. Soon after it was realised that these ultrafast lasers were ideal for producing very broadband frequency combs, particularly those with a pulse duration in the femtosecond regime [6]. If the optical spectrum of an ultrafast laser is viewed in the frequency domain, it can be seen to consist of a number of individual frequency components represented by a series of delta functions with frequency equivalent to:

$$f_n = f_0 + f_{rep} n \tag{55}$$

where n is an integer, f_0 is the carrier offset frequency and f_{rep} is the comb tooth spacing, which is equivalent to the pulse repetition frequency of the mode-locked laser. If the frequencies of this comb are known, then it can be used as a kind of "optical ruler" and can be used to determine an unknown frequency by measuring beat notes that are simply the difference in frequency between the comb frequencies and the unknown frequency.

An important application of the frequency comb is its use in optical clocks. An optical clock is one that is derived from an optical frequency standard, which is a reference based on an optical transition in certain atoms or ions that are optically trapped and laser-cooled to prevent Doppler broadening [7]. A frequency-stabilised laser can then be used to probe the transition frequency, which can then be related to an easily measurable microwave frequency via an "optical clockwork" [8]. In the past these optical clockworks were based on frequency chains, which were very complicated, expensive, and difficult to operate [9]. Frequency combs offer a far simpler and cheaper option.

Time and frequency standards are critical to a wide range of scientific advances and technology, with improvements to atomic clocks vital in establishing important technologies such as GPS and the Internet. Optical clocks offer the potential for even higher accuracy and stability than the best atomic clocks, and thus have the potential to enable many applications [10].

As many conventional femtosecond mode-locked lasers such as those based on Ti:sapphire have repetition rates around the 100 MHz mark, it useful to look at the benefits of GHz repetition rate lasers in comparison to these. These benefits include an increased power-per-mode and a larger mode-spacing, which will be discussed in the few paragraphs. As the mode-spacing between the individual components of a frequency comb is given by the repetition rate, it follows that a 1 GHz comb will have 10 times fewer modes than a 100 MHz comb with the same total span (illustrated in Figure 82).

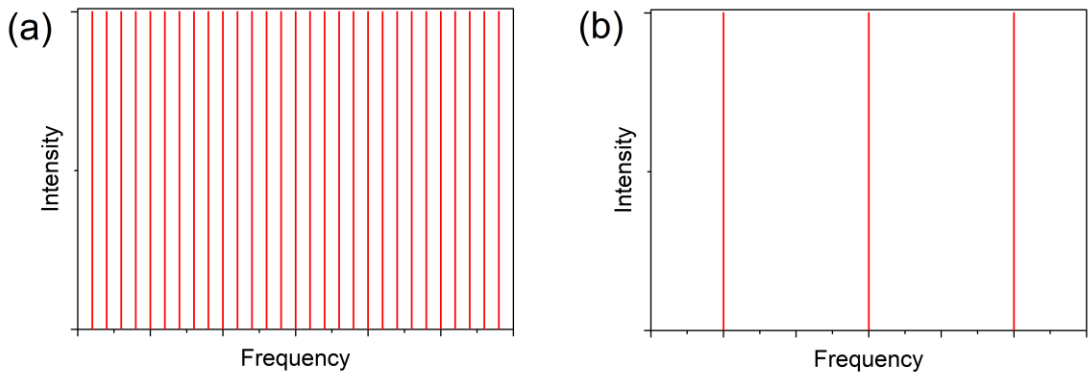

Figure 82. The difference in number of modes over the same frequency span of (a) a 100 MHz comb compared to (b) a 1 GHz comb.

A common use for a frequency comb is the identification of an unknown laser frequency. This is generally done by performing a beat measurement with the unknown laser frequency and one of the frequency comb's modes and analysing the beat frequency using a spectrometer. When an off-the-shelf spectrometer is used with a frequency comb with 100 MHz mode spacing, there will be some ambiguity as to which mode or comb tooth is actually beating against the unknown laser frequency due to the limited resolution of the spectrometer. This means that a more complex and expensive wavemeter is required. However, if a frequency comb with a mode spacing of 1 GHz is used, then the individual modes can be clearly identified. This is advantageous as it negates the need for a specialised and potentially expensive wavemeter.

Continuing the example of the 1 GHz frequency comb compared to 100 MHz frequency comb with the same optical spectrum span, then the 1 GHz comb will comprise of 10 times fewer individual modes than 100 MHz comb. If both combs have the same average power, then it follows that the individual average power-per-mode will be 10 times higher for the 1 GHz repetition rate. This enhanced power-per-mode means that there will be a higher signal-to-noise ratio, which is advantageous for measurements in direct comb spectroscopy [11].

For frequency comb applications it is often a requirement that the spectrum of the femtosecond mode-locked laser is broadened, using a highly nonlinear fibre, to at least one octave via supercontinuum generation. A key issue with these fibres is that once the input pulse energy reaches a certain threshold, nonlinear noise amplification grows rapidly causing large excess noise on the output, essentially making the output light useless. This threshold is typically around 300 pJ [12]. The average power of a laser is related to the pulse energy and repetition rate through:

$$P_{av} = \frac{E_p}{f_{rep}} \tag{56}$$

For a 100 MHz repetition rate laser with a pulse energy (E_p) of 300 pJ, the average power (P_{av}) will be 30 mW. However, for a 1 GHz laser with pulse energy of 300 pJ, the average power will be 300 mW. This means that 10 times more average power can be launched into the highly nonlinear fibre when using a 1 GHz laser used compared to a 100 MHz laser. If the power per mode is already 10 times higher, and 10 times more power can be launched into the nonlinear fibre, then up to 100 times more power per mode is achievable with the 1 GHz laser compared to a 100 MHz laser, meaning that a much higher signal to noise ratio is possible from a broadened frequency comb when using a 1 GHz laser.

Other applications where GHz frequency combs are used are the calibration of astronomical spectrographs, where the use of a GHz frequency comb has been shown to offer a 2-fold improvement to wavelength uncertainty compared the use of conventional Th-Ar lamps alone [13]. Spectroscopy is another application, where the ability to directly resolve individual comb modes permits spectroscopy to be carried out with an individual comb mode [14].

4.1.2 Multiphoton imaging

Femtosecond pulse duration Ti:sapphire lasers are ideal sources for in vitro and in vivo multiphoton microscopy of biological tissue [15], given the optical window in the near-infrared region of the spectrum where biological tissue absorbs the least amount of light [16].

The typical Ti:sapphire laser source used for multiphoton microscopy has an output pulse duration between 70-170 fs, and a pulse repetition rate in the megahertz range [17]. However, it has been shown that Ti:sapphire laser sources with a repetition rate in the gigahertz range have certain advantages [18]. The higher repetition rate allows for a higher number of pulses compared to a megahertz range source with the same peak intensity, which allows for a higher multiphoton signal intensity without increasing photon-induced damage. By the same token, it allows for the peak intensity to be reduced while maintaining the same multiphoton signal level, meaning that the likelihood for photodamage effects is reduced without compromising on the multiphoton imaging quality.

4.1.3 Second-harmonic generation imaging

Second harmonic generation (SHG) is well-established as a powerful contrast mechanism in microscopy. It has been used in a number of areas including materials science [19,20], biological research [21] and medical applications [22].

Similar to multiphoton microscopy, SHG microscopy provides good axial resolution due to the quadratic dependence on illumination intensity. No exogenous (i.e. having external origin) markers are required for SHG microscopy, eliminating the need for complex and invasive labelling procedures that are common for fluorescence-based techniques.

To obtain efficient SHG a high peak power is needed, making femtosecond laser systems ideal light sources for this purpose. The broad bandwidth of fs-pulses has the potential to make it difficult to phase-match all spectral components, however, in practical terms the condition for phase-matching is not critical for SHG interactions over the length scale commonly used in microscopy (on the order of 20 µm) [23]. Often the fs-pulses are focused through a high NA microscope objective, creating a high intensity at the biological sample. This comes with the risk that the high intensity could possibly result in permanent damage to the sample. The loss of cell viability has been demonstrated to occur at an average power of 7 mW with a 150 fs pulse, 80 MHz system, corresponding to a peak power of 0.56 kW, a peak intensity of 0.86 TW/cm^2 and a pulse energy of 0.1 nJ [24].

Generally, there is a trade-off between a high SHG average intensity and undesirable nonlinear photodamage. However, this can be best balanced by increasing the laser repetition rate [24]. Specifically, if the peak power and pulse energy in each pulse is kept constant, increasing the laser repetition rate will linearly increase the mean power of the emitted SHG. This means that with a GHz laser a higher SHG signal can be obtained for the same peak intensity and pulse energy, thus both can be kept well below the photodamage threshold.

Another advantage in favour of GHz repetition rate lasers in SHG microscopy is pixel dwelling time. This must be long enough such that the detector can collect sufficient photons. A higher repetition rate and thus a higher SHG signal intensity, means that the pixel dwelling time can be reduced and therefore the acquisition time per frame can be reduced.

4.2 Review of ultrafast GHz-repetition rate solid state lasers

In the previous sections the benefits of GHz-repetition rate ultrafast lasers compared to their MHz repetition rate counterparts were established for certain applications. Presented now is a review of various reported ultrafast lasers with GHz repetition rate, looking mainly at bulk solid-state lasers based on Ti:sapphire and various Yb gain media. Also briefly looked at are other bulk solid-state gain media, fibre lasers, and VECSELs/MIXSELs.

4.2.1 Ti:sapphire

Table 22. Table of ultrafast Ti:sapphire lasers with >1GHz repetition rate reported in literature.

Year	Diode-Pumped?	Repetition Rate	Cavity Configuration	Average Output Power	Pulse Duration	Mode-locking Method	Reference
1996	No	1.039 GHz	Z-fold	520 mW	210 ps	KLM	[25]
2002	No	1 GHz	Bow-tie, ring	1.2 W	12 fs	KLM	[26]
2006	No	1 GHz	Bow-tie, ring	890 mW	-	KLM	[27]
2007	No	1 GHz	Bow-tie, ring	500 mW	5.6 fs	KLM	[28]
2009	No	1.1 GHz	Bow-tie, ring	30 mW	9.5 fs	KLM	[29]
2006	No	1.35 GHz	Bow-tie, ring	900 mW	-	KLM	[30]
2011	No	1.77 GHz	Z-fold	400 mW	8 ps	QD SESAM	[31]
1999	No	2 GHz	Double bow-tie, ring	300 mW	23 fs	KLM	[32]
2008	No	2.12 GHz	Bow-tie, ring	950 mW	5.9 fs	KLM	[33]
2008	No	2.166 GHz	Bow-tie, ring	750 mW	-	KLM	[34]
2003	No	2.3 GHz	Z-fold	10 mW	240 fs	SESAM	[35]
2013	No	4.3 GHz	Bow-tie, ring	750 mW	-	KLM	[36]
2008	No	10 GHz	Bow-tie, ring	650 mW 1.06 W	42 fs 69 fs	KLM	[37]

As shown in Table 22, ultrafast Ti:sapphire lasers have been demonstrated with repetition rates ranging from 1-10 GHz. However, it is important to note that none of these demonstrations have been achieved using diode-pumping, which is much more challenging due to the limited power and lower beam quality of the diode laser pump.

The most common method of mode-locking is through KLM of a bow-tie shaped cavity in a ring configuration. However, GHz-repetition rates have also been reported using Z-fold shaped cavities in a standing wave configuration, using KLM and SESAM mode-locking methods. Average output power ranges from 10 mW to 1.2 W. Pulse duration ranges from 8 ps to as low as 12 fs, although values as low as 5.6 fs have been reported in the GHz-repetition rate range by using extra-cavity dispersion compensation.

4.2.2 Bulk Ytterbium-doped gain media

Table 23. Table of ultrafast lasers based on Yb-doped gain media, with >1GHz repetition rate as reported in literature.

Year	Diode-Pumped?	Gain Medium	Repetition Rate	Cavity Configuration	Average Output Power	Pulse Duration	Mode-locking Method	Reference
2014	Fibre-Coupled Diode	Yb:CALGO	1.8 GHz	Z-shape	2.95 W	59.4 fs	SESAM	[38]
2014	Fibre-Coupled Diode	Yb:CALGO	1.8 GHz	Z-shape	3.5 W	60 fs	SESAM	[39]
2010	DBR tapered diode laser	Yb:KGW	1 GHz	Z-shape	1.1 W	281 fs	SESAM	[40]
2011	DBR tapered diode laser	Yb:KGW	1 GHz	Z-shape	2.2 W 1.1 W	290 fs 100 fs	SESAM	[41]
2012	DBR tapered diode laser	Yb:KGW	4.8 GHz	Dog-leg	1.9 W	396 fs	SESAM	[42]
2013	Fibre-Coupled Diode	Yb:KGW	1.06 GHz	Folded Z-shape	3.4 W	125 fs	SESAM	[43]
2009	Fibre-Coupled Diode	Yb:KYW	1.0138 GHz	Bow-tie, ring	115 mW	200 fs	KLM	[44]
2012	Fibre-Coupled Diode	Yb:KYW	4.6 GHz	Bow-tie, ring	14.6 mW	142 fs	KLM	[45]
2010	Laser Diode	Yb:KYW	2.8 GHz	Linear-hemispherical	680 mW	162 fs	SESAM	[46]
2012	Fibre-Coupled Diode	Yb:KYW	1.024 GHz	Z-fold	770 mW	278 fs	SESAM	[47]
2013	Fibre-Coupled Diode	Yb:LuO	6 GHz	Bow-tie, ring	10 mW	148 fs	KLM	[48]
2015	Fibre-Coupled Diode	Yb:YO	15 GHz	Bow-tie, ring	60 mW	102 fs	KLM	[49]

As shown in Table 23, ultrafast lasers based on Yb-doped gain media have been demonstrated with repetition rates ranging from 1-15 GHz. The most common mode-locking mechanism is through the use of a SESAM, though KLM has also been used. The two most common cavity configurations are the bow-tie ring configuration, also commonly used ultrafast Ti:sapphire lasers to achieve GHz repetition rates, and the "Z-shape" configuration, which will be further discussed in section 4.4. Average output powers from 10 mW up to 3.5 W have demonstrated. Pulse durations range from the a few hundred femtoseconds down to roughly 60 fs.

4.2.3 Other bulk GHz lasers

Gigahertz repetition rates have been demonstrated in other types of ultrafast bulk solid-state lasers, including Cr:LiSAF, Er:Yb:glass and Nd:YVO_4. These will all be briefly discussed in the following sub-sections.

4.2.3.1 Cr:LiSAF

Table 24. Table of ultrafast lasers based on Cr:LiSAF, with >1GHz repetition rate as reported in literature.

Year	Diode-Pumped?	Repetition Rate	Cavity Configuration	Average Output Power	Pulse Duration	Mode-locking Method	Reference
2001	Laser Diode	1 GHz	Z-fold	3 mW	146 fs	SESAM	[50]
2010	Laser Diode	1 GHz	Z-fold	167 mW	103 fs	SBR/SESAM	[51]
2010	Laser Diode	1 GHz	Z-fold	110 mW	55 fs	SBR/SESAM	[52]

The first demonstration of a 1 GHz pulse repetition rate in an ultrafast Cr:LiSAF laser was realised by Kemp et al., where 146 fs transform-limited pulses were produced with an average output power of 3 mW, and a peak power of 20 W. This setup used an asymmetric Z-fold cavity, pumped by four narrow-stripe laser diodes (660 nm or 685 emission wavelength) and mode-locked by a SESAM device.

Pumping with six single-mode laser diodes emitting in the red region of the spectrum, Fujimoto et al. were able to achieve a repetition rate of 1 GHz in an ultrafast diode-pumped Cr:LiSAF laser, mode-locked with an SBR/SESAM device. They generated nearly transform-limited pulses 103 fs in duration at a centre wavelength of 866 nm. The average output power was 167 mW, resulting in 170 pJ pulses and a peak power of 1.45 kW. The same authors subsequently produced a similar system capable of producing pulses as short as 55 fs at a 1 GHz repetition rate, with 110 pJ pulse energy and 1.8 kW peak power.

4.2.3.2 Er:Yb:glass

Table 25. Table of ultrafast lasers based on Er:Yb:glass, with >1GHz repetition rate as reported in literature.

Year	Diode-Pumped?	Repetition Rate	Cavity Configuration	Average Output Power	Pulse Duration	Mode-locking Method	Reference
2002	Laser Diode	10 GHz	Dog-leg	15 mW	3.8 ps	SESAM	[53]
2016	Fibre-Coupled Diode	10 GHz	Dog-leg	10 mW	2.4 ps	QD-SESAM	[54]
2003	Fibre-Coupled Diode	25 GHz	Dog-leg	25 mW	1.9 ps	SESAM	[55]
2003	Fibre-Coupled Diode	40 GHz	Dog-leg	18 mW	4 ps	SESAM	[56]
2004	Fibre-Coupled Diode	50 GHz	Dog-leg	8 mW	1.2 ps	SESAM	[57]
2007	Fibre-Coupled Diode	77 GHz	V-shape	12 mW	3 ps	SESAM	[58]
2008	Fibre-Coupled Diode	101 GHz	V-shape	35 mW	1.6 ps	SESAM	[59]
2009	Fibre-Coupled Diode	101 GHz	V-shape	30 mW	1.1 ps	SESAM	[60]

Repetition rates ranging from 10 to 100 GHz have been demonstrated in ultrafast Er:Yb:glass lasers. Average output powers are limited to a few 10's of mW, while pulse durations range

from 4 ps down to around 1.1 ps. SESAM devices are used to mode-lock these type of lasers, with quantum-well based SESAMs mainly used but also quantum-dot SESAMs. These lasers have applications in fibre-optical communications as the emission wavelength is in 1.5 µm region.

4.2.3.3 Nd:YVO_4

Table 26. Table of ultrafast lasers based on Nd:YVO_4, with >1GHz repetition rate as reported in literature.

Year	Diode-Pumped?	Repetition rate	Cavity configuration	Average output power	Pulse duration	Mode-locking method	Reference
2002	Laser Diode	10 GHz 157 GHz	Linear-hemispherical	2100 mW 110 mW	14 ps 2.7 ps	SESAM	[61]
1999	Laser Diode	12.6 GHz 13 GHz	Linear-hemispherical	198 mW 310 mW	8.3 ps 9.5 ps	SESAM	[62]
2005	Laser Diode	40 GHz	Linear-hemispherical	288 mW	6.5 ps	SESAM	[63]

Repetition rates as high as 160 GHz have been demonstrated in an ultrafast Nd:YVO_4 laser. Pulse durations range from 14 ps down to 2.7 ps, while average output powers as high as 2.1 W have been demonstrated.

4.2.4 Er:fibre and Yb:fibre

Table 27. Table of ultrafast lasers based on Er:fibre and Yb:fibre, with >1GHz repetition rate as reported in literature.

Year	Gain Medium	Repetition Rate	Cavity Configuration	Average Output Power	Pulse Duration	Mode-locking Method	Reference
2009	Yb:fibre	1 GHz	Linear	100 mW	200 fs	SESAM	[64]
2015	Yb:fibre	1 GHz	Ring	600 mW	64 fs	NLPR	[65]
2012	Er:fibre	1 GHz	Linear	10 mW	360 fs	SBR/SESAM	[66]
2012	Yb:fibre	3 GHz	Linear	53 mW	206 fs	SBR/SESAM	[67]
2005	Er:fibre	5.2 GHz	Linear	0.17 mW	680 fs	Carbon nanotube SA	[68]
2012	Er:fibre	9.7 GHz	Linear	1.58 mW	865 fs	Graphene SA	[69]
2011	Er:fibre	4.2 GHz 9.6 GHz 19.5 GHz	Linear	0.63 mW 2.5 mW 6.3 mW	680 fs 940 fs 790 fs	Carbon nanotube SA	[70]

Various saturable absorbers have been used to mode-lock fibre lasers with GHz pulse repetition rate, including SBRs/SESAMs, carbon nanotube saturable absorbers, and graphene saturable absorbers. Average output powers tend to be limited to a few milliwatts but powers up to 100 mW have been demonstrated. Pulse durations direct from the laser oscillators tend to be in the range of a few hundred fs; however, pulses as short as 200 fs have been demonstrated. It should be noted that the above examples are all fundamentally mode-

locked, though GHz repetition rates have also been demonstrated with harmonic mode-locking of ring-cavity fibre lasers [71]. However, this adds cost and complexity to the laser system, as unwanted effects such as pulse-to-pulse jitter and supermode noise [72] needs to be supressed, which can be difficult.

4.2.5 VECSELs and MIXSELs

Many ultrafast VECSELs in the GHz pulse repetition rate operating range have been demonstrated [73–96], the highest up to 50 GHz [93]. The main mode-locking mechanism is SESAM mode-locking. Pulse durations can range from 22 ps [73] down to a few hundred fs [75,78,81], though pulses as short as 107 fs have been reported [83]. Average output power ranges from a few milliwatts [83] up to 5.1 W [89]. Peak powers up to 4.3 kW have been realised [78], as well as pulse energies up to 3 nJ [89].

The higher repetition rates were made possible with the development of quantum-dot SESAMs, which typically have a lower saturation fluence than more conventional quantum-well based SESAMs. The cavity configuration is most often a simple V-type structure, with an output coupler, gain structure and SESAM end mirror.

By incorporating the SESAM into the gain structure, higher repetition rates up to 100 GHz were theorised [97] and subsequently demonstrated [98]. This specific variant of VECSEL is called a MIXSEL (mode-locked integrated external-cavity surface emitting laser). This type of setup routinely allows for repetition rates on the order of 10's of GHz [97–99] , with repetition rates up to 101 GHz being demonstrated [98].

Pulse durations range from 35 ps [100] down to 253 fs [101], while average output power ranges from 40 mW [100] to 6.4 W [102]. Peak power is in the range of 0.36 W [100] to 240 W [101], and pulse energy ranges from a few pJ [98] to 2.56 nJ [102].

4.2.6 Discussion

In terms of the highest repetition rates, VECSELs and MIXSELs generally produce the highest repetition rates due to the very short cavity lengths employed. However, the pulse durations are typically in the picosecond regime, and while the average output power can be several Watts, the peak power is typically limited to a few hundred Watts. However, for applications such as supercontinuum generation and multiphoton imaging, a laser source generating femtosecond pulses with high peak intensity is generally required [103].

Ultrafast fibre lasers with GHz repetition rate are typically limited to around 100 mW of power and pulse durations of a few hundred femtoseconds. It can be difficult to generate GHz repetition rates with fibre lasers, as it is difficult to achieve very short resonator lengths due to the limited gain and pump absorption per unit length of the fibre [104]. To circumvent this, harmonic mode-locking can be used, where multiple ultrashort pulses are circulating in the resonator with a constant temporal spacing [105]. This brings its own problems, for example, possible fluctuating pulse energies and supermode noise [72], which both require sophisticated techniques to remedy. This obviously adds to the complexity and cost of such a system.

Another important advantage of solid-state lasers compared to fibre lasers in the context of frequency comb applications, is the much better noise performance they give due to their high-Q factor cavities. This was demonstrated by Schlit et al., where they constructed and compared the performances of combs based on Er:fibre laser and a bulk solid-state Er:Yb:Glass laser [106]. They were able to show that with the high Q-factor Er:Yb:Glass laser a lower-noise CEO-beat was produced, resulting in a tight phase lock that was much more easily achievable than with an Er:fibre based comb.

As detailed above, GHz repetition rates have been demonstrated in a variety of ultrafast lasers based on bulk solid-state gain media. The highest repetition rates have been achieved with Nd:YVO_4, with up to 157 GHz achieved. However, due to the limited gain bandwidth pulse durations are limited to a few ps in duration. With Er:Yb:Glass repetition rates up to 101 GHz have been demonstrated, however, pulse durations are again limited to around 1 ps and output powers are limited to a few 10's of mW. Repetition rates of 1 GHz have been demonstrated in Cr:LiSAF lasers with pulse durations as low as 55 fs, however, demonstrated output powers are limited to around 167 mW. Yb-doped bulk solid-state gain media offers the most attractive alternative to Ti:sapphire for GHz repetition rate ultrafast lasers, with repetition rates up to 15 GHz in Yb:YO and output powers as high as 3.5 W in Yb:CALGO. Pulse durations have been demonstrated as low as around 60 fs. However, producing pulses shorter than 100 fs is challenging with Yb-doped gain media, while this is fairly easy to do with Ti:sapphire. This is an important requirement for producing coherent supercontinuum for frequency combs.

In addition to the favourable reduction in price of using laser diodes to pump an ultrafast Ti:sapphire laser compared to conventional pumping, there is also the possibility of stabilising the CEO frequency by high-frequency modulation of the pump laser diode drive current, which is an important aspect to realising a stabilised frequency comb. In conventionally-pumped

Ti:sapphire lasers, an acousto-optic modulator is required for stabilisation through pump power modulation which further adds to the cost and complexity. However, when a diode is used as the pump laser, the pump power can be modulated directly through drive current modulation eliminating the need for an acousto-optic modulator.

The first detection and stabilisation of the CEO frequency of an ultrafast diode-pumped Ti:sapphire was demonstrated by Gurel et al. in 2017 , where green (520 nm) pump diodes were used [107]. They further measured the relative intensity noise (RIN) of the green diodes, finding that the performance was comparable with conventional pump lasers used for Ti:sapphire [108].

More recently, Reid et al. characterised and compared the performance of a stabilised ultrafast diode-pumped Ti:sapphire laser frequency comb when pumped with diodes operating in the blue region (462 nm) to diodes operating in the green region (520 nm) [109]. They concluded that while the RIN (relative intensity noise) for both blue and green diodes were low, the blue diodes offered better noise performance.

To summarise, the low-cost and lower-complexity compared to conventional pumping demonstrate that diode-pumping is an attractive option to produce low-cost Ti:sapphire laser-based frequency combs.

4.3 Challenges of GHz repetition rate resonators

Compared to a conventional 100 MHz repetition rate laser, a 1 GHz repetition rate laser will have a 10 times lower pulse energy for the same average power. This lower pulse energy poses different problems depending on the type of mode-locking used.

For SESAM mode-locking, this means that it will be more difficult to fully saturate the SESAM compared to a 100 MHz laser. This can be worked around by using a SESAM with a low saturation fluence or by tighter focusing on the SESAM to produce a smaller beam waist. The SPM experienced by the pulse is also dependent on the pulse energy, and this can also pose problems for SESAM mode-locked lasers, as the soliton mode-locking regime is based on the balance of SPM and negative GDD.

For KLM, the Kerr-lens is dependent on the intensity of the laser pulse. The Kerr-lens in conjunction with a hard aperture is what gives the effective modulation depth, thus for stable mode-locked operation the Kerr-lens needs to be strong enough to provide sufficient modulation depth. Similarly, to the soliton mode-locked regime where SESAM mode-locked lasers operate, SPM is also important to KLM lasers.

There are also the physical challenges inherent with constructing bulk free-space laser cavities for GHz repetition rates. This is because the inverse proportional relationship with the repetition rate and cavity length. The repetition rate of a passively mode-locked laser in a standing wave resonator configuration is given by:

$$f_{rep} = \frac{c}{2L} \tag{57}$$

where c is the speed of light in a vacuum and L is the total resonator length. If we consider what length of the resonator is required for a 100 MHz repetition rate, then from Equation 3 L = 1.5 m is obtained. When this is increased to 1 GHz repetition rate, the required cavity length is only 150 mm. This can make it challenging to physically fit standard optomechanic components in the cavity.

In terms of dispersion compensation, the use of prism pairs is ruled out in most cases as in order to provide sufficient negative dispersion, the required prism separation can be many times longer than the required cavity length. It can also make it difficult to add extra dispersion compensating mirrors to the cavity, and thus cavity mirrors will often have to double up with more than one function; for example, dispersive mirrors that also act as an output coupler. These non-standard multi-functional optics are not usually available off-the-shelf and generally have to be made to order.

The situation is somewhat relaxed for travelling wave resonator configurations, where the repetition rate is given by:

$$f_{rep} = \frac{c}{L} \tag{58}$$

Therefore, for a 1 GHz repetition rate the required resonator length is 300 mm. This is twice the length of the standing wave configuration with the same repetition rate and as such allows for more space to place additional components. However, the shorter resonator lengths can still prove challenging compared to the resonators of conventional repetition rate lasers.

4.4 Common resonator designs for GHz-repetition rate solid-state lasers

Over the next few sub-sections, the most common resonator designs used to achieve GHz repetition rates for ultrafast bulk solid-state lasers will be discussed. These include bow-tie ring cavities, Z-fold cavities and Z-shape cavities.

4.4.1 Bow-tie ring resonator

The most common approach for GHz-repetition rate Ti:sapphire lasers is the bow-tie ring resonator. This usually consists of four mirrors: two curved mirrors and two plane mirrors. At least one of the curved mirrors is usually dichroic, transmitting pump light and highly reflective at the laser wavelength [30,37]. One of the plane mirrors usually functions as an output coupler. Any or all of the mirrors can be chirped for dispersion compensation. Some ring resonators even incorporate an extra set of mirrors for dispersion compensation, forming a six-mirror resonator [32]:

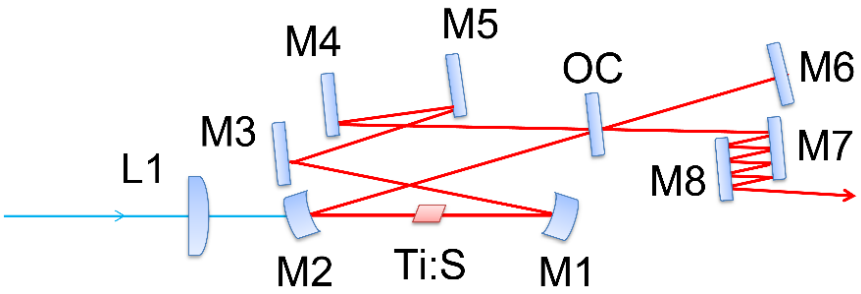

Figure 83. An example of a six-mirror ring resonator with GHz repetition rate, figure based on [32]. M1 and M2 are curved folding mirrors, while M3, M4 and M5 are plane highly reflective chirped mirrors. M6 is used to enforce unidirectional operation by reflecting one of the outputs back on the cavity. M7 and M8 are an external chirped pair of chirped mirrors providing further extracavity dispersion compensation.

Often a wedge [110] or plate [30] of dispersive material is used in order to add positive GDD to the cavity, usually inserted at Brewster angle for minimal losses. This allows for the fine tuning of the net cavity GDD. In the case of the wedge, by increasing the insertion and thus the thickness of material that the cavity beam travels through, the positive GDD introduced by the wedge can be increased [111].

4.4.2 Z-fold resonator

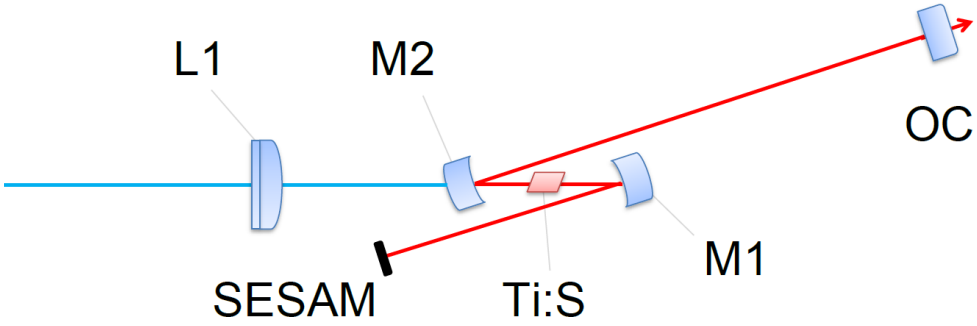

Figure 84. Example of GHz-repetition rate Z-fold resonator laser similar to that shown in [112]. Mirrors M1 and M2 are curved folding mirrors doubling up as chirped mirrors to provide negative GDD, OC is a plane output coupler, L1 is a pump focusing lens. The resonator is configured to operate stability region II producing a beam waist on the SESAM.

Shown in Figure 84, the Z-fold resonator is an approach that is less common than the ring resonator. This is due to the fact that the difficulties inherent with a shorter resonator are magnified when using a standing wave configuration compared to a travelling wave configuration. This is because a standing-wave resonator must be half the length of a travelling-wave resonator to produce the same repetition rate. Generally, a four element resonator is used, consisting of two curved mirrors, an output coupler and either a high reflecting mirror if the mode-locking mechanism is KLM, or a SESAM device if the mode-locking mechanism is SESAM mode-locking.

In the example shown in Figure 84, the resonator is set up such that it operates in stability zone II, which produces a tight beam waist in the short resonator arm on the SESAM end mirror and a collimated beam in the output coupler arm. Again, in most cases most of the mirrors serve more than one function. For example, the curved mirrors are generally dichroic, being highly reflective for the laser wavelength and highly transmissive at pump wavelengths. In the literature, any of the mirrors, excepting the SESAM, have been demonstrated to have dispersive coatings to provide dispersion compensation, though it is worth noting that SESAMs with in-built dispersion compensation have been demonstrated for lasers operating in the MHz range [113]. The dispersive mirrors can be in the form of chirped coatings or GTI-type coatings. Mode-locking has been achieved with both SESAM (quantum dot [31] and quantum well [112] and KLM techniques [25].

4.4.3 Z-shape resonator

A more unusual configuration is the Z-shape resonator, which has been employed in Yb:KGW, Yb:KYW, and Yb:CALGO to realise repetition rates ranging from 1 to 1.8 GHz (see section 4.2.2). It usually consists of 4 mirrors and a plane-cut AR-coated crystal as shown in Figure 85.

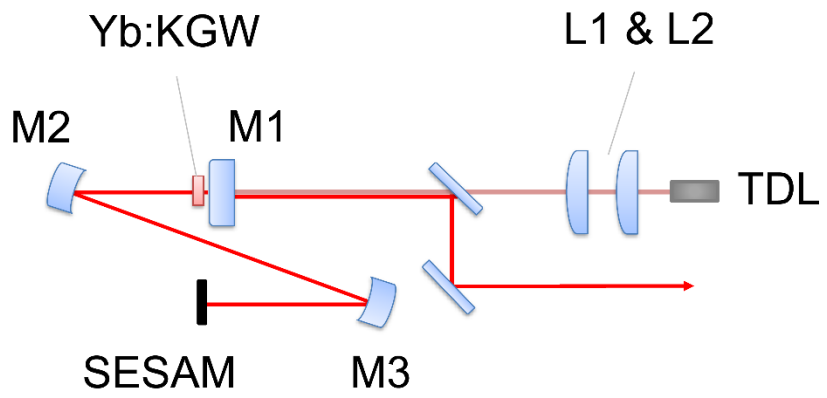

Figure 85. GHz repetition rate laser with Z-shape cavity as described in [41]. TDL – tapered diode laser, L1 & L2 – pump focusing lenses, M1 – output coupler, M2 – curved HR GTI mirror, M3 – curved HR mirror, Yb: KGW – Yb:KGW gain medium, SESAM – SESAM device.

The Z-shape resonator is not to be confused with the Z-fold resonator which is shown in Figure 84. The Z-fold resonator typically consists of two curved mirrors and two plane end mirrors. When operated in stability zone I, the intracavity beam is generally collimated between each end mirror and curved mirror and a tight beam waist is present roughly midway between the two curved mirrors. When the resonator is made to operate in stability zone II, the previously collimated beam of the shorter arm now forms a beam waist on the end mirror.

The Z-shape resonator, shown in Figure 85, is similar in that it also contains two curved mirrors and two plane end mirrors, but differs from the Z-fold resonator in that there are mode waists at each end mirror, with a collimated section between the two curved mirrors. As such, the gain medium is placed close to one of the end mirrors in a Z-shape resonator, rather than between the two curved mirrors in the case of a Z-fold resonator. Double chirped mirrors or GTI-type mirrors are used for dispersion compensation [41]. Often the cavity mirrors have more than one function, such as dispersion compensated mirrors also double up as dichroic mirrors, highly transmissive at pump wavelengths while highly reflective at the laser wavelength. For example, the laser depicted in Figure 85 as demonstrated by Pekarek et al. used a mirror (M1) that functioned as an output coupler for laser wavelengths, while being highly transmissive to pump wavelengths.

A variant of this design is the "Σ-shape" cavity [43], which essentially adds a 5th mirror to the Z-shape cavity. This has the advantage of folding the cavity at the centre, potentially adding more flexibility to the resonator footprint, while allowing for another dispersion compensating mirror.

4.4.4 Summary of resonator design options for GHz-repetition rate

To summarise, each resonator variant has its own advantages and disadvantages. Lasers based on bow-tie ring resonators allow for the highest repetition rates with up to 10 GHz demonstrated in Ti:sapphire lasers [37] and are generally easier to align given the longer resonator lengths. However, they often require an additional component to enforce unidirectional operation and use Kerr-lens mode-locking as the mode-locking mechanism (and the disadvantages inherent with this approach, such as the requirement to operate close to the cavity stability limit).

Lasers based on Z-fold resonators have been demonstrated to use KLM or SESAM ML [25,47]. However, the required short cavity length makes it more difficult to add additional intracavity components, for example for dispersion compensation, and can also make the alignment more difficult.

Lasers based on Z-shape resonators have been demonstrated to use SESAM ML [40]. An advantage to this type of resonator is that it can be configured to produce a beam waist near each end mirror (where the gain medium or SESAM can be placed). This can allow for more flexibility in cavity layout and the ability to add additional components for example, mirrors for dispersion compensation.

4.5 Chosen resonator designs

With respect to resonator design, two options were pursued. The first option was the bow-tie ring resonator. As covered in section 4.4.1, bow-tie ring resonators using KLM as the mode-locking method are well-established in realising GHz repetition rates. The longer resonator lengths involved makes physically fitting together all components that make up the resonator easier, as well as making optimising the alignment easier.

The second option chosen was the Z-shape cavity. This type of resonator has been frequently used for generating GHz repetition in ultrafast Yb-doped lasers (see section 4.4.3). This configuration has two beam waists at either end mirror position, making it easier to physically

fit a gain medium and SESAM in the resonator. Both options will be discussed in the next few sub-sections.

4.5.1 4-mirror ring resonator

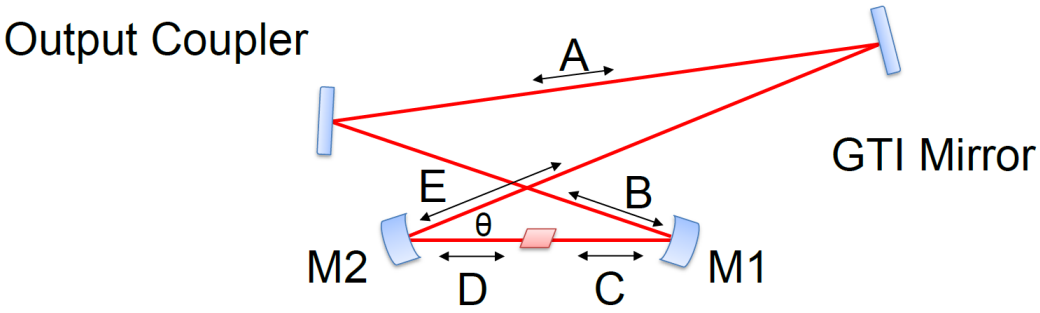

Figure 86. Planned layout of 4-mirror ring resonator.

For the four-mirror ring cavity shown in Figure 86, three pairs of folding mirrors with different ROC were considered for the folding mirrors M1 and M2; 25 mm, 30 mm and 38 mm. Analysis was performed to construct a resonator based on different ROC folding mirrors for M1 and M2, and to predict the highest practicable repetition rate for each resonator while still maintaining a similar resonator mode waist inside the crystal to the CW Ti:sapphire laser described in Chapter 2. This resulted in different separations between each mirror for each resonator configuration (see Figure 86). The results of this analysis are summarised in Table 28. Note that the optical length of the 4.8 mm Ti:sapphire crystal ($n \times L$ = 1.76 × 4.8 = 8.45 mm) is not shown but is included in the total length and subsequent estimated repetition rate calculations. The repetition rate f_{rep} is estimated from the cavity length and is given by Equation 4.

Table 28. Summary of 4-mirror ring resonator potential configurations using different M1 and M2 ROC, and the resultant estimated repetition rate (f_{rep}).

M1 & M2 ROC (mm)	A (mm)	B (mm)	C (mm)	D (mm)	E (mm)	Total (mm)	Estimated f_{rep} (GHz)	Folding angle θ (°)	Crystal waist (μm)	
									X	Y
25	26	24	12.5	14	40	124.95	2.4	14	43	26
30	25	30	15	17	40	135.45	2.21	14	50	30
38	32	35	20	22	50	167.45	1.79	11	59	35

As shown in Table 28, the highest repetition rate possible whilst maintaining a cavity mode waist inside the crystal similar in size to that of the CW Ti:sapphire laser in Chapter 2, is 2.4 GHz while using the 25 mm ROC folding mirrors.

4.5.1.1 4-mirror ring resonator – CW performance

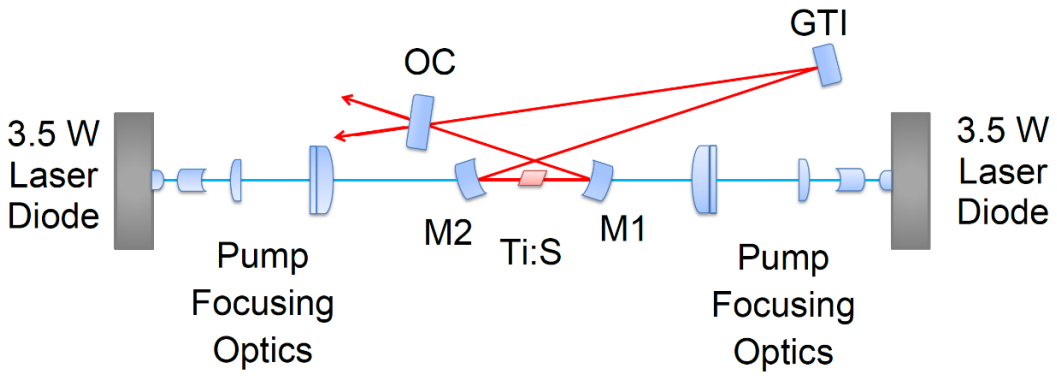

Figure 87. Experimental setup of 4 mirror ring cavity designed to produce >1 GHz pulse repetition rate when mode-locked. OC – output coupler, M1 and M2 – 25 mm ROC folding mirrors, GTI – GTI mirror, Ti:S – 4.8 mm long Brewster-cut Ti:sapphire crystal.

The resonator was set up according to Figure 87 with 25 mm ROC concave folding mirrors. A 1% transmission output coupler was used. A GTI mirror was used in the CW setup in place of a normal HR mirror, as the GTI was also highly-reflecting and would potentially simplify later attempts to achieve mode-locking with KLM. Although up to 2.4 GHz should be possible, it was decided to begin with a repetition rate closer to 1 GHz, as the higher pulse energy would potentially make achieving KLM easier. The configuration settled upon is shown in Figure 88 with a total length of 276 mm and a cavity mode waist of 23 µm × 14 µm.

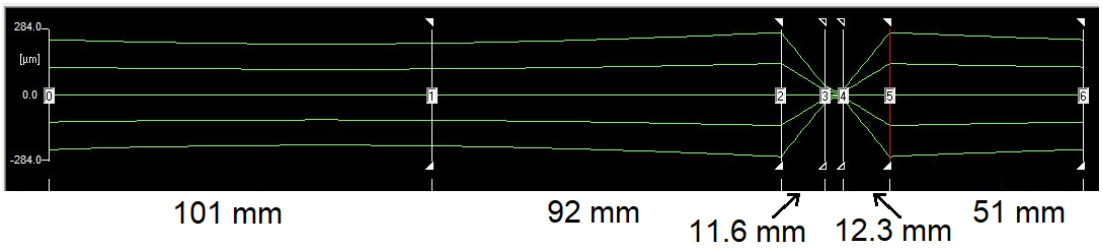

Figure 88. Cavity mode plot for the resonator shown in Figure 87. The arrow on the stability diagram points to the cavity stability position

With the cavity set up according to the LASCAD model shown in Figure 88, lasing was achieved in the CW regime. An output power of 190 mW was achieved from each output in bidirectional operation, with a drive current of 2.3 A to each diode, corresponding to 6 W incident pump power (shown in Figure 89). This is roughly in line with what we would expect given the standing-wave configuration CW Ti:sapphire laser in Chapter 2 produced around 400 mW at this pump power with 1% output coupling.

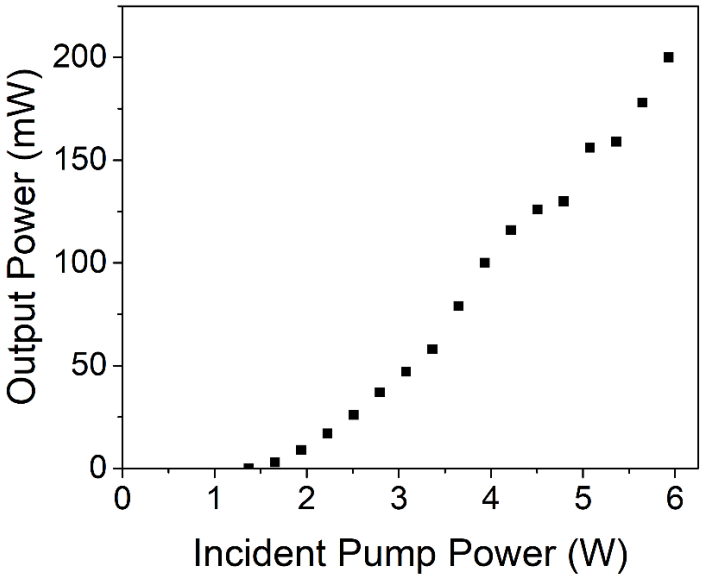

Figure 89. CW performance of four-mirror ring laser

With the laser optimised for maximum output power in the CW regime, the next stage was to attempt Kerr-lens mode-locking.

4.5.1.2 4-mirror ring resonator – Kerr-lens mode-locking

Beginning with the four-mirror ring laser operating in the CW regime, the guidelines for Kerr-lens mode-locking of Ti:sapphire ring lasers, detailed in [26], were followed. This involved first maximising the CW output power. Mirror M1 was then moved towards the crystal to shift the position of cavity stability to the short edge of the cavity stability range where KLM is most likely to occur.

For dispersion compensation a single GTI mirror was used, which provides a negative GDD of -550 fs^2 per bounce. Combined with the positive GDD of the crystal of 278 fs^2, this equates to a net cavity GDD of -272 fs^2.

4.5.1.3 4-mirror ring resonator – Discussion

Unfortunately, KLM was not realised with this setup. This is thought to be due to difficulty in being able to achieve a high enough intracavity pulse energy and thus a strong-enough Kerr effect. The factor $\delta = (1/\omega_0)(\partial\omega_0/\partial P)$, represents a power-dependent modulation of the intracavity beam and pump volume due to the Kerr nonlinearity [114], where P is the intracavity peak power and ω_0 is the beam waist radius inside the crystal. This factor describes the strength of the self-gain modulation of a circulating pulse and thus the strength of the Kerr effect. It is suspected that the factor δ is much lower for the GHz repetition rate resonator

compared to previous laser resonator configurations where KLM was successfully realised in Chapter 3, and this is due to the much higher repetition rate.

An interesting way to increase the magnitude of δ was described by Bartels et al., where they discovered that by using a slightly convex mirror (ROC ~ 1 m) in place of the high-reflecting plane mirror, they were able to increase the strength of δ by approximately a factor of 5 [26]. This is due to the fact the convex mirror creates larger power-dependent modulation of the beam waist inside the crystal compared to a plane mirror.

Applying this to the resonator shown in Figure 87, if the plane GTI mirror was replaced with a slightly convex GTI mirror, more success in realising KLM may be achieved. However, first some calculations would be necessary to verify whether this would be likely work. These calculations could be done using a Magni model [115], however, significant time and effort would need to be invested in developing this model. Unfortunately, due to time constraints it was not possible to explore this further and it was decided to switch to Z-shape configuration that utilises SESAM mode-locking as it was believed that this would provide the best route to achieving a GHz-repetition-rate diode-pumped Ti:sapphire laser in the remaining time of the project.

4.5.2 Z-shape resonator

Given the failure to achieve mode-locking with the KLM ring cavity, it was decided to switch to the Z-shape cavity configuration that uses a SESAM as the mode-locking method.

4.5.2.1 Z-shape resonator – New 5W laser diodes

Given the difficulty in double-end pumping the Z-shape cavity, it was initially planned to pump this setup with a both a 3.5 W, 450 nm laser diode and a 1 W, 520 nm laser diode, using a dichroic filter to combine the pump beams. This however brings its own challenges i.e. the difficulty in aligning both pump beams so that their beam waists coincide inside the Ti:sapphire crystal. During the course of this project, 450 nm laser diodes with higher output power became available, specifically up to 5 W per unit compared to the 3.5 W units used previously in the project. These units have a recommended drive current rating of up to 3.0 A, with an absolute maximum of 3.5 A. When driven at 3.5 A, they can provide close to 5W of optical power at the crystal position, through all pump optics (see Figure 90).

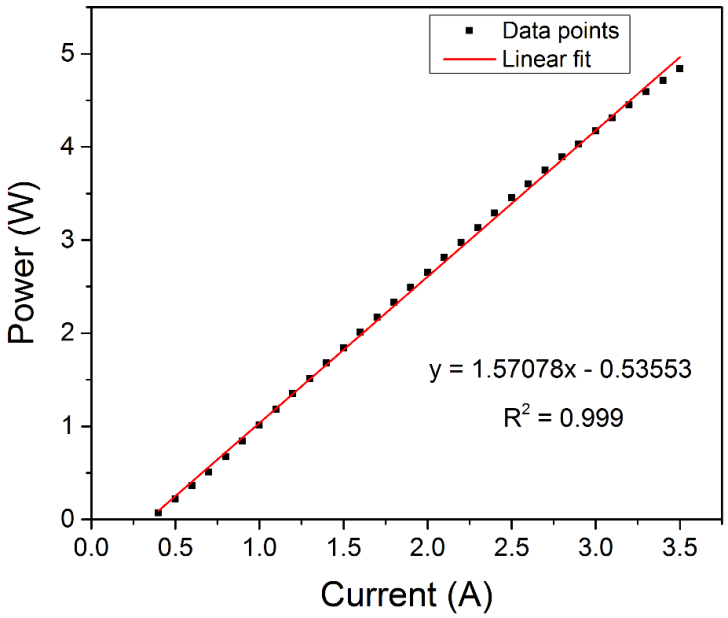

Figure 90. Measured optical output power versus drive current of 5W Nichia NDB7N75T laser diode. The optical output power was measured at the crystal position through all pump optics.

This presented an opportunity to simplify the setup as the increase in power means that only one laser diode could be capable of providing sufficient pump power to the Ti:sapphire laser such that mode-locking can be achieved.

This was also used as an opportunity to improve the pump focusing system by replacing the fixed mount that the CL2 lens was mounted on with a mount capable of rotation (in the plane perpendicular to the z-axis). This makes it easier to correct for astigmatism when the diode beam is focused down to a small spot. The new rotation mount requires a circular-shaped cylindrical lens meaning that the existing rectangular-shaped f = 80 mm cylindrical lens had to be replaced. The off-the-shelf circular cylindrical lens closest in focal length that was able to be procured had a focal length of 75 mm, therefore this was used.

The beam characterisation carried out revealed a pump beam waist of 40 µm × 13 µm using a focusing lens with a f = 75 mm, which is close to the pump beam waist of 30 µm × 11 µm recorded for the 450 nm diode focused with the f = 75 mm lens used in chapter 2 and 3.

4.5.2.2 Z-shape resonator – AR-coated plane-cut crystal

Due to the difference in layout of the Z-shape cavity, the astigmatism introduced by the Brewster-cut crystal can no longer be compensated for by the mirror folding angles. This means that a plane-cut crystal must be used.

For the following experiments, a Ti:sapphire plane-cut crystal 3mm in length was used. To keep losses due to Fresnel reflections to a minimum, plane-cut crystals often employ anti-reflection coatings at the pump and laser emission wavelength range. As the crystal's anti-reflection coating was designed for a pump wavelength of 532 nm and not 450 nm, there is a danger that a large amount of the 450 nm pump light could be reflected back to the diode emitter facet causing damage. To protect the laser diode from damage, measurements were taken to determine the amount of 450 nm light that is reflected by the new plane-cut crystal. A photodiode power meter was used to measure the amount of reflected light, with the power meter being placed as close as possible to the main pump beam. This was to ensure that the reflection angle was kept as small as possible to simulate as closely as possible the performance of the AR-coating at normal incidence. The reflection at 450 nm was found to be around 10% (roughly 5% per crystal facet-air interface). This equates to around 500 mW when the laser diode is set to 5W. In order to prevent this reflected diode radiation from being returned to the diode facet, it was decided to add a slight angle of a few degrees to the new AR-coated crystal with respect to the incident pump beam and cavity axis.

Measurements were carried out for the new crystal to calculate the amount of absorption at 450 nm. The crystal was found to absorb around 58% of incident 450 nm light in a single pass.

4.5.2.3 Z-shape resonator – Intermediate 3-mirror dog-leg resonator

After some difficulty with aligning the Z-shape resonator to begin with, it was decided to first align a simpler "dog-leg" three-mirror resonator (shown in Figure 91). As there were some questions over the potential performance of the plane-cut crystal, we decided to use the two 75 mm ROC folding mirrors used in chapter 2 and 3, and a 2% output coupler for the simpler dog-leg resonator. As these components were previously part of a working laser (detailed in chapter 2 and 3) they were used to rule out any major problems with the performance of the plane-cut crystal.

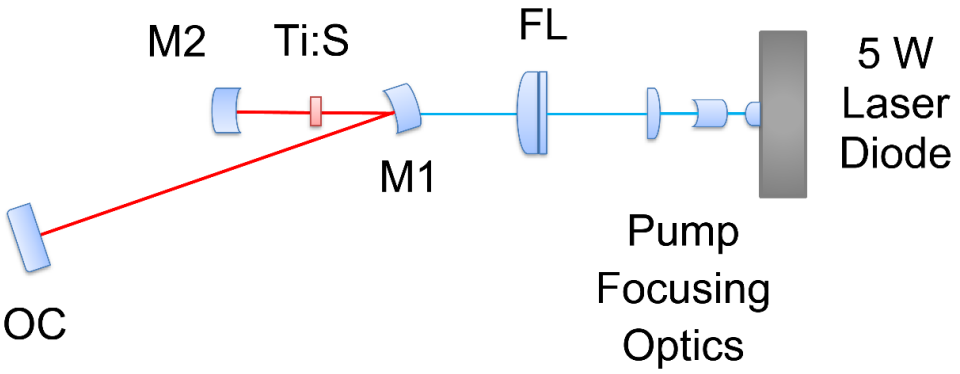

Figure 91. 3 mirror dog-leg resonator schematic. OC – output coupler, M1 and M2 - 75 mm ROC concave mirror, FL – 100 mm focusing lens.

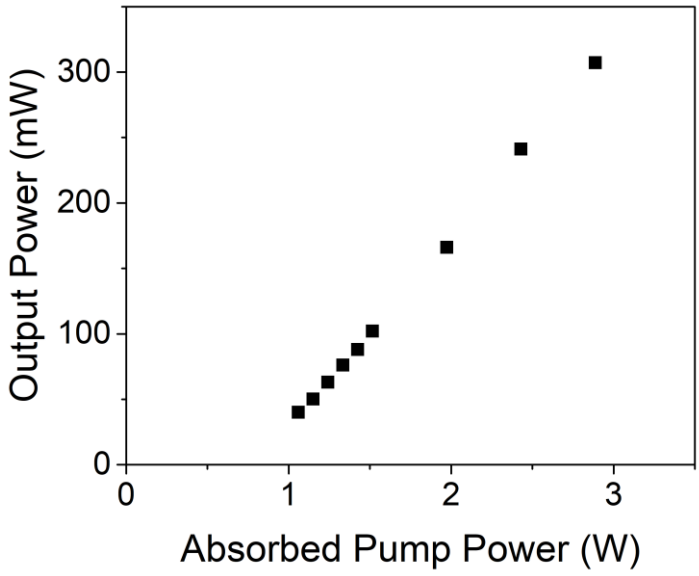

Figure 92. CW performance of laser with three mirror dog-leg resonator.

The CW performance of the three-mirror resonator is shown in Figure 92, with average output powers of up to 300 mW achieved. This gives us confidence that the 3 mm plane cut crystal operates efficiently, despite the non-optimal crystal AR-coating. With the pump beam waist and crystal position optimised, this provides a good base to transition to the four-mirror Z-shape cavity, discussed in the next sub-section.

4.5.2.4 Z-shape resonator – CW performance

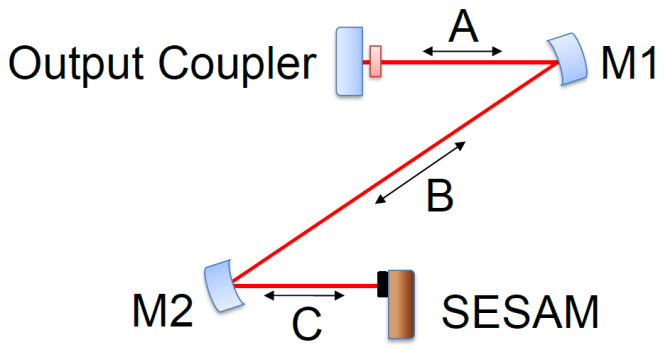

Figure 93. Planned layout of 4-mirror Z-shape resonator.

In moving from the three-mirror resonator to the four-mirror Z-shape resonator shown in Figure 93, the first task was to use a smaller ROC folding mirror so that a smaller resonator length and thus higher repetition rate could be realised. As detailed in section 4.5.1 there were three pairs of smaller ROC folding mirrors available; 25 mm, 30 mm, and 38 mm. Analysis was carried out to determine the likely achievable repetition rates with each configuration. The results of this analysis are detailed in Table 29:

Table 29. Summary of 4-mirror Z-shape resonator configurations constructed using different M1 and M2 ROC, and the resultant repetition rate (f_{rep}) .

M1 & M2 ROC (mm)	A (mm)	B (mm)	C (mm)	Total (mm)	f_{rep} (GHz)	SESAM waist radius (µm)		Crystal waist radius (µm)	
						X	Y	X	Y
25	11.5	110	13.5	140.38	1.07	19	18	24	19
30	14.5	100	16.5	136.38	1.1	26	25	28	26
38	19.5	100	21.5	146.38	1.02	35	35	36	36

Given the difficulties in aligning the three-mirror resonator with 75 mm ROC folding mirrors, it was decided to keep the folding mirror ROC as long as possible for the four-mirror resonator in order to increase the working distances, as a smaller ROC equates to a smaller focal length. As a compromise it was decided that the 30 mm ROC mirrors should be used as these give a potential repetition rate of 1.1 GHz, giving some room to play with in length, while also offering a larger working distance than the 25 mm ROC mirrors.

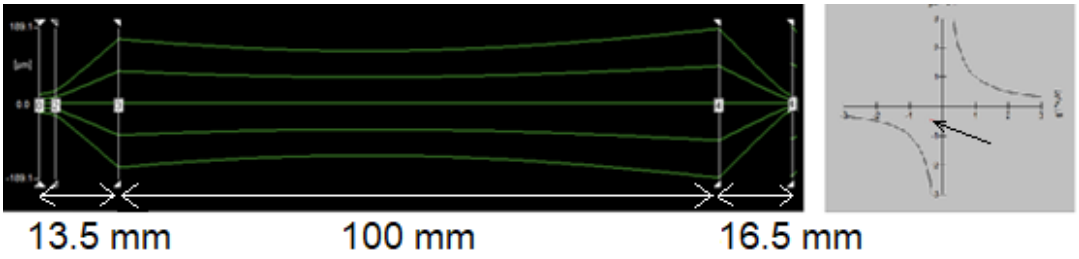

Figure 94. Cavity mode plot and corresponding cavity stability diagram for CW resonator. The arrow on the stability diagram points to the cavity stability position.

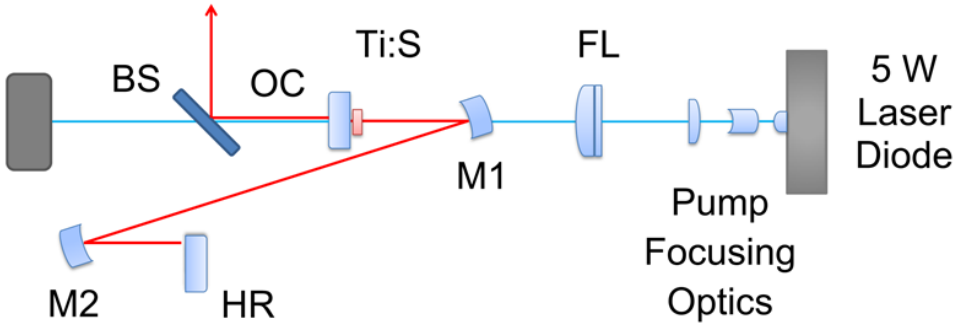

Figure 95. CW resonator schematic. BS – dichroic beamsplitter, OC – output coupler, M1 and M2 - 30 mm ROC concave mirror, HR – high-reflector plane mirror, FL – 100 mm focusing lens.

After setting the resonator up as shown in Figure 95, lasing was achieved with up 125 mW output at around 4 W incident pump power, with an output coupling of 2%. This represents a 175 mW or 58% drop compared to the 3-mirror dog-leg resonator. This is likely due to the poorer pump-resonator mode overlap, due to the resonator mode waist position being at the cavity end mirror whereas for the dog-leg resonator it was positioned between the two curved mirrors. However, the fluence calculations set out in the next section demonstrate that this average output power should be more than sufficient to provide a high enough fluence on the SESAM for mode-locking, given the 25 µm beam waist radius and the range of output couplers available.

4.5.2.5 Z-shape resonator – Fluence calculations

As stated in Chapter 3, the fluence incident upon the SESAM required for soliton mode-locking is between 3-5 times the saturation fluence of the SESAM. In the case of the SESAM used in Chapter 3, the saturation fluence of the SESAM is estimated to be around 50 µJ/cm^2. Therefore, the goal was to have a fluence of around 150 to 250 µJ/cm^2 incident upon the SESAM. Several output couplers were available, ranging from 1 to 5% transmission. Using the beam waist radius at the SESAM of 25 µm (calculated using LASCAD) and the expected pulse

repetition rate of 1.1 GHz, the resultant fluence incident upon the SESAM was calculated for a range of average output powers at the four available output coupling values. These results are shown in Figure 96:

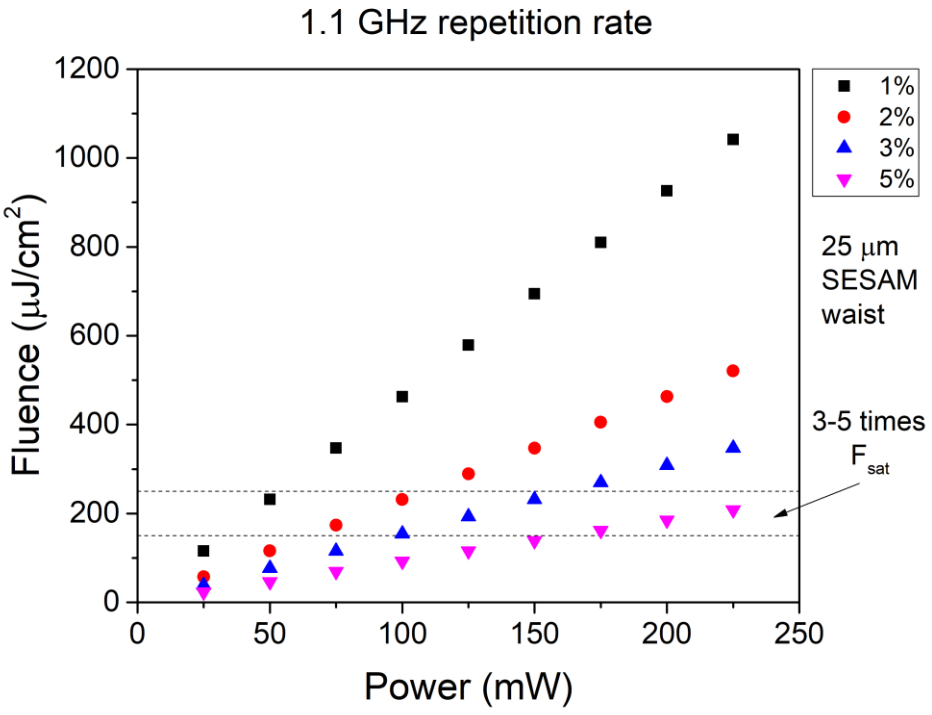

Figure 96. Resultant fluence incident upon the SESAM vs. average output power for various output coupling percentages. The SESAM beam waist radius used for calculations was 25 μm.

As shown in Figure 96, at 1% output coupling even the lowest average output power levels generate a fluence incident on the SESAM higher than required. For this reason, it was decided to use a 2% or 3% transmission output coupler to avoid potential damage to the SESAM. At 100 mW average output power, the incident fluence upon the SESAM would be 232 μJ/cm^2 for a 2% transmission output coupler and 154 μJ/cm^2 for a 3% transmission output coupler, both within the desired range of 150 to 250 μJ/cm^2.

4.5.2.6 Z-shape resonator – Crystal GDD calculation and dispersion compensation

Given that a new crystal with a shorter length of 3 mm was used, the new material dispersion introduced must be calculated. This is shown in Figure 97.

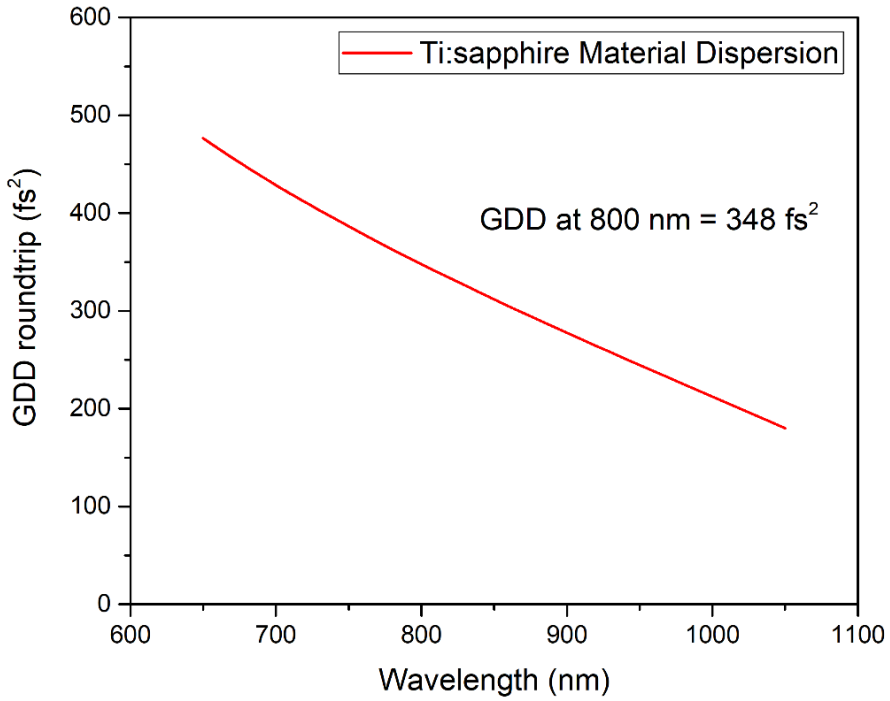

Figure 97. Calculated GDD of 3 mm long Ti:sapphire crystal.

Given that the required cavity length heavily constrains the resonator design, dispersion compensating mirrors must be used for dispersion compensation. A range of chirped mirror pairs of varying amounts of negative GDD were available as well as two GTI mirrors which offered a much higher negative GDD over their operating bandwidth (-550 fs^2 per bounce compared to -120 fs^2 per bounce). However, this is at the cost of a much narrower operating bandwidth than the various chirped mirror pairs available (30 nm for the GTI mirrors compared to 200 nm for the chirped mirror pairs). Various combinations of dispersive mirrors were experimented with in order to provide varying amounts of negative GDD.

In the end, a single GTI mirror was used that provided -550 fs^2 of negative GDD per bounce at 800 nm. This equates to -1100 fs^2 per roundtrip. Taking this into account and the crystal GDD of 348 fs^2, the net cavity GDD is -752 fs^2 per roundtrip.

4.5.2.7 Z-shape resonator – Mode-locking attempts and discussion

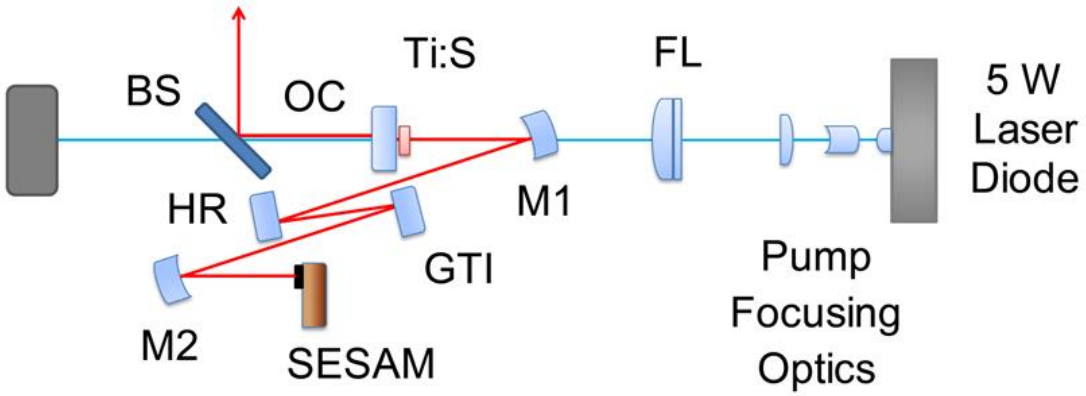

Figure 98. Ultrafast resonator schematic. BS – dichroic beamsplitter, OC – output coupler, M1 and M2 - 30 mm ROC concave mirror, HR – high-reflector plane mirror, GTI – GTI mirror, SESAM - SESAM, FL – 100 mm focusing lens.

After the SESAM was inserted in place of the HR end mirror, lasing was achieved. However, the output power was only 10 mW at around 4 W incident pump power compared to around 115 mW when the HR mirror was in place. No spectral broadening was witnessed on the spectrometer, and no RF signal at the estimated pulse repetition rate was detected using the fast photodiode, confirming that mode-locking was not achieved.

Given a 25 µm beam waist incident upon the SESAM with 2% output coupling, then 10 mW output power at a repetition rate of 1.1 GHz equates to a fluence of around 24 µJ/cm^2. As the saturation fluence of the SESAM is around 50 µJ/cm^2, this is well below the 3-5 times saturation fluence needed for mode-locked operation.

Given the project's time constraints, the reason why mode-locked operation was unable to be achieved with this configuration was not determined. It is suspected that the SESAM may have sustained damage as a result of the small incident beam waist and random intensity fluctuations present before mode-locking is established.

As for next steps, the first task would be to investigate the SESAM for signs of damage. Another avenue to investigate would be the possibility of using low-saturation fluence SESAMs. This would relax the requirements on the SESAM beam waist size and allow a larger incident beam waist size to be used, thus making damage less likely. Further optimisation of the dispersion compensation applied would also be useful, however some sort of pulsed behaviour would likely have been evident if this was only problem.

4.6 Conclusion and future work

To summarise, various cavity configurations for GHz-repetition rate mode-locking in a diode-pumped Ti:sapphire laser have been proposed and analysed. Two different mode-locking methods were explored in an attempt to realise this goal: Kerr-lens mode-locking with a ring resonator and SESAM mode-locking with a Z-shape standing wave resonator. Ultimately, mode-locked operation was not realised experimentally in either case, and the reasons why could not be fully investigated due to time constraints on the project.

In the case of the ring resonator with KLM, it is believed that the pulse energy was not sufficient to initiate KLM, as explained in section 4.5.1.3. In terms of future work, further theoretical analysis would be useful, specifically the development of a Magni model [115]. This would allow for a better understanding of the laser dynamics in the presence of the Kerr-lens, and to find the best folding mirror position for KLM. It would also be useful to try using a slightly convex mirror in place of the plane mirror to create a larger power-dependent modulation of the beam waist inside the crystal compared to a plane mirror, which has been demonstrated to make it easier to achieve mode-locking [26]. It is believed that of the two options explored in this paper, the Kerr-lens mode-locked ring resonator would be the most promising route to achieving mode-locked operation.

In the case of the Z-shape resonator, it is suspected that there may have been damage to the SESAM caused by the random intensity fluctuations present before mode-locking is established, given the small beam waist incident upon the SESAM. More investigation would be required to confirm whether this was the case or not.

4.7 References

1. T. W. Hänsch and J. L. Hall, "The Nobel Prize in Physics 2005," https://www.nobelprize.org/prizes/physics/2005/summary/.
2. M. Kourogi, T. Enami, and M. Ohtsu, "A Monolithic Optical Frequency Comb Generator," IEEE Photonics Technol. Lett. **6**(2), 214–217 (1994).
3. L. R. Brothers, D. Lee, and N. C. Wong, "Terahertz optical frequency comb generation and phase locking of an optical parametric oscillator at 665 GHz," Opt. Lett. **19**(4), 245 (1994).
4. A. S. Bell, G. M. Mcfarlane, E. Riis, and A. I. Ferguson, "Efficient optical frequency-comb generator," Opt. Lett. **20**(12), 1435 (1995).
5. L. R. Brothers and N. C. Wong, "Dispersion compensation for terahertz optical frequency comb generation," Opt. Lett. **22**(13), 1015 (1997).
6. T. Udem, J. Reichert, R. Holzwarth, and T. W. Hänsch, "Absolute optical frequency measurement of the cesium D1 line with a mode-locked laser," Phys. Rev. Lett. **82**(18), 3568–3571 (1999).
7. S. A. Diddams, "An Optical Clock Based on a Single Trapped 199Hg+ Ion," Science (80-.). **293**(5531), 825–828 (2001).

8. R. Holzwarth, M. Zimmermann, T. Udem, and T. W. Hänsch, "Optical clockworks and the measurement of laser frequencies with a mode-locked frequency comb," IEEE J. Quantum Electron. **37**(12), 1493–1501 (2001).

9. J. E. Bernard, A. A. Madej, L. Marmet, B. G. Whitford, K. J. Siemsen, and S. Cundy, "Cs-based frequency measurement of a single, trapped ion transition in the visible region of the spectrum," Phys. Rev. Lett. **82**(16), 3228–3231 (1999).

10. B. J. Bloom, T. L. Nicholson, J. R. Williams, S. L. Campbell, M. Bishof, X. Zhang, W. Zhang, S. L. Bromley, and J. Ye, "An optical lattice clock with accuracy and stability at the 10-18 level," Nature **506**(7486), 71–75 (2014).

11. M. C. Stowe, M. J. Thorpe, A. Pe'er, J. Ye, J. E. Stalnaker, V. Gerginov, and S. A. Diddams, "Direct frequency comb spectroscopy," Adv. At. Mol. Opt. Phys. **55**(07), 1–60 (2008).

12. K. L. Corwin, N. R. Newbury, J. M. Dudley, S. Coen, S. A. Diddams, K. Weber, and R. S. Windeler, "Fundamental Noise Limitations to Supercontinuum Generation in Microstructure Fiber," Phys. Rev. Lett. **90**(11), 113904 (2003).

13. R. A. McCracken, É. Depagne, R. B. Kuhn, N. Erasmus, L. A. Crause, and D. T. Reid, "Wavelength calibration of a high resolution spectrograph with a partially stabilized 15-GHz astrocomb from 550 to 890 nm," Opt. Express **25**(6), 6450 (2017).

14. D. C. Heinecke, A. Bartels, T. M. Fortier, D. A. Braje, L. Hollberg, and S. A. Diddams, "Optical frequency stabilization of a 10 GHz Ti:sapphire frequency comb by saturated absorption spectroscopy in r 87 ubidium," Phys. Rev. A - At. Mol. Opt. Phys. **80**(5), 1–7 (2009).

15. F. Helmchen and W. Denk, "Deep tissue two-photon microscopy," Nat. Methods **2**(12), 932–940 (2005).

16. A. N. Bashkatov, E. A. Genina, V. I. Kochubey, and V. V. Tuchin, "Optical properties of human skin, subcutaneous and mucous tissues in the wavelength range from 400 to 2000 nm," J. Phys. D. Appl. Phys. **38**(15), 2543–2555 (2005).

17. K. Koenig, "Multiphoton microscopy in life sciences," J. Microsc. **200**(2), 83–104 (2000).

18. A. Ehlers, I. Riemann, S. Martin, R. Le Harzic, A. Bartels, C. Janke, and K. König, "High (1 GHz) repetition rate compact femtosecond laser: A powerful multiphoton tool for nanomedicine and nanobiotechnology," J. Appl. Phys. **102**(1), 1–6 (2007).

19. J. N. Gannaway and C. J. R. Sheppard, "Second-harmonic imaging in the scanning optical microscope," Opt. Quantum Electron. **10**(5), 435–439 (1978).

20. Y. R. Chen, "Surface properties probed by second-harmonic and sum-frequency generation," Nature **337**(9), 519 (1989).

21. P. J. Campagnola, M. De Wei, A. Lewis, and L. M. Loew, "High-resolution nonlinear optical imaging of live cells by second harmonic generation," Biophys. J. **77**(6), 3341–3349 (1999).

22. Y. Guo, H. E. Savage, F. Liu, S. P. Schantz, P. P. Ho, and R. R. Alfano, "Subsurface tumor progression investigated by noninvasive optical second harmonic tomography," Proc. Natl. Acad. Sci. U. S. A. **96**(19), 10854–10856 (1999).

23. S. Tang, T. B. Krasieva, Z. Chen, G. Tempea, and B. J. Tromberg, "Effect of pulse duration on two-photon excited fluorescence and second harmonic generation in nonlinear optical microscopy," J. Biomed. Opt. **11**(2), 020501 (2006).

24. S.-W. Chu, T.-M. Liu, C.-K. Sun, C.-Y. Lin, and H.-J. Tsai, "Real-time second-harmonic-generation microscopy based on a 2-GHz repetition rate Ti:sapphire laser," Opt. Express **11**(8), 933 (2003).

25. E. Reichertb, K. Aulenbacherb, H. Euteneue, M. Schemiesb, M. Steigerwaldb, H. Trautnerb, and H. Hofmanna, "Self-starting modelocked Ti:sapphire laser at a repetition rate of 1.039 GHz," Nucl. Instruments Methods Phys. Res. Sect. A **9002**(96), (1996).

26. A. Bartels and H. Kurz, "Generation of a broadband continuum by a Ti:sapphire femtosecond oscillator with a 1-GHz repetition rate," Opt. Lett. **27**(20), 1839 (2002).

27. G. T. Nogueira and F. C. Cruz, "Efficient 1 GHz Ti:sapphire laser with improved broadband continuum in the infrared," Opt. Lett. **31**(13), 2069 (2006).

28. Y. Kobayashi, D. Yoshitomi, K. Torizuka, T. Fortier, and S. Diddams, "Sub 6-fs Pulses Generated from a Broadband 1-GHz Ti:sapphire Oscillator," in *Conference on Lasers and Electro-Optics/Quantum Electronics and Laser Science Conference and Photonic Applications Systems Technologies*, OSA Technical Digest Series (CD) (Optical Society of America, 2007), p. CTuC3.

29. Q. Zhang, Y. Zhao, and Z. Wei, "Sub-10 fs laser pulses with repetition rate of 1.1 GHz by a Ti: sapphire oscillator," Chinese Sci. Bull. **54**(20), 3649–3652 (2009).

30. T. M. Fortier, A. Bartels, and S. A. Diddams, "Octave-spanning Ti:sapphire laser with a repetition rate >1 GHz for optical frequency measurements and comparisons," Opt. Lett. **31**(7), 1011 (2006).

31. M. Butkus, G. Robertson, G. Maker, G. Malcolm, C. Hamilton, A. B. Krysa, B. J. Stevens, R. A. Hogg, Y. Qiu, T. Walther, and E. U. Rafailov, "High repetition rate Ti:sapphire laser mode-locked by inp quantum-dot saturable absorber," IEEE Photonics Technol. Lett. **23**(21), 1603–1605 (2011).

32. A. Bartels, T. Dekorsy, and H. Kurz, "Femtosecond Ti:sapphire ring laser with a 2-GHz repetition rate and its application in time-resolved spectroscopy," Opt. Lett. **24**(14), 996 (1999).

33. G. T. Nogueira, B. Xu, Y. Coello, M. Dantus, and F. C. Cruz, "Broadband 2.12 GHz Ti:sapphire laser compressed to 5.9 femtoseconds using MIIPS," Opt. Express **16**(14), 10033 (2008).

34. L.-J. Chen, A. J. Benedick, J. R. Birge, M. Y. Sander, and F. X. Kärtner, "Octave-spanning, dual-output 2.166 GHz Ti:sapphire laser," Opt. Express **16**(25), 20699–20705 (2008).

35. B. Stormont, I. G. Cormack, M. Mazilu, C. T. A. Brown, D. Burns, and W. Sibbett, "Low-threshold, multi-gigahertz repetition-rate femtosecond Ti:sapphire laser," Electron. Lett. **39**(25), 1–2 (2003).

36. A. Rolland, T. Fortier, and S. A. Diddams, "Octave-spanning Ti:Sapphire laser with repetition rate >4 GHz," in *2013 Conference on Lasers and Electro-Optics - International Quantum Electronics Conference* (Optical Society of America, 2013), p. ID_2_2.

37. A. Bartels, D. Heinecke, and S. A. Diddams, "Passively mode-locked 10 GHz femtosecond Ti:sapphire laser," Opt. Lett. **33**(16), 1905 (2008).

38. A. Klenner, M. Golling, and U. Keller, "High peak power gigahertz Yb:CALGO laser," Opt. Express **22**(10), 11884 (2014).

39. A. Klenner, M. Golling, and U. Keller, "Gigahertz diode-pumped Yb:CALGO laser with 60-fs pulses and an average output power of 3.5 W," in *CLEO: 2014*, OSA Technical Digest (Online) (Optical Society of America, 2014), p. SM4F.6.

40. S. Pekarek, C. Fiebig, M. C. Stumpf, A. E. H. Oehler, K. Paschke, G. Erbert, T. Südmeyer, and U. Keller, "Diode-pumped gigahertz femtosecond Yb:KGW laser with a peak power of 3.9 kW," Opt. Express **18**(16), 16320 (2010).

41. S. Pekarek, T. Südmeyer, S. Lecomte, S. Kundermann, J. M. Dudley, and U. Keller, "Self-referenceable frequency comb from a gigahertz diode-pumped solid-state laser," Opt. Express **19**(17), 16491–16497 (2011).

42. S. Pekarek, A. Klenner, T. Südmeyer, C. Fiebig, K. Paschke, G. Erbert, and U. Keller, "Femtosecond diode-pumped solid-state laser with a repetition rate of 4.8 GHz," Opt. Express **20**(4), 4248 (2012).

43. A. Klenner, M. Golling, and U. Keller, "A gigahertz multimode-diode-pumped Yb:KGW enables a strong frequency comb offset beat signal," Opt. Express **21**(8), 10351 (2013).

44. P. Wasylczyk, P. Wnuk, and C. Radzewicz, "Passively modelocked, diode-pumped Yb : KYW femtosecond oscillator with 1 GHz repetition rate," Opt. Express **17**(7), 21930–21935 (2009).

45. M. Endo, A. Ozawa, and Y. Kobayashi, "Kerr-lens mode-locked Yb:KYW laser at 4.6-GHz repetition rate," Opt. Express **20**(11), 12191 (2012).

46. S. Yamazoe, M. Katou, T. Adachi, and T. Kasamatsu, "Palm-top-size, 15 kW peak-power, and femtosecond (160 fs) diode-pumped mode-locked Yb^+3:KY(WO_4)_2 solid-state laser with a semiconductor saturable absorber mirror," Opt. Lett. **35**(5), 748 (2010).

47. T. C. Schratwieser, C. G. Leburn, and D. T. Reid, "Highly efficient 1 GHz repetition-frequency femtosecond Yb^3+:KY(WO_4)_2 laser," Opt. Lett. **37**(6), 1133 (2012).

48. M. Endo, A. Ozawa, and Y. Kobayashi, "6-GHz, Kerr-lens mode-locked Yb:Lu_2O_3 ceramic laser for comb-resolved broadband spectroscopy," Opt. Lett. **38**(21), 4502 (2013).

49. M. Endo, I. Ito, and Y. Kobayashi, "Direct 15-GHz mode-spacing optical frequency comb with a Kerr-lens mode-locked Yb:Y_2O_3 ceramic laser," Opt. Express **23**(2), 1276 (2015).

50. A. J. Kemp, B. Stormont, B. Agate, C. T. A. Brown, U. Keller, and W. Sibbett, "Gigahertz repetition-rate from directly diode-pumped femtosecond Cr:LiSAF laser," Electron. Lett. **37**(24), 1457 (2001).

51. D. Li, U. Demirbas, J. R. Birge, G. S. Petrich, L. A. Kolodziejski, A. Sennaroglu, F. X. Kärtner, and J. G. Fujimoto, "Diode-pumped gigahertz repetition rate femtosecond Cr: LiSAF laser," Opt. InfoBase Conf. Pap. 4–5 (2010).

52. D. Li, U. Demirbas, J. R. Birge, G. S. Petrich, L. A. Kolodziejski, A. Sennaroglu, F. X. Kärtner, and J. G. Fujimoto, "Diode-pumped passively mode-locked GHz femtosecond Cr:LiSAF laser with kW peak power," Opt. Lett. **35**(9), 1446 (2010).

53. L. Krainer, R. Paschotta, G. J. Spühler, I. Klimov, C. Y. Teisset, K. J. Weingarten, and U. Keller, "Tunable picosecond pulse-generating laser with repetition rate exceeding 10 GHz," Electron. Lett. **38**(5), 1–2 (2002).

54. B. Resan, S. Kurmulis, Z. Y. Zhang, A. E. H. Oehler, V. Markovic, M. Mangold, T. Südmeyer, U. Keller, R. A. Hogg, and K. J. Weingarten, "10 GHz pulse repetition rate Er:Yb:glass laser modelocked with quantum dot semiconductor saturable absorber mirror," Appl. Opt. **55**(14), 3776 (2016).

55. G. J. Spühler, P. S. Golding, L. Krainer, I. J. Kilburn, P. A. Crosby, M. Brownell, K. J. Weingarten, R. Paschotta, M. Haiml, R. Grange, and U. Keller, "Multi-wavelength source with 25 GHz channel spacing tunable over C-band," Electron. Lett. **39**(10), 1–2 (2003).

56. S. C. Zeller, L. Krainer, G. J. Spühler, K. J. Weingarten, R. Paschotta, and U. Keller, "Passively mode-locked 40-GHz Er:Yb:glass laser," Appl. Phys. B Lasers Opt. **76**(7), 787–788 (2003).

57. S. C. Zeller, L. Krainer, G. J. Spühler, R. Paschotta, M. Golling, D. Ebling, K. J. Weingarten, and U. Keller, "Passively modelocked 50 GHz Er:Yb:glass laser," Electron. Lett. **40**(14), 1–2 (2004).

58. S. C. Zeller, T. Südmeyer, K. J. Weingarten, and U. Keller, "Passively modelocked 77 GHz Er:Yb:glass laser," Electron. Lett. **43**(1), 1–2 (2007).

59. A. E. Oehler, T. Südmeyer, K. J. Weingarten, and U. Keller, "100 GHz passively mode-locked Er:Yb:glass laser at 15 µm with 16-ps pulses," Opt. Express **16**(26), 21930 (2008).

60. A. E. H. Oehler, T. Südmeyer, U. Keller, and K. J. Weingarten, "100 GHz passively mode-locked Er:Yb:glass laser at 1.5 µm and identification of transverse cavity-mode degeneracies," in *Conference on Lasers and Electro-Optics/International Quantum Electronics Conference*, OSA Technical Digest (CD) (Optical Society of America, 2009), p. CFO2.

61. L. Krainer, R. Paschotta, S. Lecomte, M. Moser, K. J. Weingarten, and U. Keller, "Compact Nd: YVO4 lasers with pulse repetition rates up to 160 GHz," IEEE J. Quantum Electron. **38**(10), 1331–1338 (2002).

62. L. Krainer, R. Paschotta, J. Aus der Au, C. Hönninger, U. Keller, M. Moser, D. Kopf, and K. J. Weingarten, "Passively mode-locked Nd:YVO4 laser with up to 13 GHz repetition rate," Appl. Phys. B Lasers Opt. **69**(3), 245–247 (1999).

63. S. Lecomte, M. Kalisch, L. Krainer, G. J. Spühler, R. Paschotta, M. Golling, D. Ebling, T. Ohgoh, T. Hayakawa, S. Pawlik, B. Schmidt, and U. Keller, "Diode-pumped passively mode-locked Nd: YVO4 lasers with 40-GHz repetition rate," IEEE J. Quantum Electron. **41**(1), 45–52 (2005).

64. I. Hartl, H. A. Mckay, R. Thapa, B. K. Thomas, L. Dong, and M. E. Fermann, "GHz Yb-femtosecond-fiber laser frequency comb," in *Conference on Lasers and Electro-Optics/International Quantum Electronics Conference* (OSA, 2009), p. CMN1.

65. C. Li, Y. Ma, X. Gao, F. Niu, T. Jiang, A. Wang, and Z. Zhang, "1 GHz repetition rate femtosecond Yb:fiber laser for direct generation of carrier-envelope offset frequency," Appl. Opt. **54**(28), 8350 (2015).

66. D. Chao, M. Y. Sander, G. Chang, J. L. Morse, J. A. Cox, G. S. Petrich, L. A. Kolodziejski, F. X. Kärtner, and E. P. Ippen, "Self-referenced Erbium Fiber Laser Frequency Comb at a GHz Repetition Rate," in *Optical Fiber Communication Conference* (OSA, 2012), p. OW1C.2.

67. H. Chen, G. Chang, S. Xu, Z. Yang, and F. X. Kärtner, "3 GHz, fundamentally mode-locked, femtosecond Yb-fiber laser," Opt. Lett. **37**(17), 3522 (2012).

68. S. Yamashita, Y. Inoue, K. Hsu, T. Kotake, H. Yaguchi, D. Tanaka, M. Jablonski, and S. Y. Set, "5-GHz pulsed fiber fabry-Pérot laser mode-locked using carbon nanotubes," IEEE Photonics Technol. Lett. **17**(4), 750–752 (2005).

69. A. Martinez and S. Yamashita, "10 GHz fundamental mode fiber laser using a graphene saturable absorber," Appl. Phys. Lett. **101**(4), 2010–2013 (2012).

70. A. Martinez and S. Yamashita, "Multi-gigahertz repetition rate passively modelocked fiber lasers using carbon nanotubes," Opt. Express **19**(7), 6155 (2011).

71. G. Sobon, K. Krzempek, P. Kaczmarek, K. M. Abramski, and M. Nikodem, "10 GHz passive harmonic mode-locking in Er-Yb double-clad fiber laser," Opt. Commun. **284**(18), 4203–4206 (2011).

72. O. Pottiez, O. Deparis, R. Kiyan, M. Haelterman, P. Emplit, P. Mégret, and M. Blondel, "Supermode noise of harmonically mode-locked erbium fiber lasers with composite cavity," IEEE J. Quantum Electron. **38**(3), 252–259 (2002).

73. S. Hoogland, S. Dhanjal, A. C. Tropper, J. S. Roberts, R. Häring, R. Paschotta, and U. Keller, "Passively Mode-Locked Diode-Pumped Surface-Emitting Semiconductor Laser," IEEE Photonics Technol. Lett. **12**(9), 1135–1137 (2000).

74. R. Häring, R. Paschotta, E. Gini, F. Morier-Genoud, D. Martin, H. Melchior, and U. Keller, "Picosecond surface-emitting semiconductor laser with 200 mW average power," Electron. Lett. **37**(12), 766 (2001).

75. K. G. Wilcox, Z. Mihoubi, G. J. Daniell, S. Elsmere, A. Quarterman, I. Farrer, D. A. Ritchie, and A. Tropper, "Ultrafast optical Stark mode-locked semiconductor laser," Opt. Lett. **33**(23), 2797–2799 (2008).

76. M. Hoffmann, O. D. Sieber, W. P. Pallmann, V. J. Wittwer, Y. Barbarin, T. Südmeyer, and U. Keller, "All Quantum-Dot Based Femtosecond VECSEL," Eur. Conf. 2010 **731**, 44263 (2009).

77. P. Klopp, U. Griebner, M. Zorn, A. Klehr, A. Liero, G. Erbert, and M. Weyers, "InGaAs-AlGaAs Disk Laser Generating sub-220-fs Pulses and Tapered Diode Amplifier with Ultrafast Pulse Picking," in *Advanced Solid-State Photonics* (OSA, 2009), **17**(13), p. ME3.

78. K. G. Wilcox, A. H. Quarterman, H. Beere, D. A. Ritchie, and A. C. Tropper, "High Peak Power Femtosecond Pulse Passively Mode-Locked Vertical-External-Cavity Surface-Emitting Laser," IEEE Photonics Technol. Lett. **22**(14), 1021–1023 (2010).

79. M. Hoffmann, O. D. Sieber, V. J. Wittwer, I. L. Krestnikov, D. A. Livshits, Y. Barbarin, T. Südmeyer, and U. Keller, "Femtosecond high-power quantum dot vertical external cavity surface emitting laser," Opt. Express **19**(9), 8108 (2011).

80. Y. F. Chen, Y. C. Lee, H. C. Liang, K. Y. Lin, K. W. Su, and K. F. Huang, "Femtosecond high-power spontaneous mode-locked operation in vertical-external cavity surface-emitting laser with gigahertz oscillation," Opt. Lett. **36**(23), 4581 (2011).

81. O. D. Sieber, V. J. Wittwer, M. Mangold, M. Hoffmann, M. Golling, T. Südmeyer, and U. Keller, "Femtosecond VECSEL with tunable multi-gigahertz repetition rate," Opt. Express **19**(23), 23538 (2011).

82. O. D. Sieber, M. Hoffmann, V. J. Wittwer, W. P. Pallmann, I. L. Krestnikov, S. S. Mikhrin, D. A. Livshits, M. Golling, Y. Barbarin, T. Südmeyer, and U. Keller, "Femtosecond VECSELs with up to 1-W average output power," Eur. Conf. Lasers Electro-Optics 2011 **1023**, 44263 (2011).

83. P. Klopp, U. Griebner, M. Zorn, and M. Weyers, "Pulse repetition rate up to 92 GHz or pulse duration shorter than 110 fs from a mode-locked semiconductor disk laser," Appl. Phys. Lett. **98**(7), 071103 (2011).

84. O. D. Sieber, V. J. Wittwer, M. Hoffmann, I. L. Krestnikov, S. S. Mikhrin, D. A. Livshits, M. Golling, T. Südmeyer, and U. Keller, "High-average power femtosecond VECSELs with tunable repetition rates up to 10 GHz," in *Proc.SPIE*, A. C. Tropper, ed. (2012), **8242**, p. 824210.

85. R. Haring, M. Paschotta, A. Aschwanden, E. Gini, F. Morier-Genoud, and U. Keller, "High-power passively mode-locked semiconductor lasers," IEEE J. Quantum Electron. **38**(9), 1268–1275 (2002).

86. C. R. Head, H. Y. Chan, J. S. Feehan, D. P. Shepherd, S. U. Alam, A. C. Tropper, J. H. V. Price, and K. G. Wilcox, "Supercontinuum generation with GHz repetition rate femtosecond-pulse fiber-amplified VECSELs," IEEE Photonics Technol. Lett. **25**(5), 464–467 (2013).

87. C. A. Zaugg, A. Klenner, M. Mangold, A. S. Mayer, S. M. Link, F. Emaury, M. Golling, E. Gini, C. J. Saraceno, B. W. Tilma, and U. Keller, "Gigahertz self-referenceable frequency comb from a semiconductor disk laser," Opt. Express **22**(13), 16445 (2014).

88. D. Waldburger, M. Mangold, S. M. Link, M. Golling, E. Gini, B. W. Tilma, and U. Keller, "Sub-300-femtosecond Semiconductor Disk Lasers," in *CLEO: 2015*, OSA Technical Digest (Online) (OSA, 2015), p. SM3F.2.

89. M. Scheller, T.-L. Wang, B. Kunert, W. Stolz, S. W. Koch, and J. V. Moloney, "Passively modelocked VECSEL emitting 682 fs pulses with 5.1 W of average output power," Electron. Lett. **48**(10), 588 (2012).

90. A. Garnache, S. Hoogland, A. C. Tropper, I. Sagnes, G. Saint-Girons, and J. S. Roberts, "Sub-500-fs soliton-like pulse in a passively mode-locked broadband surface-emitting laser with 100 mW average power," Appl. Phys. Lett. **80**(21), 3892–3894 (2002).

91. A. Aschwanden, D. Lorenser, H. J. Unold, R. Paschotta, E. Gini, and U. Keller, "10GHz passively mode-locked external-cavity semiconductor laser with 1.4W average output power," Appl. Phys. Lett. **86**(13), 131102 (2005).

92. A. Aschwanden, D. Lorenser, H. J. Unold, R. Paschotta, E. Gini, and U. Keller, "2.1-W picosecond passively mode-locked external-cavity semiconductor laser," Opt. Lett. **30**(3), 272 (2005).

93. D. Lorenser, D. J. H. C. Maas, H. J. Unold, A.-R. Bellancourt, B. Rudin, E. Gini, D. Ebling, and U. Keller, "50-GHz Passively Mode-Locked Surface-Emitting Semiconductor Laser With 100-mW Average Output Power," IEEE J. Quantum Electron. **42**(8), 838–847 (2006).

94. B. Rudin, D. J. H. C. Maas, D. Lorenser, A.-R. Bellancourt, H. J. Unold, U. Keller, E. Gini, and D. Ebling, "High-performance mode-locking with up to 50 GHz repetition rate from integrable VECSELs," in *2006 Conference on Lasers and Electro-Optics and 2006 Quantum Electronics and Laser Science Conference* (IEEE, 2006), pp. 1–2.

95. P. Klopp, F. Saas, M. Zorn, M. Weyers, and U. Griebner, "290-fs pulses from a semiconductor disk laser," Opt. Express **16**(8), 5770 (2008).

96. M. Hoffmann, Y. Barbarin, D. J. H. C. Maas, M. Golling, I. L. Krestnikov, S. S. Mikhrin, A. R. Kovsh, T. Südmeyer, and U. Keller, "Modelocked quantum dot vertical external cavity surface emitting laser," Appl. Phys. B **93**(4), 733–736 (2008).

97. V. J. Wittwer, M. Mangold, M. Hoffmann, O. D. Sieber, M. Golling, T. Südmeyer, and U. Keller, "High-power integrated ultrafast semiconductor disk laser: Multi-Watt 10GHz pulse generation," Electron. Lett. **48**(18), 1144–1145 (2012).

98. M. Mangold, C. A. Zaugg, S. M. Link, M. Golling, B. W. Tilma, and U. Keller, "Pulse repetition rate scaling from 5 to 100 GHz with a high-power semiconductor disk laser," Opt. Express **22**(5), 6099 (2014).

99. V. J. Wittwer, B. Rudin, D. J. H. C. Maas, M. Hoffmann, O. D. Sieber, Y. Barbarin, M. Golling, T. Südmeyer, and U. Keller, "10-GHz MIXSEL: An integrated ultrafast semiconductor disk laser with 2.2 W average power," Opt. InfoBase Conf. Pap. **18**(26), 272–274 (2011).

100. D. J. H. C. Maas, A. R. Bellancourt, B. Rudin, M. Golling, H. J. Unold, T. Südmeyer, and U. Keller, "Vertical integration of ultrafast semiconductor lasers," Appl. Phys. B Lasers Opt. **88**(4), 493–497 (2007).

101. M. Mangold, M. Golling, E. Gini, B. W. Tilma, and U. Keller, "Sub-300-femtosecond operation from a MIXSEL," Opt. Express **23**(17), 22043 (2015).

102. B. Rudin, V. J. Wittwer, D. J. H. C. Maas, M. Hoffmann, O. D. Sieber, Y. Barbarin, M. Golling, T. Südmeyer, and U. Keller, "High-power MIXSEL: an integrated ultrafast semiconductor laser with 6.4 W average power," Opt. Express **18**(26), 27582 (2010).

103. J. M. Dudley and S. Coen, "Coherence properties of supercontinuum spectra generated in photonic crystal and tapered optical fibers," Opt. Lett. **27**(13), 1180 (2002).

104. R. Paschotta, "fiber lasers," https://www.rp-photonics.com/fiber_lasers.html.

105. R. Paschotta, "harmonic mode locking," https://www.rp-photonics.com/harmonic_mode_locking.html.

106. S. Schilt, N. Bucalovic, V. Dolgovskiy, C. Schori, M. C. Stumpf, G. Di Domenico, S. Pekarek, A. E. H. Oehler, T. Südmeyer, U. Keller, and P. Thomann, "Fully stabilized optical frequency comb with sub-radian CEO phase noise from a SESAM-modelocked 15-µm solid-state laser," Opt. Express **19**(24), 24171 (2011).

107. K. Gürel, V. J. Wittwer, S. Hakobyan, S. Schilt, and T. Südmeyer, "Carrier envelope offset frequency detection and stabilization of a diode-pumped mode-locked Ti:sapphire laser," Opt. Lett. **42**(6), 1035 (2017).

108. A. Vernaleken, B. Schmidt, T. W. Hänsch, R. Holzwarth, and P. Hommelhoff, "Carrier-envelope frequency stabilization of a Ti:sapphire oscillator using different pump lasers: part II," Appl. Phys. B Lasers Opt. **117**(1), 33–39 (2014).

109. P. Castro-Marin, T. Mitchell, J. Sun, and D. T. Reid, "Characterization of a carrier-envelope-offset-stabilized blue- and green-diode-pumped Ti:sapphire frequency comb," Opt. Lett. **44**(21), 5270 (2019).

110. Q. Zhang, Y. Zhao, and Z. Wei, "Generation of sub-10fs pulses with repetition rate of 1.1 ghz from ti: Sapphire oscillator," in *Conference on Lasers and Electro-Optics/Pacific Rim 2009* (IEEE, 2009), (8), pp. 3–4.

111. U. Keller, "Ultrafast Solid State Lasers," Book (2007).

112. B. Stormont, I. G. Cormack, M. Mazilu, C. T. A. Brown, D. Burns, and W. Sibbett, "Low-threshold, multi-gigahertz repetition-rate femtosecond Ti:sapphire laser," Electron. Lett. **39**(25), 40–41 (2003).

113. D. Kopf, G. Zhang, R. Fluck, M. Moser, and U. Keller, "All-in-one dispersion-compensating saturable absorber mirror for compact femtosecond laser sources," Opt. Lett. **21**(7), 486 (1996).

114. T. Brabec, C. Spielmann, P. F. Curley, and F. Krausz, "Kerr lens mode locking," Opt. Lett. **17**(18), 1292 (1992).

115. G. Cerullo and S. De Silvestri, "Resonators for Kerr-lens mode-locked femtosecond Ti : sapphire lasers," **19**(11), 807–809 (1994).

Chapter 5: Graphene saturable absorbers for femtosecond pulse generation 164

Chapter 5: Graphene saturable absorbers for femtosecond pulse generation

5.1 Graphene background

Before talking about the applications of graphene for ultrafast lasers it is useful to understand a little about what graphene is. Graphene is essentially a single layer of carbon atoms arranged into a two-dimensional (2D) honeycomb lattice, which forms the basis of all other graphitic forms [1]. This includes graphene being wrapped into fullerenes, being rolled into carbon nanotubes or many layers being stacked to form graphite.

5.1.1 Discovery

Graphene has been studied theoretically as far back as 1947 by Wallace for the purpose of example calculations in solid-state physics text-books [2]. This included predicting the electronic structure and describing the linear dispersion relation which gives rise to graphene's unique conical energy bands (see Figure 99) [1]. McClure derived the wave equation for excitations in 1956 [3] which was later discussed by Semenoff [4], with parallels drawn to the Dirac equation.

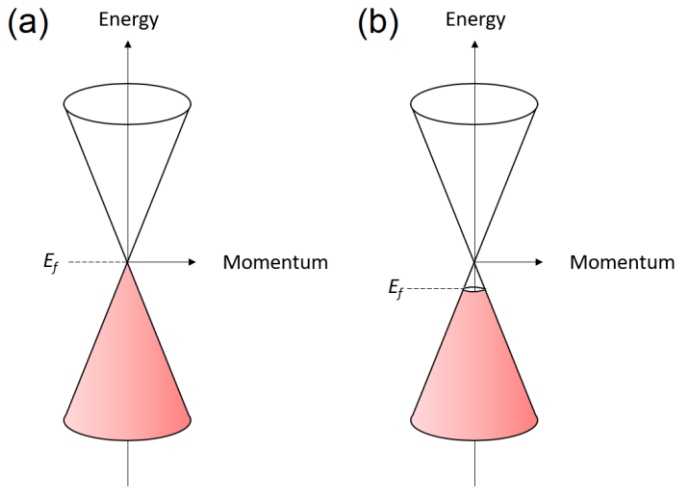

Figure 99. The conical energy bands of (a) pristine graphene and (b) graphene mounted on a substrate such as quartz. In the case of (b), mounting the graphene on a substrate has a doping effect that results in a shift in the Fermi level (see section 5.1.3.1).

Coming as a surprise to the science community, Geim and Novoselov published results on graphene, detailing the fabrication, identification, and characterisation with atomic force microscopy (AFM) in 2004 [5]. The mechanical exfoliation method, known as the "scotch tape" method, they used to extract thin layers of graphene from graphite crystal using adhesive tape

was simple and effective, with the extracted layers then transferred to a silicon substrate. They were able to both identify flakes consisting of a few layers and even flakes made up of only a single layer. They also successfully attached electrodes to these flakes in order to perform various experiments regarding its electronic properties [5].

5.1.2 2D materials

It is important to define what 2D materials or more specifically 2D crystals are. As one would expect, a single atomic layer is essentially a 2D material, while 100 atomic layers of a material would be considered a thin film of a 3D material [1]. The question is at what point is a structure considered 3D in terms of number of layers? There is no clear-cut answer on this, with even a few atomic layers of a material still regarded as 2D, but it usually comes down to the changes in the material's properties. Investigations into graphene show that its electronic structure significantly changes with addition of more layers, behaving like graphite (and thus becoming "3D") at around 10 layers [6].

At a single layer, also known as a monolayer, graphene has a simple electronic structure being a zero-gap semiconductor with one type of electron and one type of hole [1]. This is also true to a good approximation for its two-layer or bilayer version. When three or more layers are considered, the electronic structure becomes increasingly more complicated. For example, charge carriers appear and the conduction and valence bands begin to noticeably overlap [5]. The result is that monolayer, bilayer, and multi-layer (3 to 10 layers) graphene can be categorised as separate types of 2D crystals, with structures greater than 10 layers, as stated in the previous paragraph, considered as thin films of graphite.

5.1.2.1 Other 2D materials

While graphene was the first 2D material to be isolated, many other 2D materials have since been identified. This includes graphyne [7], borophene [8], germanene [9], phosphorene [10] and more [11], with some showing promise for ultrafast laser applications. In particular, black phosphorus has shown promise for femtosecond pulse generation around the 1-1.5 μm region [12,13]. $PtSe_2$ has also shown promise for picosecond pulse generation around the 1-1.5 μm region [14,15]. A useful review of non-carbon 2D materials for ultrafast photonics, including performance summaries for lasers passively Q-switched or mode-locked with non-carbon 2D material saturable absorbers, can be found in [16]. However, other 2D materials are beyond the scope of this thesis and will not be considered further.

5.1.3 Properties of graphene

Graphene has often been lauded as a wonder material due to its unique properties [17]. It is reportedly the strongest material ever tested with a breaking strength at 42 N/m [17], which is some 100 times greater than the strongest steel at 0.4 N/m [17]. When doped, the electrical conductivity is potentially very high, greater even than that of copper at room temperature [17]. The thermal conductivity has also been shown to be very high at around 1500-2500 $Wm^{-1}K^{-1}$ for suspended monolayer graphene compared to 401 $Wm^{-1}K^{-1}$ for copper [18], although this has been shown to reduce to around 500-600 $Wm^{-1}K^{-1}$ when monolayer graphene is placed on an amorphous substrate [19].

However, the most interesting properties in the context of this project are the optical properties. These include what is termed a "universal" absorption, saturable absorption, an ultrafast absorber relaxation time, and a nonlinear refractive index. These will be discussed in the following sub-sections.

5.1.3.1 Universal absorption

As a consequence of its unique electronic structure, the theoretical optical absorption spectrum of pristine monolayer graphene is predicted to be particularly simple and dependent solely upon the fine structure constant [20] leading to an absorption spectrum that is theoretically independent of wavelength. The fine structure constant is a fundamental constant that describes coupling between light and relativistic electrons and is more traditionally associated with quantum electrodynamics [20]. The fine structure constant is given by:

$$\alpha = \frac{e^2}{\hbar c} \approx \frac{1}{137} \tag{59}$$

The absorption of graphene over the infrared to visible range given by:

$$A_G = \pi\alpha \approx 2.3\% \tag{60}$$

This is the theoretical optical absorption for pristine graphene. However, in order for a practical device containing graphene to made, a supporting substrate must be used. This act of bonding graphene to a substrate will inevitably change the Fermi level (E_F) of graphene,

creating a slight bandgap. This has the effect of changing the optical conductivity σ, which is related to the absorption of graphene through the following equation:

$$A_G = \pi\alpha = \pi\frac{e^2}{\hbar c} = 4\pi c\sigma \tag{61}$$

The optical conductivity σ of graphene, which is a function of the optical frequency ω, the Fermi Level E_F and the temperature T is given by the following equation:

$$\sigma = \sigma_0\left[\frac{1}{2} + \frac{1}{72}\frac{(\hbar\omega)^2}{t^2}\right]\left(\tanh\frac{\hbar\omega + 2E_F}{4k_BT} + \tanh\frac{\hbar\omega - 2E_F}{4k_BT}\right) \tag{62}$$

where σ_0 is the optical conductivity of undoped graphene (where E_F = 0), t is the hopping parameter, k_B is the Boltzmann constant, e is the charge of an electron, $\hbar$ is the reduced Planck constant, and T is the temperature of the sample. When considering photon energies of < 2.4 eV (equivalent to $\lambda \approx$ 500 nm), the term $(\hbar\omega)^2/t^2$ can be neglected, since 1/72 × $(\hbar\omega)^2/t^2$ < 6 × 10^{-3} which is negligible in comparison to 1/2. The equation for the optical conductivity of graphene then reduces to:

$$\sigma(\omega, T) = \frac{\sigma_0}{2}\left[\tanh\left(\frac{\hbar\omega + 2E_F}{4k_BT}\right) + \tanh\left(\frac{\hbar\omega - 2E_F}{4k_BT}\right)\right] \tag{63}$$

It is apparent from the above equation that changes to the temperature and Fermi Level of the graphene sample will result in changes to the optical conductivity and therefore to the absorption. In order to use graphene in a practical device it is necessary to mount graphene onto some sort of transparent substrate such as quartz. This has the effect of altering the Fermi Level, which will then have consequences on optical conductivity and absorption of the monolayer graphene. This is observed and discussed in more detail in 5.4.1, where experiments were carried out with a spectrophotometer and the results subsequently analysed.

5.1.3.2 Saturable absorption

In order to find the macroscopic saturable absorber parameters (see section 1.4.7 of Chapter 1) of graphene, which are the saturable loss, non-saturable loss, and saturation fluence, the

correct theoretical model must be fitted to the experimental data of the saturable absorber curves. The following equation describes the saturation of an absorber [21,22]:

$$\frac{dq(t)}{dt} = \frac{q_0 - q(t)}{\tau_A} - \frac{q(t)I(t)}{F_{SAT,A}} \tag{64}$$

where $q(t)$ is the saturable loss or modulation depth, q_0 is the insertion loss, τ_A is the absorber recovery time, $I(t)$ is the intensity of incident light, and $F_{SAT,A}$ is the saturation fluence of the absorber. Graphene has a bitemporal relaxation time consisting of an initial fast component and a subsequent slow component [23]; however, for the sake of simplicity it is approximated as a fast saturable absorber [24]. Therefore, it is assumed that the pulse duration of the excitation pulse is much greater than τ_A. If the pulses are assumed to have a sech^2 pulse shape, then the loss of the absorber is given by [25]:

$$q(S) = \frac{q_S}{\sqrt{S(1+S)}} \tanh^{-1}\left(\sqrt{\frac{S}{1+S}}\right) + q_{NS} \tag{65}$$

where q_S is the saturable loss or modulation depth, q_{NS} is the non-saturable loss, and $S = F_p/F_{sat}$, which is the ratio of the pulse fluence to the saturation fluence of the graphene absorber. These parameters will be different depending on the number of layers of graphene, with the insertion loss, modulation depth and non-saturable loss all rising with increasing number of layers. These equations will be used in Section 5.4.6 where a monolayer graphene sample is characterised with the intention of using the sample to mode-lock a diode-pumped Ti:sapphire laser.

5.1.3.3 Nonlinear refractive index

Although graphene is claimed to possess a large nonlinear refractive index n_2, there is some dispute about the magnitude and sign. It has been reported to possess a giant nonlinear refractive index of 10^{-7} cm^2W^{-1} by Zhang et al. [26], which is about 9 orders of magnitude larger than bulk dielectrics. Other experimental works carried out by various authors have contradicted this [27,28], and there is also a lack of consensus amongst these reported results on the magnitude of n_2. Recent experimental results have reported an n_2 of -1.1×10^{-9} cm^2W^{-1} for monolayer graphene [29] In the past few years, several authors have carried out various

theoretical works suggesting that the sign of n_2 changes with Fermi Level E_F [30–32], which itself can be altered via doping [24] or by applying a voltage [33]. As the nonlinear refractive index of graphene is not exploited in this project it will not be considered further in this thesis.

5.1.3.4 Identification of the number of graphene layers

Identification of monolayer, bilayer, and multilayer graphene can be achieved through analysis of the Raman spectra of a sample [34]. Example Raman spectra of samples with graphene of various number of layers mounted on quartz are shown below in Figure 100. As can be seen from the Raman spectra of graphene layers with differing numbers of layers, there are some distinctive features. The two most intense features are the G peak just under 1600 cm^{-1} and the 2D peak around 2700 cm^{-1}, which is also sometimes referred to as the G' peak [35]. The 2D peak of graphene is a single sharp peak; however, for greater than one layer i.e. bilayer and above, the 2D peak is a superposition of at least two peaks and is thus a lot broader. The ratio of the intensity of the 2D peak to the G peak is roughly around 4:1 in monolayer graphene and reduces with increasing layers, until they are roughly similar in height for bulk graphite.

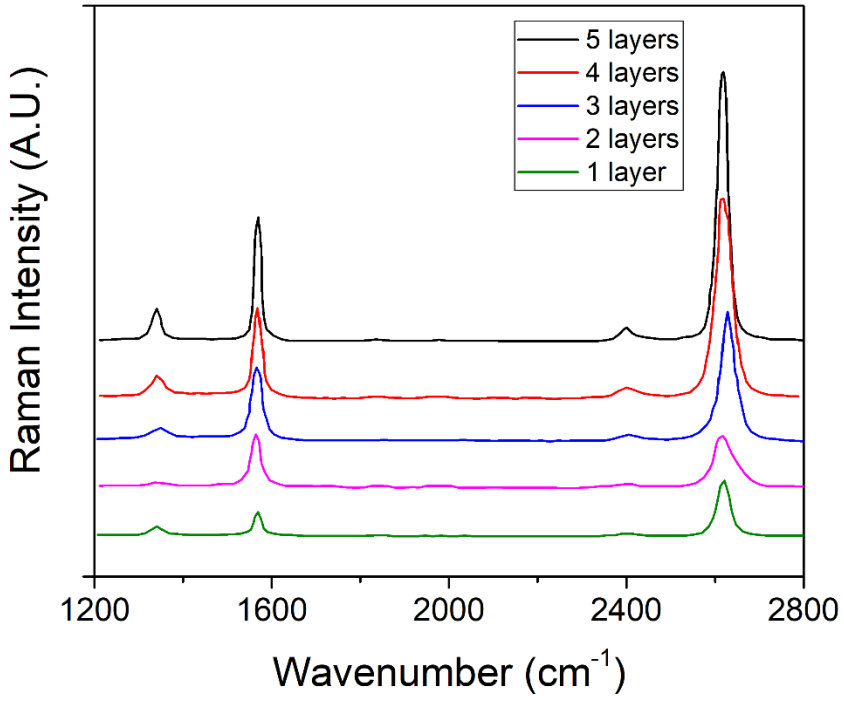

Figure 100. Example Raman spectra of various samples of graphene consisting of different numbers of layers (the spectra have been offset in the y-axis to make it easier to visualise). Adapted from [35].

The small peak sometimes seen around 1350 cm^{-1} is known as the D peak, and its presence is indicative of defects in the sample [35]. Therefore, when the D peak is small or absent this is an indication of good quality graphene. For more than 5 layers the Raman spectrum becomes nearly indistinguishable from bulk graphite and thus methods in addition to Raman spectroscopy may need to be used to quantify the number of layers [35].

5.2 Graphene production methods

As mentioned in section 5.1.1, graphene was first produced using the "scotch tape" method developed by Geim and Novoselov, which involves using adhesive tape to split graphite into graphene. Since then, various production methods have been developed and are currently used for the production of graphene. The most widely used methods are briefly discussed here.

5.2.1 Chemical Vapour Deposition

Chemical vapour deposition (CVD) is a common form of epitaxy (the deposition of a crystalline overlayer onto a crystalline substrate). More specifically, CVD is the process of the deposition of a solid material onto a heated substrate through either decomposition or chemical reaction of compounds contained in the gas passing over the substrate [36]. The gas passing over the surface contains the reactants, which are generally in either a gaseous or vapour state. Reactions then occur on or near the surface of the heated substrate, resulting in the deposition of atoms or molecules across the entire surface of the substrate.

There are various crystalline substrates upon which epitaxial graphene films can be grown such as silicon carbide [37], copper foils [38], and various others [39]. The chemical interaction can vary from strong to weak between the graphene layer and substrate, which has the effect of altering the properties of the graphene layer. For example, it has been shown that the Fermi Level is altered when bonded to the substrate, producing a slight band gap affecting the optical properties of graphene [24].

CVD is the most widely used method for the production of graphene used as a saturable absorber in ultrafast lasers as can be seen from Table 30. The advantage of CVD compared to other methods of graphene production is the ability to grow large area sheets of high optical quality graphene, with up to 7.5 m^2 demonstrated [40]. This is able to be transferred to a wide variety of substrates including quartz/fused silica, copper, and polymer [41].

One drawback of CVD is that it is expensive compared to other methods of graphene production at around 1-2 USD per cm^2 [42] compared to <0.1 USD per cm^2 for chemical exfoliation by graphene oxide reduction for example [43]. However, it should be noted that the graphene produced by chemical exfoliation is of inferior quality and production of a monolayer is not feasible [43].

5.2.2 Exfoliation

In chemistry, exfoliation is a process that essentially involves completely separating the layers of a layered material. The "scotch tape" method used to produce graphene is a type of mechanical exfoliation. Wedge-based exfoliation involves using a sharp single crystal diamond wedge to cleave layers from a graphite starting material [44]. Other exfoliation methods include sonication, graphite oxide reduction, molten salts, shearing, and electrochemical synthesis [45–49].

5.2.3 Nanotube slicing

Another method of producing graphene is nanotube slicing, where carbon nanotubes are cut open to form small sections of graphene. This can be done by cutting open multi-walled carbon nanotubes in a solution of potassium permanganate and sulphuric acid [50], or nanoribbons of graphene can be created by plasma-etching nanotubes that are partially embedded in a polymer film [51].

5.3 Review of lasers mode-locked with graphene

Several types of lasers have successfully been mode-locked using graphene, including various bulk solid-state lasers [52–55], fibre lasers [56–58], and VECSELs [59,60]. Depending on the type of laser, monolayer or multilayer graphene is used, with multiple layers offering larger modulation depths but also larger non-saturable losses. A brief review of the various graphene mode-locked lasers described in the literature is shown here in Table 1, which will be discussed the next few sections. The graphene mode-locked laser parameters recorded in the table are emission wavelength (λ), pulse duration (τ_D), and average output power (P_{av}). The graphene saturable absorber parameters recorded in the table are saturation fluence (F_{sat}), saturable loss (q_S), non-saturable loss (q_{NS}), and the fast and slow components of the absorber recovery time (τ_{R-fast} and τ_{R-slow} respectively). It should be noted that some of these parameters are not always given in the literature but Table 30 is completed where possible.

Table 30. Performance of various graphene mode-locked ultrafast lasers including saturable absorber parameters.

Year	Gain Medium	Graphene Type	λ (nm)	τ_D (fs)	P_{av} (mW)	F_{sat} (μJ/cm²)	q_S (%)	q_{NS} (%)	$\tau_{R\text{-}fast}$ (fs)	$\tau_{R\text{-}slow}$ (ps)	Growth Method	Reference
2012	Ti:sapphire	Monolayer	800	63	480	66.5	1.8	<0.9	-	1.47	CVD	[55]
2017			830	48	113	-	-	-	-	-	-	[52]
2015	Cr:LiSAF	Monolayer	850	68	11.5	28	0.62	1.9	128	1.63	CVD	[61]
2017			850	19	8.5	28	0.62	1.9	128	1.63	CVD	[62]
2011	Cr:Forsterite	Monolayer	1250	94	230	14.5	0.54	1.61	155	1.45	CVD	[63]
2013		Flakes	1250	97	137	15.8	0.11	2.28	170	1.02	Sonication	[64]
2016		Monolayer	1240	80	15	-	-	-	-	-	CVD	[65]
2018	Alexandrite	Monolayer	750	65	8	-	-	-	128	1.6	CVD	[66]
2013	Cr:YAG	Monolayer	1516	91	100	14	0.4	1.9	180	1.5	CVD	[67]
2013	Cr:ZnSe	Monolayer	2500	226	80	<14	<0.4	-	-	-	CVD	[67]
2014		Multilayer	2352	116	66	-	--		180	1285	CVD	[68]
2010	Er:Yb:Glass	Monolayer	1550	260	4.5	-	-	-	-	-	CVD	[69]
2012	Yb:KLuW	Monolayer	1040	160	160	50	0.75	1.59	200	1.5	CVD	[53]
2014	Yb:YAG	Monolayer	1048	367	1930	-	53.2	3.5	170	0.820	CVD	[70]
2014	Yb:YCOB	Multilayer	1037	152	53				180	1285	CVD	[68]
2016	Yb:CYA	Monolayer	1068	30	26.2	50	0.6-0.7	1.4-1.6	180	1.2	CVD	[71]
2010	Nd:YAG	Multilayer	1064	4,000	100	-	17.4	-	-	-	CVD	[72]
2011	$Nd:YVO_4$	-	1064	-	1000	-	-	-	-	-	-	[73]
2012	Tm:YAP	Oxide	2023	<10,000	268	-	-	-	-	-	Sonication	[74]
2013	$Tm:Lu_2O_3$	Monolayer	2067	410	270	-	-	<1	-	-	CVD	[75]
2014	Tm:CLNGG	Multilayer	2010	354	97	-	-	-	180	1285	CVD	[68]
2017	$Tm:MgWO_4$	Bilayer	2017	86	96	-	-	-	-	-	CVD	[76]
2009	Er:fibre	Polymer	1590	700	21	-	28.3	-	200	2.5 to 5	Chemical Exfoliation	[57]
2009		Multilayer	1576	415	51	0.71	66.5	-	-	-	CVD	[77]
2010			1559	460	-	-	1.3	34.3	-	-	Sonication	[78]
2012			1555	590	0.91	-	3.6	44.2	-	-	Exfoliation	[58]
2016		Monolayer	1570	980	-	-	28.5-47.7	50	-	-	CVD	[79]
2015	Er:fibre Tm:fibre	37 layers 24 layers	1559 1923	345 737	2.1 1.2	1-100	7.5 5.6	50 37.5	-	-	CVD	[80]
2016	Ho:fibre	Multilayer	2080	811	7	<110	1.8-2.84	5-10	-	-	CVD	[81]
2017	Tm:fibre	Multilayer	1950	205	13	250	13.9	38.3	-	-	CVD	[82]
2014	Yb:fibre	Oxide	1059.7 1057.1	189,000 2730	12.5 2.1	11.9	6.2	54	-	-	Sonication	[83]
2013	VECSEL	Monolayer	935-981	466-8,000	5-26	100	>0.9	~2	-	-	CVD	[59]
2014			949	466	12.5	100	5	0-10	-	-	CVD	[60]

5.3.1 Ti:sapphire lasers

Given the ultimate goal of this part of the project is to mode-lock a diode-pumped Ti:sapphire laser using a graphene saturable absorber, any demonstrations of Ti:sapphire lasers being mode-locked with graphene are the most pertinent to this work.

This was first achieved by Rotermund et al. in 2012, where a high-quality large-area monolayer graphene saturable absorber produced through CVD was used to mode-lock a Ti:sapphire laser. In this setup the graphene saturable absorber (GSA) was mounted on a quartz substrate and placed within a resonator arm at the focus of a pair of curved mirrors. Through nonlinear transmission experiments at 800 nm, they calculated various parameters of the GSA, including a saturation fluence of 66.5 $\mu J/cm^2$, a modulation depth of 1.8% and a non-saturable loss of <0.9%. With this setup near transform-limited 63 fs pulses were achieved with average output powers as high as 480 mW.

In 2017, femtosecond pulse generation was realised from a Ti:sapphire laser using a voltage-controlled GSA. By applying different bias voltages, the saturable absorber parameters of the GSA could be altered. This led to the generation of pulses as short as 48 fs at 830 nm, with average output powers of 113 mW.

In conclusion, these performance levels approach that which has been achieved with Ti:sapphire lasers mode-locked solely with SESAM devices, where output powers as high as 900 mW [84] and pulses as short as 16 fs [85] have been demonstrated. Commercial mode-locked Ti:sapphire laser systems using SESAMs with soliton mode-locking to generate femtosecond pulses and 800 mW average power are also now available [86]. This similarity in performance demonstrates that GSAs could potentially rival SESAMs for ultrashort pulse generation applications. It is also important to note that none of these demonstrations of GSA mode-locked Ti:sapphire have been diode-pumped, which is an aim of this project.

5.3.2 Other bulk solid-state lasers

Mode-locking with a graphene saturable absorber (GSA) has been demonstrated in many other bulk solid-state lasers. This includes various Cr-doped media such as Alexandrite, Cr:ZnSe, Cr:YAG, Cr:forsterite and Cr:LiSAF.

Femtosecond pulse operation has been demonstrated over a wide wavelength range in Cr-doped gain media mode-locked with graphene, from 750-2500 nm. Average output power ranges from a few mW to a maximum of 230 mW in Cr:Forsterite. Pulse durations range from

around 200 fs in Cr:ZnSe, with the shortest pulses of 19 fs achieved with Cr:LiSAF. These represent the shortest of any Cr-doped gain media mode-locked with graphene or indeed any laser mode-locked with graphene.

Various Yb-doped gain media such as Yb:YAG, Yb:CYA, and Yb:KLuW have also been successfully mode-locked with graphene, with emission at 1039-1068 nm. Average output powers range from a few 10's of mW up to almost 2 W in Yb:YAG. Pulse durations from around 367 fs in Yb:YAG , down to 30 fs in Yb:CYA .

Picosecond pulse operation has been demonstrated in graphene mode-locked Nd-doped media such as Nd:YAG and Nd:YVO_4. Emission occurs around 1064 nm, pulses as short as 4 ps have been demonstrated, and average output powers as high as 1 W .

In Tm-doped gain media such as Tm:YAP, Tm:$MgWO_4$, Tm:CNGG, and Tm:Lu_2O_3, pulses ranging from 10 ps down to 86 fs have been demonstrated using graphene mode-locking, over a wavelength range of 2010 to 2067 nm. This is with average output powers ranging from 96 to 270 mW.

5.3.3 Fibre lasers

Various fibre lasers have been mode-locked using graphene, mostly Er:fibre lasers but also Tm:fibre lasers, Ho:fibre lasers, and Yb:fibre lasers. In most cases several layers of graphene are used in the graphene saturable absorber element; however, in some cases a single layer or two layers are used. This is mainly because fibre lasers require a substantially higher modulation depth than bulk lasers, due to the stronger gain, nonlinear and dispersive effects in fibre lasers [87]. As the modulation depth (and non-saturable loss) scales with the number of graphene layers added [80], fibre lasers mostly require several layers in a graphene saturable absorber. This also has an effect on the onset of two-photon absorption, which results in an increase in absorption above a certain pulse fluence threshold, such that it occurs at lower fluence levels for an increasing number of layers of graphene [80].

5.3.4 VECSELs

Ultrashort pulse generation through graphene mode-locking has also been demonstrated in VECSELs (vertical external cavity surface emitting lasers). Pulse durations ranging from 8 ps down to 466 fs have been demonstrated, while average powers are limited to around 26 mW, over a wavelength range of 935-981 nm.

5.3.5 Discussion

To summarise, graphene has been shown to be a promising candidate for producing cheap saturable absorbers capable of mode-locking various types of lasers, from bulk solid-state lasers to fibre lasers and VECSELs. Various schemes incorporating a graphene saturable absorber into the laser have been demonstrated. A graphene absorber can be placed on a transparent substrate and inserted into the cavity at Brewster's angle, close to a beam waist for high fluence conditions [55]. Devices have been constructed that incorporate the graphene saturable absorber within a DBR mirror structure [60]. Graphene can even be deposited directly onto the ends of optical fibres [58], and also directly onto gain media potentially allowing for very compact mode-locked lasers [54].

In terms of performance pulses as short as a few tens of femtoseconds [62], average output powers from a few mW [80] to close to 2 W [70], and operation at various wavelengths ranging from 750 to 2500 nm have all been demonstrated [66,88].

The near-universal absorption [20] that allows coverage of a wide range of wavelengths with one device, is favourable compared to conventional SESAM devices that usually only offer coverage of much smaller specified wavelength operation ranges. It also potentially allows for an ultra-broad spectrum and therefore very short pulses (< 10 fs), as graphene acts as a non-resonant absorber similar to KLM.

Pulse durations as short as 19 fs [62], and average output powers close to 2 W [70] have been achieved with GSA mode-locked lasers, which is similar to what can be achieved with SESAM mode-locked lasers [84,85]. As stated in the previous paragraph graphene has potential for even shorter pulses (<10 fs), while SESAMs can usually only be used to generate pulses shorter than 50 fs through KLM assisted SESAM mode-locking [89].

As can be seen from Table 30 graphene naturally has an ultrafast bitemporal relaxation time consisting of a fast component (100-200 fs) and a slow component (1-1.5ps). In the femtosecond pulse regime, the slow component of a saturable absorber normally helps to start the initial pulse formation in the mode-locking process [22], while the modulation depth of the fast component determines the pulse duration at steady state [22].

This is advantageous compared to SESAMs, as to achieve these parameters with a SESAM low-temperature MBE must be used, which degrades optical quality as the non-saturable losses increase with reduced growth temperature [22]. This results in higher cavity losses which have

implications for achieving low-thresholds and thus efficient operation, and self-starting mode-locking.

The ability to tailor the graphene saturable absorber parameters, such as modulation depth, through the use of different numbers of layers [80] allows devices to be created that are suitable for various laser types, from bulk solid-state lasers to fibre lasers and VECSELs.

Finally, the ability to fabricate large areas of high-quality graphene relatively cheaply, simply, and rapidly through CVD is also favourable from a manufacturing point of view, as to create SESAM devices techniques such as molecular beam epitaxy (MBE) are required, which are expensive and time-consuming.

These aspects combine to form an attractive alternative to conventional saturable absorber devices based on SESAM technology.

5.4 Characterisation of the macro-optical parameters of monolayer graphene

The graphene samples in this project were sourced from commercial company Graphenea, who grew the samples via chemical vapour deposition, and then transferred them to a transparent optical-quality quartz substrate. A single-layer graphene structure was confirmed by the Raman spectra measurements performed by Graphenea. As stated in section 5.1.3.1, placing graphene on a substrate alters the Fermi Level, which in turn affects the optical properties. Thus, in order to use graphene in a practical device in a laser, the sample's macroscopic optical properties such as the saturation fluence, saturable loss, and the non-saturable loss must first be characterised. This is normally done by using an ultrafast laser in a differential transmission-based setup [80] or a reflection-based setup [90] depending on the mounting of the sample i.e. mounted on a transmissive substrate or on a reflective substrate. In this project a differential transmission based setup (detailed in section 5.4.3) was used as the samples were mounted on a transmissive substrate.

Another important measurement is that of the unsaturated linear transmission properties with respect to wavelength, which can be done with a spectrophotometer and is further discussed in the following section.

5.4.1 Spectrophotometer results

A commercial spectrophotometer (PerkinElmer LAMBDA 950) was used to characterise the graphene sample's transmission as a function of wavelength. As the graphene samples were mounted on a quartz substrate, it is important to separate and quantify the losses attributable

to the substrate from that of the graphene layer. To do this the sample transmission spectrum of the graphene and quartz substrate was measured, and the transmission spectrum of a bare quartz substrate (bare meaning without any deposited graphene) was also measured.

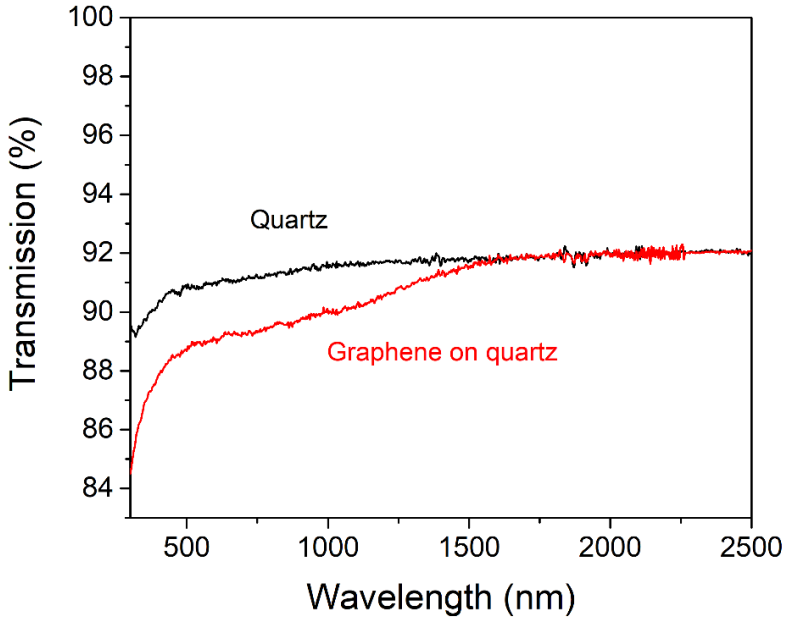

Figure 101. Transmission vs wavelength of bare quartz substrate and graphene on quartz substrate samples.

Shown above in Figure 101 is the measured transmission spectrum for graphene on a quartz substrate (T_{g+s}), and the transmission spectrum of the bare substrate (T_s). For a thin layer (defined by a thickness << λ) of material such as graphene, which is supported by a thick transparent substrate, the fractional change in transmittance is given by [91]:

$$\delta_T = \frac{T_{g+s} - T_s}{T_s} = \frac{2}{n_s + 1} A_G \tag{66}$$

where n_s is the refractive index of the quartz substrate, and A_G is the absorbance of the graphene film. This fractional change in transmittance is obtained through solving Maxwell's equations [91], assuming normal incidence. By rearranging this equation, it is possible to obtain the transmission solely due to the layer of graphene:

$$T_g = 1 - \left(\frac{n_s + 1}{2}\right)\left(\frac{1 - T_{g+s}}{T_s}\right) \tag{67}$$

In order to fully characterise the graphene on quartz substrate sample, the Fermi Level due to mounting the graphene itself on a quartz substrate is estimated. This is important as while pristine graphene has zero bandgap, to be of use in practical system the graphene must be mounted on a substrate. This mounting affects the Fermi Level creating a bandgap, which affects the transmission spectrum. The transmission spectrum of graphene is related to the optical conductivity (and hence the Fermi Level) via the following equation:

$$T_g = 1 - A_G = 1 - 4\pi c\sigma \tag{68}$$

As the optical conductivity σ is given by Equation 5, by inserting this into Equation 10 a new equation can be written for T_g that includes Fermi Level E_F and temperature T:

$$T_g = 1 - 4\pi c\left(\frac{\pi e^2}{4h}\left[\tanh\left(\frac{\hbar\omega + 2E_F}{4k_BT}\right) + \tanh\left(\frac{\hbar\omega - 2E_F}{4k_BT}\right)\right]\right) \tag{69}$$

By fitting the above equation to the data obtained for T_g, a value for the Fermi Level of the sample can be extracted, which is estimated to be E_F = 480 meV (see Figure 102).

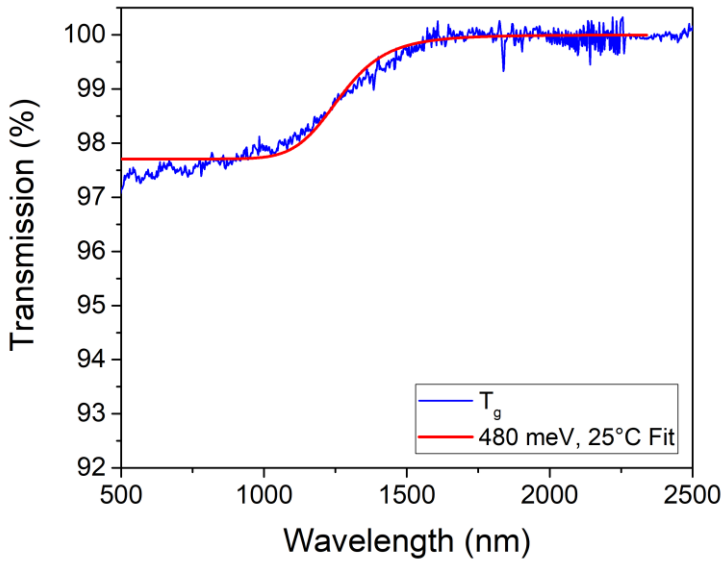

Figure 102. Transmission due to the graphene layer (given by Equation 9), and corresponding fit of Equation 11.

As shown in Figure 102, close to the predicted 2.3% absorption is obtained for the wavelength region of interest in this project (700-900 nm), coinciding well with the gain bandwidth of Ti:sapphire. The theoretical effect of different Fermi Level values is shown in Figure 103:

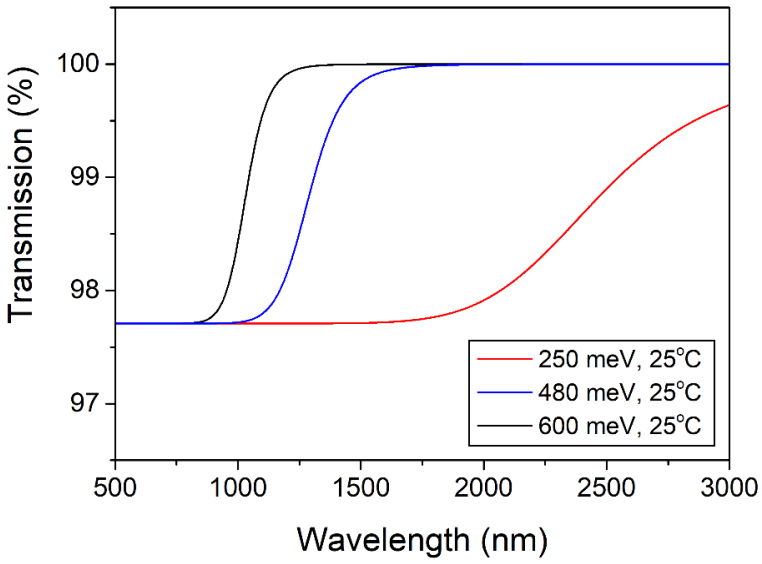

Figure 103. Example of theoretical transmission curves of graphene with various Fermi Level values E_F (250, 480 and 600 meV) at constant temperature (25°C).

It is apparent from Figure 103 that an increase in the Fermi Level results in a reduction of the wavelength range over which "universal absorbance" is obtained. It has been shown that the Fermi Level can be altered and controlled by applying a voltage to the graphene absorber [52]. However, for the purposes of this project the transmission spectrum wavelength range over which "universal absorption" is achieved is sufficient.

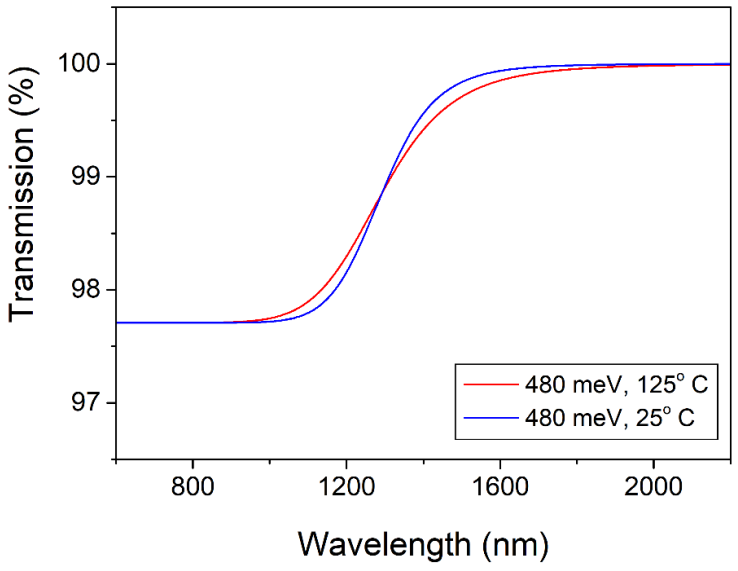

Figure 104. Example of theoretical transmission curves of graphene at two different temperatures (25°C and 125°C) with E_F = 480 meV.

The temperature of the sample also has an effect, albeit small, on the transmission spectrum of the graphene layer through changing the layer's optical conductivity. The effect is shown in

Figure 104, where the theoretical transmission spectrum of graphene is shown for E_F = 480 meV at 25°C and at 125°C.

5.4.2 Saturable absorption parameter characterisation

As the optimal saturable absorption parameters depend strongly on the laser system, it is important to precisely characterise and quantify these parameters, including saturable loss, non-saturable loss, and saturation fluence. For example, choosing an absorber with a low saturable loss or modulation depth (~1%), undesirable Q-switching instabilities can be suppressed [92].

To this end, various experimental setups have been devised to measure the saturable absorption parameters for nonlinear optical materials. Broadly speaking there are experimental setups based on transmission [93] and there are experimental setups based on reflection [90]. Which type of setup is used will depend on the geometry of the sample i.e. whether the graphene is placed on a transparent substrate or a reflective mirror.

5.4.3 Transmission experimental setup

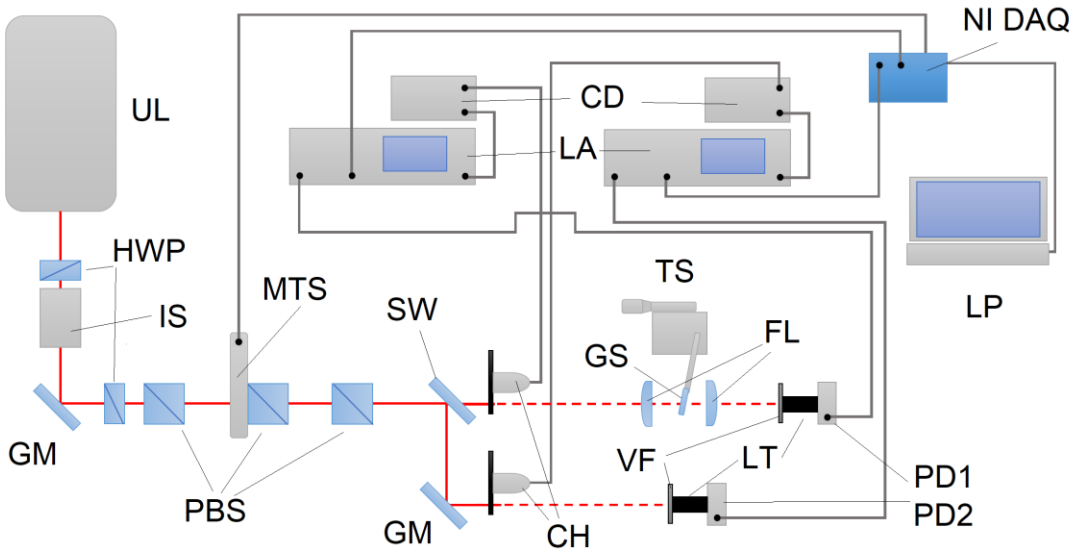

Figure 105. Schematic view of the differential transmission setup, where UL is ultrafast laser, HWP is half-wave plate, IS is optical isolator, GM is gold mirror, PBS is polarising beam splitter cube, MTS is motorised translation stage, SW is sapphire window, CH is chopper, GS is graphene sample, TS is translation stage, FL is focusing lens, VF is variable filter, LT is lens tube, PD1 and PD2 are the photodetectors, LP is the laptop, LA is lock-in amplifier, CD is chopper driver, NI DAQ is National Instruments data acquisition device.

The differential transmission experimental setup used for this project is shown in Figure 7. A commercial ultrafast Ti:sapphire laser (Sprite manufactured by M Squared Lasers) is used. This allows for sub-150 fs pulses to be delivered, with 80 MHz repetition rate and at average output powers of up to 1.5 W at 800 nm. The output beam quality is near diffraction-limited with $M^2 < 1.1$.

The output laser beam is passed through a half-wave plate (HWP) and a subsequent optical isolator. The HWP is used to rotate the polarisation of the laser beam exiting the laser so that it matches the input polariser of the isolator. The isolator is used to prevent harmful back-reflections entering the laser oscillator, which can cause undesirable mode-locking instabilities.

At the next stage, a combination of an achromatic HWP and polarising beam splitter cube (PBS) is used as a rough power attenuation stage to vary the pulse fluence at the sample. This is followed by another power attenuation stage used for fine adjustment of the laser power. It consists of an adjustable PBS, mounted on a motorised rotation stage and controlled via LabVIEW, and a fixed PBS.

Once the average power of the laser has been suitably attenuated and therefore the desired pulse fluence selected, the beam is split into two arms: the sample arm and the reference arm. For these experiments, a sapphire window was effectively used as a beam splitter, as the Fresnel reflection provided a sufficient signal for the reference arm, which in turn allowed more laser power to be available in the sample arm.

In the sample arm a 30 mm lens telescope is used to tightly focus the incoming 1.2 mm diameter beam to a 25 μm diameter spot to produce a high fluence upon the graphene sample. The beam waist was measured with a CCD camera (Thorlabs BC106N-VIS/M). The subsequent lens in the telescope is used to collimate the beam transmitted through the sample so that the beams are roughly the same size on the photodetectors in each arm.

Two amplified silicon photodetectors (New Focus 2032) were used: one to detect the light transmitted by the graphene sample in the signal arm (PD1), and one in the reference arm (PD2). These are essentially large-area photodiodes with a transimpedance amplifier. These photodetectors will output a voltage proportional to the optical power incident on the active area.

A reflective variable-ND filter was placed in front of each photodetector and used to attenuate the amount of light reaching the photodetectors. This was done for two reasons; to protect the photodetectors from damage or saturation and to equalise the signals in each arm when

no sample is present. Lens tubes were also added to the beam path of each photodetector to reduce the amount of scattered light reaching the detector.

Lock-in amplifiers were used to drastically reduce the noise present in the system by isolating the laser signal. The principle of operation of a lock-in amplifier relies on the orthogonality of sinusoidal functions; when a sinusoidal function of frequency f_1 is multiplied by another sinusoidal function of frequency f_2 (where $f_1 \neq f_2$) and integrated over a time much greater than the period of the two functions, the result of the integration is zero. However, if $f_1 = f_2$ and the two functions are in phase, the average result of the integration is equal to half the product of the two amplitudes. In other words, a lock-in amplifier takes a signal, multiplies it by the reference signal (either provided by the amplifier's internal oscillator or by an external source such as an optical chopper) and integrates over a specified time, which typically ranges from a few milliseconds to a few seconds. The result is a clean DC signal, where contributions from any signal not at precisely the same frequency as the reference signal are nearly completely attenuated.

In this way, a lock-in amplifier can extract a signal with a known carrier wave that is buried in a noisy environment. Signals up to a million times smaller than noise components can be reliably detected, depending on the amplifier's dynamic range [94]. An optical chopper (that modulates the laser signal at the reference frequency) and associated lock-in amplifier were used for each arm, so that the reference beam and signal beam could be more easily separated.

5.4.4 Differential transmission measurements

Despite using lock-in detection and careful shielding of the photodetectors, random intensity fluctuations in the probe laser's output can still cause issues. Even though these fluctuations are small, they are still significant as the aim is to measure small changes in transmission of <0.1%. To eliminate this, a differential transmission design is used for the experiment. The principle of differential transmission is as follows. There are two arms: the sample arm and the reference arm. In the sample arm changes are detected in the transmitted signal at various fluences due to the saturable absorption of the monolayer graphene sample. In the reference arm, the beam travels unhindered. The random intensity fluctuations in the laser output are replicated in both arms, therefore by subtracting the reference arm signal from the sample arm signal, the random intensity fluctuations can be eliminated leaving a clean signal given by T:

$$T = 1 - \left(\frac{V_2 - V_1}{V_2}\right) = 1 - \left(1 - \frac{V_1}{V_2}\right) = \frac{V_1}{V_2} \tag{70}$$

where V_1 is the voltage signal from the photodetector PD1 in the sample arm and V_2 is the voltage signal from the photodetector PD2 in the reference arm.

LabVIEW control is used both to control the running of the experiment by moving the PBS mount upon the motorised rotation mount in small increments (thus varying the fluence incident upon the graphene samples), and also to acquire and process the photodiode voltage signals filtered by the lock-in amplifier. The use of LabVIEW simultaneously saves time in comparison to manually taking measurements and also reduces the potential for human error.

Fluence in this context is defined as the optical energy delivered per unit area. It is a quantity often used in the context of saturable absorbers. To calculate the fluence of the beam incident upon the sample, the average power of the incident beam is measured using a Thorlabs power meter placed at the sample position. At the same time, the V_2 voltage output of PD2 in the reference arm is recorded. Using this data, a calibration curve can be produced:

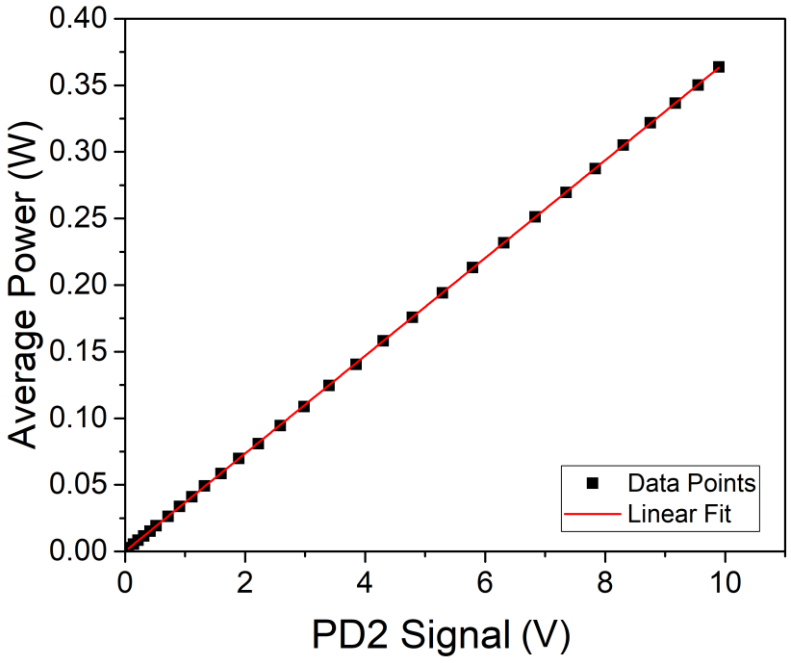

Figure 106. Calibration curve of the reference arm detector PD2 voltage vs average power of the incident beam at the sample position.

A straight-line equation can be extracted, which can subsequently be used to calculate the average power of the incident beam at the sample, using only the voltage signal detected in the reference arm. The average power P_{av}, along with the laser repetition rate f_{rep}, can be used to calculate the individual pulse energy E_p:

$$E_p = \frac{P_{av}}{f_{rep}} \tag{71}$$

The pulse energy, along with the incident beam waist at the sample ω_0 can be used to calculate the fluence F_p at the sample:

$$F_p = \frac{E_p}{\pi\omega_0^2} \tag{72}$$

5.4.5 Measurement of monolayer graphene and bare quartz substrate samples

To place the monolayer graphene sample in the telescope at the point where the beam waist is smallest, the sample is mounted on a Z-translation stage and placed roughly at the central point and at a slight angle to avoid any retro-reflections. The sample is then translated along the Z-axis around the mid-way point between the two 30 mm lenses. While doing this the live read out of the voltage signal V_1 is observed, looking out for any increase in this signal. An increase in the signal indicates that a higher percentage of the beam is being transmitted by the monolayer graphene sample. This indicates saturable absorption due to the increasing fluence, which itself is due to the reducing beam size. The fluence (and thus saturable absorption) for a given average laser power will be at a maximum at the beam waist. This then represents the optimum position as the highest fluences can be accessed here. The beam waist is therefore found by translating the sample and searching for a maximum in the voltage signal V_1.

Once this point is found, the automated LabVIEW program is run, which controls the laser fluence incident on the sample and records the filtered signal output from the lock-in amplifiers. Several experimental runs are taken to obtain average transmission values vs. fluence. This data can then be processed into a transmission versus fluence graph. Once this has been completed, the monolayer graphene sample is carefully replaced with bare quartz substrate sample and the process is repeated. At this point transmission versus fluence data for the monolayer graphene sample (T_{g+s}) and the bare quartz substrate sample (T_S) has been collected. The next step is to extract the transmission curve due solely to the monolayer graphene.

5.4.6 Calibration to remove influence of substrate from transmission spectra

It was noted that transmission spectra of the bare quartz substrate followed a repeatable pattern in terms of transmission vs V_2 signal, shown in Figure 107:

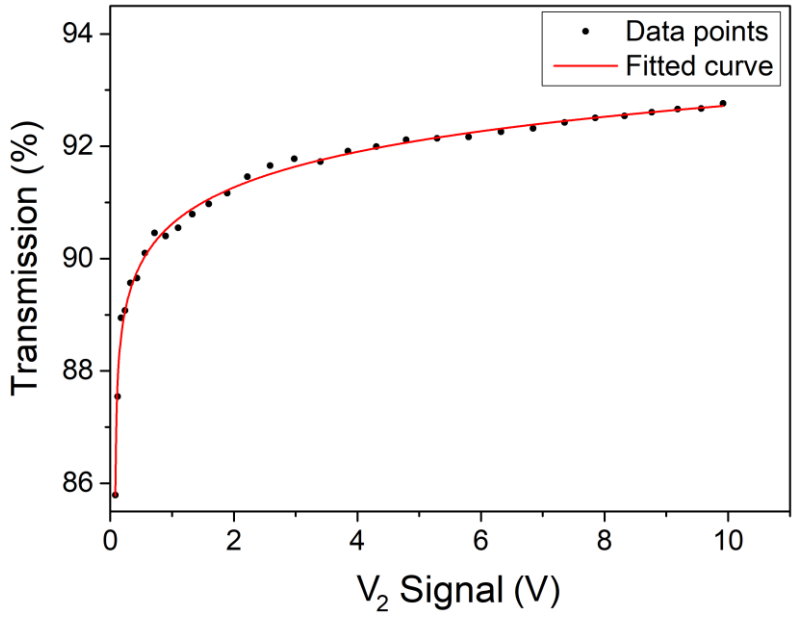

Figure 107. Transmission of bare quartz substrate vs. V_2 signal (volts).

This behaviour was attributed to the nonlinearity of the transimpedance amplifiers within the photodetectors used in the differential transmission setup. In order to attempt to remove this nonlinear influence from subsequent calculations of T_g, the logarithmic curve shown in Equation 15 was found to be a good fit with this data:

$$y = A + B\ln(x - C) \tag{73}$$

where A, B and C are constants. In this case $y = T_s$ and $x = V_2$ Signal in Volts. This provides a smooth curve for T_s and reduces the influence of noise on subsequent calculations of T_g. Using Equation 11 and the extracted parameters (A, B and C), T_s can then be calculated.

5.4.7 Calculation of T_g and extraction of saturable absorber parameters

By taking T_s and the raw experimental data for T_{g+s}, then inserting them into Equation 9, T_g can then be calculated - the transmission solely due to the monolayer graphene. This is done for several runs of T_{g+s} to obtain an averaged value for T_g further reducing noise.

The next step is to fit the equation for the transmission of the monolayer graphene T_g to the experimentally obtained results in order to extract the saturable absorber parameters. The equation is given by:

$$T_g = 1 - q(S) \tag{74}$$

where T_g is the transmission of the monolayer graphene and $q(S)$ is the loss due to the monolayer graphene as a function of S, the saturation parameter. The saturation parameter is the ratio of the incident pulse fluence F_p to the saturation fluence of the absorber F_{sat}. Expanding Equation 17 to include Equation 7, the following equation is obtained:

$$T_g = 1 - \frac{q_S}{\sqrt{S(1+S)}} \tanh^{-1}\left(\sqrt{\frac{S}{1+S}}\right) + q_{NS} \tag{75}$$

$$S = \frac{F_p}{F_{sat}} \tag{76}$$

This is implemented in Origin so that values for the parameters q_S, q_{NS}, and F_{sat} can be extracted upon fitting this equation to the data for T_g and F_p. The results are shown in Figure 108:

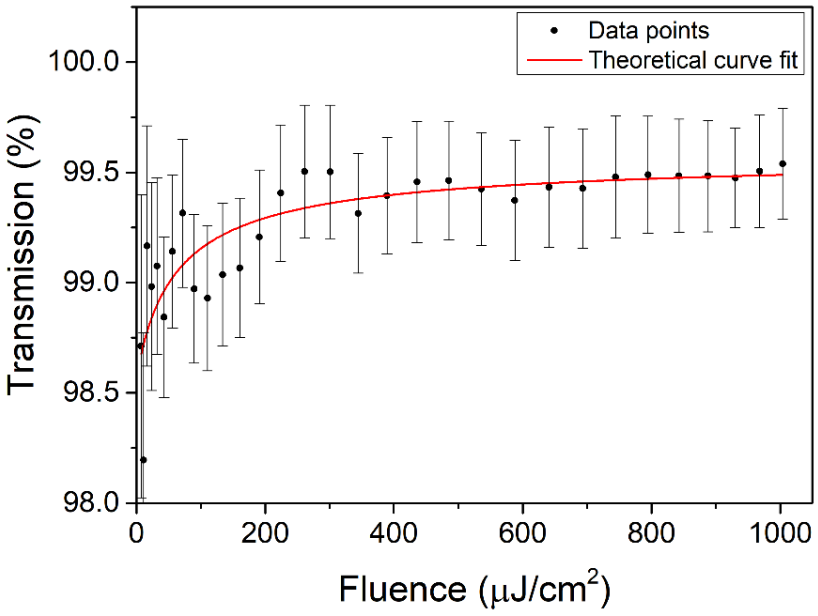

Figure 108. The transmission of the graphene samples vs. incident fluence

The following saturable absorber parameters were obtained via curve fitting: q_S = (1.01 ± 0.15)%, q_{NS} = (0.42 ± 0.09)%, and F_{sat} = (41 ± 27) μJ/cm^2. The saturation fluence measured is broadly in agreement with values reported in the literature for monolayer graphene, which range from 10-100 μJ/cm^2 [57,60]. The saturable loss measured is in a similar range (0.5-2%) to the values reported in the literature [55,63]. The non-saturable loss measured is slightly lower than that reported in the literature, which normally ranges from 1-2% [55,62]. These values suggest that the graphene samples are suitable for use as a saturable absorber in mode-locking a Ti:sapphire laser, based on what has been achieved in the literature [52,55].

5.5 Graphene saturable absorber mirror (GSAM)

Now that the macroscopic optical properties have been extracted for the monolayer graphene samples and verified to be in the suitable range for mode-locking Ti:sapphire lasers, this information can be used to design a laser mirror that incorporates a saturable absorber layer of graphene. This will be referred to as graphene saturable absorber mirror or GSAM. A layer of graphene incorporated into a laser mirror offers some advantages over one that is mounted on a transparent substrate, such as that demonstrated by Rotermund et al. [55]. It reduces the number of required intracavity elements by eliminating the need for a second beam waist within the cavity, which a transparent substrate mounted graphene absorber would require. Minimising the amount of intracavity elements, minimises residual losses and system complexity. It also offers a more environmentally stable and robust design, by encapsulating the graphene layer within the GSAM with a layer of material such as SiO_2 (see the following sections for more detail).

5.5.1 GSAM modelling using Essential Macleod

In order for a GSAM device to operate correctly, the layer of graphene must be placed at the correct depth with respect to the laser's intracavity electric field intensity. This process was modelled using a software package The Essential Macleod. This software package is used for the design, analysis, manufacture, and troubleshooting of thin film optical coatings. The laser mirror used for graphene layer incorporation was a high-reflector dielectric coating on a fused silica substrate. The dielectric coating comprised of 41 layers of SiO_2/Ta_2O_5 and was grown by LaserOptik GmbH.

A theoretical explanation of the optimal placement of the graphene layer within a Bragg reflector is given by Zaugg et al. and is reproduced here [95]. Incoming light with an intensity normalised to 1 creates a standing wave pattern within the mirror structure from the incoming

and reflected waves [96]. The field intensity enhancement factor ξ is defined as the maximum field intensity relative to the incoming field intensity [95]. The field intensity enhancement factor $\xi(z)$ at a distance z from the mirror surface can be written as:

$$\xi(z) = \frac{|\epsilon_{in}(z) + \epsilon_{out}(z)|^2}{|\epsilon_{in}(z)|^2} \tag{77}$$

where ϵ_{in} and ϵ_{out} are the electric fields of the reflected and incident waves given by:

$$\epsilon_{in/out}(z) = \epsilon_{in/out,0} e^{-i(\omega t \pm k_n z)} \tag{78}$$

where $k_n = 2\pi n/\lambda$ is the wave number in the material, n is the refractive index of the material in which the light is propagating, and λ is the wavelength. Using Equation 19, the field intensity enhancement for an anti-resonant reflection mirror without any additional coating is given by:

$$\xi(z) = \frac{|\epsilon_{in}(z) + \epsilon_{out}(z)|^2}{|\epsilon_{in}(z)|^2} = |2isin(k_n z)|^2 = 4\sin^2\left(\frac{2\pi n_{air} z}{\lambda}\right) \tag{79}$$

where n_{air} is the refractive index of air. By changing the optical distance z between the mirror surface and the layer of graphene, it is possible to alter the amount of light the graphene absorbs. The amount of light that the monolayer of graphene absorbs becomes $\alpha\xi_{abs}$, where $\alpha \approx 2.3\%$ is the absorption of pristine, undoped graphene, and ξ_{abs} is the field intensity enhancement at the location of the graphene absorber.

As an example, if a monolayer of graphene is placed directly onto the mirror surface (i.e. at z = 0), then ξ_{abs}= 0 is obtained, and therefore no absorption due to destructive interference between the incoming and reflected waves. If the monolayer of graphene is placed at $z = \lambda/4$, then ξ_{abs}= 4 and the absorption will increase to 400% (i.e. 4 × 2.3% ≈ 9.2%) due to constructive interference. This means that the non-saturated absorption can be controlled to some extent, along with the modulation depth and non-saturable loss, depending on the position of the layer of graphene.

5.5.2 GSAM designs

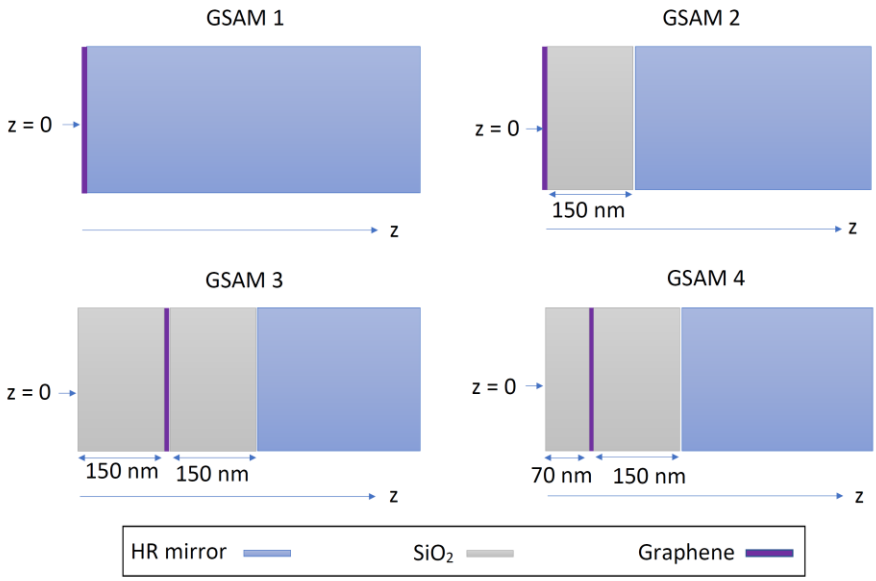

Figure 109. Simplified diagrams of GSAM samples, showing placement of graphene layer and additional layers of SiO_2. Note that the mirror substrate thickness is the same throughout and that the above diagrams are for reference only.

Various designs were created based on this work, a summary of which can be seen in Table 31 and simplified diagrams in Figure 109, with each design possessing a different optical field intensity enhancement factor. The distance from the surface (z) represents the position of the graphene layer with respect to the surface of the GSAM e.g. a position of 0 represents the graphene deposited directly on the surface of the GSAM. It should be noted that some designs contained additional layers of SiO_2 acting as a spacer and altering the field intensity enhancement at the graphene layer. More detail on the position and thickness of the SiO_2 layers of the various designs are given in the following paragraphs.

Table 31. Parameters of the various graphene saturable absorber mirror designs.

GSAM Sample Number	z (nm)	ξ	Expected Insertion Loss α × ξ (%)
1	0	0	0
2	0	3.8	8.7
3	150	1.8	4.1
4	150	1	2.3

Initially GSAM sample 1 was fabricated. At this point the field enhancement factor had not been considered and as such no modelling of the mirrors had been undertaken using the Essential Macleod software. Therefore GSAM 1 had the graphene layer deposited directly

upon the mirror surface, where the field enhancement factor for this design was later calculated to be 0.

GSAM 2 first had a 150 nm thick layer of SiO_2 deposited on the HR mirror surface. A single layer of graphene was deposited upon this and was calculated to have a field enhancement factor of 3.8.

GSAM 3 also had an initial 150 nm-thick layer of SiO_2 deposited on the HR mirror surface. A single layer of graphene was deposited on this, and a further 150 nm-thick layer of SiO_2 was then deposited on this. The field enhancement factor was calculated to be 1.8.

GSAM 4 also had an initial 150 nm-thick layer of SiO_2 deposited on the HR mirror surface. A single layer of graphene was deposited on this and a further 70 nm-thick layer of SiO_2 was then deposited on this. The field enhancement factor was calculated to be 1.

5.6 Initial graphene mode-locking tests

The initial design (GSAM 1) was the first used in the laser. A CW regime diode-pumped Ti:sapphire laser was configured in a similar layout to the SESAM diode-pumped Ti:sapphire laser shown in Chapter 3, Figure 5,with a HR end mirror used in place of the SESAM. After substituting the HR end mirror with the GSAM, some power drop would be expected due to insertion loss of the GSAM, similar to that as witnessed when the SESAM was installed in Chapter 3. However, virtually no power drop was witnessed indicating that the intracavity field was not interacting with graphene layer at all or very little. In hindsight this actually makes sense as manufacturers will design mirrors in this way such that there is a node at the mirror surface in order to avoid damage to the mirror [95].

With this in mind, a closer look at the design of the mirrors was taken. With information on the layer parameters (thickness, material, refractive index) received from the manufacturer Laseroptik, the Essential Macleod software was used to model and optimise various designs with respect to graphene layer placement and field enhancement factor. This is discussed in the following sub-section.

5.6.1 Further graphene mode-locking tests

As described in 5.5.2, three further designs were produced with varying levels of field intensity enhancement factors using the Essential Macleod software; GSA 2, GSA 3 and GSA 4. When GSA 2 was placed in the resonator, significant output power drop was witnessed, from 700 mW before GSA 2 was inserted to around 85 mW after. No spectral broadening was detected

on the OSA and no RF signal was detected on the fast photodiode, both of which would give an indication of mode-locked operation. With a field enhancement factor of 3.8, the absorption would be $\alpha\xi$ = 2.3% × 3.8 = 8.7%. This a large amount of absorption therefore it makes sense that such a significant power drop would be seen.

It was therefore hoped that GSA designs 3 and 4 would provide the optimal saturable absorber parameters for mode-locking. Unfortunately, when these GSAM designs were placed into the diode-pumped Ti:sapphire laser, no lasing action was achieved. It was possible to achieve CW operation near the edges of the GSA 3; however, the output power was very low and obtaining mode-locked operation was not possible. It is believed that full coverage of the mirror substrate surface was not achieved and as such no graphene layer was located at this position, hence the losses were lower and as such lasing, albeit with very low output power, was achievable. Further work is needed to determine why mode-locking was not achieved and why lasing was only achieved using the edge of GSAM 3. This is discussed in the future work section.

5.7 Discussion and future work

To summarise/conclude novel graphene-based saturable laser mirrors were designed and characterised for passive mode-locking in the near-IR range. From the differential transmission measurements of a monolayer graphene on quartz substrate sample the saturation fluence was determined to be (41 ± 27) μJ/cm^2, the saturable loss to be (1.01 ± 0.15) % and the non-saturable loss to be (0.42 ± 0.09) %. The values for these parameters are in broad agreement with other's work on monolayer graphene, with saturation fluences ranging from 10 to 100 μJ/cm^2 for a monolayer of graphene [60,88], modulation depth ranging from 0.5% to 2% [55,63], and non-saturable losses ranging from 1% to 2% [55,62]. The values obtained in this project are in the suitable range for passive mode-locking of solid-state lasers given the low saturation fluence, the low non-saturable loss, and the small saturable loss. The saturable absorber parameters for the monolayer graphene samples are comparable to typical saturable absorber parameters of SESAMs used for mode-locking of bulk solid-state lasers [84,85].

More investigation is needed to ascertain why mode-locking was unable to be achieved with any of these designs, or indeed even lasing in the case of GSAMs 3 and 4. There are various techniques/tests that would be useful to pin down a root cause.

The first avenue to investigate would be to directly measure the saturable absorber parameters of the mirror samples. Previously, only the saturable absorber parameters of the graphene samples mounted on a fused silica substrate were measured, and not the saturable absorber parameters of the GSAM devices. The problem with this is that it is assumed that the manufacturing process has worked exactly as expected and that no manufacturing defects were introduced at any stage of the process. Given that the GSAMs were built in several stages and were transported back and forth from SLS, Graphenea and FCAP, it is feasible that some contamination could have been introduced at some point affecting the device performance.

Additionally, the unknown nonlinear refractive index (n_2) of the GSAM devices could potentially have an effect on the mode-locking regime. Experiments to quantify the n_2 parameter could be undertaken, using the z-scan technique for example [26], however, this would have to be undertaken using graphene on a transparent substrate, and again this may present issues with the sample being measured not in the same configuration as the final device design used.

As detailed in section 5.1.3.4, Raman spectroscopy of the samples would be a useful tool in detecting whether graphene is present, what form it takes (e.g. monolayer, bilayer etc.), and also to determine how uniform the graphene layer is.

Measuring the GSAM samples' saturable absorber parameters would require reworking the existing differential transmission such that it would operate on reflection. This type of setup is described by Maas et al. where they use a high-sensitivity reflection-based setup to achieve an accuracy of <0.05% over a dynamic range of 10^4 [90]. To do this would represent a substantial amount of work as the experimental setup would have to be significantly altered and the LabVIEW code would also have to be largely rewritten.

To conclude, there is still work to be done before graphene-based saturable absorbers will rival semiconductor saturable absorbers for solid state lasers. In the context of the work described here, depending on results from the suggested further investigations as to why the GSAM devices did not work as expected, optimisation and better control of the manufacturing process could lead to GSAMs capable of mode-locking solid-state lasers. Successfully mode-locking the diode-pumped Ti:sapphire laser described in section 5.6 with an improved GSAM device would then allow a direct comparison to be made between the SESAM mode-locked diode-pumped Ti:sapphire laser described in Chapter 3.

5.8 References

1. A. K. Geim and K. S. Novoselov, "The rise of graphene," Nat. Mater. **6**(3), 183–191 (2007).
2. P. R. Wallace, "The Band Theory of Graphite," Phys. Rev. **71**(9), 622–634 (1947).
3. J. W. McClure, "Diamagnetism of Graphite," Phys. Rev. **104**(3), 666–671 (1956).
4. G. W. Semenoff, "Condensed-Matter Simulation of a Three-Dimensional Anomaly," Phys. Rev. Lett. **53**(26), 2449–2452 (1984).
5. K. S. Novoselov, A. K. Geim, S. V Morozov, D. Jiang, Y. Zhang, S. V Dubonos, I. V Grigorieva, and A. A. Firsov, "Electric Field Effect in Atomically Thin Carbon Films," Science (80-.). **306**(5696), 666–669 (2004).
6. B. Partoens and F. M. Peeters, "From graphene to graphite: Electronic structure around the K point," Phys. Rev. B **74**(7), 075404 (2006).
7. D. Malko, C. Neiss, F. Viñes, and A. Görling, "Competition for graphene: Graphynes with direction-dependent dirac cones," Phys. Rev. Lett. **108**(8), 1–4 (2012).
8. A. J. Mannix, X.-F. Zhou, B. Kiraly, J. D. Wood, D. Alducin, B. D. Myers, X. Liu, B. L. Fisher, U. Santiago, J. R. Guest, M. J. Yacaman, A. Ponce, A. R. Oganov, M. C. Hersam, and N. P. Guisinger, "Synthesis of borophenes: Anisotropic, two-dimensional boron polymorphs," Science (80-.). **350**(6267), 1513–1516 (2015).
9. P. Bampoulis, L. Zhang, A. Safaei, R. van Gastel, B. Poelsema, and H. J. W. Zandvliet, "Germanene termination of Ge 2 Pt crystals on Ge(110)," J. Phys. Condens. Matter **26**(44), 442001 (2014).
10. L. Li, Y. Yu, G. J. Ye, Q. Ge, X. Ou, H. Wu, D. Feng, X. H. Chen, and Y. Zhang, "Black phosphorus field-effect transistors," Nat. Nanotechnol. **9**(5), 372–377 (2014).
11. M. Xu, T. Liang, M. Shi, and H. Chen, "Graphene-Like Two-Dimensional Materials," Chem. Rev. **113**(5), 3766–3798 (2013).
12. X. Jin, G. Hu, M. Zhang, Y. Hu, T. Albrow-Owen, R. C. T. Howe, T.-C. Wu, Q. Wu, Z. Zheng, and T. Hasan, "102 fs pulse generation from a long-term stable, inkjet-printed black phosphorus-mode-locked fiber laser," Opt. Express **26**(10), 12506 (2018).
13. X. Su, Y. Wang, B. Zhang, R. Zhao, K. Yang, J. He, Q. Hu, Z. Jia, and X. Tao, "Femtosecond solid-state laser based on a few-layered black phosphorus saturable absorber," Opt. Lett. **41**(9), 1945 (2016).
14. B. Huang, L. Du, Q. Yi, L. Yang, J. Li, L. Miao, C. Zhao, and S. Wen, "Bulk-structured PtSe 2 for femtosecond fiber laser mode-locking," Opt. Express **27**(3), 2604 (2019).
15. L. Tao, X. Huang, J. He, Y. Lou, L. Zeng, Y. Li, H. Long, J. Li, L. Zhang, and Y. H. Tsang, "Vertically standing PtSe 2 film: a saturable absorber for a passively mode-locked Nd:LuVO 4 laser," Photonics Res. **6**(7), 750 (2018).
16. B. G. Bo Guo, "2D noncarbon materials-based nonlinear optical devices for ultrafast photonics [Invited]," Chinese Opt. Lett. **16**(2), 020004 (2018).
17. Y. Kopelevich and I. A. Luk'yanchuk, "Graphite vs graphene: scientific background," Nobel Prize Phys. 2010 **50005**(October), 0–10 (2010).
18. W. Cai, A. L. Moore, Y. Zhu, X. Li, S. Chen, L. Shi, and R. S. Ruoff, "Thermal transport in suspended and supported monolayer graphene grown by chemical vapor deposition," Nano Lett. **10**(5), 1645–1651 (2010).
19. J. H. Seol, I. Jo, A. L. Moore, L. Lindsay, Z. H. Aitken, M. T. Pettes, X. Li, Z. Yao, R. Huang, D. Broido, N. Mingo, R. S. Ruoff, and L. Shi, "Two-Dimensional Phonon Transport in Supported Graphene," Science (80-.). **328**(5975), 213–216 (2010).
20. R. R. Nair, P. Blake, A. N. Grigorenko, K. S. Novoselov, T. J. Booth, T. Stauber, N. M. R. Peres, and A. K. Geim, "Fine Structure Constant Defines Visual Transparency of Graphene," Science (80-.). **320**(5881), 1308–1308 (2008).
21. G. P. Agrawal and N. A. Olsson, "Self-Phase Modulation and Spectral Broadening of Optical Pulses in Semiconductor Laser Amplifiers," IEEE J. Quantum Electron. **25**(11), 2297–2306 (1989).
22. U. Keller, *Ultrafast Solid State Lasers* (2007).
23. R. W. Newson, J. Dean, B. Schmidt, and H. M. van Driel, "Ultrafast carrier kinetics in exfoliated graphene and thin graphite films.," Opt. Express **17**(4), 2326–2333 (2009).
24. C. C. Lee, J. M. Miller, and T. R. Schibli, "Doping-induced changes in the saturable absorption of monolayer graphene," Appl. Phys. B Lasers Opt. **108**(1), 129–135 (2012).

25. T. R. Schibli, E. R. Thoen, F. X. Kärtner, and E. P. Ippen, "Suppression of Q-switched mode locking and break-up into multiple pulses by inverse saturable absorption," Appl. Phys. B Lasers Opt. **70**(SUPPL. 1), 41–49 (2000).

26. H. Zhang, S. Virally, Q. Bao, L. Kian Ping, S. Massar, N. Godbout, and P. Kockaert, "Z-scan measurement of the nonlinear refractive index of graphene," Opt. Lett. **37**(11), 1856 (2012).

27. E. Hendry, P. J. Hale, J. Moger, A. K. Savchenko, and S. A. Mikhailov, "Coherent nonlinear optical response of graphene," Phys. Rev. Lett. **105**(9), 1–4 (2010).

28. L. Miao, Y. Jiang, S. Lu, B. Shi, C. Zhao, H. Zhang, and S. Wen, "Broadband ultrafast nonlinear optical response of few-layers graphene: toward the mid-infrared regime," Photonics Res. **3**(5), 214 (2015).

29. E. Dremetsika, B. Dlubak, S.-P. Gorza, C. Ciret, M.-B. Martin, S. Hofmann, P. Seneor, D. Dolfi, S. Massar, P. Emplit, and P. Kockaert, "Measuring the nonlinear refractive index of graphene using the optical Kerr effect method," Opt. Lett. **41**(14), 3281 (2016).

30. K. J. A. Ooi, L. K. Ang, and D. T. H. Tan, "Waveguide engineering of graphene's nonlinearity," Appl. Phys. Lett. **105**(11), 111110 (2014).

31. J. L. Cheng, N. Vermeulen, and J. E. Sipe, "Numerical study of the optical nonlinearity of doped and gapped graphene: From weak to strong field excitation," Phys. Rev. B **92**(23), 235307 (2015).

32. B. Semnani, R. Jago, S. Safavi-Naeini, H. Majedi, E. Malic, and P. Tassin, "Anomalous optical saturation of low-energy Dirac states in graphene and its implication for nonlinear optics," 2D Mater. **6**(3), 031003 (2019).

33. I. Baylam, S. Ozharar, N. Kakenov, C. Kocabas, and A. Sennaroglu, "Femtosecond pulse generation from a Ti^3+:sapphire laser near 800 nm with voltage reconfigurable graphene saturable absorbers," Opt. Lett. **42**(7), 1404 (2017).

34. A. C. Ferrari, J. C. Meyer, V. Scardaci, C. Casiraghi, M. Lazzeri, F. Mauri, S. Piscanec, D. Jiang, K. S. Novoselov, S. Roth, and A. K. Geim, "Raman spectrum of graphene and graphene layers," Phys. Rev. Lett. **97**(18), 1–4 (2006).

35. Q. Bao, H. Zhang, Y. Wang, Z. Ni, Y. Yan, Z. X. Shen, K. P. Loh, and D. Y. Tang, "Atomic-Layer Graphene as a Saturable Absorber for Ultrafast Pulsed Lasers," Adv. Funct. Mater. **19**(19), 3077–3083 (2009).

36. K. Choy, "Chemical vapour deposition of coatings," Prog. Mater. Sci. **48**(2), 57–170 (2003).

37. Z. Y. Juang, C. Y. Wu, C. W. Lo, W. Y. Chen, C. F. Huang, J. C. Hwang, F. R. Chen, K. C. Leou, and C. H. Tsai, "Synthesis of graphene on silicon carbide substrates at low temperature," Carbon N. Y. **47**(8), 2026–2031 (2009).

38. W. Liu, H. Li, C. Xu, Y. Khatami, and K. Banerjee, "Synthesis of high-quality monolayer and bilayer graphene on copper using chemical vapor deposition," Carbon N. Y. **49**(13), 4122–4130 (2011).

39. J. Plutnar, M. Pumera, and Z. Sofer, "The chemistry of CVD graphene," J. Mater. Chem. C **6**(23), 6082–6101 (2018).

40. W. Ren and H. M. Cheng, "The global growth of graphene," Nat. Nanotechnol. **9**(10), 726–730 (2014).

41. K. S. Kim, Y. Zhao, H. Jang, S. Y. Lee, J. M. Kim, K. S. Kim, J. H. Ahn, P. Kim, J. Y. Choi, and B. H. Hong, "Large-scale pattern growth of graphene films for stretchable transparent electrodes," Nature **457**(7230), 706–710 (2009).

42. T. H. Bointon, M. D. Barnes, S. Russo, and M. F. Craciun, "High Quality Monolayer Graphene Synthesized by Resistive Heating Cold Wall Chemical Vapor Deposition," Adv. Mater. **27**(28), 4200–4206 (2015).

43. Z. Ereš and S. Hrabar, "Low-cost synthesis of high-quality graphene in do-it-yourself CVD reactor," Automatika **59**(3–4), 254–260 (2018).

44. B. Jayasena and S. Subbiah, "A novel mechanical cleavage method for synthesizing few-layer graphenes," Nanoscale Res. Lett. **6**(1), 95 (2011).

45. K. R. Paton, E. Varrla, C. Backes, R. J. Smith, U. Khan, A. O'Neill, C. Boland, M. Lotya, O. M. Istrate, P. King, T. Higgins, S. Barwich, P. May, P. Puczkarski, I. Ahmed, M. Moebius, H. Pettersson, E. Long, J. Coelho, S. E. O'Brien, E. K. McGuire, B. M. Sanchez, G. S. Duesberg, N. McEvoy, T. J. Pennycook, C. Downing, A. Crossley, V. Nicolosi, and J. N. Coleman, "Scalable production of large quantities of defect-free few-layer graphene by shear exfoliation in liquids," Nat. Mater. **13**(6), 624–630 (2014).

46. A. R. Kamali and D. J. Fray, "Molten salt corrosion of graphite as a possible way to make carbon nanostructures," Carbon N. Y. **56**, 121–131 (2013).

47. M. Hofmann, W.-Y. Chiang, T. D Nguyễn, and Y.-P. Hsieh, "Controlling the properties of graphene produced by electrochemical exfoliation," Nanotechnology **26**(33), 335607 (2015).

48. Y. Hernandez, V. Nicolosi, M. Lotya, F. M. Blighe, Z. Sun, S. De, I. T. McGovern, B. Holland, M. Byrne, Y. K. Gun'Ko, J. J. Boland, P. Niraj, G. Duesberg, S. Krishnamurthy, R. Goodhue, J. Hutchison, V. Scardaci, A. C. Ferrari, and J. N. Coleman, "High-yield production of graphene by liquid-phase exfoliation of graphite," Nat. Nanotechnol. **3**(9), 563–568 (2008).

49. S. Eigler, M. Enzelberger-Heim, S. Grimm, P. Hofmann, W. Kroener, A. Geworski, C. Dotzer, M. Röckert, J. Xiao, C. Papp, O. Lytken, H.-P. Steinrück, P. Müller, and A. Hirsch, "Wet Chemical Synthesis of Graphene," Adv. Mater. **25**(26), 3583–3587 (2013).

50. D. V. Kosynkin, A. L. Higginbotham, A. Sinitskii, J. R. Lomeda, A. Dimiev, B. K. Price, and J. M. Tour, "Longitudinal unzipping of carbon nanotubes to form graphene nanoribbons," Nature **458**(7240), 872–876 (2009).

51. L. Jiao, L. Zhang, X. Wang, G. Diankov, and H. Dai, "Narrow graphene nanoribbons from carbon nanotubes," Nature **458**(7240), 877–880 (2009).

52. I. Baylam, S. Ozharar, N. Kakenov, C. Kocabas, and A. Sennaroglu, "Femtosecond pulse generation from a Ti^3+:sapphire laser near 800 nm with voltage reconfigurable graphene saturable absorbers," Opt. Lett. **42**(7), 1404 (2017).

53. E. Ugolotti, A. Schmidt, V. Petrov, J. Wan Kim, D.-I. Yeom, F. Rotermund, S. Bae, B. Hee Hong, A. Agnesi, C. Fiebig, G. Erbert, X. Mateos, M. Aguiló, F. Diaz, and U. Griebner, "Graphene mode-locked femtosecond Yb:KLuW laser," Appl. Phys. Lett. **101**(16), 161112 (2012).

54. R. Mary, G. Brown, S. J. Beecher, F. Torrisi, S. Milana, D. Popa, T. Hasan, Z. Sun, E. Lidorikis, S. Ohara, A. C. Ferrari, and A. K. Kar, "1.5 GHz picosecond pulse generation from a monolithic waveguide laser with a graphene-film saturable output coupler," Opt. Express **21**(7), 7943 (2013).

55. I. H. Baek, H. W. Lee, S. Bae, B. H. Hong, Y. H. Ahn, D.-I. Yeom, and F. Rotermund, "Efficient Mode-Locking of Sub-70-fs Ti:Sapphire Laser by Graphene Saturable Absorber," Appl. Phys. Express **5**(3), 032701 (2012).

56. Z. Sun, T. Hasan, F. Torrisi, D. Popa, G. Privitera, F. Wang, F. Bonaccorso, D. M. Basko, and A. C. Ferrari, "Graphene Mode-Locked Ultrafast Laser," ACS Nano **4**(2), 803–810 (2010).

57. H. Zhang, Q. Bao, D. Tang, L. Zhao, and K. Loh, "Large energy soliton erbium-doped fiber laser with a graphene-polymer composite mode locker," Appl. Phys. Lett. **95**(14), 141103 (2009).

58. G. Sobon, J. Sotor, and K. M. Abramski, "All-polarization maintaining femtosecond Er-doped fiber laser mode-locked by graphene saturable absorber," Laser Phys. Lett. **9**(8), 581–586 (2012).

59. C. a. Zaugg, Z. Sun, D. Popa, S. Milana, T. Kulmala, R. S. Sundaram, V. J. Wittwer, M. Mangold, M. Golling, Y. Lee, J. H. Ahn, a. C. Ferrari, and U. Keller, "Passively modelocked VECSEL using a single-layer graphene saturable absorber mirror," in *2013 Conference on Lasers & Electro-Optics Europe & International Quantum Electronics Conference CLEO EUROPE/IQEC* (IEEE, 2013), **032701**(2012), pp. 1–1.

60. C. a. Zaugg, V. J. Wittwer, Z. Sun, D. Popa, S. Milana, T. S. Kulmala, R. S. Sundaram, M. Mangold, M. Golling, Y. Lee, J. H. Ahn, a. C. Ferrari, and U. Keller, "Graphene modelocked VECSELs," SPIE Photonics West 2014-LASE Lasers Sources **8966**, 896607 (2014).

61. F. Canbaz, N. Kakenov, C. Kocabas, U. Demirbas, and A. Sennaroglu, "Graphene mode-locked Cr:LiSAF laser at 850 nm," Opt. Lett. **40**(17), 4110 (2015).

62. F. Canbaz, N. Kakenov, C. Kocabas, U. Demırbas, and A. Sennaroglu, "Generation of sub-20-fs pulses from a graphene mode-locked laser," Opt. Express **25**(3), 2834 (2017).

63. W. B. Cho, J. W. Kim, H. W. Lee, S. Bae, B. H. Hong, S. Y. Choi, I. H. Baek, K. Kim, D.-I. Yeom, and F. Rotermund, "High-quality, large-area monolayer graphene for efficient bulk laser mode-locking near 1.25 μm," Opt. Lett. **36**(20), 4089 (2011).

64. J. W. Kim, S. Y. Choi, B. H. Jung, D. Il Yeom, and F. Rotermund, "Applicability of graphene flakes as saturable absorber for bulk laser mode-locking," Appl. Phys. Express **6**(3), (2013).

65. I. Baylam, O. Balci, N. Kakenov, C. Kocabas, and A. Sennaroglu, "Graphene-gold supercapacitor as a voltage controlled saturable absorber for femtosecond pulse generation," Opt. Lett. **41**(5), 910 (2016).

66. C. Cihan, C. Kocabas, U. Demirbas, and A. Sennaroglu, "Graphene mode-locked femtosecond Alexandrite laser," Opt. Lett. **43**(16), 3969 (2018).

67. S. D. Di Dio Cafiso, E. Ugolotti, A. Schmidt, V. Petrov, U. Griebner, A. Agnesi, W. B. Cho, B. H. Jung, F. Rotermund, S. Bae, B. H. Hong, G. Reali, and F. Pirzio, "Sub-100-fs mode-locking of the Cr: YAG laser using monolayer graphene saturable absorber," CLEO Sci. Innov. CLEO_SI 2013 **38**(10), 1745–1747 (2013).

68. J. Ma, G. Xie, P. Lv, W. Gao, P. Yuan, L. Qian, U. Griebner, V. Petrov, H. Yu, H. Zhang, and J. Wang, "Wavelength-Versatile Graphene-Gold Film Saturable Absorber Mirror for Ultra-Broadband Mode-Locking of Bulk Lasers," Sci. Rep. **4**(1), 5016 (2015).

69. C.-C. Lee, T. R. Schibli, G. Acosta, and J. S. Bunch, "Ultra-short optical pulse generation with single-layer graphene," J. Nonlinear Opt. Phys. Mater. **19**(04), 767–771 (2010).

70. S. C. Xu, B. Y. Man, S. Z. Jiang, C. S. Chen, M. Liu, C. Yang, S. B. Gao, D. J. Feng, G. D. Hu, Q. J. Huang, X. F. Chen, and C. Zhang, "Direct growth of graphene on quartz substrate as saturable absorber for femtosecond solid-state laser," Laser Phys. Lett. **11**(8), 085801 (2014).

71. J. Ma, H. Huang, K. Ning, X. Xu, G. Xie, L. Qian, K. P. Loh, and D. Tang, "Generation of 30 fs pulses from a diode-pumped graphene mode-locked Yb:CaYAlO_4 laser," Opt. Lett. **41**(5), 890 (2016).

72. W. D. Tan, C. Y. Su, R. J. Knize, G. Q. Xie, L. J. Li, and D. Y. Tang, "Mode locking of ceramic Nd:yttrium aluminum garnet with graphene as a saturable absorber," Appl. Phys. Lett. **96**(3), 031106 (2010).

73. Z. Sun, X. C. Lin, H. J. Yu, T. Hasan, F. Torrisi, L. Zhang, L. Sun, L. Guo, W. Hou, J. M. Li, and A. C. Ferrari, "High-power Ultrafast Solid-state Laser Using Graphene Based Saturable Absorber," in *CLEO:2011 - Laser Applications to Photonic Applications* (OSA, 2011), **4**(12), p. JWA79.

74. J. Liu, Y. G. Wang, Z. S. Qu, L. H. Zheng, L. B. Su, and J. Xu, "Graphene oxide absorber for 2 μm passive mode-locking Tm:YAlO3 laser," Laser Phys. Lett. **9**(1), 15–19 (2012).

75. A. A. Lagatsky, Z. Sun, T. S. Kulmala, R. S. Sundaram, S. Milana, F. Torrisi, O. L. Antipov, Y. Lee, J. H. Ahn, C. T. a Brown, W. Sibbett, and a. C. Ferrari, "2 μm solid-state laser mode-locked by single-layer graphene," Appl. Phys. Lett. **102**(1), 013113 (2013).

76. Y. Wang, W. Chen, M. Mero, L. Zhang, H. Lin, Z. Lin, G. Zhang, F. Rotermund, Y. J. Cho, P. Loiko, X. Mateos, U. Griebner, and V. Petrov, "Sub-100 fs Tm:MgWO_4 laser at 2017 nm mode locked by a graphene saturable absorber," Opt. Lett. **42**(16), 3076 (2017).

77. H. Zhang, D. Y. Tang, L. M. Zhao, Q. L. Bao, and K. P. Loh, "Large energy mode locking of an erbium-doped fiber laser with atomic layer graphene," Opt. Express **17**(20), 17630 (2009).

78. Z. Sun, T. Hasan, F. Torrisi, D. Popa, G. Privitera, F. Wang, F. Bonaccorso, D. M. Basko, and A. C. Ferrari, "Graphene Mode-Locked Ultrafast Laser," ACS Nano **4**(2), 803–810 (2010).

79. J. Gene, N. H. Park, H. Jeong, S. Y. Choi, F. Rotermund, D.-I. Yeom, and B. Y. Kim, "Optically controlled in-line graphene saturable absorber for the manipulation of pulsed fiber laser operation," Opt. Express **24**(19), 21301 (2016).

80. G. Sobon, J. Sotor, I. Pasternak, A. Krajewska, W. Strupinski, and K. M. Abramski, "Multilayer graphene-based saturable absorbers with scalable modulation depth for mode-locked Er- and Tm-doped fiber lasers," Opt. Mater. Express **5**(12), 2884 (2015).

81. J. Sotor, M. Pawliszewska, G. Sobon, P. Kaczmarek, A. Przewolka, I. Pasternak, J. Cajzl, P. Peterka, P. Honzátko, I. Kašík, W. Strupinski, and K. Abramski, "All-fiber Ho-doped mode-locked oscillator based on a graphene saturable absorber," Opt. Lett. **41**(11), 2592 (2016).

82. J. Sotor, J. Bogusławski, T. Martynkien, P. Mergo, A. Krajewska, A. Przewłoka, W. StrupiŃski, and G. SoboŃ, "All-polarization-maintaining, stretched-pulse Tm-doped fiber laser, mode-locked by a graphene saturable absorber," Opt. Lett. **42**(8), 1592 (2017).

83. H.-R. Chen, C.-Y. Tsai, H.-M. Cheng, K.-H. Lin, and W.-F. Hsieh, "Passive mode locking of ytterbium- and erbium-doped all-fiber lasers using graphene oxide saturable absorbers," Opt. Express **22**(11), 12880 (2014).

84. M. J. Lederer, B. Luther-Davies, H. H. Tan, and C. Jagadish, "An antiresonant Fabry-Perot saturable absorber for passive mode-locking fabricated by metal-organic vapor phase epitaxy and ion implantation design, characterization, and mode-locking," IEEE J. Quantum Electron. **34**(11), 2150–2161 (1998).

85. F. X. Kartner, I. D. Jung, and U. Keller, "Soliton mode-locking with saturable absorbers," IEEE J. Sel. Top. Quantum Electron. **2**(3), 540–556 (1996).

86. Lumentum, "PALLAS Compact Ti:sapphire Laser Datasheet," https://www.photonicsolutions.co.uk/upfiles/pallas-web.pdf.

87. O. Svelto, *Principles of Lasers* (n.d.).

88. M. N. Cizmeciyan, J. W. Kim, S. Bae, B. H. Hong, F. Rotermund, and a Sennaroglu, "Graphene mode-locked femtosecond Cr:ZnSe laser at 2500 nm.," Opt. Lett. **38**(3), 341–3 (2013).

89. R. Akbari, K. A. Fedorova, E. U. Rafailov, and A. Major, "Diode-pumped ultrafast Yb:KGW laser with 56 fs pulses and multi-100 kW peak power based on SESAM and Kerr-lens mode locking," Appl. Phys. B **123**(4), 123 (2017).

90. D. J. H. C. Maas, B. Rudin, A.-R. Bellancourt, D. Iwaniuk, S. V. Marchese, T. Südmeyer, and U. Keller, "High precision optical characterization of semiconductor saturable absorber mirrors," Opt. Express **16**(10), 7571 (2008).

91. K. F. Mak, M. Y. Sfeir, Y. Wu, C. H. Lui, J. a. Misewich, and T. F. Heinz, "Measurement of the Optical Conductivity of Graphene," Phys. Rev. Lett. **101**(19), 196405 (2008).

92. C. Hönninger, R. Paschotta, F. Morier-Genoud, M. Moser, and U. Keller, "Q-switching stability limits of continuous-wave passive mode locking," J. Opt. Soc. Am. B **16**(1), 46 (1999).

93. G. D. Houser and E. Garmire, "Balanced detection technique to measure small changes in transmission," Appl. Opt. **33**(6), 1059 (1994).

94. Stanford Research Systems, "Lock-In Amplifier Application Notes," https://www.thinksrs.com/downloads/pdfs/applicationnotes/AboutLIAs.pdf.

95. C. A. Zaugg, Z. Sun, V. J. Wittwer, D. Popa, S. Milana, T. S. Kulmala, R. S. Sundaram, M. Mangold, O. D. Sieber, M. Golling, Y. Lee, J. H. Ahn, A. C. Ferrari, and U. Keller, "Ultrafast and widely tuneable vertical-external-cavity surface-emitting laser, mode-locked by a graphene-integrated distributed Bragg reflector," Opt. Express **21**(25), 31548 (2013).

96. G. J. Spühler, K. J. Weingarten, R. Grange, L. Krainer, M. Haiml, V. Liverini, M. Golling, S. Schön, and U. Keller, "Semiconductor saturable absorber mirror structures with low saturation fluence," Appl. Phys. B Lasers Opt. **81**(1), 27–32 (2005).

Chapter 6: Final remarks

6.1 Summary and future work

The subject matter of this thesis centres around the design and development of ultrafast Ti:sapphire lasers in a compact and low-cost context. Titanium-doped sapphire is one of the most versatile and widely used laser gain media today, which is mainly due to the ultrabroad gain bandwidth, allowing for widely-tunable lasers and femtosecond pulse generation [1]. Its excellent thermo-mechanical properties also allow for average power in the Watts to tens of Watts regimes and high pulse energy operation. However, Ti:sapphire lasers remain expensive, bulky, and complex, mainly due to the pump source, which is typically a frequency-doubled diode-pumped solid state laser (DPSSL) or a frequency-doubled optically pumped semiconductor laser (OPSL). An attractive solution to reduce the size, cost and complexity of these lasers is to replace the conventional pump source with laser diodes.

In Chapter 1 an overview of ultrafast lasers was given, including their properties and applications. Some background theory regarding ultrashort pulse generation and characterisation was also given. A comparative review of the various types of ultrafast laser sources was given, including justification as to why diode-pumped Ti:sapphire lasers are an attractive option to consider in the pursuit of lower-cost and compact ultrashort pulse laser sources, and identification of areas in which they could be improved.

In Chapter 2 the background theory of Ti:sapphire material properties were discussed, as were the advantages and disadvantages of diode-pumping when compared to conventional pump laser options. The design, construction, and characterisation of a CW diode-pumped Ti:sapphire laser was described. Various available Ti:sapphire crystals of differing FOM and length were tested and characterised in the setup with the performance recorded for each. It was concluded that when pumping at 450 nm, supplier-stated FOM cannot be relied upon to predict performance as the pump-induced loss associated with pump wavelengths less than 478 nm can result in significant parasitic losses at the laser wavelength. The best-performing crystal in terms of output power was chosen for the mode-locking experiments in Chapter 3.

In Chapter 3 the design, construction, and characterisation of various ultrafast diode-pumped Ti:sapphire lasers with broad tunability were described. As far as the author is aware this is the first time broad wavelength tunability has been demonstrated with ultrafast diode-pumped Ti:sapphire lasers. Beginning with a SESAM mode-locked diode-pumped Ti:sapphire laser, output powers as high as 433 mW were produced and pulses as short as 62 fs in

duration. Femtosecond pulse operation was maintained over a centre wavelength tuning range of 788-825 nm (37 nm). Wavelength tuning was achieved by combination of an intracavity prism pair (used for dispersion compensation) and an intracavity slit. The tuning range was ultimately limited by the operating reflectivity (775-840 nm) of the SESAM device itself in this configuration.

To further increase the wavelength tunability of the ultrafast diode-pumped Ti:sapphire laser, the mode-locking mechanism was changed from SESAM mode-locking to Kerr-lens mode-locking (KLM), as KLM is not limited in bandwidth in the same way the SESAM is. In the first design iteration, an un-optimised resonator design was used, with only minor changes to the resonator compared to the SESAM mode-locked design. This was successful in extending the centre wavelength tuning range to 755-875 nm (120 nm). Shorter pulses were achieved in this configuration, with the shortest being 40 fs in duration. However, the average output power was reduced, with a maximum of 158 mW in this configuration.

In the second design iteration of the KLM diode-pumped Ti:sapphire laser, steps were taken to optimise the resonator design for hard-aperture KLM. Once these design changes were implemented, significantly higher average output powers were realised, up to a maximum of 382 mW. The improved performance was assumed to due to the better pump-cavity mode overlap at the edge of cavity stability when comparing the optimised and un-optimised resonator designs. It was also assumed that better discrimination between KLM and CW regime cavity modes was achieved, as the optimised resonator had a larger cavity mode allowing for more precise use of the hard aperture, and that this contributed to the improved performance. The centre wavelength tuning range in this configuration was 755-875 nm (120 nm) and the shortest pulses produced were 54 fs.

The degree of wavelength tunability demonstrated here while maintaining femtosecond pulse operation moves ultrafast diode-pumped Ti:sapphire lasers a step closer to the performance of conventionally-pumped ultrafast Ti:sapphire laser technology and thus more compact, less costly, and complex ultrafast Ti:sapphire lasers. Wide wavelength tunabilty is an important aspect for many applications, including multiphoton microscopy [2,3] and supercontinuum generation [4].

In Chapter 4 various cavity configurations were analysed and proposed with the intention of realising GHz pulse repetition rates in an ultrafast diode-pumped Ti:sapphire laser. Ultrafast lasers with a GHz repetition rate are interesting for a number of applications, including femtosecond laser-based frequency combs where the large spacing of the comb's modes

enables much easier individual mode identification with off the shelf equipment compared to an ultrafast laser operating in the MHz range. This aspect is beneficial to applications in spectroscopy [5] and the calibration of astronomical spectrographs [6]. Ultrafast lasers with GHz repetition rate also have a higher power-per-mode as the mode spacing is given by the repetition rate, therefore when comparing ultrafast lasers with 1 GHz and 100 MHz repetition rates, the 1 GHz laser will have 10 times fewer modes for the same total span and thus 10 times higher power-per-mode. Studies have noted potential advantages for a number of applications including direct comb spectroscopy [7], multiphoton imaging [8], and second harmonic generation imaging [9].

Two different cavity configurations were designed and analysed: KLM in a ring resonator configuration and SESAM mode-locking in a Z-shape standing wave resonator configuration. Efficient continuous wave operation was achieved, however, mode-locked operation was not reached with either configuration, with project time constraints preventing full investigation into the reasons why.

In the KLM ring resonator configuration, it was suspected that the failure to achieve pulsed operation was due to the intracavity pulse energy not being sufficient to initiate KLM given the potential high repetition rate dictated by the cavity length. A better understanding of the laser dynamics in the presence of the Kerr-lens through development of a Magni model [10] would lead to a better understanding of the optimal resonator configuration. Other avenues to investigate would be using a slightly convex mirror in place of one of the plane resonator mirrors, which has been shown to create a larger power-dependent modulation of the beam waist inside the crystal and thus make it easier to achieve mode-locking [11].

In Z-shape resonator configuration, it was suspected that mode-locked operation was prevented by damage to the SESAM, caused by a combination of random intensity fluctuations present before mode-locking is established and the small beam waist incident on the SESAM leading to high fluence. More investigation would be required to determine whether this was the case.

In Chapter 5 monolayer graphene samples were characterised in a differential transmission setup and assessed on the suitability for their use in mode-locking a diode-pumped Ti:sapphire laser. The saturable absorption parameters of the graphene samples were extracted via curve fitting, resulting in a saturation fluence of (41 ± 27) μJ/cm^2, a saturable loss of (1.01 ± 0.15) % and a non-saturable loss of (0.42 ± 0.09) %. These measured values are in broad agreement with other's work on monolayer graphene, with saturation fluences in the range of 10-100

μJ/cm^2, saturable losses in the range of 0.5-2%, and non-saturable losses in the range of 1-2% [12–16]. The saturable absorption parameters measured in this project were concluded to be suitable for passive mode-locking of bulk-solid state lasers, and comparable to typical saturable absorber parameters of SESAMs used for this purpose.

Building on this work, a range of laser mirrors incorporating a monolayer of graphene (GSAMs) were designed using a software package for thin-film optical coating design. These designs were then manufactured by external companies (SLS Optics Limited and Graphenea). These GSAM designs were then tested in a diode-pumped Ti:sapphire laser test bed. Ultimately none of the designs manufactured were successful in realising mode-locked operation. More investigation would be required to ascertain the reasons why mode-locking was not achieved. To this end it would be useful to directly measure the saturable absorber parameters of the GSAMs themselves to see if similar values are obtained as with the monolayer graphene on quartz substrate samples. It is possible that some contamination could have been introduced at some point during the manufacturing process having some unknown effect on device performance, as the devices needed to be sent to different supplier to carry out different stages of the manufacturing process. This task would require reworking the differential transmission setup so that it operates on reflection [17].

Another avenue to investigate would be Raman spectroscopy of the GSAMs, which help identify whether graphene is present, what form it takes (monolayer, bilayer etc.), and how uniform the layer is. Finally, quantifying the nonlinear refractive index (n_2) of the GSAM devices would be useful, as this could potentially have an effect on the mode-locking regime.

6.2 Outlook

With the continued development and improvements seen in GaN laser diode technology since the first demonstration of diode-pumped Ti:sapphire in 2009, the gap in performance levels between conventionally-pumped and diode-pumped ultrafast Ti:sapphire lasers has continued to narrow with many important applications being demonstrated [18–20].

The diode-pumped Ti:sapphire laser sources developed during the course of this thesis can be said to have demonstrated important performance parameters that bring them closer to matching the performance of their conventionally pumped counterparts, namely a wide wavelength tunability while maintaining femtosecond pulse operation and high average and peak powers suitable for many applications [9,18–20]. Investigation into the suitability of graphene saturable absorber parameters for femtosecond pulse generation in diode-pumped

Ti:sapphire has shown that they have the potential to enable cheaper lasers over a greater wavelength range than those that use SESAM technology, and with more alignment flexibility than KLM Ti:sapphire lasers. However, work still needs to be done to determine why the GSAM designs did not work and demonstrate them experimentally. The work carried out in this thesis on the topic of achieving GHz repetition rates in diode-pumped Ti:sapphire should provide a good basis for realising GHz ultrafast Ti:sapphire experimentally – something which has not yet been achieved. This would require a bit more work to understand the KLM dynamics in the case of the ring resonator design, or alternatively, an investigation into suspected damage of the SESAM in the Z-shape resonator design and perhaps research in lower saturation fluence SESAMs.

To conclude, as the performance levels continue to improve a new generation of low-cost and compact ultrafast Ti:sapphire lasers using laser diodes as their pump source are highly likely to find more widespread use in a variety of applications new and old [21–24].

6.3 References

1. W. Koechner, *Solid-State Laser Engineering - 6th Edition* (2014).
2. K. Koenig, "Multiphoton microscopy in life sciences," J. Microsc. **200**(2), 83–104 (2000).
3. J. M. Girkin and G. McConnell, "Advances in laser sources for confocal and multiphoton microscopy," Microsc. Res. Tech. **67**(1), 8–14 (2005).
4. K. P. Hansen, J. R. Jensen, D. Birkedal, J. M. Hvam, and A. Bjarklev, "Pumping wavelength dependence of super continuum generation in photonic crystal fibers," in *Optical Fiber Communication Conference and Exhibit* (Opt Soc. America, 2002), (3), pp. 622–624.
5. D. C. Heinecke, A. Bartels, T. M. Fortier, D. A. Braje, L. Hollberg, and S. A. Diddams, "Optical frequency stabilization of a 10 GHz Ti:sapphire frequency comb by saturated absorption spectroscopy in r 87 ubidium," Phys. Rev. A - At. Mol. Opt. Phys. **80**(5), 1–7 (2009).
6. R. A. McCracken, É. Depagne, R. B. Kuhn, N. Erasmus, L. A. Crause, and D. T. Reid, "Wavelength calibration of a high resolution spectrograph with a partially stabilized 15-GHz astrocomb from 550 to 890 nm," Opt. Express **25**(6), 6450 (2017).
7. M. C. Stowe, M. J. Thorpe, A. Pe'er, J. Ye, J. E. Stalnaker, V. Gerginov, and S. A. Diddams, "Direct frequency comb spectroscopy," Adv. At. Mol. Opt. Phys. **55**(07), 1–60 (2008).
8. A. Ehlers, I. Riemann, S. Martin, R. Le Harzic, A. Bartels, C. Janke, and K. König, "High (1 GHz) repetition rate compact femtosecond laser: A powerful multiphoton tool for nanomedicine and nanobiotechnology," J. Appl. Phys. **102**(1), 1–6 (2007).
9. S.-W. Chu, T.-M. Liu, C.-K. Sun, C.-Y. Lin, and H.-J. Tsai, "Real-time second-harmonic-generation microscopy based on a 2-GHz repetition rate Ti:sapphire laser," Opt. Express **11**(8), 933 (2003).
10. G. Cerullo, S. De Silvestri, and V. Magni, "Self-starting Kerr-lens mode locking of a Ti:sapphire laser," Opt. Lett. **19**(14), 1040 (1994).
11. T. M. Fortier, A. Bartels, and S. A. Diddams, "Octave-spanning Ti:sapphire laser with a repetition rate >1 GHz for optical frequency measurements and comparisons," Opt. Lett. **31**(7), 1011 (2006).
12. M. N. Cizmeciyan, J. W. Kim, S. Bae, B. H. Hong, F. Rotermund, and a Sennaroglu, "Graphene mode-locked femtosecond Cr:ZnSe laser at 2500 nm.," Opt. Lett. **38**(3), 341–3 (2013).
13. C. a. Zaugg, V. J. Wittwer, Z. Sun, D. Popa, S. Milana, T. S. Kulmala, R. S. Sundaram, M. Mangold, M. Golling, Y. Lee, J. H. Ahn, a. C. Ferrari, and U. Keller, "Graphene modelocked VECSELs," SPIE Photonics West 2014-LASE Lasers Sources **8966**, 896607 (2014).

14. W. B. Cho, J. W. Kim, H. W. Lee, S. Bae, B. H. Hong, S. Y. Choi, I. H. Baek, K. Kim, D.-I. Yeom, and F. Rotermund, "High-quality, large-area monolayer graphene for efficient bulk laser mode-locking near 1.25 μm," Opt. Lett. **36**(20), 4089 (2011).

15. I. H. Baek, H. W. Lee, S. Bae, B. H. Hong, Y. H. Ahn, D.-I. Yeom, and F. Rotermund, "Efficient Mode-Locking of Sub-70-fs Ti:Sapphire Laser by Graphene Saturable Absorber," Appl. Phys. Express **5**(3), 032701 (2012).

16. F. Canbaz, N. Kakenov, C. Kocabas, U. Demırbas, and A. Sennaroglu, "Generation of sub-20-fs pulses from a graphene mode-locked laser," Opt. Express **25**(3), 2834 (2017).

17. D. J. H. C. Maas, B. Rudin, A.-R. Bellancourt, D. Iwaniuk, S. V. Marchese, T. Südmeyer, and U. Keller, "High precision optical characterization of semiconductor saturable absorber mirrors," Opt. Express **16**(10), 7571 (2008).

18. K. Gürel, V. J. Wittwer, S. Hakobyan, S. Schilt, and T. Südmeyer, "Carrier envelope offset frequency detection and stabilization of a diode-pumped mode-locked Ti:sapphire laser," Opt. Lett. **42**(6), 1035 (2017).

19. P. Castro-Marin, T. Mitchell, J. Sun, and D. T. Reid, "Characterization of a carrier-envelope-offset-stabilized blue- and green-diode-pumped Ti:sapphire frequency comb," Opt. Lett. **44**(21), 5270 (2019).

20. A. Rohrbacher, O. E. Olarte, V. Villamaina, P. Loza-Alvarez, and B. Resan, "Multiphoton imaging with blue-diode-pumped SESAM-modelocked Ti:sapphire oscillator generating 5 nJ 82 fs pulses," Opt. Express **25**(9), 10677 (2017).

21. D. Stevenson, B. Agate, X. Tsampoula, P. Fischer, C. T. A. Brown, W. Sibbett, A. Riches, F. Gunn-Moore, and K. Dholakia, "Femtosecond optical transfection of cells:viability and efficiency," Opt. Express **14**(16), 7125 (2006).

22. J. Ando, G. Bautista, N. Smith, K. Fujita, and V. R. Daria, "Optical trapping and surgery of living yeast cells using a single laser," Rev. Sci. Instrum. **79**(10), (2008).

23. A. Bartels, T. Dekorsy, and H. Kurz, "Femtosecond Ti:sapphire ring laser with a 2-GHz repetition rate and its application in time-resolved spectroscopy," Opt. Lett. **24**(14), 996 (1999).

24. M.-C. Chen, M. R. Gerrity, S. Backus, T. Popmintchev, X. Zhou, P. Arpin, X. Zhang, H. C. Kapteyn, and M. M. Murnane, "Spatially coherent, phase matched, high-order harmonic EUV beams at 50 kHz," Opt. Express **17**(20), 17376 (2009).

Appendix

List of publications

Journals

1. Jamie C. E. Coyle, Alan J. Kemp, John-Mark Hopkins, and Alexander A. Lagatsky, "Ultrafast diode-pumped Ti:sapphire laser with broad tunability," Opt. Express 26, 6826-6832 (2018)

Conferences

1. J. C. E. Coyle, A. J. Kemp, J. Hopkins, and A. A. Lagatsky, "A Broadly Tunable Ultrafast Diode-Pumped Ti:sapphire Laser," in *Laser Congress 2017 (ASSL, LAC)*, OSA Technical Digest (online) (Optical Society of America, 2017), paper JTh2A.21.
2. J. C. E. Coyle, J. Hopkins, A. A. Lagatsky, and A. J. Kemp, "Titanium Sapphire: A Decade of Diode-laser Pumping," in *2019 Conference on Lasers and Electro-Optics Europe and European Quantum Electronics Conference*, OSA Technical Digest (Optical Society of America, 2019), paper ca_7_1.